Investigation of interfacial and bulk physical properties of hybrid perovskite-based devices

Yan-Fang Chen

université de BORDEAUX

THÈSE PRÉSENTÉE

POUR OBTENIR LE GRADE DE

DOCTEUR DE

L'UNIVERSITÉ DE BORDEAUX

ÉCOLE DOCTORALE DES SCIENCES PHYSIQUES ET DE L'INGENIEUR

SPÉCIALITÉ : ELECTRONIQUE

Par Yan-Fang CHEN

Investigation of interfacial and bulk physical properties of hybrid perovskite-based devices

Sous la direction de : Dr. Lionel HIRSCH
(co-directeur : Dr. Dario BASSANI)

Soutenue le : 22 novembre 2016

Membres du jury :

Mme DELEPORTE, Emmanuelle	Professeur, ENS Cachan	Rapporteur
M. EVEN, Jacky	Professeur, INSA de Rennes	Rapporteur
M. CAHEN, David	Professeur, Weizmann Institute of Science	Examinateur
M. TOUPANCE, Thierry	Professeur, Université de Bordeaux	Examinateur
M. HIRSCH, Lionel	Directeur de Recherche, Université de Bordeaux	Directeur de thèse
M. BASSANI, Dario	Directeur de Recherche, Université de Bordeaux	Directeur de thèse

Acknowledgement

Someone once said: “Bad students ask questions that are short, but with long answers.” In this sense, I am certainly the worst student in scientific research, as I have always asked the shortest question: What is science, and what is research?

The following 150 or so pages represent a partial answer to these questions, which, even though far from being complete, is already long. In the end, I think the appropriate question to be posed should be in a different form: Instead of asking what, the real question is “who,” *i. e.*, who is doing the research.

For this I have learned most from my two supervisors, Dr. Lionel Hirsch and Dr. Dario Bassani. Learning from their examples is the most valuable experience I received over the past 4 years. Be it not possible to capture their whole personalities on paper, a few examples will have to do. When I started to write the thesis, Lionel told me that “impossible is not a French word.” And indeed it is not. This optimism and humor were one important factor getting me through the uncertain process of writing. Dario’s rebuttal on parts of my thesis: “This is simply wrong” also means a lot, while in a much different sense. For me that means a difference of opinion had surfaced, and the dialogue, which is an important part of research, could begin.

Other than their encouragement and patience, I’m also immensely grateful for their joint effort in pushing me through. The heart-rending weekly meetings posed strong pressure on me but also meant my supervisors had to put into much effort and time. During the last phase, their meticulous reading, giving suggestions and corrections were what made the content presentable.

To this I also have to thank the jury member for reviewing my thesis and giving invaluable suggestions. The day of the defense is one of the days I should not forget.

The completion of this thesis in its current form wouldn’t have happened without all the happening in the world, but we do need to define a certain range of relevance. Most directly, it would not have happened without the fateful week I spent in ICMoL, University of Valencia. With the guidance of Dr. Henk Bolink and David Forgács, we were able to make the “good” material for the first time and further studies could begin. Therefore, I owe much to their kindness, hospitality, and willingness to share and discuss.

With the UPS measurement from Prof. Dr. Wolfram Jaegermann, Dr. Tomas Mayer, and Michael Wussler at Technological University of Darmstadt, and the simulation performed by Prof. Raphaël Clerc from University of Lyon, the first major result was completed and we were able to move on to other phases.

Needless to say, the daily operation of the labs is indispensible for any work to be done. To this I have to thank all the members from IMS and ISM, in particular Dr. Sylvain Chambon, Dr. Mamatimin Abbas, and Sokha Khiev for their assistance and teaching in making experiments. Also thank Dr. Guillaume Wantz, Dr. Laurence Vignau, Dr. Thérèse Gorisse, Dr. Uyxing Vongsaysy, Dr. Florian Colleaux, Dr. Frederic Guillain, Dr. Maxime Le Bail, Dr. Abduleziz Ablat, Dr. Gildas Laurans, Dr. Mylène Le Borgne, Dr. Élodie Destouesse, Dr. Marcin Kielar, Dr. William Greenbank, Geoffroy Houin, Yolande Murat, Marco Pereira, and Florence Archet for their help on many aspects, and for their forgiveness when I messed with their experiments inadvertently. Their friendliness is one of the best impressions I have about France.

I would also like to thank Ms. Sabine Goma from ENSCBP for performing the XRD analysis, and Dr. Gilles Pecastaings of LCPO for AFM measurements.

Special thanks to Dr. Chih-Kai Liang, whose help in my first year in France was lifesaving. His assistance and patience both in the lab and in personal life are much appreciated.

Another person I would like to give thanks to is Dr. Yu-Tang Tsai. His little-more-than-one-year stay in Bordeaux saved me from a potential social black hole. It is safe to say that without his company and discussions I would not have gotten to this point.

Résumé

Les Pérovskites hybrides organique-inorganique (PHOIs) ont suscité d'intenses recherches au cours des dernières années. Dans cette thèse, nous avons dans un premier temps mis au point les différents processus de préparation des échantillons et réalisé une caractérisation complète des films par microscopie à force atomique, spectroscopie photo-électronique par rayons X, mesure du potentiel de surface par sonde de Kelvin et mesure de la mobilité des charges par temps de vol. La distribution des pièges à l'interface PHOI/Au a été étudiée via des mesure *J-V-L* en fonction de la température combinées avec des simulations numériques. Les relaxations diélectriques dans les PHOIs, tels que la migration des ions et l'orientation du dipôle du cation organique, ont été étudiés par spectroscopie d'impédance en fonction de la température. Dans la dernière partie de cette thèse, nous présentons une étude originale qui démontre un mouvement des protons du groupement ammonium des cations organiques à l'interface avec le PEDOT : PSS.

Mots clés : semi-conducteurs hybrides, effet d'interface, pièges, relaxations diélectriques, spectroscopie d'impédance

Abstract

Hybrid-organic-inorganic perovskites (HOIPs) have provoked intense research over the recent years. In this thesis, we contribute to this investigation by first examining the results of different solution preparation processes, followed by characterizing the films using atomic force microscopy, X-ray diffraction, ultra-violet photoelectron spectroscopy, X-ray photoelectron spectroscopy, Kelvin probe surface potential measurement, and time-of-flight mobility measurement. The state distribution of the HOIP/Au interface was then studied by low temperature *J–V–L* measurement combined with numerical simulation. In the process of these characterizations, it became clear that the dielectric relaxations in HOIPs, such as ion migration and organic cation dipole orientation, play an important role in the material, and the next part of the thesis presents an analysis of these mechanisms with the help of temperature dependent impedance spectroscopy measurement. These studies built the foundations for the final part of the thesis, where we investigated a so far elusive subject in HOIPs, the migration of protons.

Keywords : Hybrid semiconductors, interface effects, trap states, dielectric relaxation, impedance spectroscopy

Unité de recherche : Laboratoire de l'intégration du matériau au système (IMS) – UMR 5218, et l'institut des Sciences Moléculaires (ISM) – UMR 5255

Contents

Chapter 1

Introduction

Hybrid organic-inorganic perovskite (HOIP) materials have drawn immense interest due to the recent rise in their applications found in optoelectronic devices. Their use in solar cells started in 2009 with a photoconversion efficiency of a few %, advancing to more than 20% in less than 10 years.[1] The rate of increase is unprecedented amongst photovoltaic technologies, making HOIP materials one of the most promising candidates for the next generation of solar cells to solve the earth's energy crisis (Fig. 1-1). Besides photovoltaics, applications in photodetectors,[2] light emitting diodes,[3,4,5] and lasers,[6,7] have also been explored and shown promising results.

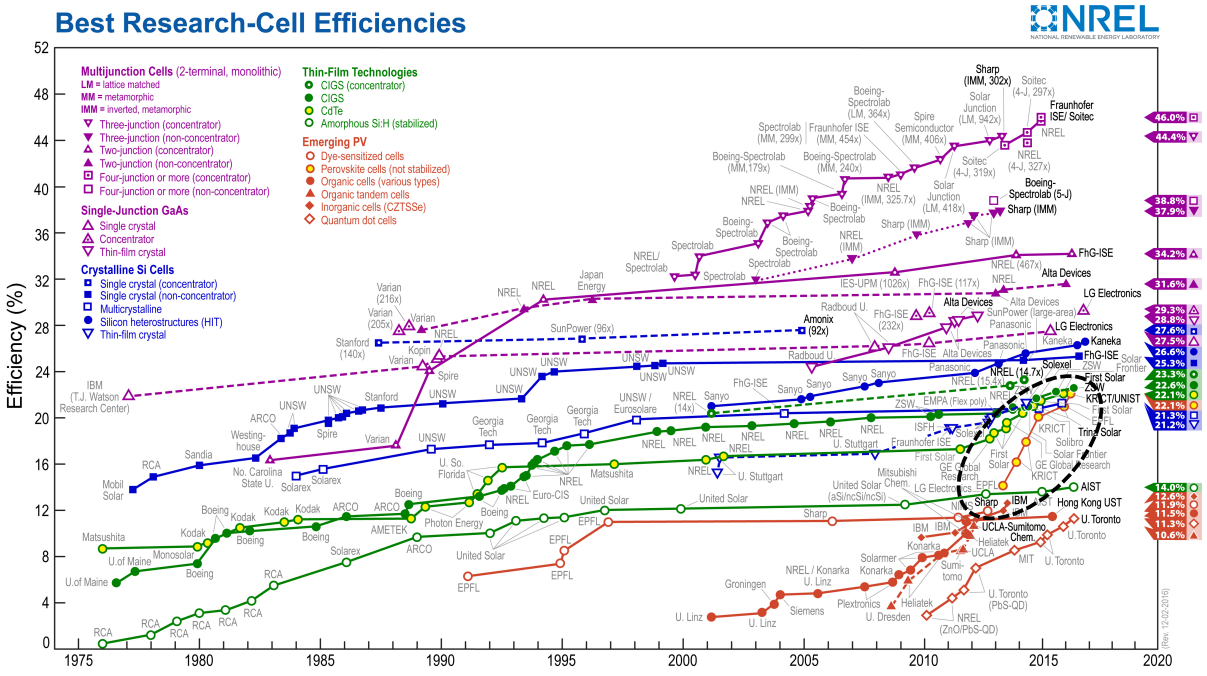

Fig. 1-1 NERL solar cell efficiency chart. The increase rate of HOIP solar cell efficiency is remarkable compared to other materials and technologies. Figure adapted from ref 1.

HOIPs process a crystal structure belonging to the mineral group of perovskites, formed by an inorganic framework and organic cations. The perovskite crystal structure, named after the Russian mineralogist Lev Perovski, has the formula ABX_3, with A and B denoting two different species of cations, and X an anion (Fig. 1-2 left). The A sites are 12-coordinated while the B sites 6-coordinated, and the size of A is larger than that of B. With the A sites in the interstices, the BX_6 forms a corner-sharing octahedral network,[8] which becomes distorted from the cubic structure when the crystal assumes other crystalline phases, e. g., tetragonal, orthorhombic, or rhombohedral. For HOIPs, the A sites are occupied by organic cations such as methylammonium (MA) or formamidinium (FA) ions, while the B sites are either lead (II),

tin (II), or germanium ions, and the X sites are generally halides (Fig. 1-2 right).

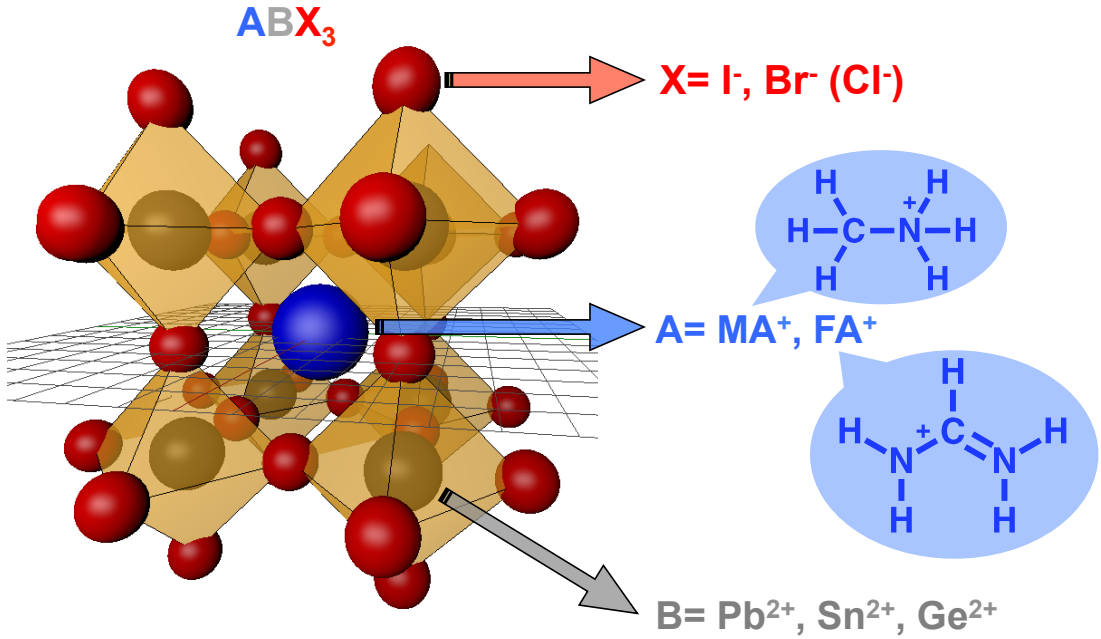

Fig. 1-2 Illustration of the perovskite crystal structure (left) and compositions of commonly used HOIPs (right). For simplicity, the crystal structure is in the cubic phase, while tetragonal, orthorhombic or rhombohedral distortions are also frequent in perovskites.

HOIPs combine the advantages of both organic and inorganic semiconductors. The long carrier diffusion length, low exciton binding energy, and low trap state formation in HOIPs are desirable properties that are more typically found in traditional inorganic semiconductors. On the other hand, low temperature (< 150 ^{o}C) solution processing of HOIPs is characteristic of organic semiconductors. Admittedly, the jump-start of HOIP device fabrication is greatly indebted to the existing technology of organic semiconductor fabrication processes. Examples of the preparation of polycrystalline HOIP thin films are shown in Fig. 1-3. In the thermal evaporation preparation of HOIPs, methylammonium halide and lead halide are evaporated on top of the substrate simultaneously,[9] or sequentially.[10] Other evaporation methods such as flash evaporation are also reported and show good film quality.[11] Likewise, the solution process of HOIP has improved in order to reproducibly achieve high quality films, from one step spin-coating to stacking layer interdiffusion, and other advanced methods.[12] The sample fabrication procedure used in this thesis (Chapter 2) is a solution process due to its advantage of low cost, fast processing, and easier extension towards large area production.

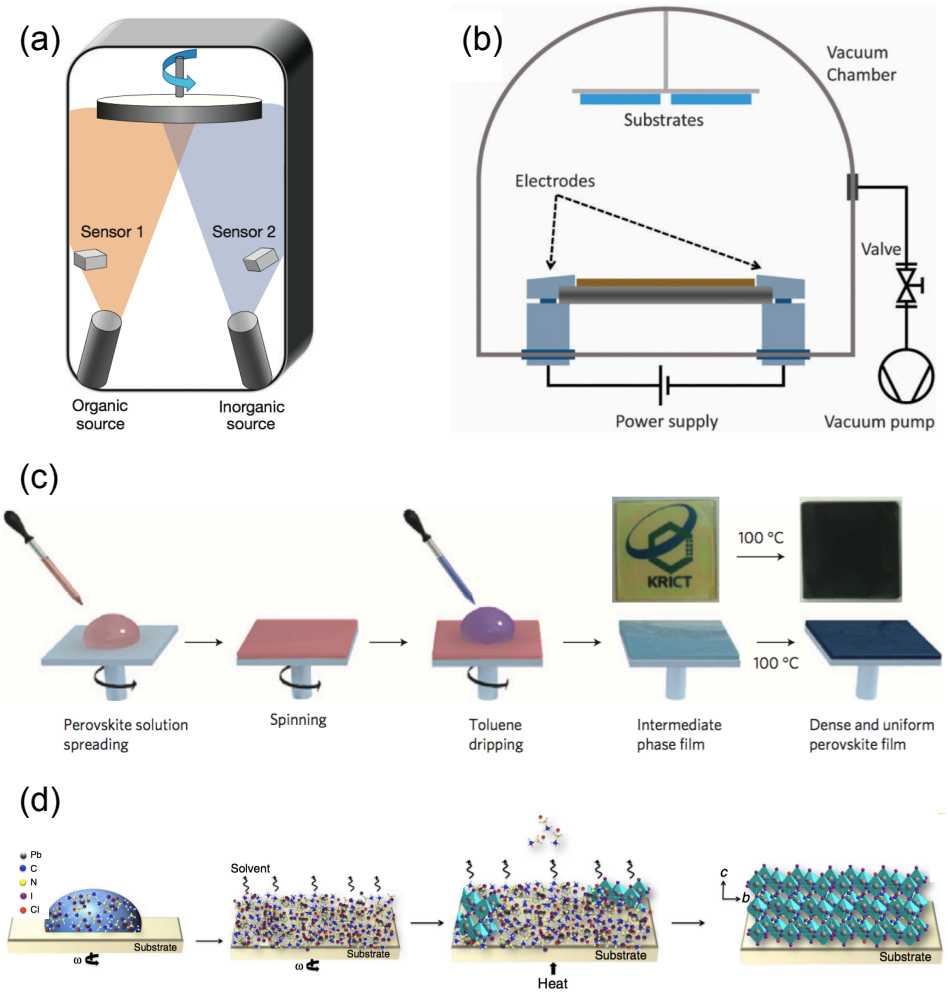

Fig. 1-3 Examples of polycrystalline HOIP thin film preparation: (a), (b) Thermal evaporation. (c), (d) Solution process. Figures adapted with permission form refs 9, 11, 13, and 14, respectively. Copyright 2013, 2014,2015 Nature Publishing Group, 2015 The Royal Chemical Society.

The above-mentioned preparation processes have been applied to the fabrication of HOIP solar cells since Kojima *et al*. used a thin layer of $CH_3NH_3PbI_3$ to replace the dyes in dye-sensitized solar cells (DSCs) in 2009.[15] The so-called extremely-thin-layer (ETA) cells achieved photo conversion efficiency of 3.8% but with poor stability due to the dissolution of the HOIPs in the liquid electrolyte. Afterwards, the study by Lee *et al*. showed that the operation of HOIP solar cell is different from that of DSCs.[16] They showed that the HOIPs can conduct electrons to the anode without the help of TiO_2, which is instead essential for a functional DSC. Further study by Etgar *et al.* showed that $CH_3NH_3PbI_3$ can itself conduct holes.[17] These discoveries paved the way to the construction of "mesoscopic" HOIP solar cells, in which the hole transport material is not infiltrated into the TiO_2 scaffold or is eliminated completely.[18] Later developments showed that planar heterojunction HOIP solar

cells can also achieve comparable efficiency to mesoscopic devices, whether in the direct,[19] or inverted structure.[20,21] The structure evolution of HOIP solar cell is shown in Fig. 1-4.

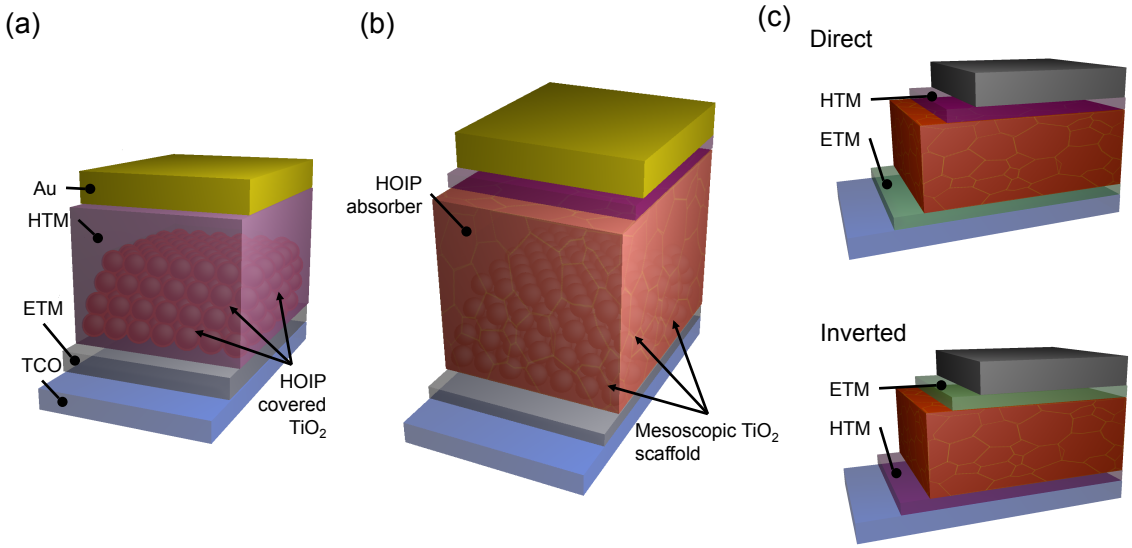

Fig. 1-4 Evolution of HOIP solar cell device architecture. From (a) extremely thin absorber (ETA) cells, (b) mesoscopic structure, to (c) planar heterojunction. The planar heterojunction can be further divided into direct (bottom electron transport layer), and inverted (top electron transport layer) structure. Both mesoscopic structure and planar heterojunction HOIP solar cells have been shown to exhibit high photo conversion efficiencies.

Despite the apparent success in solar cell applications, some issues still beset HOIP solar cells. HOIP solar cells are known to exhibit *I–V* curve hysteresis (dependence of characteristics on scanning rate and direction), which hinders the correct estimate of the power output under defined conditions.[22] Also, the lack of stability is a major drawback for commercialization. Improvements on these issues have been made over the years,[23,24,25,26] but they are far from being resolved yet.

In terms of device physics, many aspects of the photo conversion mechanism remain unclear. Generally, the operation of a solar cell can be classified into either excitonic or non-excitonic (Fig. 1-5). One example of the former is the organic bulk heterojunction solar cell, with exciton binding energy at the order of 1 eV. Silicon photovoltaic belongs to the latter, where photogenerated electron–hole pair can be considered as free charges because the exciton binding energy is less than the thermal energy at room temperature. The low exciton binding energy of HOIPs suggests that the electron–hole pair should be akin to be free from each

other.[27] However, the simple dichotomy doesn't seem to apply in this case, as D'Innocenzo *et al.*[28] provided simulation results showing that at high photoexcitation, excitons become the dominant species, and Zhu *et al.*[29] suggested that the formation of large polarons might play a role in the charge separation.

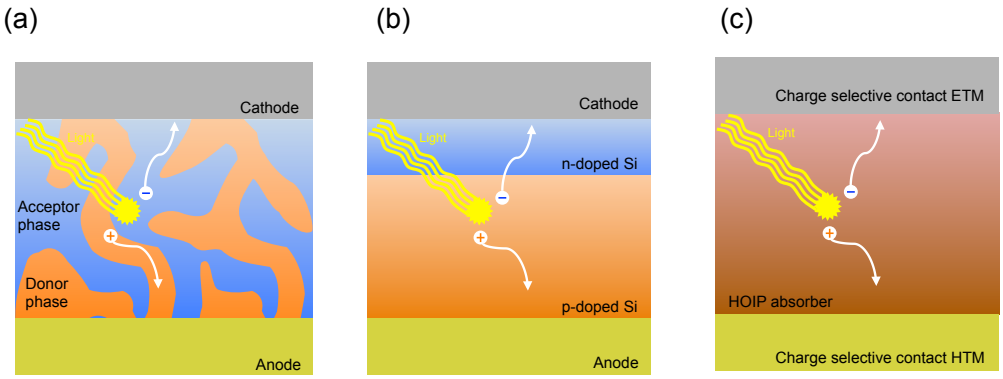

Fig. 1-5 Charge separation in different kinds of solar cells. (a) Organic bulk heterojunction solar cells. (b) Silicon p-n junction. (c) HOIP solar cell. In (a), electron–hole pairs from excitons, the separation of which is achieved by charge selective contacts. In (b), the electron–hole pairs are considered as free carriers and drift to cathodes and anodes. The charge separation mechanism for (c) is still under debate.

Studies of traditional perovskites, starting as early as 1950,[30] provide information about the phenomenon involved in HOIPs. For example, $CaTiO_3$ and $BaZrO_3$ have been known to form oxide defects, which serve as pathways for ion conduction.[31] Spontaneous formation of domains of aligning electric dipole moments is also observed in perovskite crystals. This property is called ferroelectricity as it is analogous to ferromagnetism, but the aligned dipoles are electric ones.[32] $BaTiO_3$ and $PdZrO_3$ are known to be representative ferroelectric materials.

In HOIPs, ferroelectric behavior and ion migration have been considered extensively in the literature,[8,33] but discrepancies persist and the general consensus has not been reached yet. In this thesis, it is our intention to clarify some aspects of these issues. In particular, trap state formation, ion conduction, and dipole orientation in HOIPs are approached by examining the existing literature along with experiments designed to investigate them.

In chapter 2, the different solution processes of HOIPs are reviewed and tested in order to identify a reproducible fabrication technique for high quality films. Chapter 3 includes various electrical and spectroscopic characterizations of the HOIP films. In particular, the

combination of low temperature *J–V–L* measurements and simulation results enables us to investigate the energetics of the HOIP/Au interface quantitatively. In chapters 4 and 5, the dielectric properties of the bulk and the interfaces of HOIP layers are examined using impedance spectroscopy. The dipole orientation and ion migration are studied in chapter 4, and in chapter 5 an observation of the proton migration behavior in HOIPs is presented.

References

[1] Research Cell Efficiency Records http://www.nrel.gov/ncpv (National Renewable Energy Laboratory, accessed December 2016).
[2] Dou, L. *et al.* Solution-processed hybrid perovskite photodetectors with high detectivity. *Nat. Commun.* **5,** 5404 (2014). DOI: 10.1038/ncomms6404
[3] Tan, Z.-K. *et al.* Bright light-emitting diodes based on organometal halide perovskite. *Nat Nano* **9,** 687 (2014). DOI: 10.1038/NNANO.2014.149
[4] Gil-Escrig, L. N. *et al.* Efficient photovoltaic and electroluminescent perovskite devices. *Chem. Commun. Chem. Commun* **51,** 569 (2015). DOI: 10.1039/c4cc07518h
[5] Sadhanala, A. *et al.* Electroluminescence from organometallic lead halide perovskite-conjugated polymer diodes. *Adv. Electron. Mater.* **1,** 1500008 (2015). DOI: 10.1002/aelm.201500008
[6] Sutherland, B. R. & Sargent, E. H. Perovskite photonic sources. *Nat. Photonics* **10,** 295 (2016). DOI: 10.1038/NPHOTON.2016.62
[7] Veldhuis, S. A. *et al.* Perovskite materials for light-emitting diodes and lasers. *Adv. Mater.* **28,** 6804 (2016). DOI: 10.1002/adma.201600669
[8] Brenner, T. M., Egger, D. a., Kronik, L., Hodes, G. & Cahen, D. Hybrid organic-inorganic perovskites: low-cost semiconductors with intriguing charge transport properties. *Nat. Rev. Mater.* **1,** 15007 (2016). DOI: 10.1038/natrevmats.2015.7
[9] Liu, M., Johnston, M. B. & Snaith, H. J. Efficient planar heterojunction perovskite solar cells by vapour deposition. *Nature* **501,** 395 (2013). DOI: 10.1038/nature12509
[10] Ng, A. *et al.* Efficiency enhancement by defect engineering in perovskite photovoltaic cells prepared using evaporated PbI2/CH3NH3I multilayers. *J. Mater. Chem. A* **3,** 9223 (2015). DOI: 10.1039/c4ta05070c
[11] Longo, G., Gil-Escrig, L., Degen, M. J., Sessolo, M. & Bolink, H. J. Perovskite solar cells prepared by flash evaporation. *Chem. Commun.* **51,** 7376 (2015). DOI: 10.1039/c5cc01103e
[12] Chen, Q. *et al.* Under the spotlight : The organic-inorganic hybrid halide perovskite for optoelectronic applications. *Nano Today* **10,** 355 (2015). DOI: 10.1016/j.nantod.2015.04.009
[13] Jeon, N. J. *et al.* Solvent engineering for high-performance inorganic-organic hybrid perovskite solar cells. *Nat. Mater.* **13,** 897 (2014). DOI: 10.1038/NMAT4014
[14] Zhang, W. *et al.* Ultrasmooth organic-inorganic perovskite thin-film formation and crystallization for efficient planar heterojunction solar cells. *Nat Commun* **6,** 6142 (2015). DOI: 10.1038/ncomms7142
[15] Kojima, A., Teshima, K., Shirai, Y. & Miyasaka, T. Organometal halide perovskites as visible-light sensitizers for photovoltaic cells. *J. Am. Chem. Soc.* **131,** 6050 (2009). DOI: 10.1021/ja809598r
[16] Lee, M. M., Teuscher, J., Miyasaka, Takurou, T., Murakami, H., & Snaith, H. J. Efficient hybrid solar cells based on meso-superstructured organometal halide perovskites. *Science* **338,** 643 (2012). DOI: 10.1126/science.1228604
[17] Etgar, L. *et al.* Mesoscopic CH3NH3PbI3/TiO2 heterojunction solar cells. *J. Am. Chem. Soc.* **134,** 17396 (2012). DOI: 10.1021/ja307789s
[18] Mei, A. *et al.* A hole-conductor free, fully printable mesoscopic perovskite solar cell with high stability. *Science* **345,** 295 (2014). DOI: 10.1126/science.1254763
[19] Yoon, H., Kang, S. M., Lee, J.-K. & Choi, M. Hysteresis-free low-temperature-processed

planar perovskite solar cells with 19.1% efficiency. *Energy Environ. Sci.* **9,** 2262 (2016). DOI: 10.1039/C6EE01037G

[20] Heo, J. H., Han, H. J., Kim, D., Ahn, T. K. & Im, S. H. Hysteresis-less inverted CH3NH3PbI3 planar perovskite hybrid solar cells with 18.1% power conversion efficiency. *Energy Environ. Sci.* **8,** 1602 (2015) DOI: 10.1039/c5ee00120j

[21] Chiang, C.-H. & Wu, C.-G. Bulk heterojunction perovskite–PCBM solar cells with high fill factor. *Nat Phot.* **10,** 196 (2016). DOI:10.1038/nphoton.2016.3

[22] Christians, J. A., Manser, J. S. & Kamat, P. V. Best practices in perovskite solar cell efficiency measurements. Avoiding the error of Making Bad Cells Look Good. *J. Phys. Chem. Lett.* **6,** 852 (2015). DOI: 10.1021/acs.jpclett.5b00289

[23] Tress, W. *et al.* Understanding the rate-dependent J–V hysteresis, slow time component, and aging in CH 3 NH 3 PbI 3 perovskite solar cells: the role of a compensated electric field. *Energy Environ. Sci.* **8,** 995 (2015). DOI: 10.1039/c4ee03664f

[24] Meloni, S. *et al.* Ionic polarization-induced current–voltage hysteresis in CH3NH3PbX3 perovskite solar cells. *Nat. Commun.* **7,** 10334 (2016). DOI: 10.1038/ncomms10334

[25] You, J. *et al.* Improved air stability of perovskite solar cells via solution-processed metal oxide transport layers. *Nat Nano* **11,** 75 (2016). DOI: 10.1038/NNANO.2015.230

[26] Niu, G., Guo, X. & Wang, L. Review of recent progress in chemical stability of perovskite solar cells. *J. Mater. Chem. A* **3,** 8970 (2015). DOI: 10.1039/C4TA04994B

[27] Miyata, A. *et al.* Direct measurement of the exciton binding energy and effective masses for charge carriers in organic-inorganic tri-halide perovskites. *Nat. Phys.* **11,** 582 (2015). DOI: 10.1038/NPHYS3357

[28] D'Innocenzo, V. *et al.* Excitons versus free charges in organo-lead tri-halide perovskites. *Nat Commun* **5,** 3586 (2014). DOI: 10.1038/ncomms4586

[29] Zhu, X. Y. & Podzorov, V. Charge carriers in hybrid organic-inorganic lead halide perovskites might be protected as large polarons. *J. Phys. Chem. Lett.* **6,** 4758 (2015). DOI: 10.1021/acs.jpclett.5b02462

[30] Slater, J. C. The lorentz correction in barium titanate. *Phys. Rev.* **78,** 748 (1950). DOI: 10.1103/PhysRev.78.748

[31] Ishihara, T., *Perovskite Oxide for Solid Oxide Fuel Cells*, Springer, New York, 2009.

[32] Dawber, M., Rabe, K. M. & Scott, J. F. Physics of thin-film ferroelectric oxides. *Rev. Mod. Phys.* **77,** 1083 (2005). DOI: 10.1103/RevModPhys.77.1083

[33] Berry, J. *et al.* Hybrid organic–inorganic perovskites (HOIPs): Opportunities and challenges. *Adv. Mater.* **27,** 5102 (2015). DOI: 10.1002/adma.201502294

Chapter 2

Preparation of polycrystalline methylammonium lead triiodide perovskite thin films for photovoltaic application by solution process

As discussed in the introduction, further studies and characterization are necessary to elucidate the basic properties and mechanisms of the processes occurring within HOIPs. A uniform and pinhole-free film of HOIP is desirable for the studies envisaged because roughness and incomplete surface coverage may complicate data analysis for, e. g., absorption spectra,[1] current–voltage characterization,[2] or impedance spectroscopy.[3,4] On the other hand, while some interesting investigations have been carried out on HOIP pellets,[5,6] it is preferable to study films similar to those used in solar cell applications, as this is the main reason for the recent surge of interest in HOIPs. With this in mind, this chapter introduces the various solution preparation procedures.

Of all the commonly used HOIPs, methylammonium lead triiodide perovskite ($MAPbI_3$, Fig. 2-1) shows high performance in photovoltaic applications (for example, refs 7,8,9,10). Generally speaking, the efficiencies of $MAPbI_3$ based solar cells are better than those of $MAPbBr_3$,[11,12] due to the smaller band gap of $MAPbI_3$ (~1.6 eV compared to ~2.3 eV for $MAPbBr_3$).[13] The addition of chloride ions into $MAPbI_3$ (forming $MAPbI_{3-x}Cl_x$) was shown to improve the charge carrier transport properties.[7] However, the exact proportion of Cl^- (the *x* in the formula) is unclear, as is the role played by Cl^- in the charge transport in HOIP.[14,15] On the other hand, some success has been shown by replacing the lead (II) in the crystal structure with tin (II),[16,17,18] or germanium (II),[19] but these materials are still in the early stages of development. Due to these considerations, $MAPbI_3$ was selected as the starting point for the study of HOIPs (Fig. 2-1).

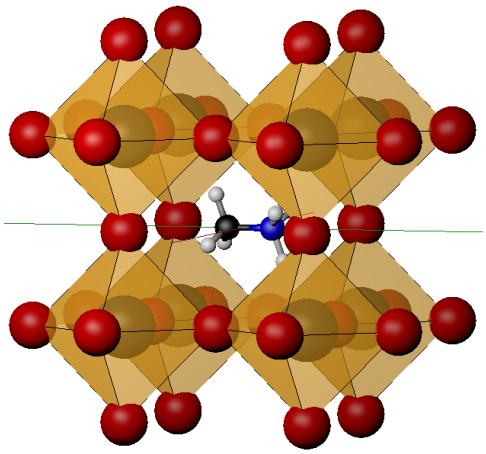

Fig. 2-1 Crystal structure of methylammonium lead triiodide perovskite. Red balls are iodide ions, gray balls are lead (II) ions, and the organic methylammonium (MA^+) ion located in the center.

2.1 General solution process procedure of $MAPbI_3$

Fig. 2-2 shows the different stages of HOIP formation from solution. Specifically, 3 different strategies can be employed to locate the methylammonium ions in the right position in the inorganic framework. The first is by mixing the 2 precursors, lead (II) iodide and methylammonium iodide, in solution, followed by spin-coating the mixture. This is often referred to as the one-step method.[20,21] The second method consists in dipping a lead (II) iodide film into an MAI solution (the dipping method).[22,23] The third approach relies on first spin-coating lead (II) iodide, followed by spin-coating MAI. After this, $MAPbI_3$ is formed by the interdiffusion of the 2 layers at elevated temperatures (the stacking layer method).[24,25] These 3 methods were tested and evaluated in the following section.

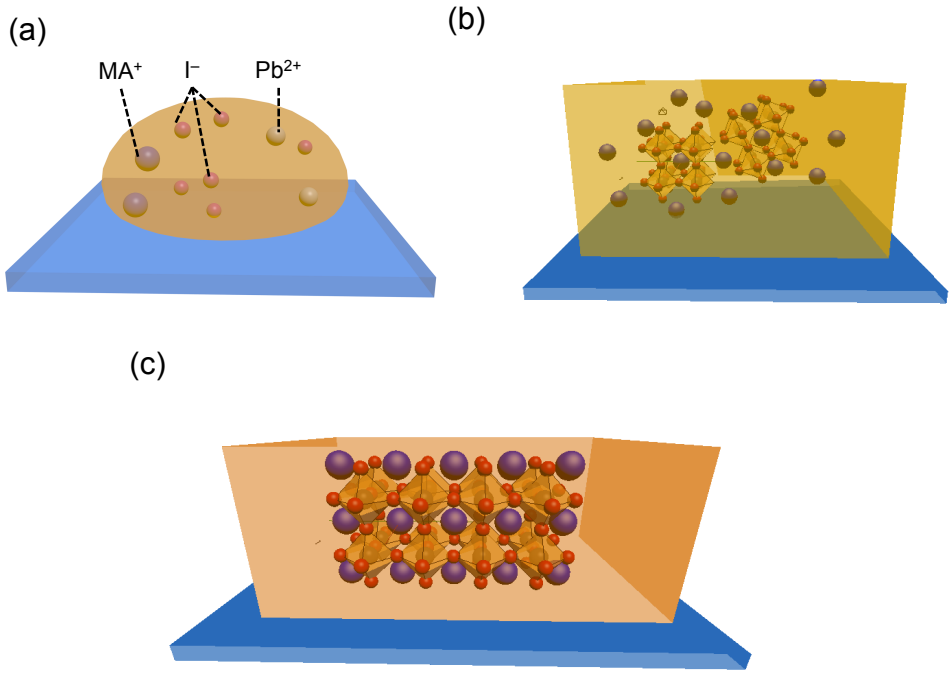

Fig. 2-2 Schematic representation of the different stages of the constitution of $MAPbI_3$ perovskite formed from solution: (a) The solution state, (b) incorporation of organic ions in the inorganic crystal framework, (c) crystal formation.

One-step method

The one-step method of $MAPbI_3$ film formation is illustrated in Fig. 2-3. The precursors lead (II) iodide (PbI_2) and methylammonium iodide (MAI) are dissolved in γ-butyrolactone (GBL)

or dimethylformamide (DMF) at a high concentration in equimolar proportion (a). The solution is then spread onto the substrate by spin-coating (b), after which an intermediate phase of the film is formed (c). During annealing (d), the film turns dark brown indicating the crystallization of $MAPbI_3$. High concentrations (~1 M) and high spinning speed (> 3000 rpm) are employed to ensure adequate crystal growth.

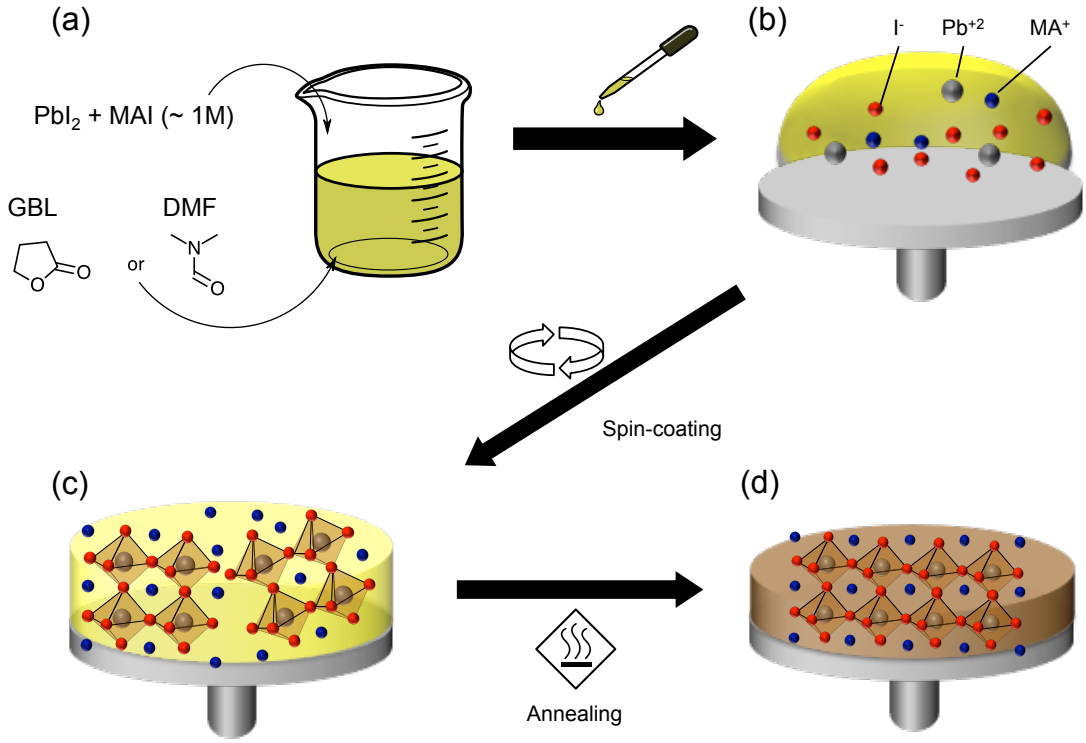

Fig. 2-3 Illustration of the one-step method for $MAPbI_3$ thin film preparation.

The properties of the film prepared by this method are shown in Fig. 2-4. Details of the experimental procedure and AFM characterization can be found in Appendix 7.1.2, and 7.2.1, respectively.

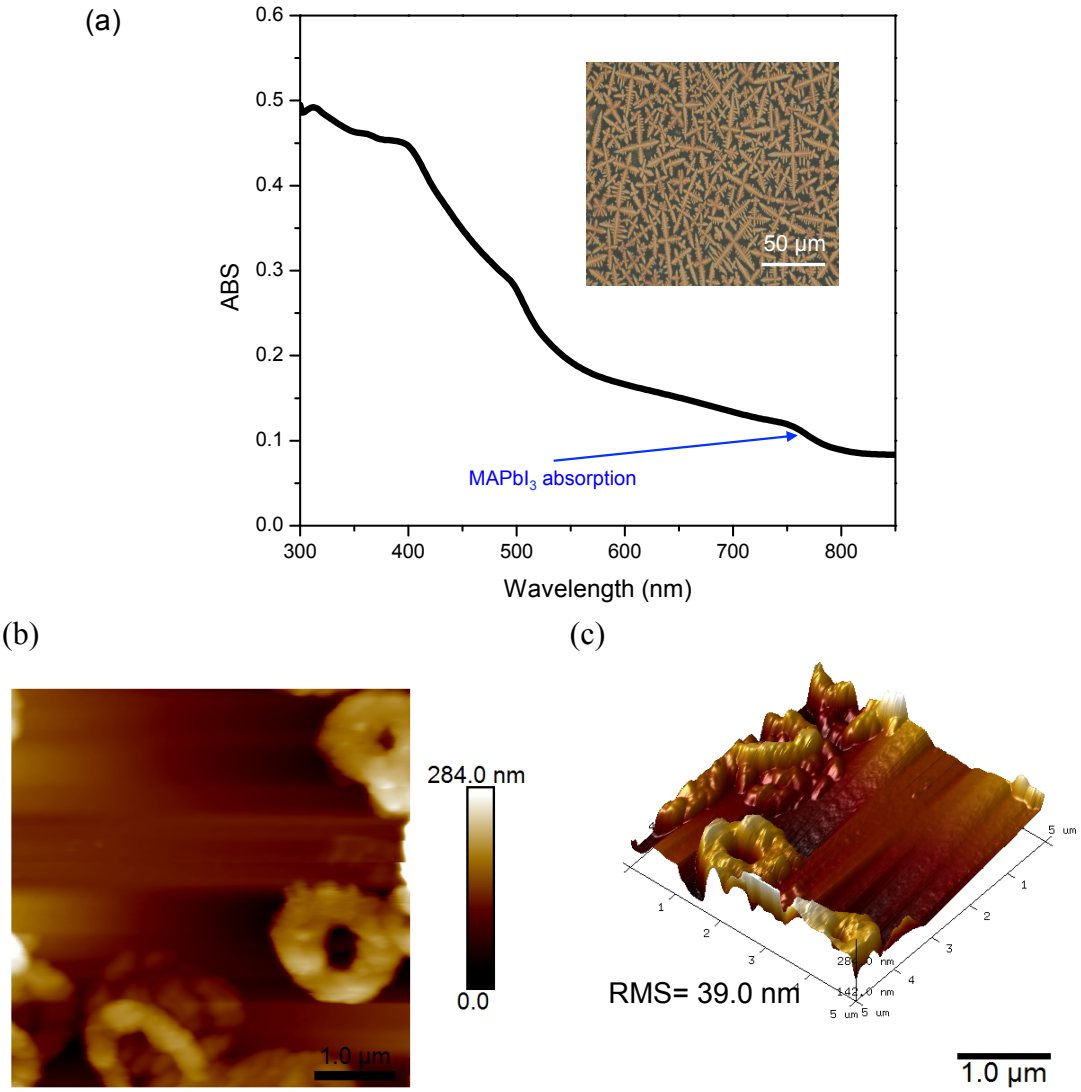

Fig. 2-4 Characterization of the film prepared by the one step method. (a) Absorption spectra (inset: optical microscopy image), (b) AFM topography, (c) 3D AFM topography processed from (b).

The formation of $MAPbI_3$ was suggested from the UV–vis absorption spectra. The increase of absorption at around 750 nm and 500 nm is characteristic for $MAPbI_3$. [26,27,28] However, from the optical microscopy image and AFM data, it is evident that the film was not uniform and consisted of isolated aggregated domains. This explains the light scattering observed in the UV–vis spectrum above 750 nm. More attempts in tuning the experimental conditions were made to improve the film morphology, which can be found in the Appendix 7.1.2, but the general features remained the same.

The inhomogeneity and pinhole formation in the film would not only reduce the solar cell efficiency,[29] but also complicate the analysis of the electronic properties as explained at the

beginning of this chapter. This morphology seems to occur frequently in the one-step preparation method.[1,20,21] Before turning to the improvement of this method, which is introduced in 2.2, the other 2 basic solution processes are tested below:

The dipping method and the stacking layer method both start with a PbI_2 film and are promising since obtaining a smooth film of PbI_2 by spin-coating is less difficult. As shown in Fig. 2-5, a 100-nm-thick PbI_2 film spin-coated on an ITO/PEDOT:PSS substrate from a dimethylformamide solution (0.8 M) showed a smooth surface.

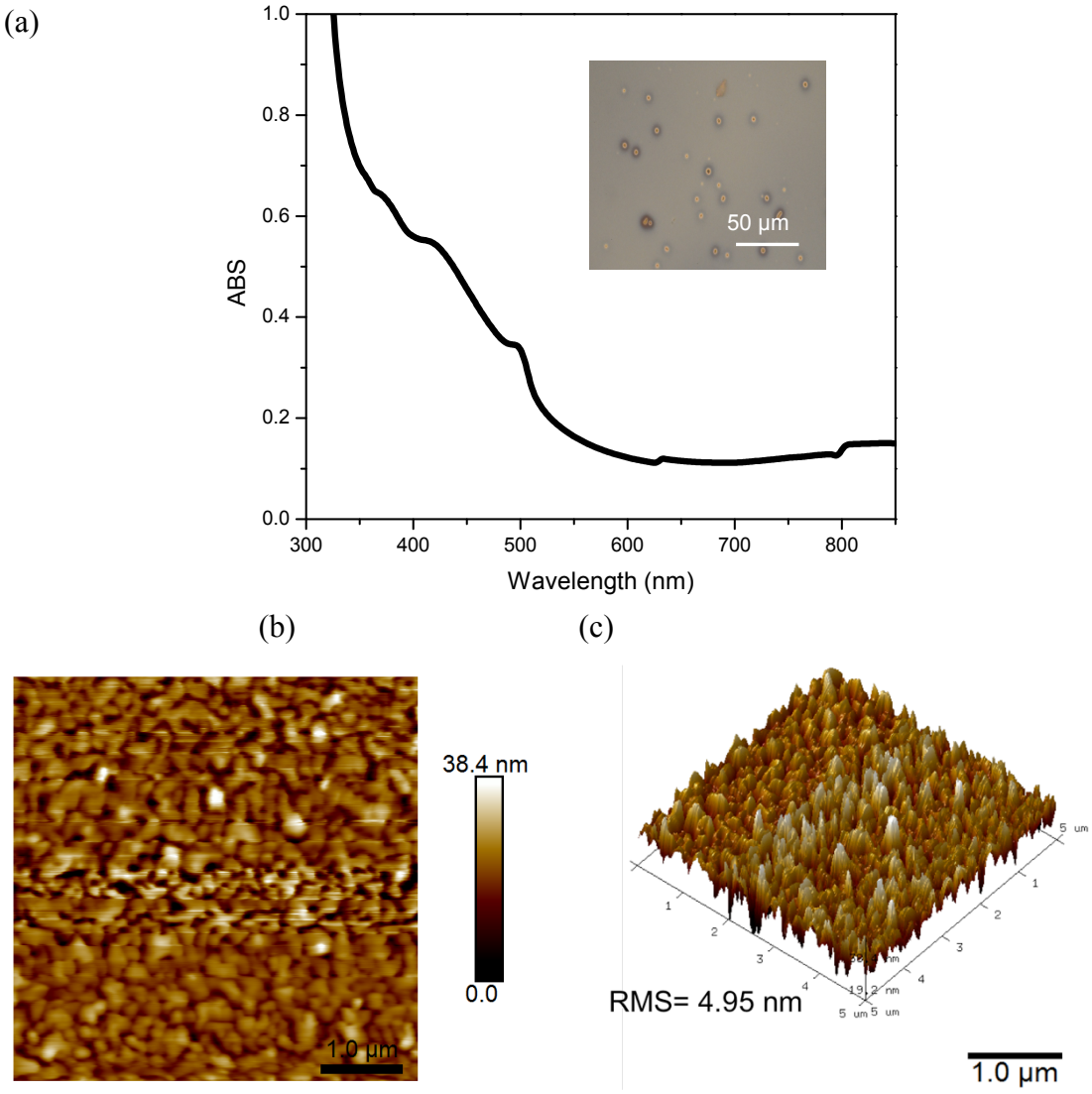

Fig. 2-5 Characterization of the spin-coated PbI_2 film (a) absorption spectra, (inset: optical microscopy image), (b) AFM topography, (c) 3D AFM topography

Dipping method

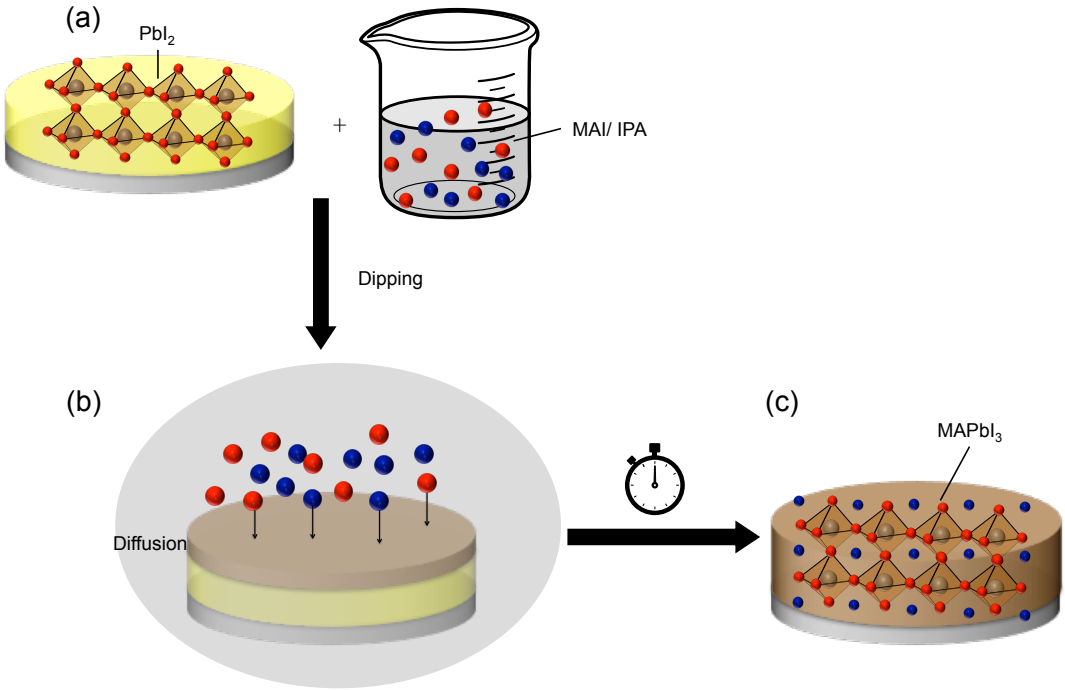

Fig. 2-6 Illustration of the dipping method for $MAPbI_3$ thin film preparation.

The dipping method process is shown in Fig. 2-6. A 100-nm-thick PbI_2 film is dipped in a 10 mg/mL methlammionium iodide (MAI) solution in isopropyl alcohol (IPA), which does not dissolve PbI_2. The MAI then starts to diffuse into the film, forming $MAPbI_3$. (Details of the procedure can be found in Appendix 7.1.3)

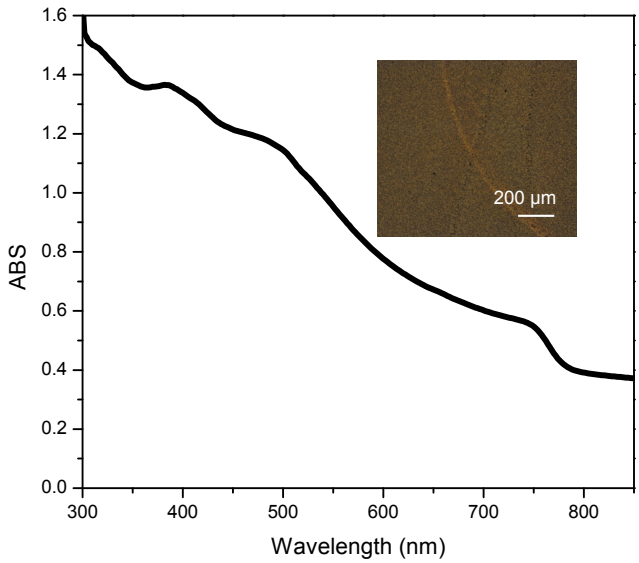

Fig. 2-7 Characterization of the film prepared by the dipping method: absorption spectra (main plot) and optical microscopy (inset).

Typical absorption and optical microscopy images of the films prepared by this technique are shown in Fig. 2-7. Again, the absorption showed the formation of $MAPbI_3$. However, a closer inspection of the UV–vis spectra in the long wavelength region shows that it tends to a value of ~0.3, instead of approaching 0. This indicates that the surface scatters a significant amount of light. This is confirmed by the significant features in the optical microscopy image. In fact, the roughness exceeded the limit of the AFM z range (~2 μm), so obtaining AFM topography in this case was not feasible.

Stacking layer method

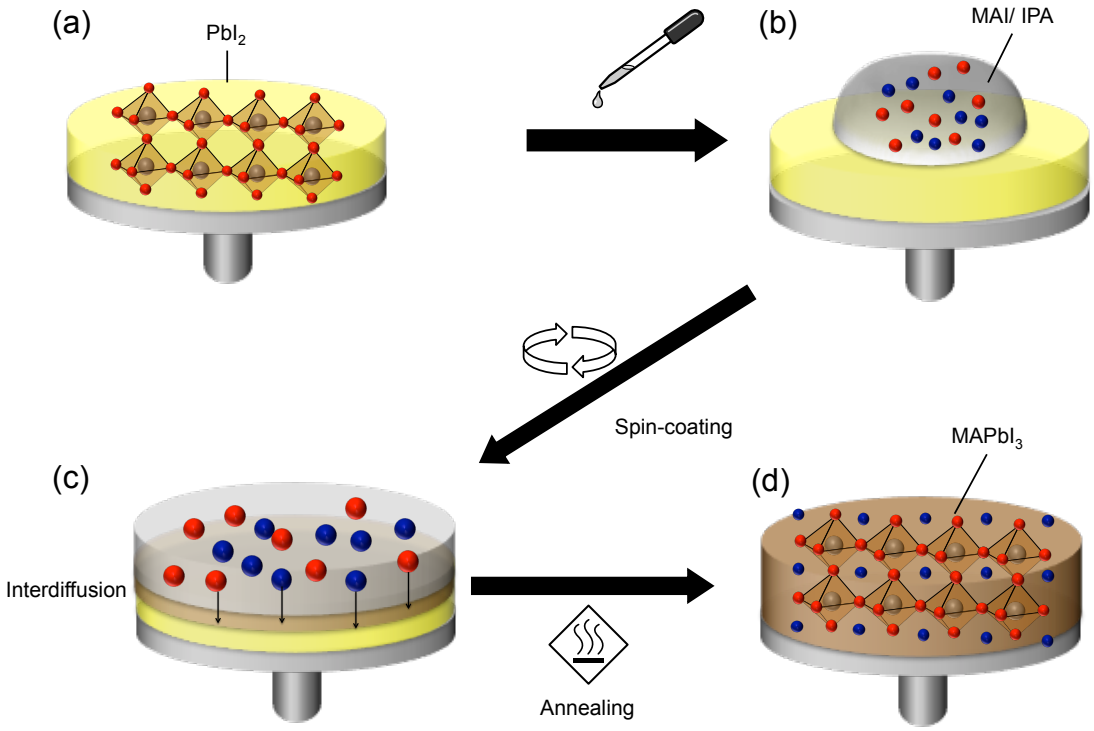

Fig. 2-8 Illustration of the stacking layer method for $MAPbI_3$ thin film preparation.

This process also begins with a PbI_2 layer onto which a layer of MAI is subsequently deposited. The process of the stacking layer method is illustrated in Fig. 2-8. An MAI solution in IPA is spin-coated on top of the PbI_2 film, forming a stacked layer of MAI and PbI_2 (Fig. 2-8(b), (c)). The two materials then start to inter-diffuse and form $MAPbI_3$ perovskite, a process facilitated by thermal annealing (Fig. 2-8 (d)).

Following the parameters detailed in Appendix 7.1.4, the $MAPbI_3$ film shown in Fig. 2-9 is obtained. It may appear that an important issue in this method is to ensure the correct stoichiometry between PbI_2 and MAI. However, excess MAI is likely to sublime during annealing and it would therefore be optimal to use an excess of MAI.[30] Experiments investigating the concentration dependence of MAI are shown in Appendix 7.1.4. In our hands, the issue with this method was still the rough film morphology that is obtained.

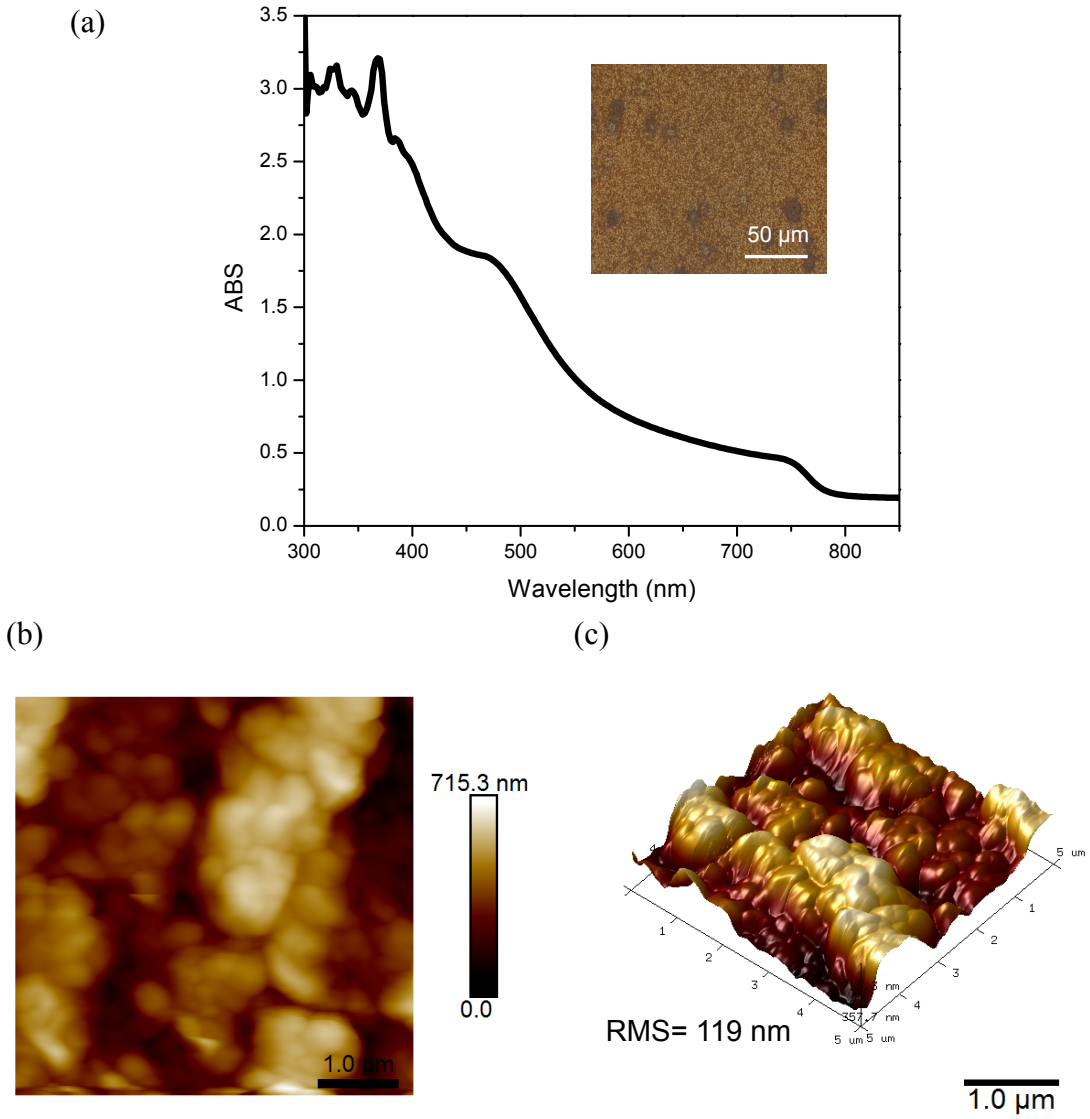

Fig. 2-9 Characterization of the film prepared by the stacking layer method. (a) absorption spectra, (inset: optical microscopy image), (b) AFM topography, (c) 3D AFM topography processed from (b)

The preliminary experiments with these three basic solution processes have the merit of demonstrating the general film formation of $MAPbI_3$ perovskite. However, our experimental results showed that to reproducibly obtain a film suitable for further electronic studies using

these methods is challenging. More advanced preparation methods based on a better understanding of the film formation process are therefore necessary.

2.2 Advanced solution process method

Since its first publication as promising photovoltaic material,[31] the preparation method of HOIPs has evolved with the aim to improve the film quality and reproducibility. In particular, the basic solution process method as described in 2.1 has been modified by many techniques, such as solvent engineering,[8,32] additives in solution,[33,34,35] solvent annealing,[36] change of precursor materials and ratio,[9,10,37] and hot-casting.[38] We found that two of the techniques, solvent engineering and change in precursor material, significantly improve the film morphology and can be used to build efficient planar HOIP solar cells.

2.2.1 Solvent engineering with orthogonal solvent washing

As first introduced by Jeon *et al*,[8] the method involves the dissolution of the two precursor compounds (PbI_2 and methylammonium iodide) in a mixed solvent of γ-butyrolactone (GBL) and dimethyl sulfoxide (DMSO) instead of a single composition solvent. During spin-coating, a drop of an "orthogonal solvent" (i.e., that doesn't dissolve either precursor, such as toluene or chlorobenzene),[32] is added onto the substrate. The solution composition and the process scheme can be seen in Fig. 2-10.

The inclusion of DMSO in the solvent has the advantage of forming a MAI-PbI_2-DMSO intermediate phase before annealing. The drop of solvent added during spin-coating washes off some of the solution, rearranging the ions (See Fig. 2-10 (c)–(d)), and enhancing the crystallization dynamics. To achieve optimal rearrangement for smooth film surface, the addition of the orthogonal solvent must be carefully timed.[8]

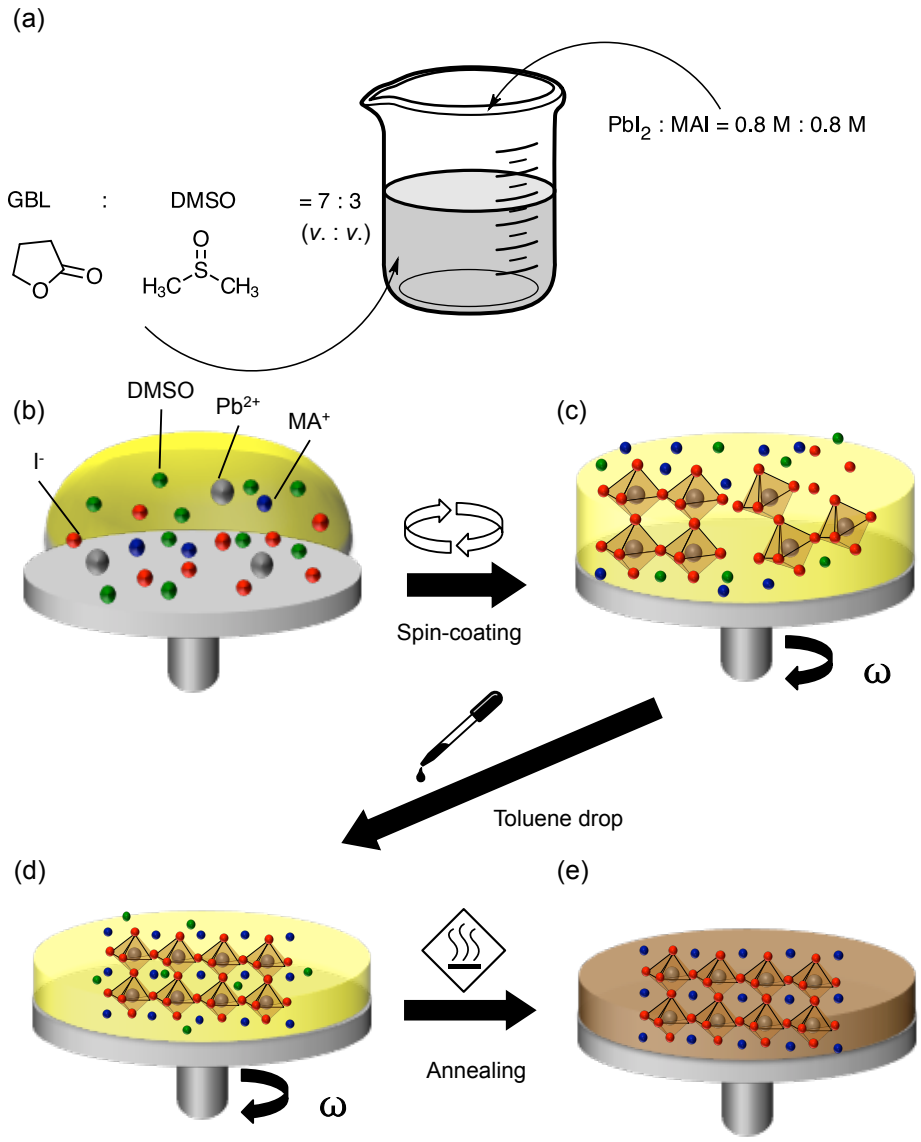

Fig. 2-10 Illustration of the solvent washing process. The precursor solution composition is shown in (a) and then drop cast onto the substrate (b). After spin-coating for a few seconds, the solution forms a disordered intermediary state (c). A drop of orthogonal solvent (toluene) is then applied to the surface while the substrate is still spinning, which washes out most of the remaining DMSO and locates the MA^+ ions into the correct positions to be crystalized (d). The $MAPbI_3$ polycrystalline film is obtained after annealing at 100 °C for 10 minutes (e).

The resulting smooth film that can be obtained according to this method can be seen in Fig. 2-11. For comparison, the right of Fig. 2-11(b) shows the coarser film when the drop was applied out of the optimal time window for smooth film formation, which is typically around 2 seconds. Details of the preparation and more experiments on this method can be found in Appendix 7.1.7.

(a)

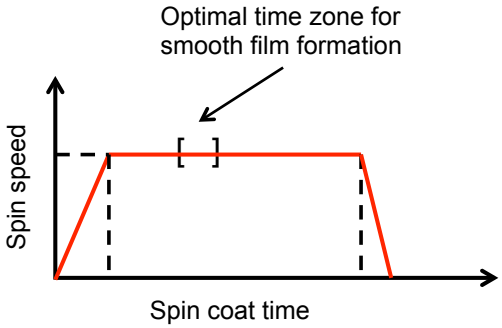

(b)

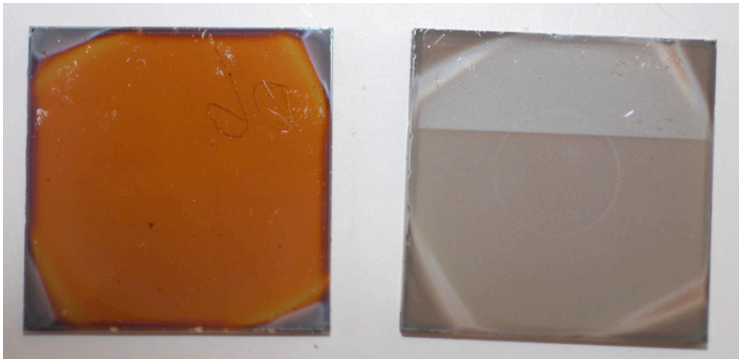

Fig. 2-11 (a) The spinning speed profile of the spin-coating procedure in the solvent engineering method. (b) the resulting film with the drop in (left) and out (right) of the optimal time zone.

The AFM topography of the film (Fig. 2-12) further shows that the surface is smooth and consists of tens-of-nanometer-sized grains. The film thickness measured using a stylus profiler is ca.150 nm. This method is also applicable to other substrate surfaces, such as ITO/MoO_3, ITO/C_{60}, or ITO/TiO_x (see Appendix 7.1.5).

(a)

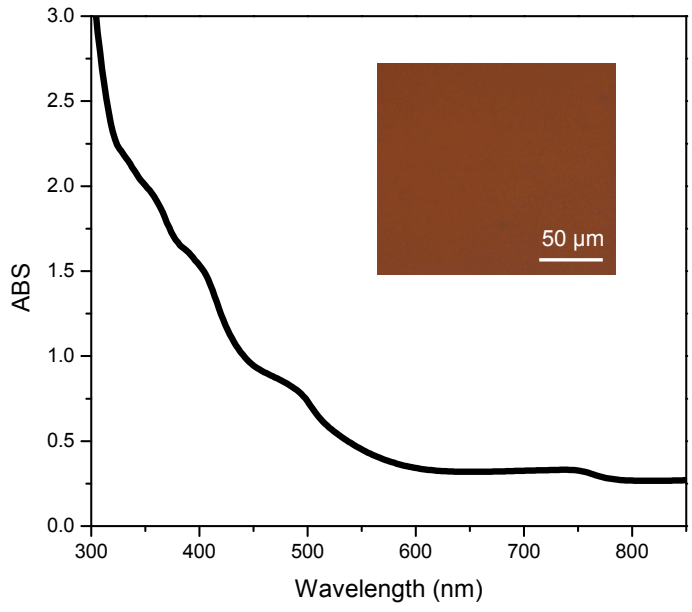

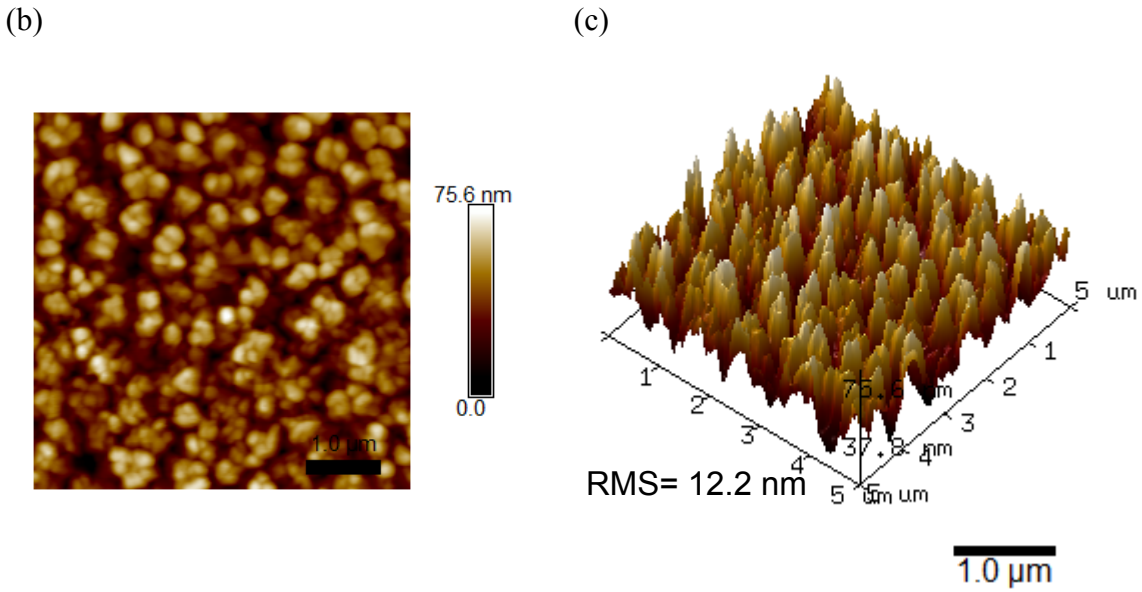

Fig. 2-12 Characterization of the film prepared by the stacking layer method. (a) absorption spectra, (inset: optical microscopy image), (b) AFM topography, (c) 3D AFM topography processed from (b).

The smooth film obtained is useful for planar solar cell applications. Here, we demonstrate an example of the preparation of a direct solar cell [ITO/TiO_x (30 nm)/$MAPbI_3$ (150 nm)/spiro-OMeTAD (80 nm)/MoO_3 (5 nm)/Ag]. The device architecture and energy levels are shown in Fig. 2-13 (a) and (b). The solar cell was constructed following the preparation procedure in Appendix 7.1.6, and the device characteristics are collected in Fig. 2-13 (c), (d). Details of device characterization can be found in Appendix 7.2.2.

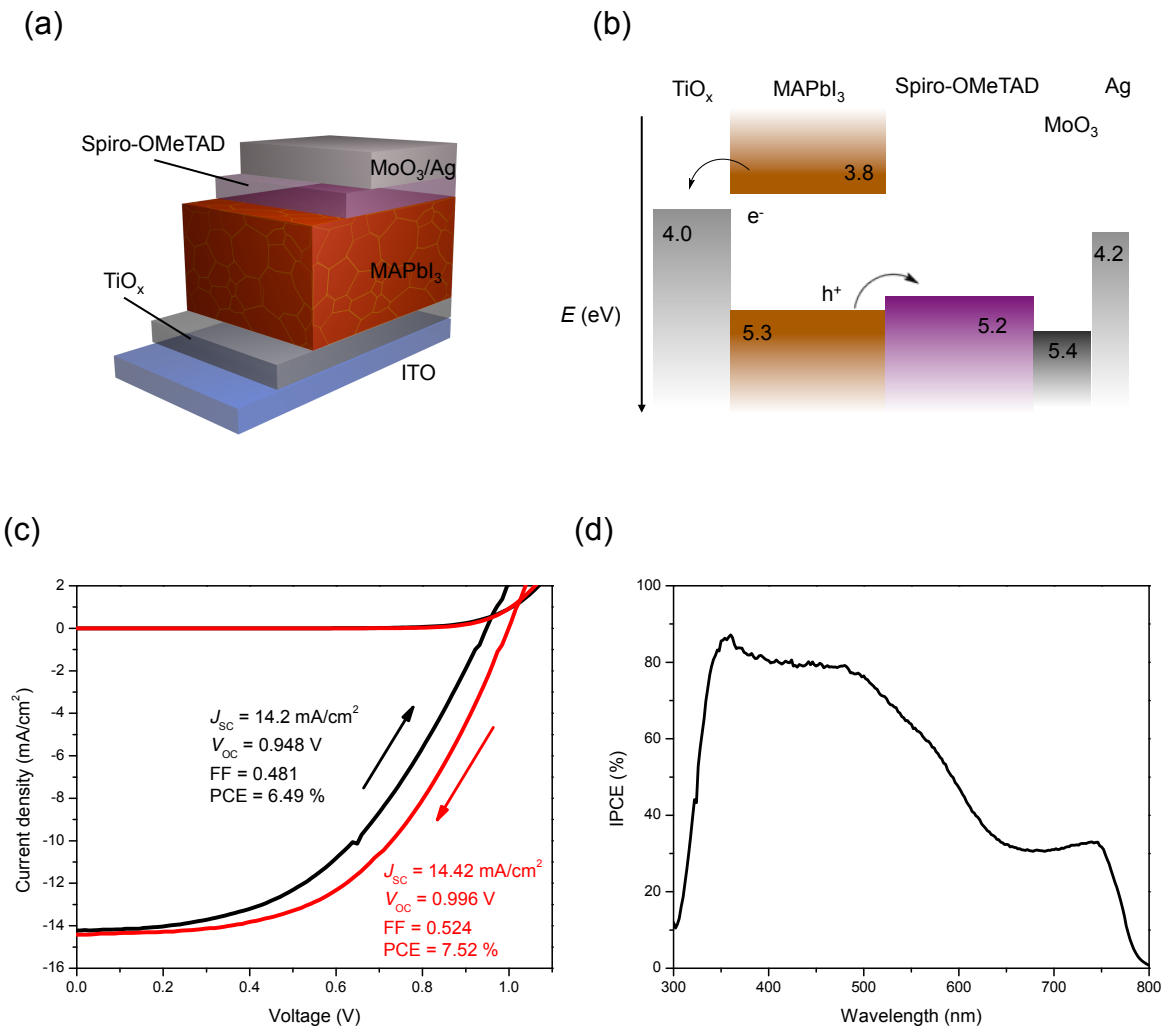

Fig. 2-13 Performance of the directed planar $MAPbI_3$ solar cells prepared using the solvent washing techniques. (a) Device architecture. (b) Energy levels. (c) Current–voltage characteristics under dark and light (AM 1.5G) conditions. Black lines indicate forward scanning, and red lines indicate backward scanning. In both cases, the voltage sweeping rate was ~0.2 V/s. (d) Incident photon-to-electron conversion efficiency (IPCE) spectrum. The energy levels of $MAPbI_3$ and spiro-OMeTAD are from ref. 39.

The difference between the forward and backward scanning shows significant hysteresis, which is common with this kind of architecture.[40,41,42] The efficiency was somewhat lower than expected and the cell showed poor stability over time.

To understand the issue of stability, further characterization was carried out using X-ray diffraction (XRD). The spectra can be used to determine the crystalline structure,[43] and the $MAPbI_3$ perovskites exhibit a tetragonal crystal structure with 3 perpendicular symmetry axes and lattice constants $a = b \neq c$ at room temperature.

The XRD spectra of the film prepared according to the solvent engineering method can be seen in Fig. 2-14 (For more details, see Appendix 7.2.3). The tetragonal structure of $MAPbI_3$ can be clearly distinguished from the peaks at 12.67°, 19.99° and 24.52°, as indicated in the Miller indices above the peaks. The lattice constants calculated from the spectrum are $a = b =$ 8.87 Å and c = 12.70 Å, which are in agreement with $MAPbI_3$ indices from the literature (see, for example, ref 44). The position of the peak at $2\theta = 12.5°$ is the same as the (0 0 3) peak in hexagonal PbI_2.[45] We thus conclude that this peak indicates incomplete formation of the $MAPbI_3$ crystal, resulting in the presence of residual PbI_2.

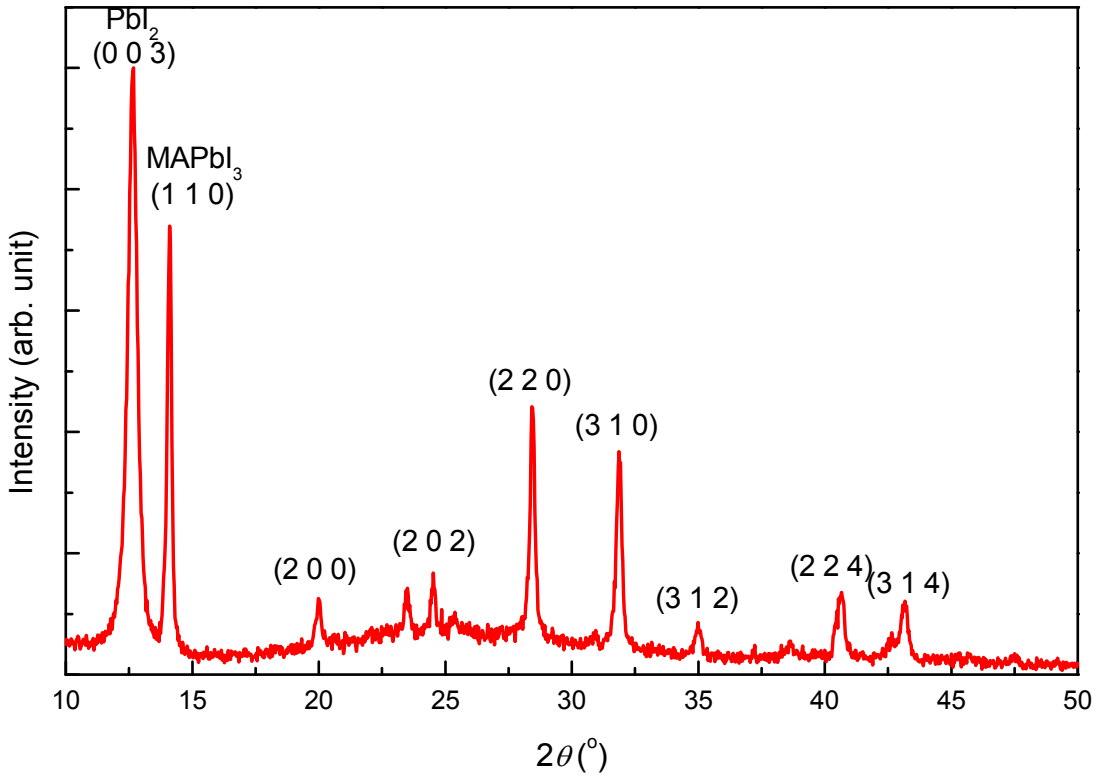

Fig. 2-14 XRD spectra of the film prepared by the solvent engineering method. The presence of PbI_2 is clearly seen.

The presence of residual PbI_2 in solution-processed $MAPbI_3$ was previously reported in the literature,[45] and its effect on the material properties is ambiguous. Some reports suggested that residual PbI_2 preserves the interfaces and reduces trap formation, improving solar cell performance as a result.[46,47,48] On the other hand, other reports argued that the formation of PbI_2 is unfavorable for electron extraction,[30] or subject to light degradation.[49,50] In the above experiment, the poor stability of the solar cells supports the latter argument.

In short, this method yielded a good film morphology that is smooth and pinhole free. However, the initial attempts at solar cell fabrication reveal some shortcomings. As discussed above, the modest efficiency and poor stability showed that the processing condition results in residual PbI_2 in the $MAPbI_3$ layer. Under these conditions, the study of the basic properties and mechanisms would be unnecessarily complicated. Therefore, further effort was put in to the preparation of $MAPbI_3$ films.

2.2.2 Lead acetate as the precursor for ultrasmooth film formation

The possibility of forming $MAPbI_3$ perovskite from different precursors has been tested since the initial interest in the material. The general strategy was to replace PbI_2 with other lead salts, such as acetate or nitrate.[37] In this case, the amount of MAI must be increased 3 times to compensate the loss of iodide from these salts. Moreover, the MA^+ ions are presumed to combine with acetate (or nitrate) and dissipate during annealing, a process that might play an important role in the formation of the $MAPbI_3$ perovskite.[51]

An important breakthrough in this line of methods was achieved by Zhang *et al*,[9] who used lead acetate ($PbAc_2$) as the lead source for the formation of ultrasmooth $MAPbI_3$ thin films. According to the first report, the surface of the solution-processed film is even more flat than thermally evaporated $MAPbI_3$. The authors conjectured that the removal of MA(Ac) during annealing is relatively quick, causing favorable conditions for $MAPbI_3$ crystallization.

This method is illustrated in Fig. 2-15, where a solution of lead acetate ($PbAc_2$) and methylammonium iodide is dissolved in DMF and the solution spin-coated onto substrates, after which the film is annealed. During the annealing process, excess MA^+ and Ac^- ions are removed and the $MAPbI_3$ crystalizes, and the film turns dark brown.

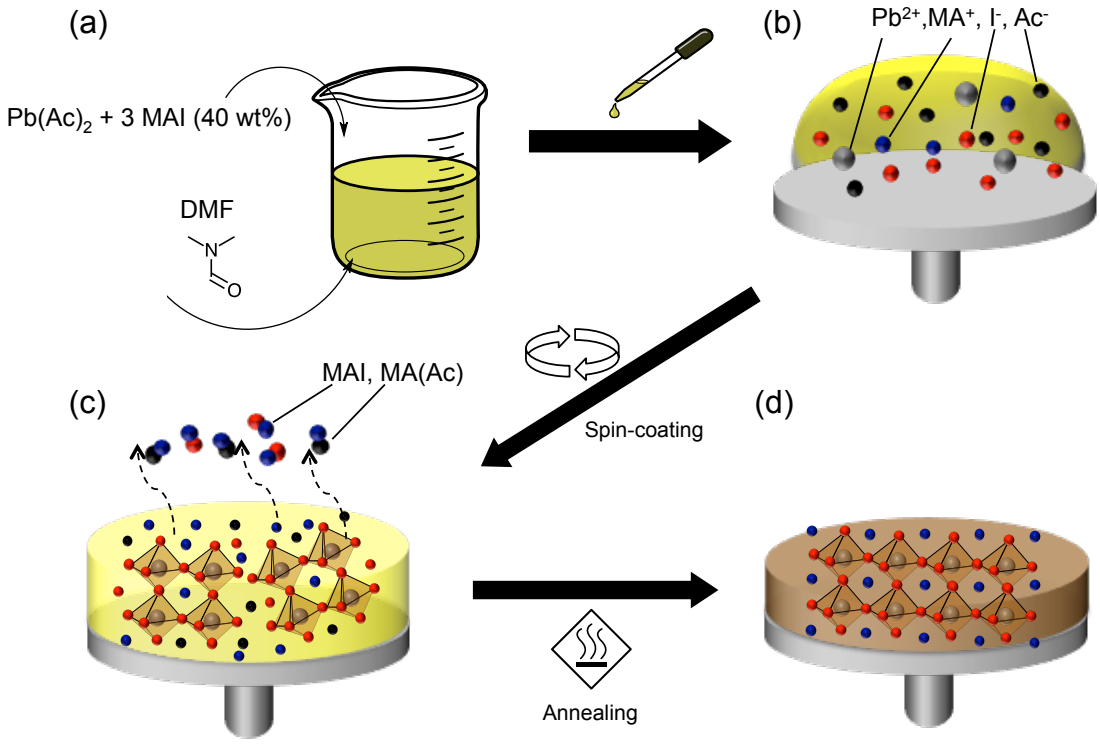

Fig. 2-15 Illustration of $MAPbI_3$ formation from lead acetate

Following the conditions specified in Appendix 7.1.6, we prepared $MAPbI_3$ films on top of ITO/PEDOT:PSS as shown in Fig. 2-16.* The resulting films showed superior smoothness and homogeneity compared to previous results. Besides the AFM topography, the total coverage of the film can also be inferred from the absorption spectra, where the features from $MAPbI_3$ perovskite are clear and the features arising from scattering and insufficient surface coverage were minimal.[1]

*The experimental procedure was performed with the guidance of Mr. David Forgács and Dr. Henk Bolink at Instituto de Ciencia Molecular (ICMol), Universidad de Valencia.

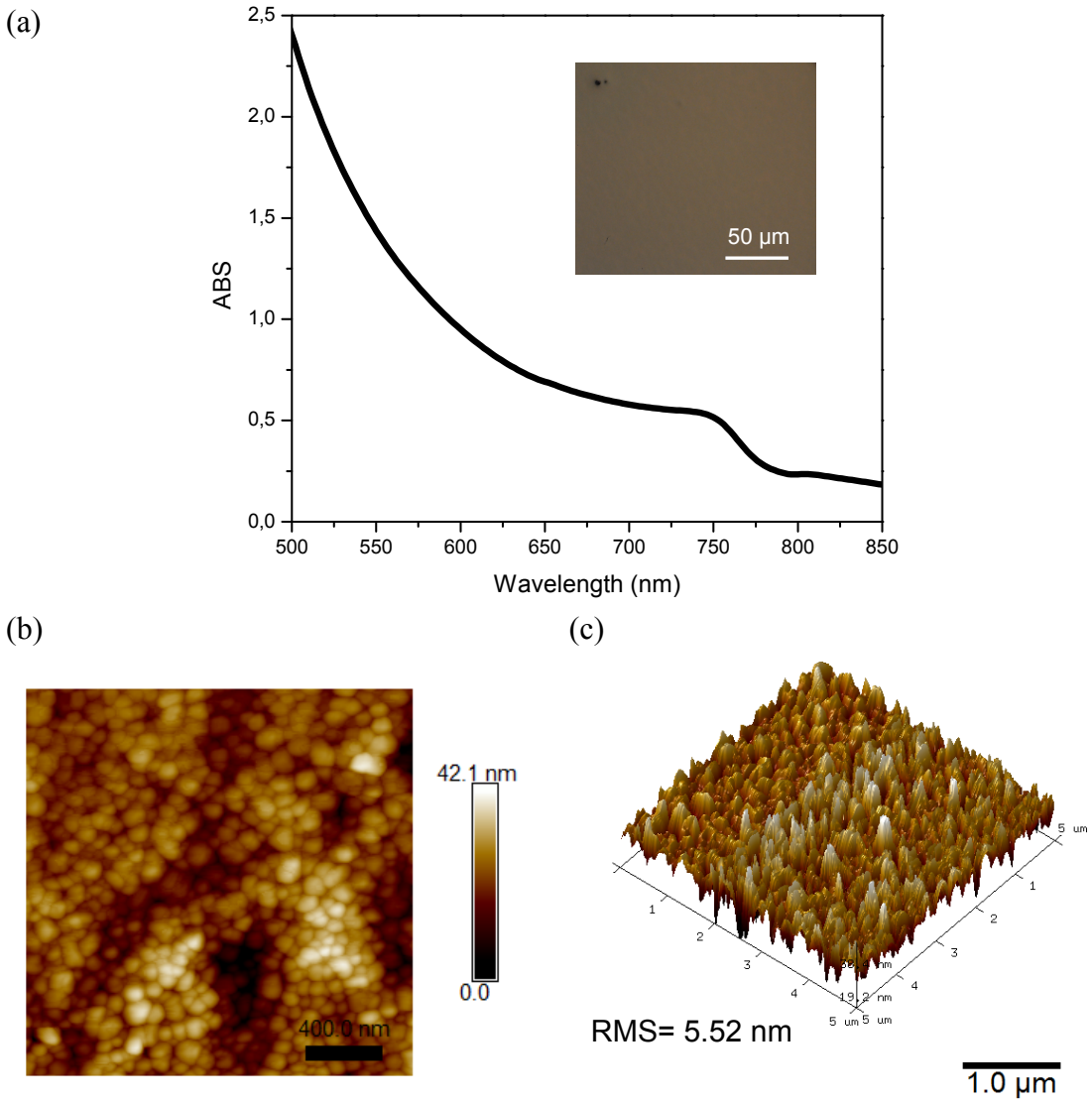

Fig. 2-16 Characterization of the film prepared with lead acetate as precursor. (a) absorption spectra, (inset: optical microscopy image), (b) AFM topography, (c) 3D AFM topography processed from (b).

The XRD spectra (Fig. 2-17) of the films showed the clean formation $MAPbI_3$ in the tetragonal structure with lattice constants $a = b = 8.89$ Å and $c = 12.63$ Å, again in close agreement with the values reported in the literature. No residual signal attributed to PbI_2 was observed. The peaks are clear and the lack of signal from the underlying substrate (ITO/PEDOT:PSS) further testifies the total coverage of the film.

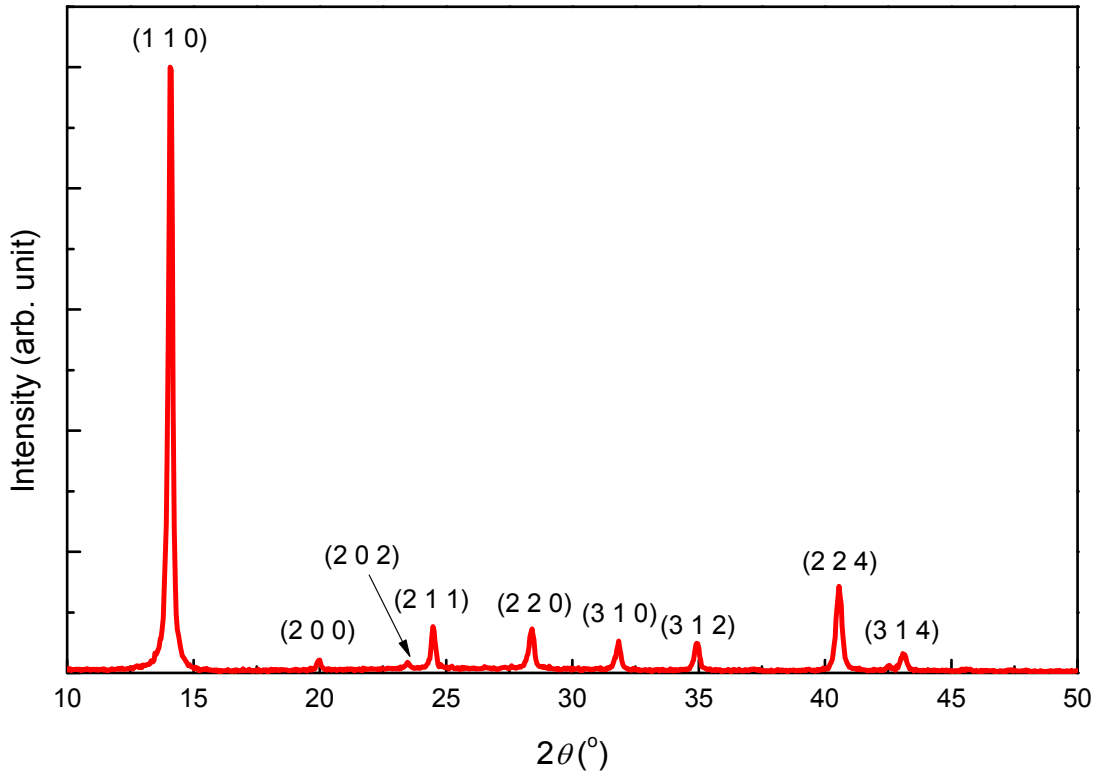

Fig. 2-17 XRD spectra of the film prepared with lead acetate as precursor

After checking the film quality with all the commonly used characterization techniques, we fabricated planar inverted solar cells based on these films. The hole transport layer used was poly(3,4-ethylenedioxythiophene) polystyrene sulfonate (PEDOT:PSS) and the electron transport layer was phenyl-C_{61}-butyric acid methyl ester ($PC_{61}BM$). This device architecture is known for its low hysteresis and relative easiness in fabrication. The detail procedure of the device fabrication can be found in Appendix 7.1.8.

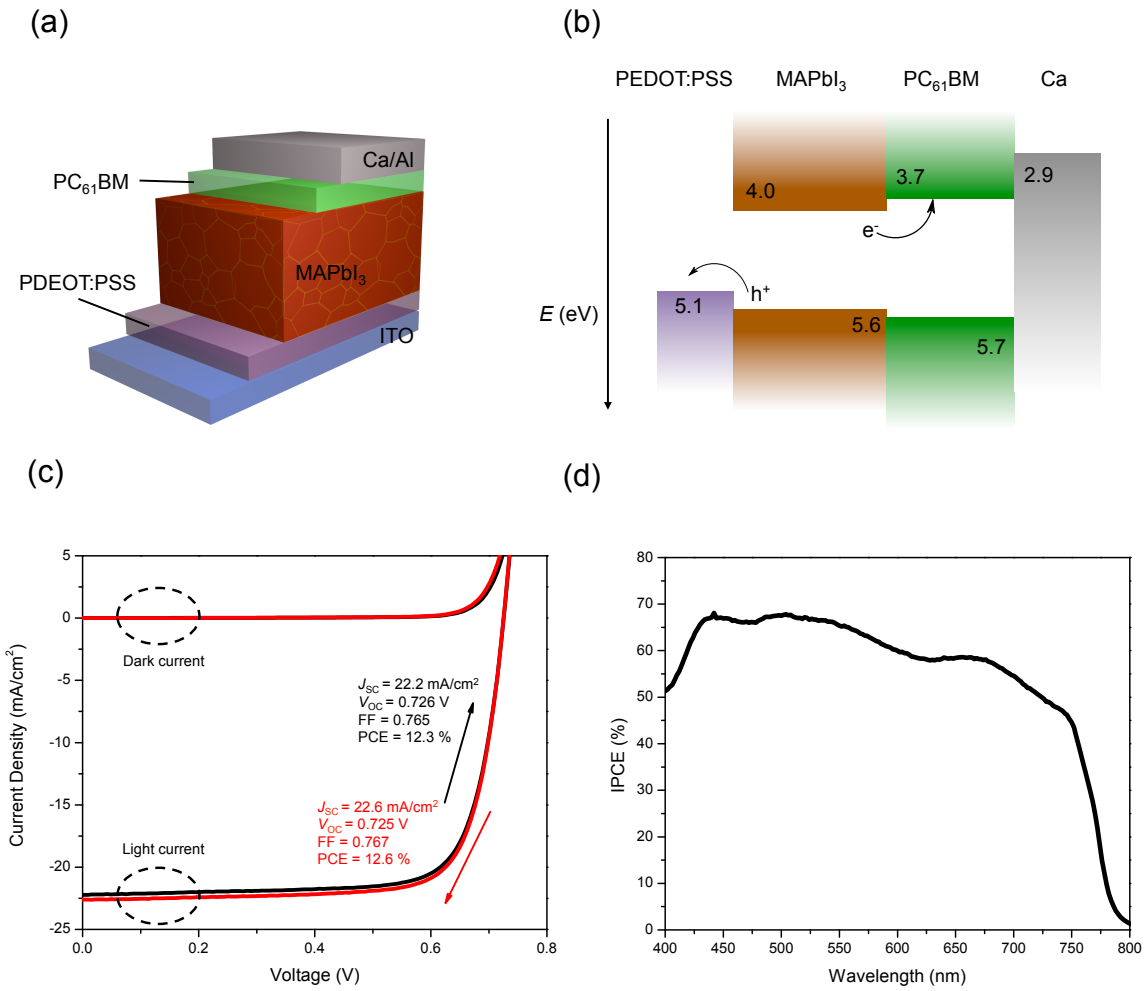

Fig. 2-18 Performance of inverted $MAPbI_3$ solar cells preparing from $PbAc_2$. (a) Device architecture. (b) Energy levels. (c) Current–voltage characteristics under dark and light (AM 1.5G) conditions. Black lines indicate forward scanning, and red lines indicate backward scanning. In both cases, the voltage sweeping rate was ~0.2 V/s. (d) incident photon-to-electron conversion efficiency (IPCE) spectrum. The energy levels of $MAPbI_3$ are obtained from ultraviolet photoelectron spectroscopy measurement (see chapter 3). The LUMO and HOMO of $PC_{61}BM$ are from ref. 52.

Fig. 2-18 shows a typical device performance prepared according this procedure. The voltage scanning rate is 0.2 V/s and the hysteresis as shown in the forward scan (black) and backward scan (red) is minimal. Satisfactory device performance was obtained (PCE = 12.5%). The statistics of the efficiency over 90 devices are shown in Fig. 2-19, with the best performing device achieving 15%. As discussed in Chapter 1, state of the art HOIP solar cells have been demonstrated to have power conversion efficiency over 20%. However, the optimization of the device depends on the device architecture (direct, inverted, planar, with or without scaffold, etc.). Our main purpose here is to demonstrate that the quality of the $MAPbI_3$ film obtained is comparable to that in the literature. Therefore, the performance should be

compared to devices using the same device architecture. To the best of our knowledge, the best performing solar cell with the same structure achieves ca. 16–18%,[53,54] and our best performing device is not far from this value. Furthermore, the average values are in agreement with most publications studying $MAPbI_3$ properties.[55,56,57] Our active layer is about 100 nm thinner than the optimal HOIP solar cells in other reports and the device open circuit voltage somewhat lower.[58] Besides increased thickness, other procedures like optimizing the properties of the PEDOT:PSS layer, such as work function and conductivity, modifying the top electrode composition (LiF/Al for example), and changing the composition of electron transport layer would further optimize the solar cell performances. These results demonstrate the usefulness of the lead acetate preparation process with respect to its use in further studies.

In conclusion, several methods have been tested and an optimal process to reliably obtain smooth and pinhole-free $MAPbI_3$ perovskite film was established. The morphology and composition of the film show that it is suitable for further characterization aimed at elucidating the underlying processes within hybrid perovskites. Solar cells with good efficiency were fabricated, which can be used for further studies connecting the underlying process and devices performance.

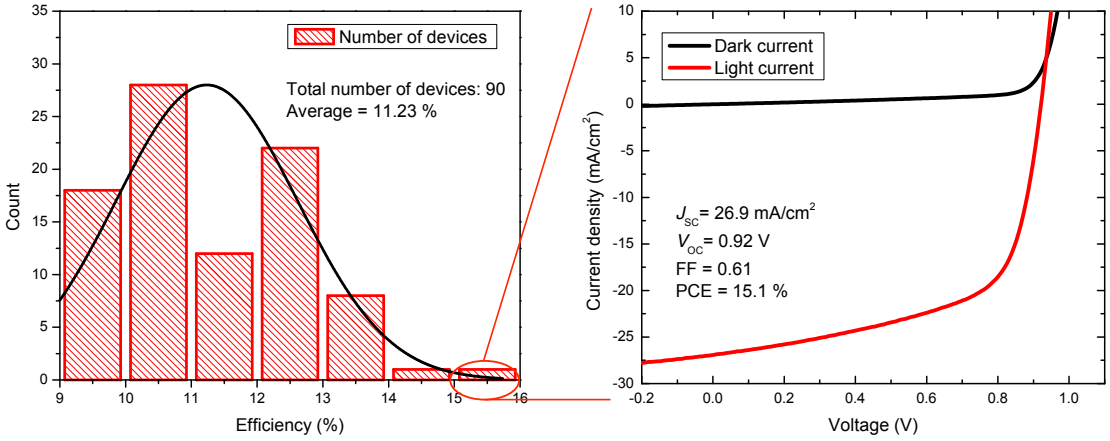

Fig. 2-19 The statistics of the regular solar cell device efficiency (left) and the current–voltage characteristics of the best performing device (right).

References

[1] Tian, Y. & Scheblykin, I. G. Artifacts in absorption measurements of organometal halide perovskite materials: what are the real spectra? *J. Phys. Chem. Lett.* **6,** 3466 (2015). DOI: 10.1021/acs.jpclett.5b01406

[2] Bruno, J. D. & Hurley, J. S. Effect of interface roughness on the current-voltage characteristic of a resonant tunneling diode. *Superlattices Microstruct.* **11,** 23 (1992). DOI: 10.1016/0749-6036(92)90356-A

[3] Macdonald, J. R. & Johnson, W. B., *Impedance Spectroscopy*, John Wiley & Sons, Inc., 2005.

[4] Abakarov, M. A., Giraev, M. A. & Shabanov, O. M. Effect of the surface roughness on the impedance spectrum of a tellurium electrode. *Russ. J. Electrochem.* **41,** 1017 (2005).

[5] Onoda-Yamamuro, N., Matsuo, T. & Suga, H. Dielectric study of CH3NH3PbX3 (X = Cl, Br, I). *J. Phys. Chem. Solids* **53**, 935 (1992). DOI: 10.1016/0022-3697(92)90121-S

[6] Yang, T. Y., Gregori, G., Pellet, N., Gratzel, M. & Maier, J. The significance of ion conduction in a hybrid organic-inorganic lead-iodide-based perovskite photosensitizer. *Angew. Chemie - Int. Ed.* **54,** 7905 (2015). DOI: 10.1002/anie.201500014

[7] Stranks, S. D. *et al.* Electron-hole diffusion lengths exceeding 1 micrometer in an organometal trihalide perovskite absorber. *Science* **342,** 341 (2013). DOI: 10.1126/science.1243982

[8] Jeon, N. J. *et al.* Solvent engineering for high-performance inorganic-organic hybrid perovskite solar cells. *Nat. Mater.* **13,** 897 (2014). DOI: 10.1038/NMAT4014

[9] Zhang, W. *et al.* Ultrasmooth organic-inorganic perovskite thin-film formation and crystallization for efficient planar heterojunction solar cells. *Nat Commun* **6,** 6142 (2015). DOI: 10.1038/ncomms7142

[10] Forgács, D., Sessolo, M. & Bolink, H. J. Lead acetate precursor based p-i-n perovskite solar cells with enhanced reproducibility and low hysteresis. *J. Mater. Chem. A* 14121 (2015). DOI: 10.1039/c5ta03169a

[11] Heo, J. H., Song, D. H. & Im, S. H. Planar CH3NH3PbBr3 hybrid solar cells with 10.4% power conversion efficiency, fabricated by controlled crystallization in the spin-coating process. *Adv. Mater.* **26,** 8179 (2014) DOI: 10.1002/adma.201403140

[12] Sheng, R. *et al.* Methylammonium lead bromide perovskite-based solar cells by vapor-assisted deposition. *J. Phys. Chem. C* **119,** 3545 (2015). DOI: 10.1021/jp512936z

[13] Saidaminov, M. I. *et al.* High-quality bulk hybrid perovskite single crystals within minutes by inverse temperature crystallization. *Nat. Commun.* **6,** 7586 (2015). DOI: 10.1038/ncomms8586

[14] Colella, S. *et al.* Elusive presence of chloride in mixed halide perovskite solar cells. *J. Phys. Chem. Lett.* **5,** 3532 (2014). DOI:10.1021/jz501869f

[15] Yu, H. *et al.* The role of chlorine in the formation process of 'CH3NH3PbI3-xClx' perovskite. *Adv. Funct. Mater.* **24,** 7102 (2014). DOI: 10.1002/adfm.201401872

[16] Hao, F., Stoumpos, C. C., Cao, D. H., Chang, R. P. H. & Kanatzidis, M. G. Lead-free solid-state organic-inorganic halide perovskite solar cells. *Nat. Phot.* **8,** 489 (2014). DOI:10.1038/nphoton.2014.82

[17] Noel, N. K. *et al.* Lead-free organic-inorganic tin halide perovskites for photovoltaic applications. *Energy Environ. Sci.* **7,** 3061 (2014). DOI: 10.1039/c4ee01076k

[18] Yokoyama, T. *et al.* Overcoming short-circuit in lead-free CH3NH3SnI3 perovskite solar cells via kinetically controlled gas-solid reaction film fabrication process. *J. Phys. Chem. Lett.* **7,** 776 (2016). DOI:10.1021/acs.jpclett.6b00118

[19] Krishnamoorthy, T. *et al.* Lead-free germanium iodide perovskite materials for photovoltaic applications. *J. Mater. Chem. A* **3,** 23829 (2015). DOI: 10.1039/c5ta05741h

[20] Jeng, J.-Y. *et al.* CH3NH3PbI3 perovskite/fullerene planar-heterojunction hybrid solar cells. *Adv. Mater.* **25,** 3727 (2013). DOI: 10.1002/adma.201301327

[21] Wang, Q. *et al.* Large fill-factor bilayer iodine perovskite solar cells fabricated by a low-temperature solution-process. *Energy Environ. Sci.* **7,** 2359 (2014). DOI: 10.1039/c4ee00233d

[22] Burschka, J. *et al.* Sequential deposition as a route to high-performance perovskite-sensitized solar cells. *Nature* **499,** 316 (2013). DOI: 10.1038/nature12340

[23] Liu, D., Gangishetty, M. K. & Kelly, T. L. Effect of CH3NH3PbI3 thickness on device efficiency in planar heterojunction perovskite solar cells. *J. Mater. Chem. A* **2,** 19873 (2014). DOI: 10.1039/c4ta02637c

[24] Wu, Y. *et al.* Retarding the crystallization of PbI2 for highly reproducible planar-structured perovskite solar cells via sequential deposition. *Energy Environ. Sci.* **7,** 2934 (2014). DOI: 10.1039/c4ee01624f

[25] Xiao, Z. *et al.* Efficient, high yield perovskite photovoltaic devices grown by interdiffusion of solution-processed precursor stacking layers. *Energy Environ. Sci.* **7,** 2619 (2014). DOI: 10.1039/c4ee01138d

[26] Zhu, X., Su, H., Marcus, R. A. & Michel-Beyerle, M. E. Computed and experimental absorption spectra of the perovskite CH3NH3PbI3. *J. Phys. Chem. Lett.* **5,** 3061 (2014). DOI: 10.1021/jz501174e

[27] Im, J.-H., Lee, C.-R., Lee, J.-W., Park, S.-W. & Park, N.-G. 6.5% efficient perovskite quantum-dot-sensitized solar cell. *Nanoscale* **3,** 4088 (2011). DOI: 10.1039/C1NR10867K

[28] Seo, J. *et al.* Benefits of very thin PCBM and LiF layers for solution-processed p-i-n perovskite solar cells. *Energy Environ. Sci.* **7,** 2642 (2014). DOI: 10.1039/C4EE01216J

[29] Eperon, G. E., Burlakov, V. M., Docampo, P., Goriely, A. & Snaith, H. J. Morphological control for high performance, solution-processed planar heterojunction perovskite solar cells. *Adv. Funct. Mater.* **24,** 151 (2014). DOI: 10.1002/adfm.201302090

[30] Zhang, H. *et al.* A smooth CH3NH3PbI3 film via a new approach for forming the pbi2 nanostructure together with strategically high CH3NH3I concentration for high efficient planar-heterojunction solar cells. *Adv. Energy Mater.* **5,** 1501354 (2015). DOI: 10.1002/aenm.201501354

[31] Kojima, A., Teshima, K., Shirai, Y. & Miyasaka, T. Organometal halide perovskites as visible-light sensitizers for photovoltaic cells. *J. Am. Chem. Soc.* **131,** 6050 (2009). DOI: 10.1021/ja809598r

[32] Xiao, M. *et al.* A fast deposition-crystallization procedure for highly efficient lead iodide perovskite thin-film solar cells. *Angew. Chemie* **126,** 10056 (2014). DOI: 10.1002/ange.201405334

[33] Li, X. *et al.* Improved performance and stability of perovskite solar cells by crystal crosslinking with alkylphosphonic acid ω-ammonium chlorides. *Nat. Chem.* **7,** 703 (2015). DOI: 10.1038/NCHEM.2324

[34] Liang, P. W. *et al.* Additive enhanced crystallization of solution-processed perovskite for highly efficient planar-heterojunction solar cells. *Adv. Mater.* **26,** 3748 (2014). DOI: 10.1002/adma.201400231
[35] Zuo, C. & Ding, L. An 80.11% FF record achieved for perovskite solar cells by using the NH4Cl additive. *Nanoscale* **6,** 9935 (2014). DOI: 10.1039/c4nr02425g
[36] Liu, J. *et al.* Improved crystallization of perovskite films by optimized solvent annealing for high efficiency solar cell. *ACS Appl. Mater. Interfaces* **7,** 24008 (2015). DOI: 10.1021/acsami.5b06780
[37] Aldibaja, F. K. *et al.* Effect of different lead precursors on perovskite solar cell performance and stability. *J. Mater. Chem. A* **3,** 9194 (2015). DOI: 10.1039/c4ta06198e
[38] Nie, W. *et al.* High-efficiency solution-processed perovskite solar cells with millimeter-scale grains. *Science* **347,** 522 (2015). DOI: 10.1126/science.aaa0472
[39] Zhou, H. P. *et al.* Interface engineering of highly efficient perovskite solar cells. *Science* **345,** 542 (2014). DOI: 10.1126/science.1254050
[40] De Bastiani, M. *et al.* Ion migration and the role of preconditioning cycles in the stabilization of the J-V characteristics of inverted hybrid perovskite solar cells. *Adv. Energy Mater.* **6,** 1501453 (2016). DOI: 10.1002/aenm.201501453
[41] Tress, W. *et al.* Understanding the rate-dependent J–V hysteresis, slow time component, and aging in CH3NH3PbI3 perovskite solar cells: the role of a compensated electric field. *Energy Environ. Sci.* **8,** 995 (2015). DOI: 10.1039/c4ee03664f
[42] Unger, E. L. *et al.* Hysteresis and transient behavior in current-voltage measurements of hybrid-perovskite absorber solar cells. *Energy Environ. Sci.* **7,** 3690 (2014). DOI: 10.1039/C4EE02465F
[43] Wased, Y., Matsubara, E. & Shinoda, K. "Chpater 4: Diffraction from Polycrystalline Samples and Determination of Crystal Structure." *X-Ray Diffraction Crystallography Introduction, Examples, and Solved Problems*, Springer, 2011, page 107–167.
[44] Poglitsch, A. & Weber, D. Dynamic disorder in methylammoniumtrihalogenoplumbates (II) observed by millimeter-wave spectroscopy. *J. Chem. Phys.* **87,** 6373 (1987). DOI: 10.1063/1.453467
[45] Wang, S. *et al.* Credible evidence for the passivation effect of remnant PbI2 in CH3NH3PbI3 films in improving the performance of perovskite solar cells. *Nanoscale* **8,** 6600 (2016). DOI: 10.1039/c5nr08344c
[46] Supasai, T., Rujisamphan, N., Ullrich, K., Chemseddine, A. & Dittrich, T. Formation of a passivating CH3NH3PbI3/PbI2 interface during moderate heating of CH3NH3PbI3 layers. *Appl. Phys. Lett.* **103,** 183906 (2013). DOI: 10.1063/1.4826116
[47] Chen, Q. *et al.* Controllable self-induced passivation of hybrid lead iodide perovskites toward high performance solar cells. *Nano Lett.* **14,** 4158 (2014). DOI: 10.1021/nl501838y
[48] Wang, S. *et al.* Credible evidence for the passivation effect of remnant PbI2 in CH3NH3PbI3 films in improving the performance of perovskite solar cells. *Nanoscale* **8,** 6600 (2016). DOI: 10.1039/c5nr08344c
[49] Schoonman, J. Organic–inorganic lead halide perovskite solar cell materials: A possible stability problem. *Chem. Phys. Lett.* **619,** 193 (2015). DOI: 10.1016/j.cplett.2014.11.063
[50] Liu, F. *et al.* Is excess PbI2 beneficial for perovskite solar cell performance? *Adv. Energy Mater.* **6,** 1502206 (2016). DOI: 10.1002/aenm.201502206

[51] Moore, D. T. *et al.* Crystallization kinetics of organic-inorganic trihalide perovskites and the role of the lead anion in crystal growth. *J. Am. Chem. Soc.* **137,** 2350 (2015). DOI: 10.1021/ja512117e

[52] Khim, D. *et al.* Control of Ambipolar and Unipolar Transport in Organic Transistors by Selective Inkjet-Printed Chemical Doping for High Performance Complementary Circuits. *Adv. Funct. Mater.* **24,** 6252 (2014). DOI: 10.1002/adfm.201400850

[53] Heo, J. H., Han, H. J., Kim, D., Ahn, T. K. & Im, S. H. Hysteresis-less inverted CH3NH3PbI3 planar perovskite hybrid solar cells with 18.1% power conversion efficiency. *Energy Environ. Sci.* **8,** 1602 (2015) DOI: 10.1039/c5ee00120j

[54] Chiang, C.-H. & Wu, C.-G. Bulk heterojunction perovskite–PCBM solar cells with high fill factor. *Nat Phot.* **10,** 196 (2016). DOI:10.1038/nphoton.2016.3

[55] Bryant, D. *et al.* Observable hysteresis at low temperature in 'hysteresis free' organic-inorganic lead halide perovskite solar cells. *J. Phys. Chem. Lett.* **6,** 3190 (2015). DOI: 10.1021/acs.jpclett.5b01381

[56] Bag, M. *et al.* Kinetics of ion transport in perovskite active layers and its implications for active layer stability. *J. Am. Chem. Soc.* **137,** 13130 (2015). DOI**:** 10.1021/jacs.5b08535

[57] Labram, J. G. *et al.* Temperature-dependent polarization in field-effect transport and photovoltaic measurements of methylammonium lead iodide. *J. Phys. Chem. Lett.* **6,** 3565 (2015).DOI: 10.1021/acs.jpclett.5b01669

[58] Liu, D., Gangishetty, M. K. & Kelly, T. L. Effect of CH3NH3PbI3 Thickness on Device Efficiency in Planar Heterojunction Perovskite Solar Cells. *J. Mater. Chem. A* **2,** 19873 (2014). DOI: 10.1039/c4ta02637c

Chapter 3

Investigation of the optoelectronic parameters of solution-processed $MAPbI_3$ perovskites

The availability of high-quality films with good reproducibility is a prerequisite for advanced characterization of planar structure-based devices. The process outlined in the last chapter led us to select the use of lead acetate ($PbAc_2$) as a precursor to obtain good quality films, and we can now turn to the study of the fundamental device properties of with the aim to better understand the working mechanisms. In this chapter, several concepts and parameters derived from traditional semiconductor physics are discussed and measured. In particular, the energy levels of $MAPbI_3$ were studied using photoelectron spectroscopy and Kelvin probe, the temperature-dependent mobility was measured using the time-of-flight technique, and the tunneling current injection was investigated using low temperature current–voltage–luminance (*J–V–L*) measurements. An introduction to the basic concepts of optoelectronic parameters in photovoltaic materials and their relationships with each is presented below, followed by the details of experiments and their discussion in sections 3.1–3.3.

The concept of energy levels in a crystalline material can be pictured in a simplified form according to general solid-state theory as shown in Fig. 3-1. The energy states available for the electrons form the conduction band (red cone) while holes form the valence band (yellow cone). The difference between the conduction band minimum (CBM) and the valence band maximum (VBM) represents the electrical band gap E_g. Furthermore, the near band edge region can generally be approximated using a parabolic function:

$$E \approx \frac{\hbar^2 k^2}{2m^*}, \qquad \text{Eq. 3-1}$$

where $\hbar$ is the reduced Planck's constant and k is the magnitude of the wave vector. The parabolic coefficient of the *E–k* relationship is arranged so that its form is the same as the kinetic energy of electrons in vacuum with the mass replaced by m^*. Therefore, m^* is the termed the effective mass. This value is extensively used in semi-classical descriptions of the material. Because the band structure can be simulated from the crystal structure using density functional theory, m^* provides a crucial connection between theoretical calculations and experimental results. One example of the simulated band structure of $MAPbI_3$ perovskite is shown in Fig. 3-1 (b).

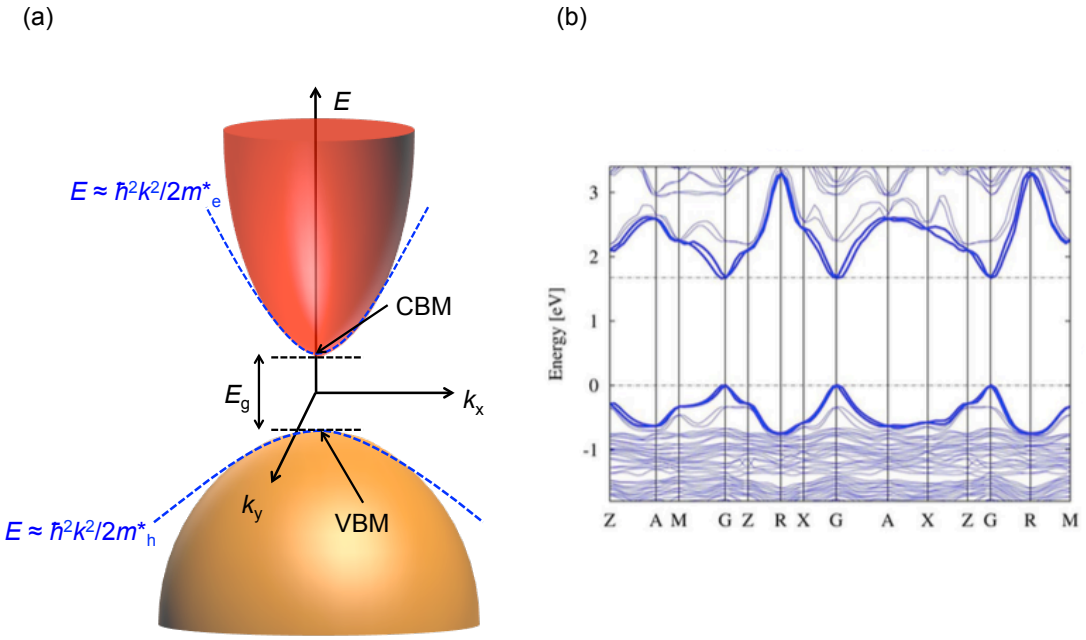

Fig. 3-1 (a) Simplified band structure of a general crystalline material in the reciprocal space and (b) calculated $MAPbI_3$ perovskite band structure. (b) Adapted with permission from ref 1. Copyright 2014 Nature Publishing Group.

The basic processes in optoelectronic materials are shown in Fig. 3-2. After generation of an electron–hole pair by light absorption, the charge carriers drift towards the selective contacts, a process characterized by the drift mobility, μ, given by:

$$\mathbf{v}_\mathrm{d} = \mu\mathbf{E}\,, \qquad \text{Eq. 3-2}$$

where $\mathbf{v}_\mathrm{d}$ is the drift velocity and $\mathbf{E}$ is the electric field. The drift mobility thus denotes the velocity of the carriers under the influence of an electric field and is limited by scattering processes such as defects and/or phonon scattering. With a scattering time of τ_s, the relationship between carrier mobility μ and the effective mass m^* is given by:

$$\mu = \frac{q}{m^*}\tau_\mathrm{s}\,, \qquad \text{Eq. 3-3}$$

according to the classical scattering model (Debye model).

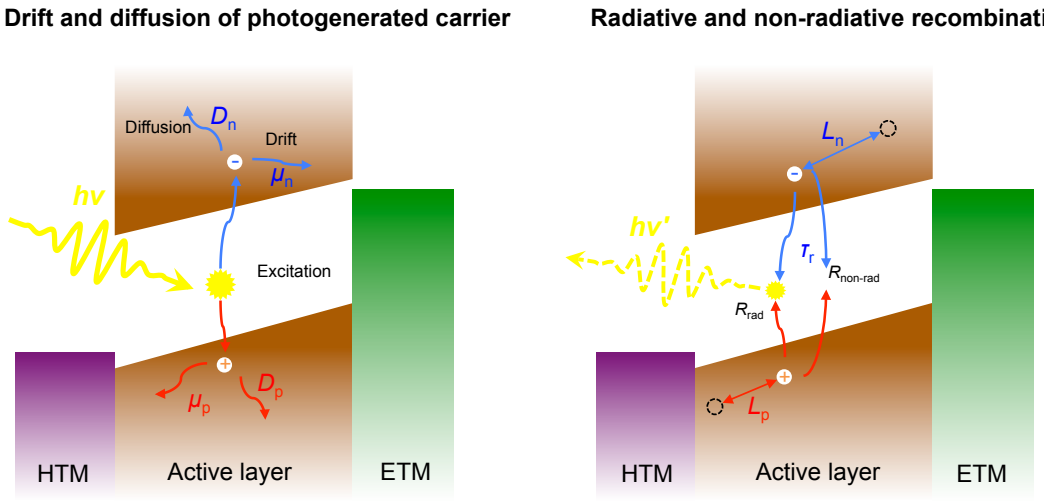

Fig. 3-2 Schematic diagram of the processes in optoelectronic materials. Left: Following the electron–hole pair generation by photoexcitation, the electrons and hole diffuse in the active layer with diffusion constant D_n and D_p, respectively. When an electric field is present, the charge carriers also drift according to Eq. 3-2 with drift mobility μ_n and μ_p. Right: The electrons and holes recombine radiatively or non-radiatively with recombination constants R_{rad} and $R_{non\text{-}rad}$, both of which contribute to the finite average life time of the carrier, denoted by τ_r. Before recombination, the average distance the charge carriers travel is denoted by L_n and L_P for electrons and holes, respectively.

The diffusion of charge carriers can be described by Fick's second law:

$$\frac{\partial C}{\partial t} = D\frac{\partial^2 C}{\partial x^2}, \qquad \text{Eq. 3-4}$$

where C is the carrier concentration, D is the diffusivity, and (x, t) are the space time parameters.

Also, the mobility μ is related to the diffusivity D by Einstein's relation:

$$\mu = \frac{qD}{k_B T}, \qquad \text{Eq. 3-5}$$

where q is the elementary charge, k_B is the Boltzmann constant, and T is the absolute temperature.

The electrostatic attraction between electrons and holes makes the formation of spatially-bound electron–hole pairs favored. The latter are termed excitons, and are characterized by an exciton binding energy (E_B) which, in traditional semiconductors, is usually smaller than thermal energy at room temperature. Therefore, the photogenerated

charges can be considered to be free carriers. On the other hand, the large exciton binding energy in organic semiconductors forms localized excitons, and the dissociation is achieved only in the vicinity of a charge selective contact. Otherwise, recombination is the dominant process. The recombination, characterized by the carrier lifetime (τ_r), can be radiative and/or non-radiative,. The parameter denoting the average distance travelled before the carriers recombine is the carrier diffusion length (L), which is related to the diffusivity and carrier lifetime by:

$$L = \sqrt{D\tau_r}\,. \qquad \text{Eq. 3-6}$$

As discussed in Chapter 1, HOIPs have been shown to process a low trap density, long carrier diffusion lengths and lifetimes, and low exciton binding energy, all of which contribute to their outstanding photovoltaic performances. While these parameters have been calculated or measured experimentally, some ambiguity and discrepancies still remain between reports, possibly due to the sensitivity to processing conditions and/or differences in data interpretation.

3.1 $MAPbI_3$ energy levels

In the previous chapter, we characterized the $MAPbI_3$ thin films using various spectroscopic and microscopy techniques. The spectroscopic techniques (absorption, photoluminescence, electroluminescence) provided information about the band gap of the HOIP films. From XRD, we were able to determine the crystalline phase and the lattice constants. Optical microscopy and AFM provided information on the HOIP surface. However, to better understand the operation of solar cells and the interface properties, other data such as electron affinity, ionization potential, and Fermi level are also important.

The electron affinity (EA) is defined by the energy released during the addition of an electron to a neutral material:

$$\text{Material} + e^- \rightarrow \text{Material}^- + \text{EA}\,.$$

In semiconductors, this energy corresponds to the difference between the vacuum level and the valence band maximum.

The ionization potential (IP) is the energy required to remove one electron from the material:

$$\text{Material} + \text{IP} \rightarrow \text{Material}^+ + e^- .$$

This corresponds to the conduction band maximum in the band structure of semiconductors.

The Fermi level indicates the energy level up to which electrons are filled according to the Fermi–Dirac distribution:

$$n(E) \propto \frac{1}{1 + e^{E-\mu}}, \qquad \text{Eq. 3-7}$$

where n is the density of states, μ is the Fermi level. The Fermi level lies in the conduction band in metals, and in the optical gap for semiconductors or insulators.

Photoelectron spectroscopy is a powerful technique in determining the energy of these levels. The concept originates from Einstein's photoelectron experiment, in which the energy of photoelectrons is analyzed to obtain the energy levels in a sample. Different excitation sources give different photoelectron energy ranges and resolution due to changes in the absorption cross sections. For example, using X-rays excites the high-energy core electrons of the elements so that the core energy levels can be determined. On the other hand, using the emission line of helium (for example, HeI, with a photon energy of 21.22 eV) as a light source allows the work function and valence band edge to be more accurately determined because of the larger absorption cross section at this excitation region. The working principles of photoelectron spectroscopy are shown in Fig. 3-3.

X-ray and HeI are the two most commonly used light sources in photoelectron spectroscopy. These specific techniques are termed X-ray photoelectron spectroscopy (XPS) and ultraviolet photoelectron spectroscopy (UPS), respectively.

A general survey of photoelectron spectroscopy studies of $MAPbI_3$ in the literature shows significant discrepancies in surface energy levels between reports.[2,3,4,5,6,7] For example, the work function reported range from 4.0 eV to 4.9 eV. This gives evidence that the properties of HOIP strongly depend on processing conditions and that the characterization of a given preparation recipe is important.

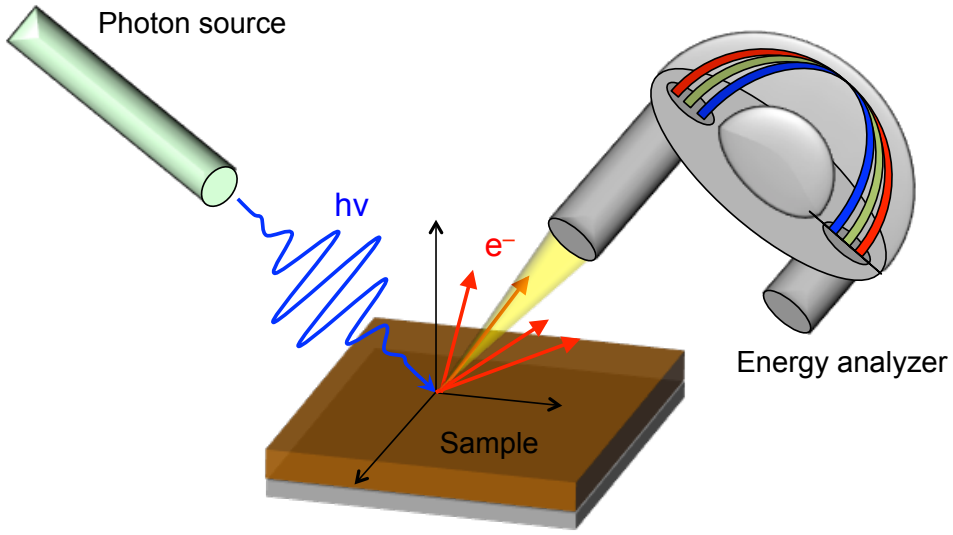

Fig. 3-3 Illustration of the operation of photoelectron spectroscopy

The X-ray photoelectron spectra of $MAPbI_3$ films (thickness 300 nm, prepared according to the procedure described in section 2.2.2) with the index of the core electron levels is shown in Fig. 3-4 (a).[†] The peaks from the elements (carbon, nitrogen, iodine, and lead) are readily observed. From the peak heights, the stoichiometry can be roughly estimated to be C : N : Pb : I ~ 1 : 0.3 : 1 : 2.5. Considering the 30% error range of this data analysis intrinsic to XPS measurements, the lead and iodide ratio are consistent with the chemical formula ($CH_3NH_3PbI_3$), while the deviation of the nitrogen ration might be from enviromental contanmination and/or X-ray induced surface damages.

[†] The XPS and UPS measurement were performed with the help of Mr. Michael Wussler and Dr. Mayer at Darmstadt University of Technology. Details can be found in Appendix 7.2.4.

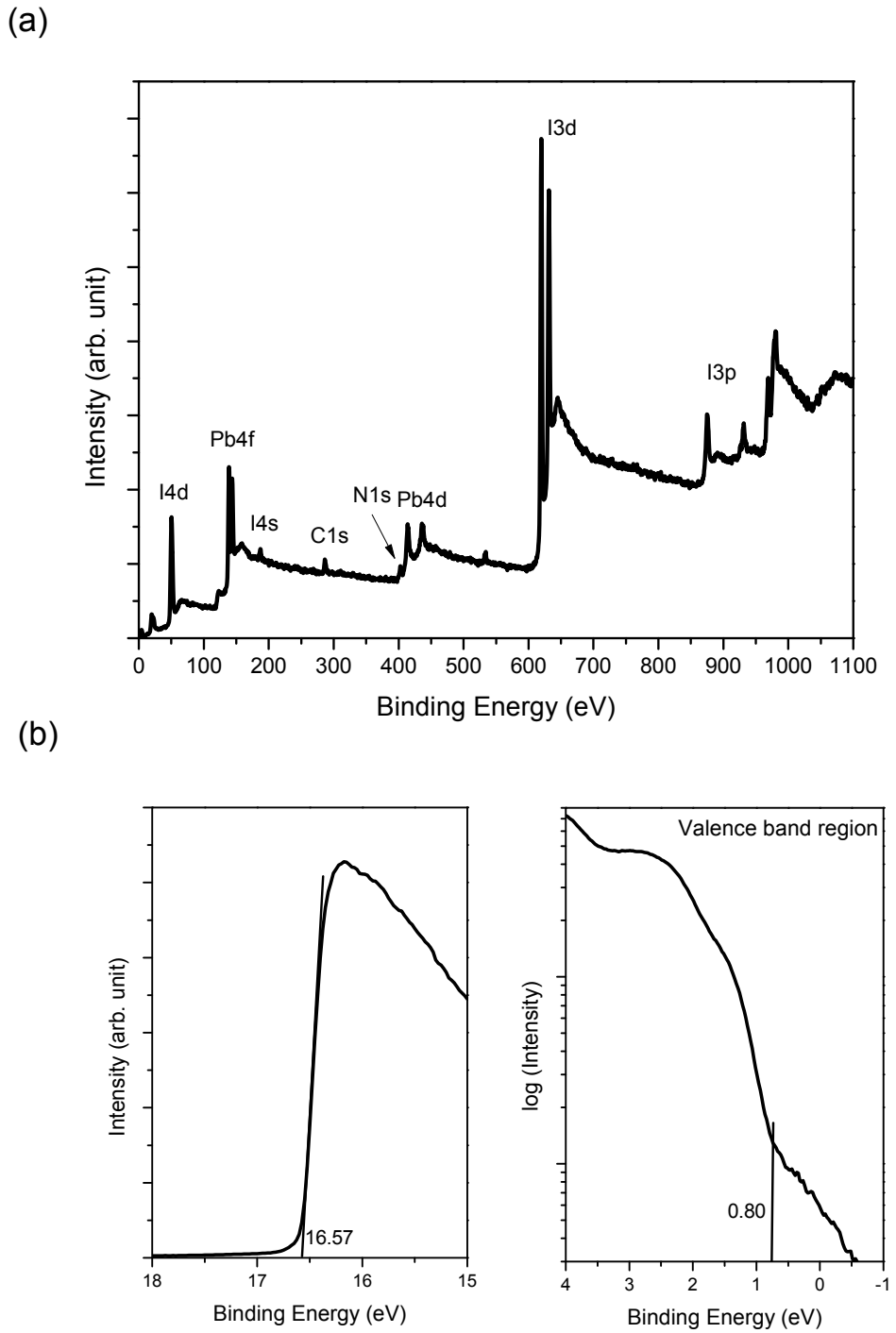

Fig. 3-4 (a) XPS and (b) UPS spectra of the $MAPbI_3$ surface. The sample structure was ITO/PEDOT:PSS/$MAPbI_3$ (200 nm) with the photons incident from the $MAPbI_3$ side. The valence band region is plotted in logarithmic scale as the valence band edge is determined more accurately in the log scale due to the intra-bandgap trap states of $MAPbI_3$ according to a recent report.[8]

The energetics of the $MAPbI_3$ film is derived from the HeI spectra (Fig. 3-4 (b)) according to: E_F = (the incident photon energy) – (the intercept on the cut-off region) = 21.22 – 16.57 = 4.65 (eV), and IP = E_F + (the intercept on the valence band region) = 4.65 + 0.80 = 5.45 (eV).

To obtain the energy level diagram of the $MAPbI_3$ film, the only information missing is the electrical band gap, which we obtained from electroluminescence of an ITO/PEDOT:PSS/$MAPbI_3$ (200 nm)/$PC_{61}BM$ (50 nm)/Ca/Al (Fig. 3-5). The center of the peak (760 nm) can be used to calculate the optical band gap = 1240/760 = 1.63 (eV). Due to the low exciton binding energy of this system (< 10 meV, see refs 9, 10, 11), we can equate the electrical and optical band gap as they are very close to each other.

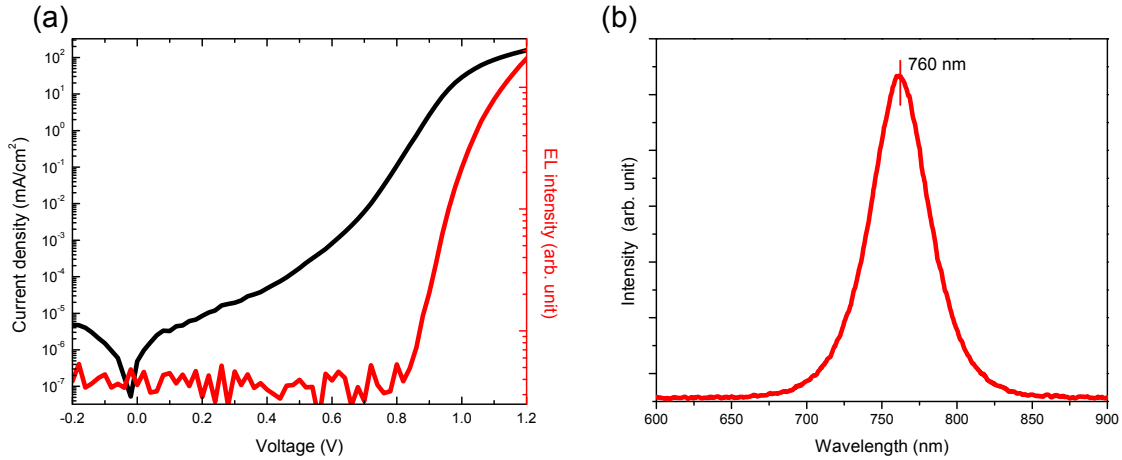

Fig. 3-5 Electroluminescence of an ITO/PEDOT:PSS/$MAPbI_3$/$PC_{61}BM$ /Ca/Al device. (a) Current–voltage–luminance characteristic, and (b) electroluminescence spectra. The details of the measurement can be found in Appendix 7.2.5.

The energy levels of $MAPbI_3$ as determined from the above experiments are summarized in Fig. 3-6.

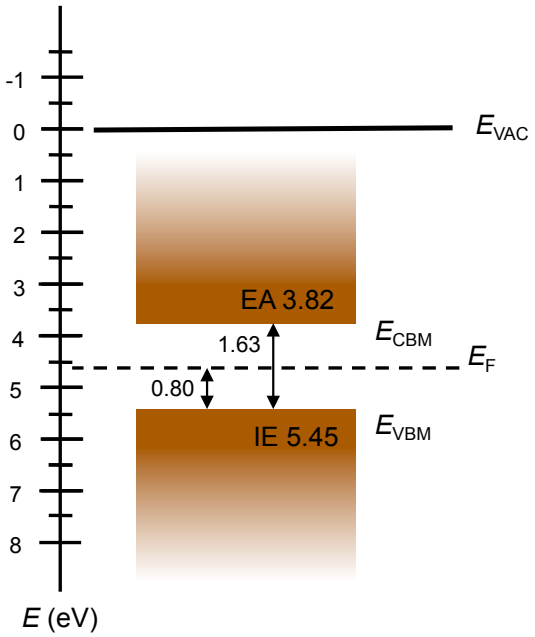

Fig. 3-6 Experimentally determined energy level diagram of $MAPbI_3$ (EA: electron affinity, IE: ionization energy, E_{VAC}: vacuum level, E_F: Fermi level)

For comparison, the energy levels of $MAPbI_3$ found in the literature are summuarized in Table 2-1. There are significant discrepancy between reports, as noted above, and our results lie within the its range.

Table 2-1 Summary of solution processed $MAPbI_3$ electron affinity and ionization potential reported in the literature

ref.	EA (eV)	IP (eV)
2	4.0	5.7
3	3.9	5.6
4	4.53	6.23
5	3.97	5.52
6	3.83	5.53

Different thicknesses (200, 300, and 400 nm) of the $MAPbI_3$ film were measured and the same procedure was applied to determined the energy levels of the surfaces. Additionally, the work function was also measured under ambient atmosphere using a Kelvin probe to provide additional confirmation of the energy levels. (Details of the Kelvin probe measurements can be found in Appendix 7.2.6). The results are summarized in Table 3- 1. The similiarity of the energy levels over different thicknesses indicates that band bending effect occurs at depths less than 200 nm. Unforunately, the measurement of films less than 200 nm in thickness,

although likely to provide valuable information concerning band bending, is challenging since the solution process of HOIP film has a limited range of thickness over which the film morphology remains similar. The energy of the Fermi level measured under ambient atmosphere is in good agreement with the values in ultra high vacuum, considering the difference in experimental conditions and calibration of equipment.

Table 3- 1 Surface energy levels of different thicknesses of $MAPbI_3$

$MAPbI_3$ thickness (nm)	E_F (eV)	EA (eV)	IE (eV)	E_F in atmosphere (eV)
200	4.60	3.84	5.47	4.72
300	4.65	3.82	5.45	4.73
400	4.67	3.83	5.46	4.77

3.2 Time-of-flight mobility measurements

As discussed in the introduction, the mobility of a material strongly depends on the scattering processes impeding charge movement. Therefore, the mobility depends strongly on each material studied as well as on the processing conditions. To measure the mobility of a material, several methods can be employed, such as time-of-flight (TOF) measurements, charge extraction by linearly increasing voltage (CELIV), field effect transistor configuration (FET), and space charge limited conduction (SCLC) (for a review of theses techniques, see ref 12). Some measured mobility values of commonly used semiconductors are list as below:

Table 3- 2 Carrier mobility (μ) of commonly used material

	μ (cm^2/Vs)	
material	electron	hole
Si crystal[a]	1500	500
CdTe crystal[a]	<~1000	<~100
GaAs crystal[a]	~8000	~400
PbTe crystal[a]	~6000	~4000
Naphthalene crystal[b]	~1	~1
$MAPbI_3$ crystal[a]	≤~100	≤~100

[a]Data from ref 13. [b]Data from ref 14.

In Table 3- 2, the carrier mobility of single crystal $MAPbI_3$ is also listed for comparison. In the literature, the mobility of HOIP is usually considered to be "high," compared to organic semiconductors. However, Brenner *et al.* recently argued that because HOIPs have crystal structures resembling those of an inorganic crystals and their carrier effective mass is small, the mobility of HOIP should be compared with that of inorganic semiconductors.[13] In this context, the question arose as to why the carrier mobility of HOIP is generally smaller than that of traditional inorganic semiconductors.

On the other hand, while the reported carrier mobility of single crystal HOIPs are more or less consistent, those for polycrystalline thin films show large variations from ~10 cm^2/Vs,[15,16] $\sim10^{-1}$ cm^2/Vs,[17] $\sim10^{-3}$ cm^2/Vs,[18] to $\sim10^{-4}$ cm^2/Vs.[19] Such variations might be due to differences in sample configuration, interfacial effects, processing conditions, or measurement methods. For example, the highest reported carrier mobility values of $MAPbI_3$ polycrystalline thin films (~10 cm^2/Vs) are generally estimated using THz spectroscopy, whose wave pulses extend only a few unit cells within the material. These only detect the conductivity behavior over short time and length scales,[20] ignoring the larger scale effects which might play important roles in polycrystalline materials.[21,22]

To estimate large-scale effects, we measured the carrier mobility using the time-of-flight configuration (Fig. 3-7). A 532-nm laser (Continuum Minilite) with pulses less than 7 ns generated photocarriers from the transparent side of a sample. A bias voltage of a few volts was applied to separate the photogenerated electron–hole pairs. The photocurrent was then monitored using a digital oscilloscope (Tektronix). To ensure minimum oxygen and humidity exposure, the samples were transferred directly from a nitrogen-filled glove box to a cryostat without exposure to the atmosphere. The cryostat was then placed under vacuum ($\sim10^{-5}$ mbar) before measurement.

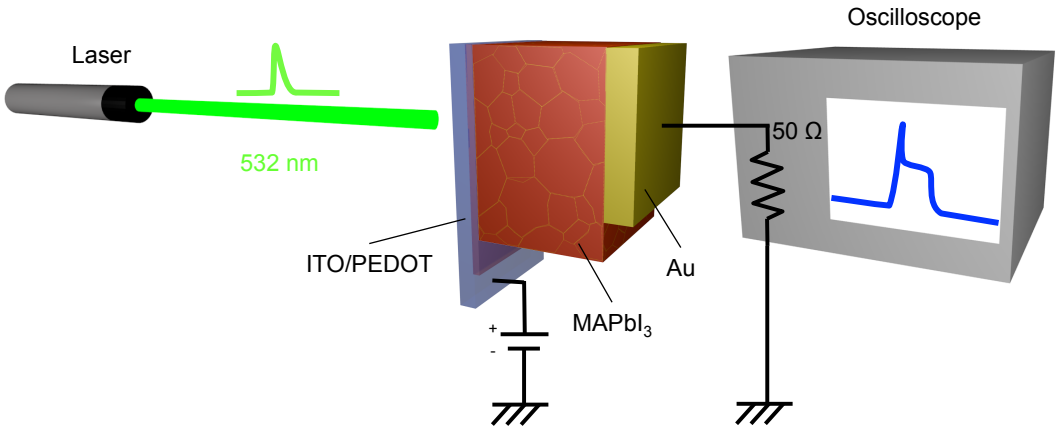

Fig. 3-7 Schematics of time-of-flight (TOF) measurement

The sample structure chosen to evaluate the hole mobility of the material was ITO/PEDOT:PSS/$MAPbI_3$/Au. Electrodes with better electron extraction, such as silver and calcium, were also tested but without success. These electrodes seem to react with $MAPbI_3$ and the samples became unusable soon after preparation. Aluminum showed better stability but its work function is too high for efficient electron extraction.

The sample thickness for TOF measurements needs to generally be around a few μm. However, to obtain $MAPbI_3$ films in this thickness using a solution process is likely to change the film morphology significantly, and therefore defeat the original purpose of the experiments. As a tradeoff, a film thickness of 300 nm was chosen in order to be similar to that of a working solar cell device. The absorption depth of $MAPbI_3$ at 532 nm is ca. 150 nm, as estimated from the absorption spectra,[23] showing that the majority of the incident laser energy is absorbed in the 300-nm-thick sample.

The photocurrent measured at room temperature at various applied biases is shown in Fig. 3-8. Some abnormalities can be readily observed: the photocurrent is negative with an applied bias as high as 1.5 V and no clear plateau can be observed at higher voltages. As a matter of fact, the sample broke down at an applied voltage of 5 V, as evidenced by the decrease in photocurrent.

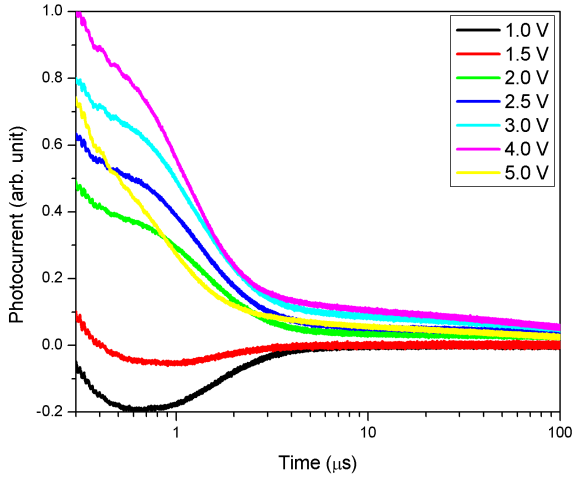

Fig. 3-8 Time-of-flight photocurrent of an ITO/PEDOT:PSS/$MAPbI_3$ (300 nm)/Au device at room temperature with applied voltage from 1 V to 5 V.

To explain such abnormal behavior, the material properties of HOIP have to be taken into account. As discussed in Chapter 1, perovskite materials are known for their ionic conductivity. In HOIP, it has been shown that ion accumulations have a significant effect on solar cell performance and are therefore not negligible.[24,25] Other reports suggest that ions accumulate at the interface and cause a built-in voltage.[26] Mobile ions are likely to compensate the applied voltage and prevent photocurrent generation. However, ion movement is highly temperature dependent (estimated activation energy ~1 eV). It is therefore reasonable to infer that if ionic displacement plays an important role in the TOF results, the photocurrent pattern would be strongly dependent on the sample temperature. Specifically, at lower temperatures ion movement should be less significant and the TOF might provide reasonable results for estimating the carrier mobility.

The TOF photocurrent measured at 180 K and 80 K are shown in Fig. 3-9. At these low temperatures, the negative photocurrent disappeared and plateaus can be clearly observed in the photocurrent patterns. $MAPbI_3$ undergoes a orthorhombic–to–tetragonal phase transition at 162 K,[27] which means that at 80 K the material is actually in the orthorhombic phase instead of the room temperature tetragonal phase.

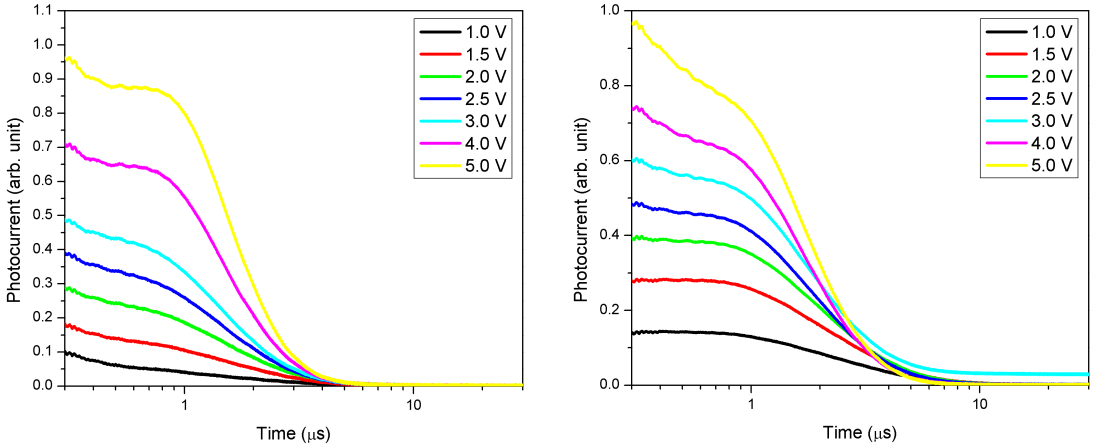

Fig. 3-9 Time-of-flight photocurrent of an ITO/PEDOT:PSS/$MAPbI_3$ (300 nm)/Au device at 180 K (left) and 80 K (right) with applied voltage from 1 V to 5 V.

The transit time (t_T) is estimated from the intercept of the 2 slopes on the normalized photocurrent plot (Fig. 3-10). Ideally, the carrier mobility μ is related to t_T by:

$$\mu = \frac{d^2}{V t_T}, \qquad \text{Eq. 3-8}$$

where d is sample thickness and V is the applied voltage.

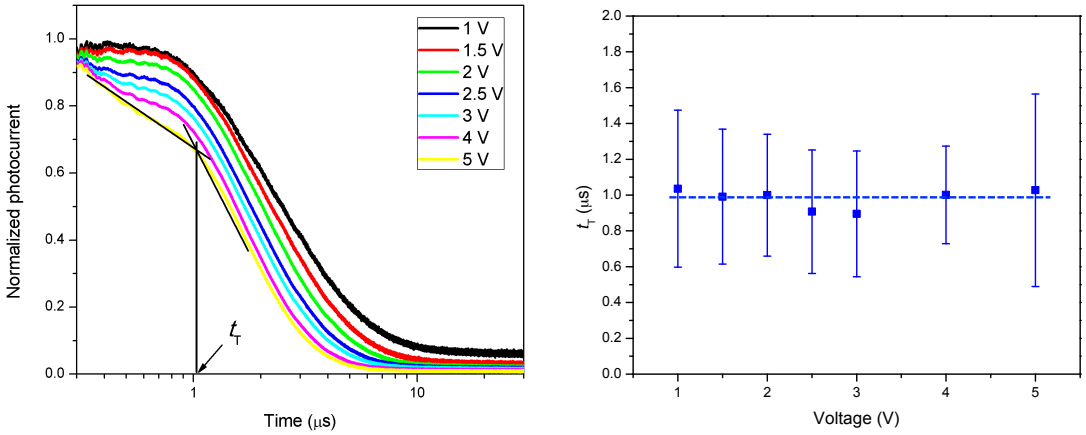

Fig. 3-10 Normalized photocurrent (left) and voltage dependence of the transit time (t_T) (right) of the time-of flight measurement of an ITO/PEDOT:PSS/$MAPbI_3$ (300 nm)/Au device at 80 K. The error bars were estimated from the standard deviations of the fitted lines.

The hole mobility of polycrystalline $MAPbI_3$ is therefore calculated to be ca. 10^{-4} cm^2/Vs, which is consistent with a previous literature report of TOF measurement,[19] although being surprisingly low compared to the results from other measurement methods. The low mobility appears to be contradictory to the outstanding photovoltaic performance of HOIP solar cells, but it has been suggested that the low diffusion length might increase the recombination

lifetime in polycrystalline materials (provided the main recombination process occurs at grain boundaries).[17] The relative independence of t_T on the applied voltage suggests that some voltage compensating effect might still be occurring at temperatures as low as 80 K. This may indicate that the TOF mobility value obtained is a rough estimate.

To gain more insight into the scattering process of the $MAPbI_3$ material, temperature dependent mobility measurements were carried out. In the literature, the temperature dependence of $MAPbI_3$ mobility has been shown to be proportional to $T^{-3/2}$, consistent with a phonon scattering mechanism. These studies are either performed on single crystal,[28] or using THz spectroscopy.[29] Here, TOF measurements were carried out on the polycrystalline films at temperatures ranging from 80 to 300 K. The applied bias was 3 V for all temperatures to get a clear plateau on the photocurrent patterns while not too high to damage the sample. The temperature dependence of the photocurrent and carrier mobility (calculated using Eq. 3-8)) are shown in Fig. 3-11.

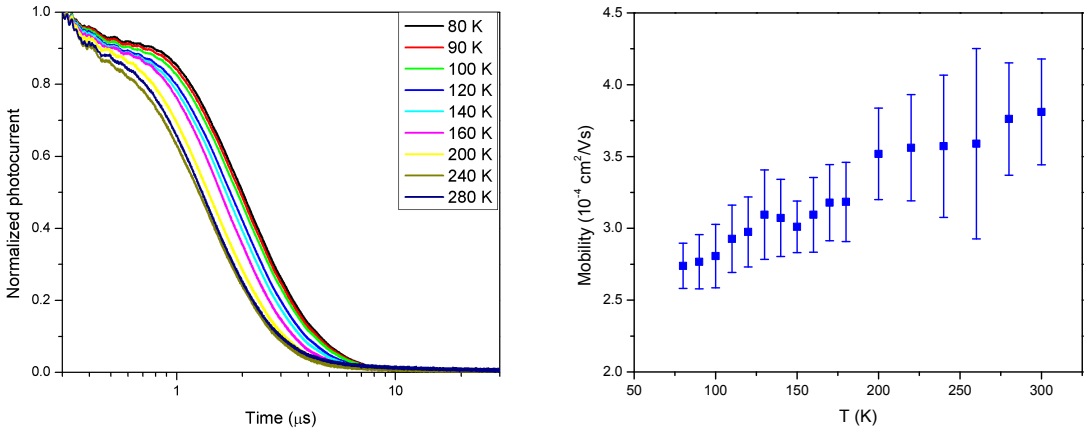

Fig. 3-11 Temperature dependence of the normalized photocurrent (left) and the hole mobility (right) from the time-of-flight measurements of an ITO/PEDOT:PSS/$MAPbI_3$ (300 nm)/Au device from 80 to 280 K. The error bars were estimated from the standard deviations of the fitted lines.

The TOF mobility increases with temperature (Fig. 3-11 right), in contradiction with measurements performed on single crystal $MAPbI_3$ or THz measurements.[28,29] This thermally-activated behavior is in agreement with a trapping–detrapping conduction mechanism, which is common in polycrystalline materials.[30] A jump is observed at ca. 160 K, which may be due to the orthorhombic-to-tetragonal phase transition in the material. One way of quantifying this type of conduction is through the variable range hopping (VRH) model, in

which the temperature dependence of the mobility is given by:[31,32]

$$\mu \propto \frac{e^{-\left(\frac{T_0}{T}\right)^{\alpha}}}{T}, \qquad \text{Eq. 3-9}$$

where T_0 is a constant, α can be either 1/4, 1/3, or 1/2 depending on the material.

The plot of ln (μT) versus $1/T^{1/2}$ is shown in Fig. 3-12. The linear behavior provides strong evidence that the scattering process is dominated by trapping effect in polycrystalline $MAPbI_3$ film (likely located at grain boundaries), contrary to phonon scattering in single crystal $MAPbI_3$. This difference, has so far not been recognized in the literature to the best of out knowledge, and has important implications in the operation of the thin film HOIP solar cells.

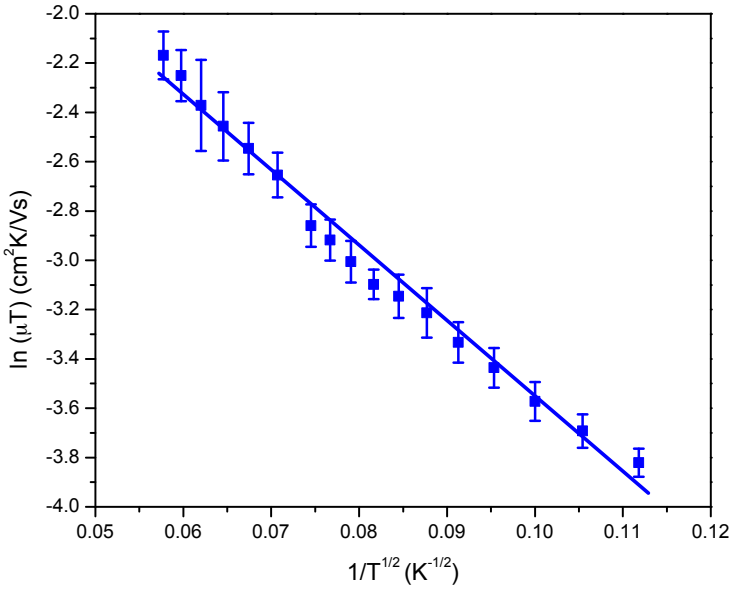

Fig. 3-12 VRH model fitting of the mobility temperature dependence

In conclusion, the hole mobility in HOIP thin films was characterized using the TOF technique. The temperature-dependence and voltage-dependence of the TOF photocurrent were studied. We propose that some voltage compensating mechanism is present in the $MAPbI_3$ films and that the trap effect is dominating the scattering process. The peculiar behavior of the TOF measurement at room temperature motivated us to further investigate the low temperature charge transport behavior of an ITO/PEDOT:PSS/$MAPbI_3$/Au device by analyzing its current–voltage–luminance (*J–V–L*) characteristics. The results are shown in the next section.

3.3 Low temperature *J–V–L* measurement

As mentioned above, we have reason to suspect that ion migration might still have an effect on charge conduction in $MAPbI_3$ perovskite at temperatures as low as 80K. To eliminate this complexity, we employed a helium compressor in connection with a cryostat (Advanced research systems, Fig. 3-13), which has the capacity to lower the sample temperature to < 10K. Instead of cooling from the substrate side, this setup cools the sample by the heat conduction of the helium filling the sample chamber. This configuration therefore minimizes the problem of sample temperature gradient and ensures accurate temperature control. The device current was then measured using a Keithley 4200 source meter and the electroluminescence (EL) intensity monitored using a silicon photodetector (Hamamatsu S2281-01, area 1 cm^2, coupled to a Hamamatsu C9329 preamplifier set in the high resolution mode).

Fig. 3-13 Experimental setup for low temperature *J–V–L* measurement: Cryostat (upper left), helium compressor (upper right) and sampling rod (down).

The high work function of ITO/PEDOT:PSS and gold makes the sample investigated (ITO/PEDOT:PSS/$MAPbI_3$/Au) a "hole-only" device. The large barrier for electron injection (> 1 eV) allows us to assume that the current observed is thus mostly contributed by holes. The EL intensity should therefore be proportional to the minority carrier current (electron current in this case). The possibility of transient current is eliminated by the slow scanning rate employed during measurement (~0.03 V/s), which makes the measurement quasi-static.

To illustrate the necessity of the low temperature measurements, the current–voltage in an ITO/PEDOT:PSS/$MAPbI_3$ (200 nm)/Au device was repeatedly measured at room temperature and at 10 K, shown in Fig. 3-14. At room temperature, the curves changed with consecutive measurement, a phenomenon that disappeared completely at 10 K.

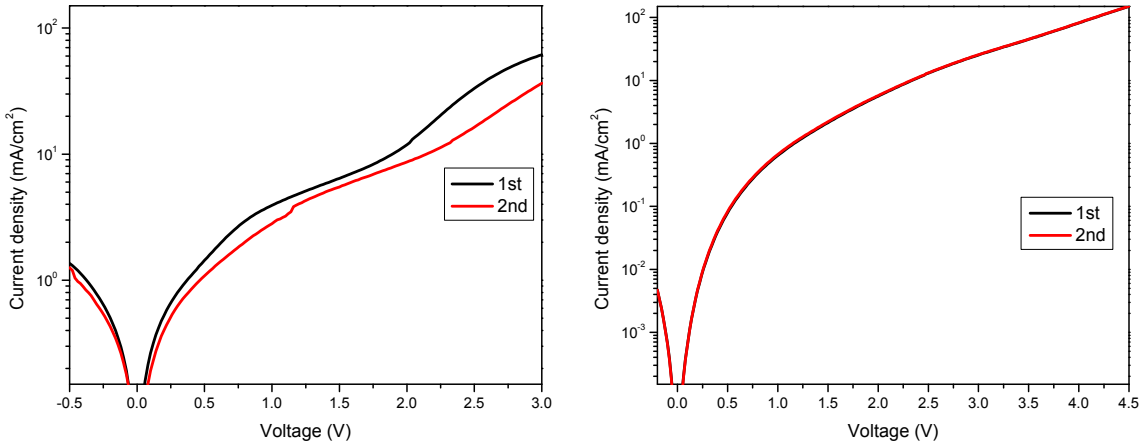

Fig. 3-14 Repeated current–voltage measurement of an ITO/PEDOT:PSS/$MAPbI_3$ (200 nm)/Au device. Left: at room temperature, right: at 10 K.

The *J–V–L* characteristics of an ITO/PEDOT:PSS/$MAPbI_3$ (200 nm)/Au device are shown in Fig. 3-15 (a). EL intensity was observed when the applied voltage bias was higher than 3.5 V. Based on the discussion above, it is reasonable to assume that EL intensity is proportional to the current resulting from the injected electrons (Fig. 3-15 (b)).

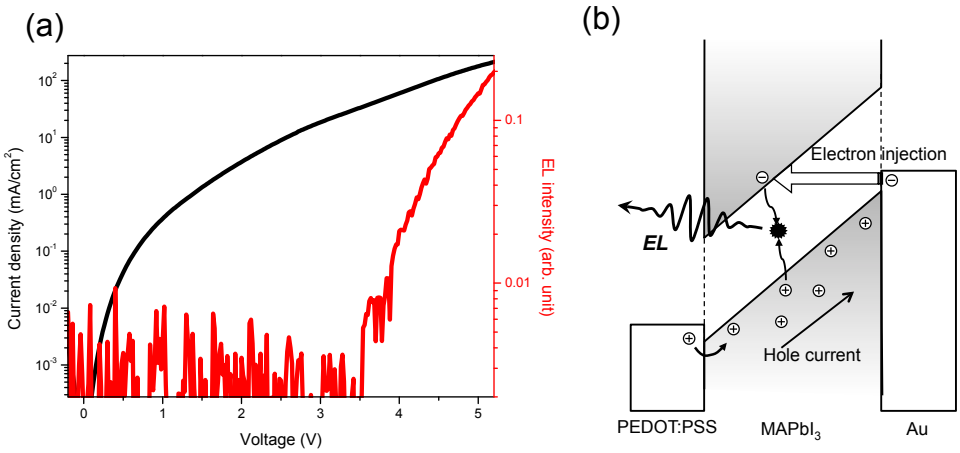

Fig. 3-15 (a) Current–voltage–luminance characteristics of an ITO/PEDOT:PSS /$MAPbI_3$ (200 nm)/Au device measured at 10 K. (b) Illustration of the current and injection process in this sample.

The high barrier for electron injection and the low temperature environment renders thermionic emission from gold to $MAPbI_3$ impossible. This leaves us with tunneling as the main mechanism for electron injection. The tunneling injection current is given by the Fowler–Nordheim equation:[33]

$$J_{FN} \propto E^2 exp\left[-\frac{4}{3}\left(\frac{2m^*}{\hbar^2}\right)^{1/2}\frac{\Phi_C^{3/2}}{qE}\right], \qquad \text{Eq. 3-10}$$

where E is the electrical field, m^* is the carrier effective mass, Φ_C is the injection barrier, and q is the elementary charge. The tunneling injection is not thermally activated and therefore the injection current should not change with temperature.

To check the validity of tunneling injection mechanism, the *J–V–L* characteristics were measured at temperatures from 10 K to 100 K, as shown in Fig. 3-16. The magnitude of EL intensity remains the same in this temperature range, thus validating the tunneling injection mechanism.

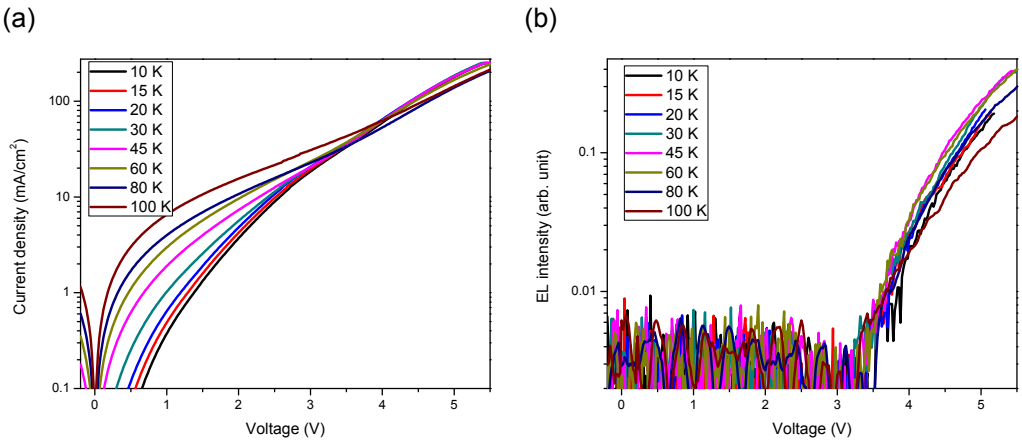

Fig. 3-16 Temperature dependence of *J–V–L* characteristics of an ITO/PEDOT:PSS/$MAPbI_3$ (200 nm)/Au device. (a) Current density and (b) EL intensity as a function of applied voltage from 10 K to 100 K.

Further analysis was carried out by plotting ln (J/E^2) vs. $1/E$, the so-called Flower–Nordheim plot.[34,35] Here we assume uniform distribution of the electrical field within the active layer, *i. e.*, $E = V/d$, and plot ln (EL/V^2) versus $1/V$ is shown in Fig. 3-17.

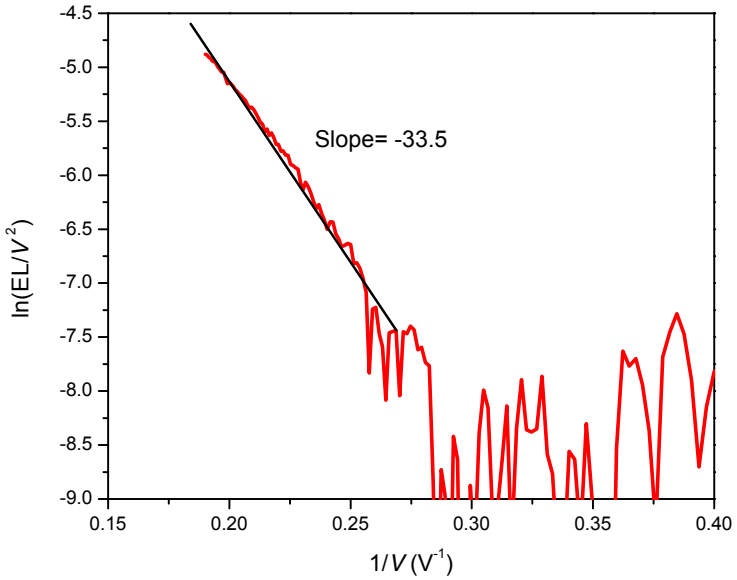

Fig. 3-17 Fowler–Nordheim plot of the EL intensity of an ITO/PEDOT:PSS /$MAPbI_3$ (200 nm)/Au device at 10 K.

According to Eq. 3-10, the slope of the Fowler–Nordheim plot (S) is given by:

$$S = \frac{4}{3}\left(\frac{2m^*}{\hbar^2}\right)^{1/2}\frac{\Phi_C^{3/2}d}{q}. \qquad \text{Eq. 3-11}$$

Generally, the lower the slope, the easier the tunneling injection.

The theoretical value of the slope in Eq. 3-11 can be calculated by assuming a triangular barrier for electron injection. The electron effective mass of $MAPbI_3$ is around 0.2 m_0 (where m_0 is the electron mass), determined using magneto-absorption technique,[36,37] and from theoretical calculations. [1,38] The injection barrier = gold work function – $MAPbI_3$ electron affinity = 1.28 eV. With these parameters, the slope is found to be ca. 360, much larger than the experimental value of 33.5 (Fig. 3-17).

The discrepancy in calculated versus experimental slope indicates enhanced electron injection under the experimental conditions. Two possibilities may contribute to this effect (Fig. 3-18). The first possibility is that the injection barrier may deviate significantly from the simple difference in energy levels (the gold work function and $MAPbI_3$ electron affinity) due to the interaction between surfaces at the interface.[39,40,41] The formation of an "interface dipole" might reduce the injection barrier and enhance electron injection. The second possibility is that the electric field is not uniform. The closeness of Fermi level with the middle of the band gap, as demonstrated by the UPS measurement in section 3.1, indicates that the free carrier concentration of $MAPbI_3$ is low and is therefore unlikely to cause significant band bending. However, it is possible that other mechanisms might contribute to the charge balance and cause band bending within the material. The ensuing increase in the electric field near the interface would enhance charge injection.

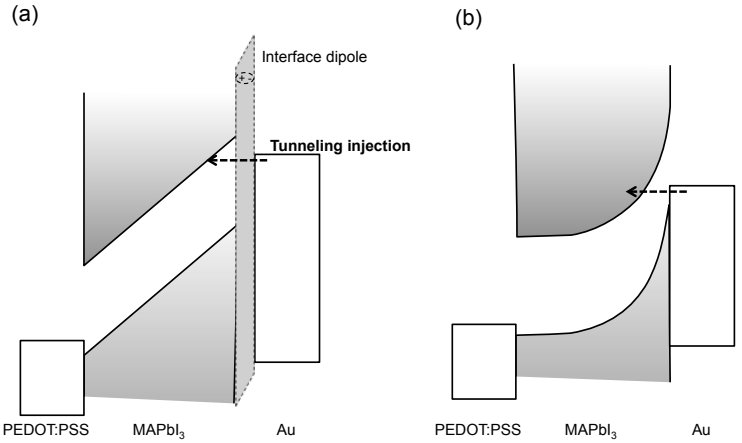

Fig. 3-18 Possible origins of the enhanced electron injection: (a) Interface dipole, (b) band-bending.

For the first hypothesis to account for the enhanced injection, the injection barrier would need

to be about 0.26 eV, which implies an interface dipole of 1.02 eV. In the HOIP literature, Liu *et al.* has studied the Au/$MAPbI_3$ interfacial effect using UPS,[2] and their results showed an interface dipole of 0.1 eV.

To test the two hypotheses, we measured the *J–V–L* characteristics with different sample thicknesses at 10 K (Fig. 3-19). The EL intensities are similar for all 3 thicknesses as are the onset at ca. 3.5 V. The thickness independence of these properties indicates that the electron injection is interface limited.

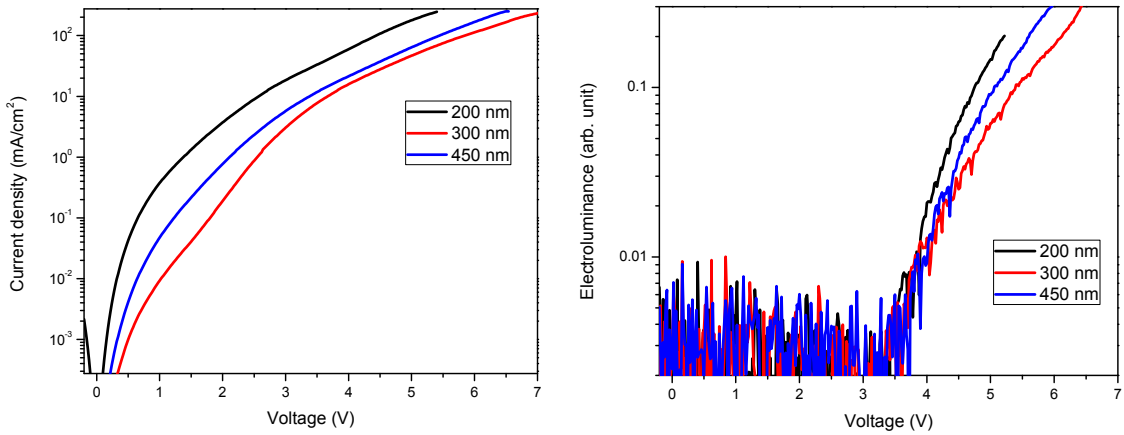

Fig. 3-19 Thickness-dependent current–voltage–luminance characteristics of an ITO/PEDOT:PSS/$MAPbI_3$/Au device measured at 10 K. Three thicknesses of the $MAPbI_3$ layer (200, 300, 450 nm) were measured.

The band bending effect can usually be studied using capacitance–voltage measurements or, more specifically, by plotting the square inverse of the capacitance versus voltage (Mott–Schottky plot).[33] The Mott–Schottky plot of an ITO/PEDOT:PSS/$MAPbI_3$ (200 nm)/Au device measured at 15 K using a Bio-logic impedance analyzer is shown in Fig. 3-20. No band bending was observed near zero applied voltage as evidenced by the independence of the capacitance on the voltage in this region. This result is in accordance with the previous energy level diagrams, which show that the free carrier concentration is low in $MAPbI_3$ perovskites.

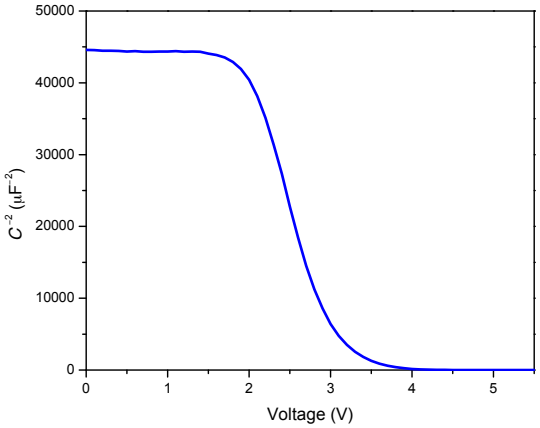

Fig. 3-20 Mott–Schottky plot of an ITO/PEDOT:PSS/$MAPbI_3$ (200 nm)/Au device at 15 K (recorded at frequency 10 kHz).

We are therefore led to conclude that the observed band bending is voltage induced, *i. e.*, it happens when there is an applied voltage. As the possibility of ionic redistribution under an applied bias is unlikely under the low temperature condition of the measurements, the working hypothesis of the origin of the induced band bend effect is that trap states at the $MAPbI_3$/ Au interface are being filled by holes as the bias voltage is applied. To quantify the trap states involved,* numerical simulation was carried out assuming that the trap concentration as a function of the distance from the gold electrode (x) obeys

$$N_{\mathrm{T}}(x) = N_{\mathrm{T1}} + N_{\mathrm{T2}} \exp\left(\frac{t-x}{\lambda}\right), \qquad \text{Eq. 3-12}$$

where N_{T1} is the volume trap concentration, N_{T2} the interface trap concentration, λ the typical distance, t the active layer thickness. The electrostatic potential $V(x)$ can then be deduced from the trap concentration by solving the Poisson equation, leading to:

$$V(x) = V_{\mathrm{a}}\left(\frac{x}{t} - 1\right) + \frac{eN_{\mathrm{T1}}}{2\varepsilon}(x^2 - tx) + \frac{eN_{\mathrm{T2}}\lambda^2}{\varepsilon}\left[\exp\left(-\frac{t-x}{\lambda}\right) - \exp\left(-\frac{t}{\lambda}\right)\left(1 - \frac{x}{t}\right) - \frac{x}{t}\right], \qquad \text{Eq. 3-13}$$

where V_{a} is the applied voltage, ε is the dielectric constant (assumed to be 30 in this simulation).

Once the band curvature is known, the electron tunneling current can be numerically

*The simulation was performed by Prof. Raphael Clerc of the Institut d'optique, site Rhône Alpes, Laboratoire Hubert Curien.

calculated using the injection transparency $T(E, V_a)$ from the Wentzel–Kramers–Brillouin (WKB) approximation:

$$T(E, V_a) = \exp\left[-2\int_0^{a(E)} \sqrt{\frac{2m(\phi - eV(x) - E)}{\hbar^2}}\, dx\right], \qquad \text{Eq. 3-14}$$

and then the injection current $J(V_a)$ is given by:

$$J(V_a) = \frac{4\pi m e^2 kT}{h^3} \int_0^{\infty} T(E, V_a) \ln\left(1 + \exp\left(\frac{E - E_F}{kT}\right)\right) dE\,, \qquad \text{Eq. 3-15}$$

The fitted results are shown in Fig. 3-21. Compared with the triangular barrier injection model (Fig. 3-21 (a)), this model including bulk and surface trapping (Fig. 3-21 (b)) shows much better fitting with experimental emission rates.

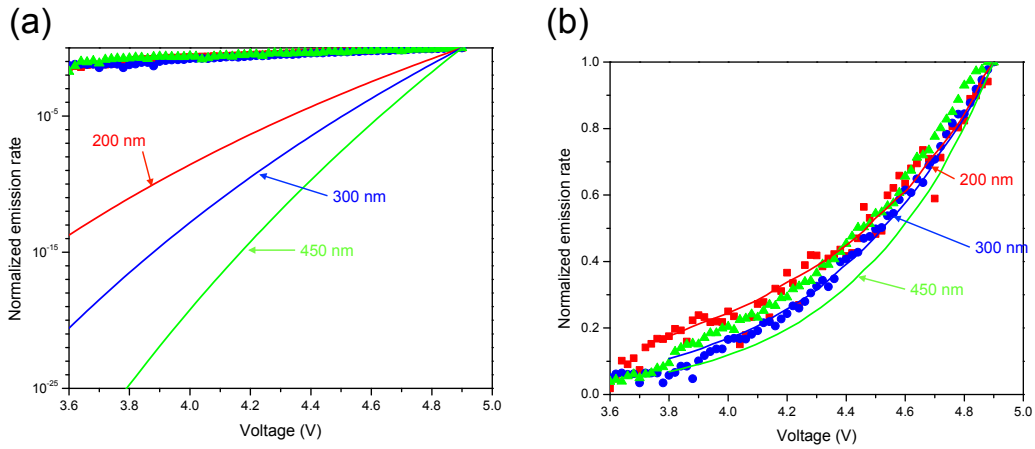

Fig. 3-21 Numerical simulation of the normalized emission rate (dots: experimental, lines: simulated). Fowler–Nordheim tunneling (a) trough an ideal triangular barrier and (b) with the effects of bulk and surface traps.

The simulated *J–V* characteristics of models with/without interface trap and with/without interface injection are shown in Fig. 3-22. Without traps, the space charge limited current (SCLC) model delivered unsatisfactory fitting results. With volume traps, the fitting improved significantly when the interface traps are taken into account, demonstrating the necessity of introducing interface traps. The fitting parameters of the complete models are shown in Table 3-3.

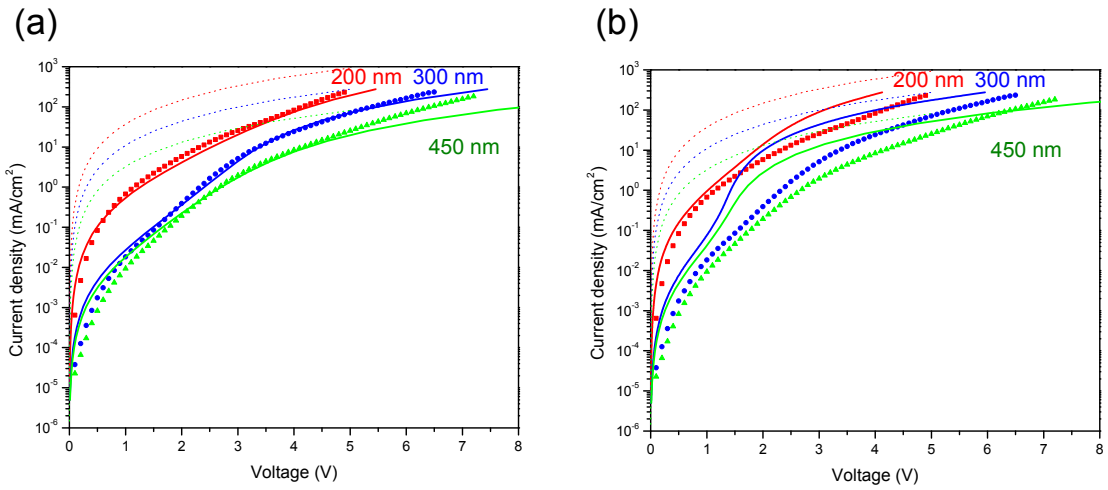

Fig. 3-22 Comparison of simulation models. (a) Full model including volume and interface traps. (b) Model with volume trap only. Models are the solid lines, experimental data filled circles. Dotted lines represent the pure SCLC model with no traps. Three thickness of the active layer (200, 300, and 450 nm) are presented.

Table 3-3 Fitting parameters of the complete fitting model including bulk and interface traps.

Sample thickness (nm)	200	300	450
Mobility (cm^2/Vs)		10^{-4}	
N_{T2} (cm^{-3})		5.5×10^{19}	
λ (nm)		6.5	
N_{T1} (cm^{-3})	1.6×10^{17}	5.0×10^{16}	2.3×10^{16}
p_1 (cm^{-3})	2×10^{15}	8×10^{13}	8×10^{13}
E_T (meV)	3.7	6.0	6.0

The fitted mobility ~10^{-4} cm^2/V s is in agreement with the previously determined charge carrier mobility derived from TOF. Also, the surface defect density can be estimated to be $q N_{T2}\lambda \sim 6.5$ μC/cm^2. Also, the trap state energy lie within the typical Urbach energy of samples at room temperature, which is around 10 meV,[42] suggesting that these states might play a role at operation conditions.

3.4 Conclusion

In this chapter, the properties of a typical polycrystalline $MAPbI_3$ layer used in the fabrication

of solar cell has been investigated by means of physical (XPS, UPS, X-ray diffraction) and electrical (*J–V–L*, EL, TOF) experiments at low temperature and simulations. Combining the results from these studies, the presence of strong band bending at the Au/$MAPbI_3$ interface at temperatures as low as 10 K was found. As this band bending cannot be the consequence of residual doping or ion accumulation, it is attributed to an excess of hole acceptor traps localized at this interface. Further comparison between SCLC simulations including both volume and interface traps have confirmed this assumption, allowing us to extract both hole mobility ~ 10^{-4} cm^2 /Vs (in agreement with the TOF experiments), volume shallow trap density ~ 10^{16} cm^{-3} and interface traps (in concentration up to 5.5×10^{19} cm^{-3}). These results provide essential information regarding the role of volume and interface defects in $MAPbI_3$/Au interfaces. The occurrence of trapping has to be taken into account for the conception and simulation of perovskite based devices.

References

[1] Umari, P., Mosconi, E. & De Angelis, F. Relativistic GW calculations on CH3NH3PbI3 and CH3NH3SnI3 perovskites for solar cell applications. *Sci. Rep.* **4,** 4467 (2014). DOI: 10.1038/srep04467

[2] Liu, X. *et al.* Electronic structures at the interface between Au and CH3NH3PbI3. *Phys. Chem. Chem. Phys.* **17,** 896 (2014). DOI: 10.1039/C4CP03842H

[3] Wang, C. *et al.* Surface analytical investigation on organometal triiodide perovskite. *J. Vac. Sci. Technol. B,* **33,** 032401 (2015). DOI: 10.1116/1.4915499

[4] Lo, M. F., Guan, Z. Q., Ng, T. W., Chan, C. Y. & Lee, C. S. Electronic structures and photoconversion mechanism in perovskite/fullerene heterojunctions. *Adv. Funct. Mater.* **25,** 1213 (2015). DOI: 10.1002/adfm.201402692

[5] Chen, S. *et al.* Energy level alignment at the methylammonium lead iodide/copper phthalocyanine interface. *APL Mater.* **2,** 081512 (2014). DOI: 10.1063/1.4889844

[6] Liu, P. *et al.* Interfacial electronic structure at the CH3NH3PbI3 / MoOx interface. *Appl. Phys. Lett.* **106,** 193903 (2015). DOI: 10.1063/1.4921339

[7] Wang, C. *et al.* Electronic structure evolution of fullerene on CH3NH3PbI3. *Appl. Phys. Lett.* **106,** 111603 (2015). DOI: 10.1063/1.4916079

[8] Endres, J. *et al.* Valence and Conduction Band Densities of States of Metal Halide Perovskites: A Combined Experimental–Theoretical Study. *J. Phys. Chem. Lett.* **7,** 2722 (2016). DOI: 10.1021/acs.jpclett.6b00946

[9] D'Innocenzo, V. *et al.* Excitons versus free charges in organo-lead tri-halide perovskites. *Nat. Commun.* **5,** 3586 (2014). DOI: 10.1038/ncomms4586

[10] Green, M. A., Ho-Baillie, A. & Snaith, H. J. The emergence of perovskite solar cells. *Nat. Photonics* **8,** 506 (2014). DOI: 10.1038/NPHOTON.2014.134

[11] Lin, Q., Armin, A., Nagiri, R. C. R., Burn, P. L. & Meredith, P. Electro-optics of perovskite solar cells. *Nat. Photonics* **9,** 106 (2014). DOI: 10.1038/NPHOTON.2014.284

[12] Kokil, A., Yang, K. & Kumar, J. Techniques for characterization of charge carrier mobility in organic semiconductors. *J. Polym. Sci. Part B Polym. Phys.* **50,** 1130 (2012). DOI: 10.1002/polb.23103

[13] Brenner, T. M. *et al.* Are Mobilities in Hybrid Organic-Inorganic Halide Perovskites Actually 'high'? *J. Phys. Chem. Lett.* **6,** 4754 (2015). DOI: 10.1021/acs.jpclett.5b02390

[14] Coropceanu, V. *et al.* Charge transport in organic semiconductors. *Chem. Rev.* **107,** 926 (2007). DOI: 10.1021/cr050140x

[15] Wehrenfennig, C., Eperon, G. E., Johnston, M. B., Snaith, H. J. & Herz, L. M. High charge carrier mobilities and lifetimes in organolead trihalide perovskites. *Adv. Mater.* **26,** 1584 (2014). DOI: 10.1002/adma.201305172

[16] Leijtens, T. *et al.* Electronic properties of meso-superstructured and planar organometal halide perovskite films: charge trapping, photodoping, and carrier mobility. *ACS Nano* **8,** 7147 (2014). DOI: 10.1021/nn502115k

[17] Maynard, B. *et al.* Electron and hole drift mobility measurements on methylammonium lead iodide perovskite solar cells. *Appl. Phys. Lett.* **108,** 173505 (2016). DOI: 10.1063/1.4948344

[18] Ahn, N. *et al.* Highly reproducible perovskite solar cells with average efficiency of 18.3% and best efficiency of 19.7% fabricated via lewis base adduct of lead(ii) iodide. *J. Am. Chem.*

Soc. **137,** 8696 (2015). DOI: 10.1021/jacs.5b04930
[19] Chen, Y., Peng, J., Su, D., Chen, X. & Liang, Z. Efficient and balanced charge transport revealed in planar perovskite solar cells. *ACS Appl. Mater. Interfaces* **7,** 4471 (2015). DOI: 10.1021/acsami.5b00077
[20] Karakus, M. *et al.* Phonon-electron scattering limits free charge mobility in methylammonium lead iodide perovskites. *J. Phys. Chem. Lett.* **6,** 4991 (2015). DOI: 10.1021/acs.jpclett.5b02485
[21] Seto, J. Y. W. The electrical properties of polycrystalline silicon films. *J. Appl. Phys.* **46,** 5247 (1975). DOI: 10.1063/1.321593
[22] Baccarani, G., Ricco, B. & Spadini, G. Transport properties of polycrystalline silicon films. *J. Appl. Phys.* **49,** 5565 (1978). DOI: 10.1063/1.324477
[23] De Wolf, S. *et al.* Organometallic halide perovskites: sharp optical absorption edge and its relation to photovoltaic performance. *J. Phys. Chem. Lett.* **5,** 1035 (2014). DOI: 10.1021/jz500279b
[24] Xiao, Z. *et al.* Giant switchable photovoltaic effect in organometal trihalide perovskite devices. *Nat. Mater.* **14,** 193 (2014). DOI: 10.1038/NMAT4150
[25] Chen, B. *et al.* Impact of capacitive effect and ion migration on the hysteretic behavior of perovskite solar cells. *J. Phys. Chem. Lett.* **6,** 4693 (2015). DOI: 10.1021/acs.jpclett.5b02229
[26] Zarazua, I., Bisquert, J. & Garcia-Belmonte, G. Light-induced space-charge accumulation zone as photovoltaic mechanism in perovskite solar cells. *J. Phys. Chem. Lett.* **7,** 525 (2016). DOI: 10.1021/acs.jpclett.5b02810
[27] Weller, M. T., Weber, O. J., Henry, P. F., Di Pumpo, A. M. & Hansen, T. C. Complete structure and cation orientation in the perovskite photovoltaic methylammonium lead iodide between 100 and 352 K. *Chem. Commun.* **51,** 4180 (2015). DOI: 10.1039/c4cc09944c
[28] Yi, H. T., Wu, X., Zhu, X. & Podzorov, V. Intrinsic charge transport across phase transitions in hybrid organo-inorganic perovskites. *Adv. Mater.* **28,** 6509 (2016). DOI: 10.1002/adma.201600011
[29] Savenije, T. J. *et al.* Thermally activated exciton dissociation and recombination control the carrier dynamics in organometal halide perovskite. *J. Phys. Chem. Lett.* **5,** 2189 (2014). DOI: 10.1021/jz500858a
[30] Alberi, K. *et al.* Measuring long-range carrier diffusion across multiple grains in polycrystalline semiconductors by photoluminescence imaging. *Nat. Commun.* **4,** 2699 (2013). DOI: 10.1038/ncomms3699
[31] Paasch, G., Lindner, T. & Scheinert, S. Variable range hopping as possible origin of a universal relation between conductivity and mobility in disordered organic semiconductors. *Synth. Met.* **132,** 97 (2002). DOI: 10.1016/S0379-6779(02)00236-9
[32] Han, H., Davis, C. & Nino, J. C. Variable range hopping conduction in BaTiO3 ceramics exhibiting colossal permittivity. *J. Phys. Chem. C* **118,** 9137 (2014). DOI: 10.1021/jp502314r
[33] Sze, S. M., *Semiconductor Devices Physics and technology*, 2nd edition, John Wiley & Sons, Inc., New Jersey, 2002.
[34] Sun, X. *et al.* Room-temperature air-stable spin transport in bathocuproine-based spin valves. *Nat. Commun.* **4,** 2794 (2013). DOI: 10.1038/ncomms3794
[35] Beebe, J. M., Kim, B., Gadzuk, J. W., Frisbie, C. D. & Kushmerick, J. G. Transition from direct tunneling to field emission in metal-molecule-metal junctions. *Phys. Rev. Lett.* **97,** 026801 (2006). DOI: 10.1103/PhysRevLett.97.026801

[36] Miyata, A. *et al.* Direct measurement of the exciton binding energy and effective masses for charge carriers in organic-inorganic tri-halide perovskites. *Nat. Phys.* **11,** 582 (2015). DOI: 10.1038/NPHYS3357

[37] Tanaka, K. *et al.* Comparative study on the excitons in lead-halide-based perovskite-type crystals CH3NH3PbBr3 CH3NH 3PbI3. *Solid State Commun.* **127,** 619 (2003). DOI: 10.1016/S0038-1098(03)00566-0

[38] Giorgi, G., Fujisawa, J. I., Segawa, H. & Yamashita, K. Small photocarrier effective masses featuring ambipolar transport in methylammonium lead iodide perovskite: A density functional analysis. *J. Phys. Chem. Lett.* **4,** 4213 (2013). DOI: 10.1021/jz4023865

[39] Hill, I. G., Milliron, D., Schwartz, J. & Kahn, A. Organic semiconductor interfaces: electronic structure and transport properties. *Appl. Surf. Sci.* **166,** 354 (2000). DOI:10.1016/S0169-4332(00)00449-9

[40] Osikowicz, W., De Jong, M. P. & Salaneck, W. R. Formation of the interfacial dipole at organic-organic interfaces: C 60/polymer interfaces. *Adv. Mater.* **19,** 4213 (2007). DOI: 10.1002/adma.200700622

[41] Lee, C. S., Tang, J. X., Zhou, Y. C. & Lee, S. T. Interface dipole at metal-organic interfaces: Contribution of metal induced interface states. *Appl. Phys. Lett.* **94,** 11 (2009). DOI: 10.1063/1.3099836

[42] Zhang, W. *et al.* Ultrasmooth organic-inorganic perovskite thin-film formation and crystallization for efficient planar heterojunction solar cells. *Nat Commun* **6,** 6142 (2015). DOI: 10.1038/ncomms7142

Chapter 4

Dipole orientation and ion migration in $MAPbI_3$ elucidated by impedance spectroscopy

4.1 Permittivity of HOIPs and its measurement

As discussed in the previous chapter, special care must be taken during the study of the electrical properties of HOIPs. Based on a broad review of the literature, several points were taken into account in order to interpret the experimental data. These points generally include the slow electrical response of HOIP materials, where "slow" implies long time scales (> 10 µs) of the processes involved in the study. The electron clouds, the inorganic crystal scaffold, and the rotating organic ions each strongly impact on the electrical properties of HOIP materials. The studies of electrical responses are generally termed dielectric spectroscopy.[1] The dielectric response of HOIP can be summarized in Fig. 4-1, where the real part of the dielectric constant (ε') is plotted versus the response frequency. The fastest response is the displacement of the electron cloud, which can respond nearly instantaneously, hence generally termed ε_∞. A step increase in ε' happens around 10^{14} Hz, when the lattice vibration (phonon) effect sets in. The effect of rotating dipoles gives rise to the dielectric response with frequencies less than ~10^9 Hz. Then, finally, the relaxation frequency of defect migration is generally observed at the frequency range of 1 kHz.

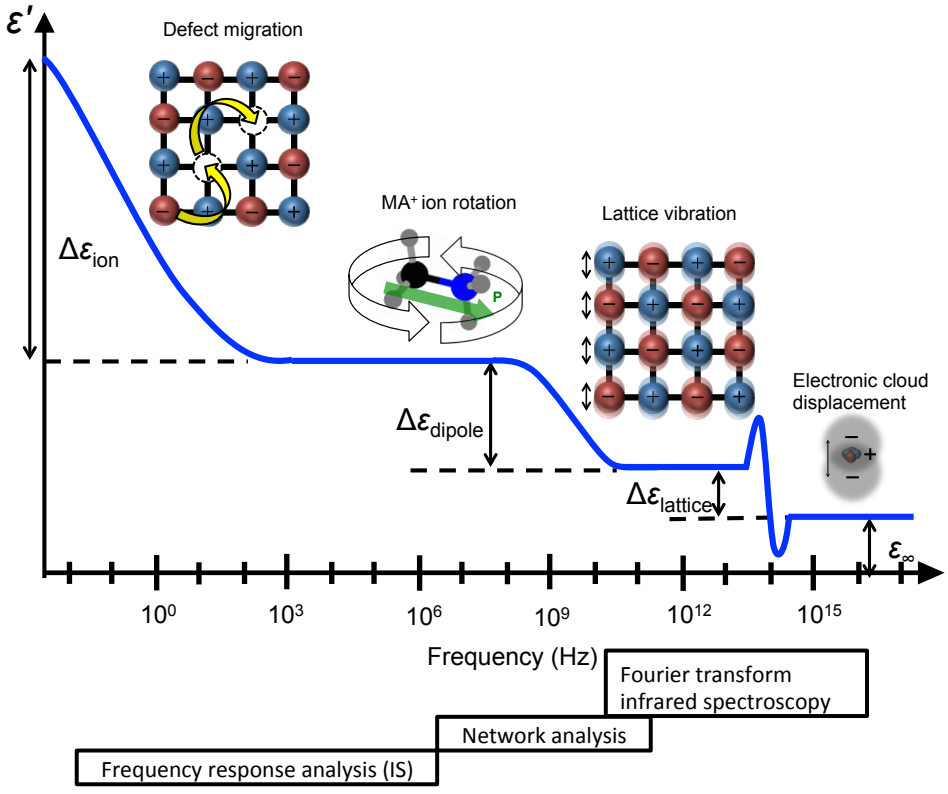

Fig. 4-1 Dielectric spectra of HOIP material

Different measurement techniques can be used to probe different frequency ranges. For example, for frequencies higher than 10^{10} Hz, Fourier transform infrared spectroscopy can be use to detect the dielectric response, while network analysis is applicable in the range of 10^6–10^{12} Hz. For lower frequencies, impedance spectroscopy (IS) is suitable.

The principle of impedance spectroscopy is shown in Fig. 4-2. A sinusoidal voltage is applied to the sample and the current response is analyzed in both amplitude and phase. The complex impedance is given by:

$$Z = Z(\omega) = \frac{V}{I} e^{j\phi} . \qquad \text{Eq. 4-1}$$

According to Fourier transform theory, if the function of $Z(\omega)$ is known, the temporal response of the system can be completely characterized.

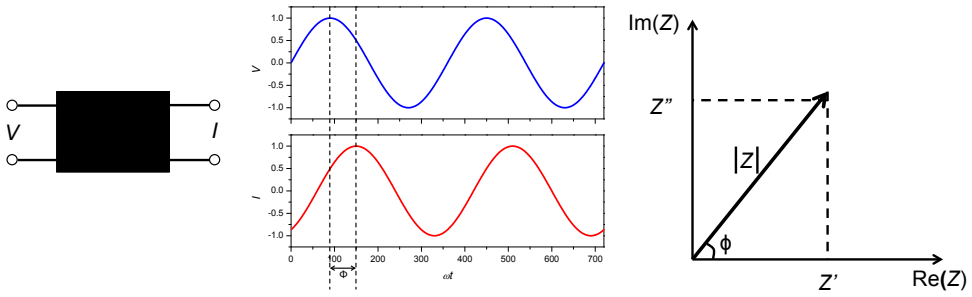

Fig. 4-2 Principle of IS measurement

Alternatively, the impedance function $Z(\omega)$ can also be represented by other complex functions, including admittance $Y = 1/Z$, modulus $M = j\omega C_c Z$, or dielectric permittivity $\varepsilon = 1/M$ (C_C is the capacitance of the empty cell). The relationships between the different experssions are summarized in Table 4-1.† With the assumption of homogeneity, ε can be readily interpreted as the dielectric permittivity (relative dielectric constant) of the material.

† Following the convention in the literature, the complex function $F(\omega)$ is denoted by $F(\omega) = F'(\omega) - jF''(\omega)$, where F' is the real part of F, F'' is the imaginary part of F.

Table 4-1 Relationships between representations of impedance analysis ($\mu = j\omega C_c$ is the impedance of the empty cell).

	Z	Y	M	ε
Z	Z	Y^{-1}	$\mu^{-1}M$	$\mu^{-1}\varepsilon^{-1}$
Y	Z^{-1}	Y	μM^{-1}	$\mu\varepsilon$
M	μZ	μY^{-1}	M	ε^{-1}
ε	$\mu^{-1}Z^{-1}$	$\mu^{-1}Y$	M^{-1}	ε

Although IS is a powerful tool to characterize the electrical process of electrode–material–electrode systems, data analysis can be a far from trivial task. Generally, it fares better when a series of samples is investigated so that a coherent picture can be obtained. A simplified work flow of the data analysis process to reach an interpretation is shown in Fig. 4-3. First, the impedance measurement is carried out on the system and an adequate theory of the process constructed or conjectured. The theory is then used to build a physical model from which the mathematical form of the impedance function can be calculated. Numerical curve fitting between the experimental curve and the mathematical model is made by varying some or all of the parameters. When a satisfactory fitting is obtained, the physical parameters can be extracted and interpreted accordingly.

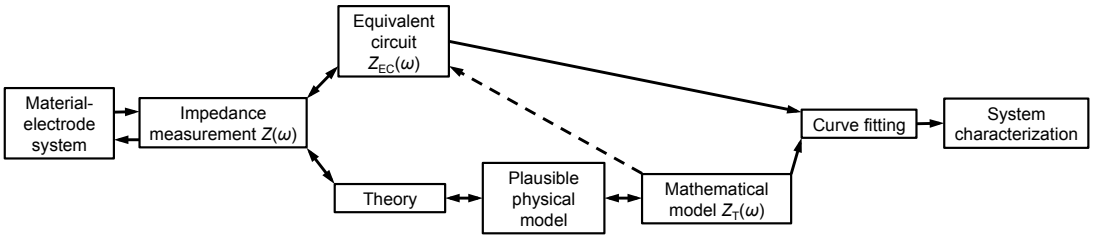

Fig. 4-3 Flow diagram for the measurement and characterization of a material–electrode system. Figure adapted with permission from ref 2. Copyright 2005 John Wiley & Sons, Inc.

Besides the motivation from the last chapter, the study of the dielectric properties of HOIP materials is of interest because it is also relevant for explaining charge separation in HOIP solar cells, an issue that is still under much debate.[3,4,5,6,7] The high dielectric constant of HOIP has been conjectured to serve as the screening mechanism contributing to the low

exciton binding energy (Fig. 4-4). While the dielectric properties of most-commonly used semiconductors have been generally agreed upon (Table 4-2), the reported dielectric properties of HOIP vary significantly between one another. Due to its highly dispersive nature and the lack of general consensus in data interpretation, the analysis of HOIP dielectric properties still presents disagreement in the literature. For example, Juarez-Perez, *et al.* reported the occurrence of photoinduced giant dielectric effect in HOIP,[8] a result being later considered as of no physical importance by Almond & Bowen.[9]

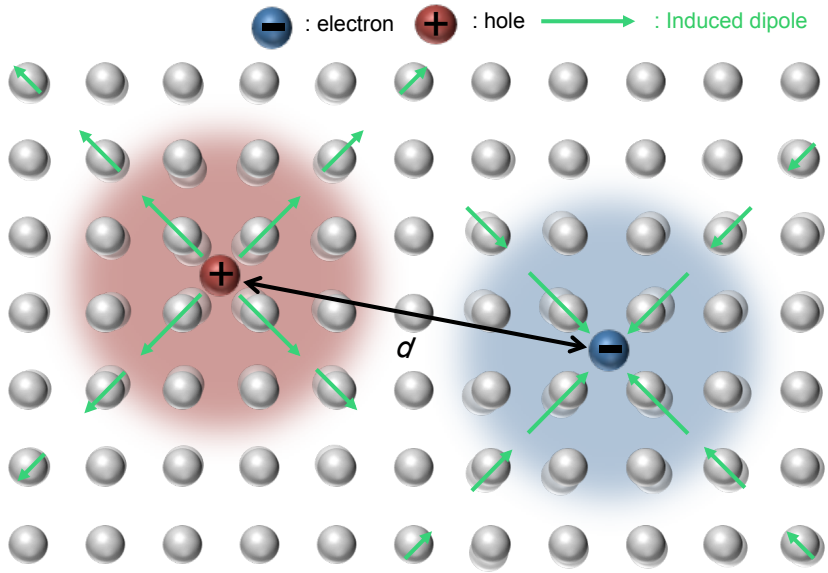

Fig. 4-4 Screening of electron–hole pair in dielectrics

Table 4-2 Dielectric constants of commonly used semiconductors

	Si	GaAs	CdTe	P3HT	PCBM	$MAPbI_3$
ε	12[a]	13[a]	10[a]	3.5[b]	3.9[c]	35[d], 70[e], 500[f]

[a]Data from ref 10, [b]data from ref 11, [c]data from ref 12, [d]data from ref 13, [e]data from ref 3, [f]data from ref 14.

In the remaining part of this chapter, the dielectric spectroscopy of several devices were measured with a *Biologic SP-300* impedance analyzer under controlled experimental sample conditions, including temperature, thickness and illumination. By doing so, we were able to clarify some ambiguities in the data interpretation and demonstrate that IS is a suitable technique in obtaining information that can be used to gain valuable insight into the operation of HOIP optoelectronic process.

4.2 High frequency dielectric constant of $MAPbI_3$ and its origin

Because of the impedance of the connecting cables, the upper frequency limit of IS technique is between 100 kHz and 1 MHz. Therefore, in the IS characterization of the dielectric properties, the higher frequency components, *i. e.*, the response of electronic cloud, the vibration of lattice, and the rotation of the organic dipoles, can only be inferred from the absolute value of the dielectric constant. Previous studies have shown that at the ~100 kHz range, the dielectric response of HOIP is dominated by dipole rotation.[13,15] These studies were carried out on HOIP single crystals or pellets. Therefore, a comparison with solution-processed film is of interest and could help us to determine the applicability of the experimental setup.

To measure the dielectric properties of $MAPbI_3$ films, the sample structure of ITO/Al_2O_3 (45 nm)/$MAPbI_3$/Al_2O_3 (45 nm)/Al was used. The aluminum oxide layer serves as a blocking electrode to minimize the electrode polarization effect.[1,16,17] Both aluminum oxide and aluminum top electrode were deposited with an e-beam evaporator under a vacuum of ~10^{-6} mbar at a rate of 0.2 nm/s. The $MAPbI_3$ film was prepared according to the procedure described in section 2.3, with a thickness of 280 nm as measured using a stylus profiler. In this device architecture, the aluminum oxide layer contributes to the total capacitance. Therefore, the sample without the active layer, *i. e.*, ITO/Al_2O_3 (90 nm)/Al, was also measured.

The results are shown in Fig. 4-5, where the capacitance C is related to the admittance Y by:

$$C = \frac{Y}{j\omega} = C' + jC'', \qquad \text{Eq. 4-2}$$

where $Y = 1/Z = Y' + jY''$ is the complex admittance, and ω is the angular frequency.

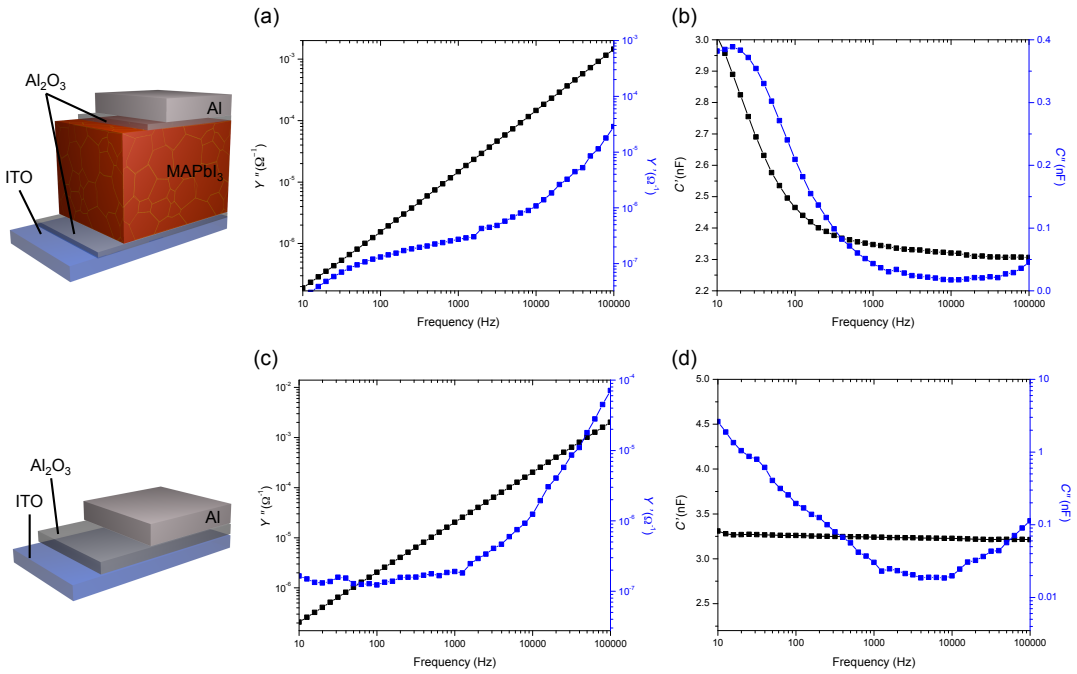

Fig. 4-5 Frequency dependent admittance of (a) ITO/Al_2O_3 (45 nm)/$MAPbI_3$ (280 nm)/Al_2O_3 (45 nm)/Al and (b) ITO/Al_2O_3 (90 nm)/Al devices. The capacitance C is calculated from the admittance Y in Eq. 4-2 and plotted in (b) and (d).

At the frequency regime of 1 kHz to 100 kHz, the imaginary part of capacitance is much less than the real part, *i. e.*, the system exhibits a purely capacitive behavior; while at lower frequencies, interfacial effects are likely to set in.[1] Therefore, in the high frequency region, the impedance of ITO/Al_2O_3/$MAPbI_3$/Al_2O_3 /Al can be approximated as 2 capacitors in series, one from the dielectric response of Al_2O_3 (C'_{AlO}), the other from $MAPbI_3$ (C'_{HOIP}):

$$\frac{1}{C'_{All}} = \frac{1}{C'_{AlO}} + \frac{1}{C'_{HOIP}}, \qquad C'_{HOIP} = \frac{C'_{All}C'_{AlO}}{C'_{AlO} - C'_{All}} = \varepsilon'\varepsilon_0\frac{A}{d}, \qquad \text{Eq. 4-3}$$

where C'_{All} is the measured capacitance of ITO/Al_2O_3/$MAPbI_3$/Al_2O_3/Al, ε' is the permittivity of $MAPbI_3$, $\varepsilon_0 = 8.85 \times 10^{-12}$ F/m is the vacuum permittivity, A is the device area, and d is the $MAPbI_3$ thickness. The capacitance and permittivity of the 280-nm solution processed $MAPbI_3$ layer obtained is shown in Fig. 4-6. The measured relative permittivity of $MAPbI_3$ remains at the same value of 65 over 2 orders of magnitude of the frequency range. The result is in good agreement with the report by Young and Fredericske on $MAPbI_3$ pellets.[13]

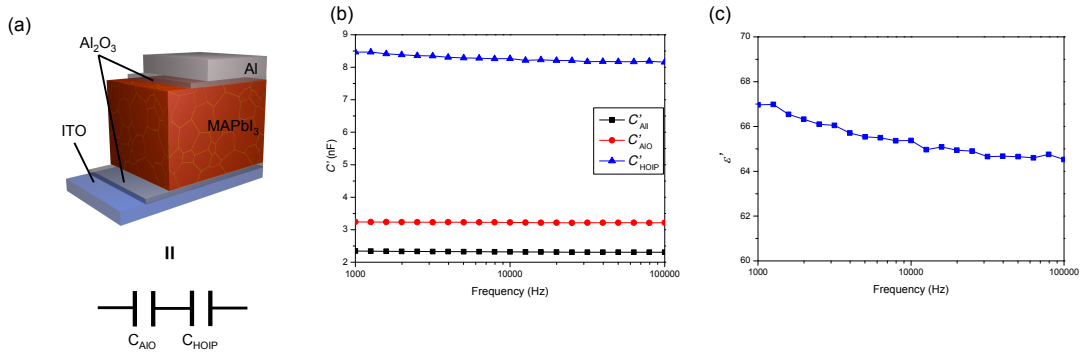

Fig. 4-6 (a) Equivalent circuit of an ITO/Al_2O_3 (45 nm)/$MAPbI_3$ (280 nm)/ Al_2O_3 (45 nm)/Al device. Frequency dependence of (b) capacitance and (c) $MAPbI_3$ relative permittivity.

Temperature dependent measurement of the dielectric constant can be used to gain more insight into the nature of the dielectric process. Here, the low temperature cryostat described in section 3.4 and the same data analysis procedure as described above was used for the measurements. The temperature dependent permittivity of solution-processed $MAPbI_3$ film is shown in Fig. 4-7.

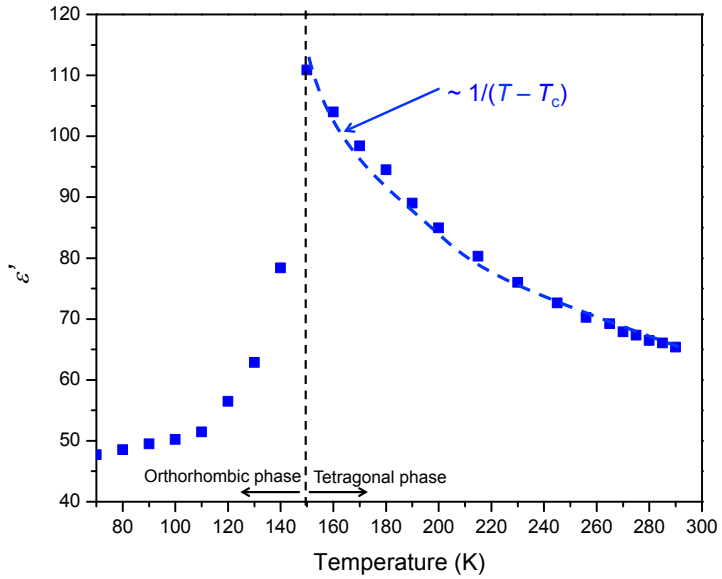

Fig. 4-7 Temperature dependent relative permittitivity of solution-processed $MAPbI_3$ thin film with thickness of 280 nm. The blue dotted line is a guide to the eye.

The measured relative permittivity shows a clear discontinuity at temperatures around 150 K, roughly corresponding to the tetragonal-to-orthorhombic phase transition known for $MAPbI_3$ perovskites. The exact temperature of the phase transition is generally located at 162 K.[18,19] However, it is not unusual for thin films to exhibit a delayed phase transition

due to strain, as observed in other reports on HOIPs.[20,21]

In the tetragonal phase, the permittivity exhibits a roughly $1/T$ (or $1/(T - T_C)$) behavior, which is a strong indication of the existence of disordered dipole moments. This explanation is in line with the general agreement that the tetragonal-to-orthorhombic phase transition in HOIP restricts the rotation of the organic cations.[18,22,23] As can be seen in Fig. 4-7, in the orthorhombic phase the $1/(T - T_C)$ trend is broken, which can be attributed to the fixed directions of the methylammonium (MA^+) cations in this phase.

Based on the above discussion, further analysis of the temperature dependent permittivity in the tetragonal phase can be carried out by the application of the Kirkwood–Fröhlich–Onsager equation, which is a simple but powerful model to characterize the relationship between dipole moment and dielectric constant, first developed to describe polar solutions.[1,24] The Kirkwood–Fröhlich–Onsager equation is written as:

$$\frac{(\varepsilon' - \varepsilon'_\infty)(2\varepsilon' + \varepsilon'_\infty)}{\varepsilon'(\varepsilon'_\infty + 2)^2} = \frac{1}{9\varepsilon_0} g \frac{N\mu^2}{k(T - T_C)}, \qquad \text{Eq. 4-4}$$

where ε' is the low frequency permittivity, ε'_∞ is the high frequency permittivity limit, $\varepsilon_0 = 8.85 \times 10^{-12}$ F/m is the vacuum permittivity, g is the Kirkwood correlation factor, N is the dipole density, μ is the magnitude of the dipole moment, k is the Boltzmann constant, T is the absolute temperature of the sample, and T_C is a constant called the Curie–Weiss temperature. The $1/(T - T_C)$ behavior is a generalized form of the equation, which is in accordance with the phase transition of perovskite materials.[25,26]

The correlation factor g is a measure of the interaction between individual dipoles:[1,13]

$$g = \frac{\langle \sum_i \boldsymbol{\mu}_i \sum_j \boldsymbol{\mu}_j \rangle}{N\mu^2} = 1 + \frac{\langle \sum_i \sum_{i<j} \boldsymbol{\mu}_i \boldsymbol{\mu}_j \rangle}{N\mu^2} = \frac{\mu^2_{\text{interact}}}{\mu^2}, \qquad \text{Eq. 4-5}$$

where $\boldsymbol{\mu}_i$ represents individual dipoles. The value of g is larger than 1 when there is a tendency for parallel orientation, while smaller than 1 for anti-parallel orientation of the dipoles.

The elegance of this equation lies in the fact that the permittivity is given implicitly, and that the high frequency limit permittivity ε'_∞ and Curie–Weiss temperature T_C can be fitted through the temperature dependence of ε'. The best linear fit of $(\varepsilon' - \varepsilon'_\infty)(2\varepsilon' + \varepsilon'_\infty)/\varepsilon'$ (ε'_∞

$+ 2)^2$ versus $1/(T - T_C)$ in tetragonal phase is shown in Fig. 4-8, giving optimized parameters of $\varepsilon'_\infty = 32.4$ and $T_C = 34.4$ K.

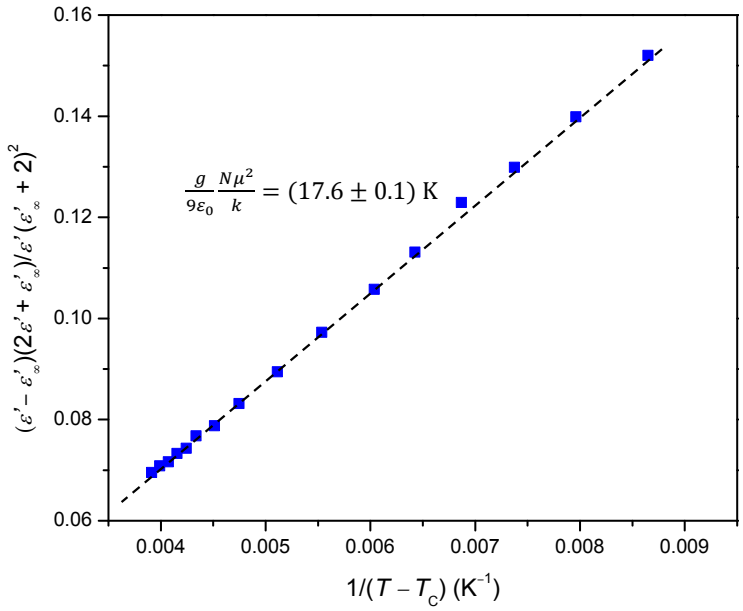

Fig. 4-8 Fitting of the $MAPbI_3$ pemittivity to Kirkwood–Fröhlich–Onsager equation in the tetragonal phase. Best-fit values of $\varepsilon'_\infty = 32.4$, $T_C = 34.4$ K are used.

The obtained high frequency limit permittivity ε'_∞ is somewhat higher (32.4 versus 23.3 and ~7) than the results from experiments on $MAPbI_3$ pellets,[13] and first-principle DFT calculations.[27] The Curie–Weiss temperature also differs with the result from ref 13. These might be due to the difference in crystallinity of the material and some of the assumptions made in the DFT calculations, such as the anisotropy of the unity crystals.

Important information can be obtained with the knowledge of the correlation factor g, whose calculation from the fitted line is as follows: the dipole density N is calculated from XRD data in section 2.2.2 to be 4.01×10^{27} m^{-3}, [19] and the dipole moment of MA^+ ions μ has been calculated from density functional theory to be 2 D (1 Debye = 10^{-10} esu Å ≈ 3.34×10^{-30} C m).[27,28,29] Therefore, the correlation factor g can be calculated from the fitted slope on Fig. 4-8. The slope $gN\mu^2/9\varepsilon_0 k = (17.6 \pm 0.1)$ K, giving g to be 0.11 ± 0.1.

The observation that the correlation factor $g < 1$ provides experimental evidence of the anti-parallel arrangement of the MA^+ ions in $MAPbI_3$ (Fig. 4-9), which has long been conjectured in the literature ("antiferroelectric") by theoretical calculation at room

temperature.[30,31,32,33] This ordering might come from the interaction of the MA^+ ions with the inorganic cage,[34] or be due to hydrogen bonding,[35] and is related to the tetragonal crystal structure of $MAPbI_3$ present at room temperature.[36]

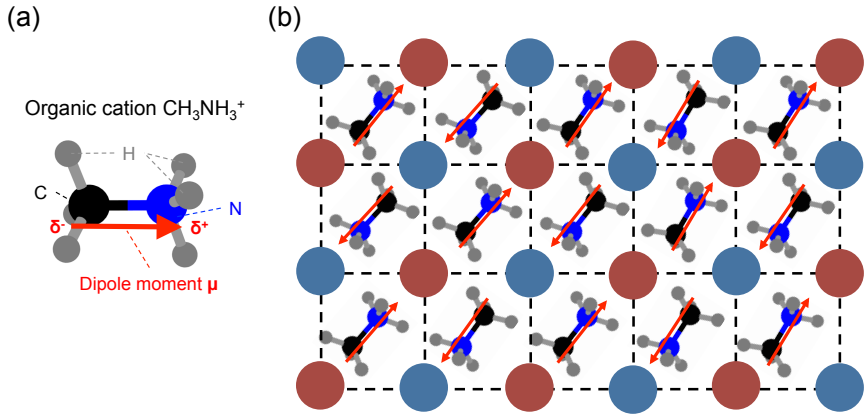

Fig. 4-9 Dipole arrangement in $MAPbI_3$ perovskite. (a) The difference in electron affinity between the carbon and positively charged nitrogen atoms causes a dipole moment **μ** orientated along the C–N axis of the MA^+ ion. (b) Anti-parallel arrangememnt of the MA^+ ions in $MAPbI_3$ deduced from the temperature dependece of the permittivity.

The problem of dipole orientation in HOIP is a much debated topic, which so far has been studied using theoretical simulations,[31,32,33,36,37] ultrafast 2D vibration spectroscopy,[37] or neutron scattering technique.[22] Here the problem is experimentally elucidated by the relatively simple IS technique and a straightforward conclusion is made. In the next section, we will examine the low frequency component of the dielectric spectra as measured using IS.

4.3 Analysis of ion migration in $MAPbI_3$

The electrode polarization effect, which has been minimized in the previous section by the use of two blocking electrodes, is of interest because it can be used to study the interfacial effects which have significant implications in the performance of solar cells, and the observation of the giant dielectric constant.[8] As a starting point of this study, this section presents the IS measurement of an ITO/PEDOT:PSS/$MAPbI_3$/Au device, where both interfaces, *i. e.*, PEDOT:PSS/$MAPbI_3$ and $MAPbI_3$/Au have significance in solar cell applications. As mentioned in the introduction of this chapter, the ambiguities in IS data interpretation must be carefully taken into account and it would be helpful to see the data

in different ways. With temperature dependent measurement and equivalent circuit fitting, it can be shown that the low frequency component of the capacitance spectra is closely related to the ion migration within the HOIP layer. From the fitting model, the ion diffusivity and activation energy can be obtained and compared to theoretical simulations found in the literature.

The complex permittivity ($\varepsilon = \varepsilon' - j\varepsilon''$) and conductivity ($\sigma = \varepsilon''\varepsilon_0\omega$) of a 250-nm-thick $MAPbI_3$ film sandwiched between PEDOT:PSS and gold electrodes are shown in Fig. 4-10. The drop in ε' at around 1 MHz is caused by the series resistance of the contact layers and the connection cables. At around 100 kHz, ε' is around the value of the intrinsic permittivity as measured in the last section. The real and imaginary parts of the permittivity further increase with decreasing frequency over several orders of magnitude. At low frequencies, the imaginary part is larger than the real part, meaning that the sample should not be considered as a capacitor and that the conduction effect must be taken into account. The slope is close to 1, corresponding to a constant AC electrical conductivity $\sigma \sim 10^{-5}$ S/m (Fig. 4-10 (b)).

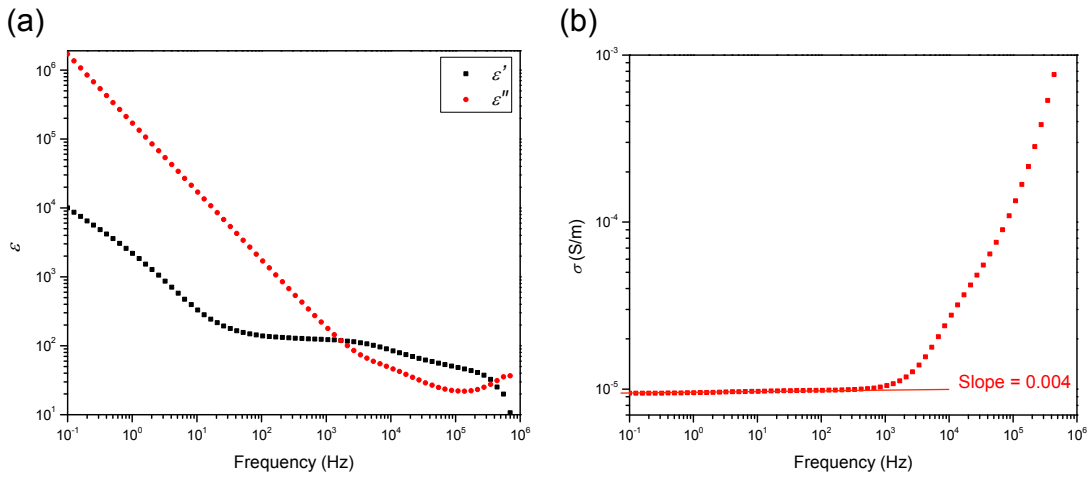

Fig. 4-10 Frequency dependent complex permittivity (a) and conductivity (b) of an ITO/PEDOT:PSS/$MAPbI_3$ (250 nm)/Au device at room temperature.

The low frequency component is likely to be dominated by ion migration in the material. In HOIP, the existence of ion migration has been generally recognized using theoretical simulations, [38, 39] transient photocurrent measurements, [40, 41] current–voltage hysteresis, [42, 43, 44] local photoluminescence, [45] electroabsorption spectroscopy, [46]

photothermal induced resonance (PTIR) microscopy and Kelvin probe force microscopy.[47] IS measurements have also been employed,[8,48,49,50,51] but these studies, except for ref 51, are carried out on complete solar cell devices with hole or electron transport layers (TiO_2, spiro-OMeTAD, or $PC_{61}BM$), which inevitably complicates the data analysis. For example, the low intrinsic permittivity derived in ref 8 ($\varepsilon' \sim 7$) might be due to non-compensated capacitance of the spiro-OMeTAD layer.

It should be noted that Almond and Bowen have suggested that the low frequency component in the IS of HOIP might be due to the porous nature of the material and not from physical mechanisms like ion migration.[9] However, their referencing data comes from a device constructed using a mesoporous TiO_2 interface to maximize surface area,[8] and shows significantly larger low frequency dispersions than the planar devices studied here (slope of 0.066 in ref 9 compared with 0.004 in Fig. 4-10 (b)). This means that the "universal dielectric response" effect is much weaker,[52,53] if not absent, in the planar device. Therefore, it is possible that the explanation given in ref 9 is not complete and that the studies of a planar device architecture would provide additional information. In the remaining part of this section, the analysis of the temperature-dependent and illumination-dependent IS data of a planar ITO/PEDOT:PSS/$MAPbI_3$/Au device is presented.

The temperature dependent dielectric measurement of an ITO/PEDOT:PSS/$MAPbI_3$ (250 nm)/Au device is shown in Fig. 4-11. The $MAPbI_3$ undergoes a tetragonal-to-cubic phase transition at 327 K.[19,54] Therefore, this measurement covers the phase transition region and some changes in electrical properties due to the change in crystalline phase are expected.

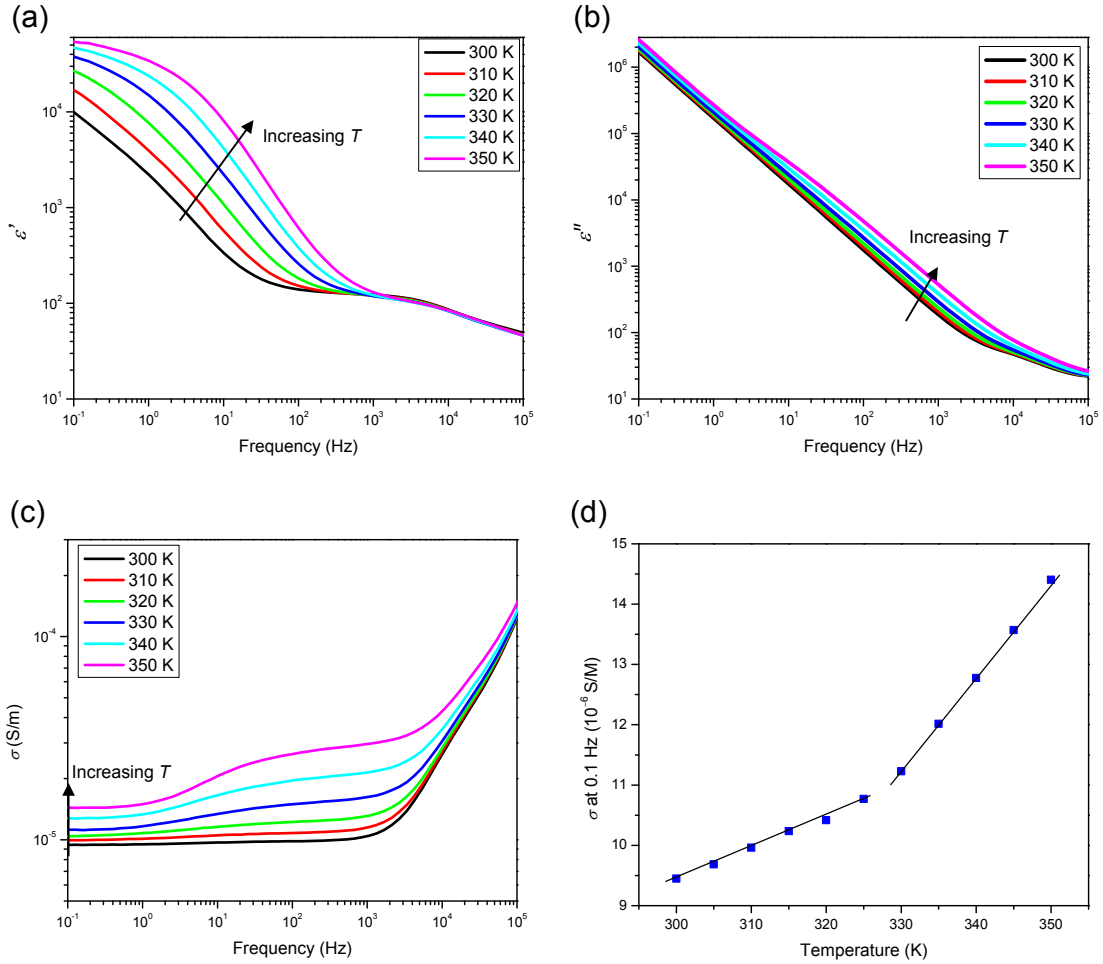

Fig. 4-11 Temperature dependent dielectric measurement of a nPEDOT:PSS /$MAPbI_3$ (250 nm)/Au device. (a) Real part of the permittivity ε'. (b) Imaginary part of the permittivity ε''. (c) Conductivity ($\sigma = \varepsilon''\varepsilon_0\omega$). (d) Conductivity at 0.1 Hz versus temperature.

As shown in Fig. 4-11 (a), ε' increases with increasing temperature and even at temperatures as high as 350 K, no clear plateau is observed over the measured frequency range, indicating that the relaxation process is not Debye-like. The increase in ε'' (Fig. 4-11 (b)) with temperature indicates the increase of conductivity with elevating temperature (Fig. 4-11 (c)). The change of slope around 330 K on the conductivity at 0.1 Hz (Fig. 4-11 (d)) is related to the tetragonal-to-cubic phase transition.

The non-Debye like relaxation behavior renders data analysis more complicated. The general approach is to assume a distribution function of relaxation times to fit the experimental data,[1] but this complex fitting is out of our capacity. The other approach to quantify the experimental data is thorough equivalent circuit fitting, where the specific

nature of each process has to be assumed. As discussed above, the assumption of ion migration dominating the low frequency component is reasonable. Therefore, an ionic diffusion process should be included in the equivalent circuit, which is usually done by introducing a Warburg element, the impedance of which is given by:[2,55]

$$Z_{\mathrm{w}} = R_{\mathrm{W}} \frac{\tanh\sqrt{j\omega T_{\mathrm{W}}}}{\sqrt{j\omega T_{\mathrm{W}}}}, \qquad \text{Eq. 4-6}$$

where Z_{W} is called the Warburg impedance, R_{W} the Warburg resistance, T_{W} the Warburg time constant. The equation was first derived by E. Warburg in 1899 solving the diffusion equation with oscillating ion concentration at a boundary (Fig. 4-12).[56]

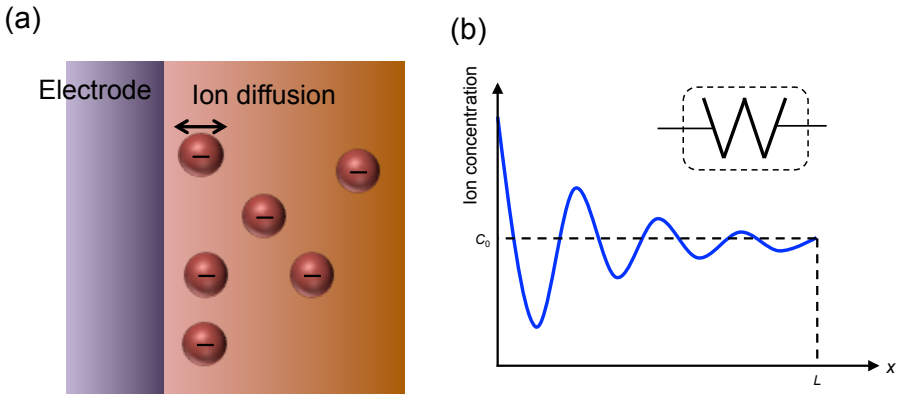

Fig. 4-12 Representation of the ion diffusion process in HOIP by a Warburg element. (a) Illustration of the ion diffusion in a HOIP layer. (b) Oscillating ion concentration profile during IS measurement (inset: the electrical symbol of the Warburg element).

The Warburg time constant T_{W} is related to the diffusivity D and is generally expressed by:[50,57,58,59]

$$T_{\mathrm{w}} = \frac{t^2}{D}, \qquad \text{Eq. 4-7}$$

where t is the thickness of the active layer.

To fit the experimental data, we take advantage of an existing model which has been used to describe HOIP solar cells.[57] In this model, the carrier conduction (electrons and holes) is modeled by a resistance R_{carrier}, while the intrinsic capacitive effect is modeled by a capacitor C_{bulk}. The low frequency component is introduced by a Randle circuit with a Warburg element ($C_{\mathrm{dl}}/(R_{\mathrm{ct}} + W_{\mathrm{d}})$). With an additional series resistance R_{s} and trace resistance R_{tr}, the total equivalent circuit is shown in Fig. 4-13. This model has been shown

to fit the IS data of inverted planar HOIP solar cell satisfactorily, and there is no specific term to account for the effect of the $PC_{61}BM$ layer. Therefore, we employ the same model on the data shown in Fig. 4-11. Simpler models were also tested but resulted in the loss of the goodness of fit.

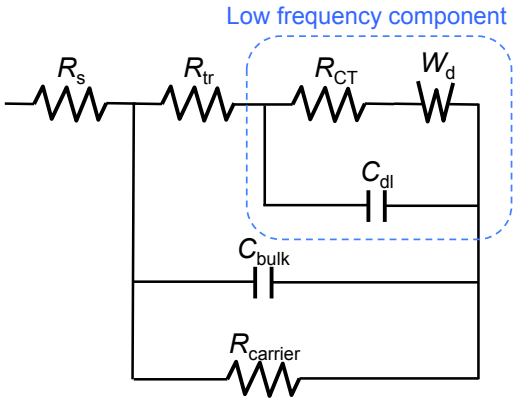

Fig. 4-13 Equivalent circuit used to fit the data shown in Fig. 4-11. The total impedance Z is given by: $Z = R_s + R_{carrier}/C_{bulk}/(R_{tr} + C_{dl}/(R_{ct} + W_d))$.

With the fitting parameters of the curve at 350 K given in Table 4-3, the comparison between the calculated and measured impedance are shown in the Bode and Cole–Cole presentation (Fig. 4-14 (a), (b), respectively). The closeness of the model and experimental data and the physically reasonable fitted parameter concur to support the applicability of the model.

Table 4-3 Fitting parameters of the curve at 350 K

R_s (Ω)	C_{bulk} (nF)	R_{tr} (Ω)	R_{ct} (Ω)	$R_{carrier}$ (Ω)
54.7	8.52	1010	1880	5520
C_{dl} (nF)	R_W (Ω)	T_W (s)	D (cm^2/s)	
15.5	13500	0.308	1.30×10^{-9}	

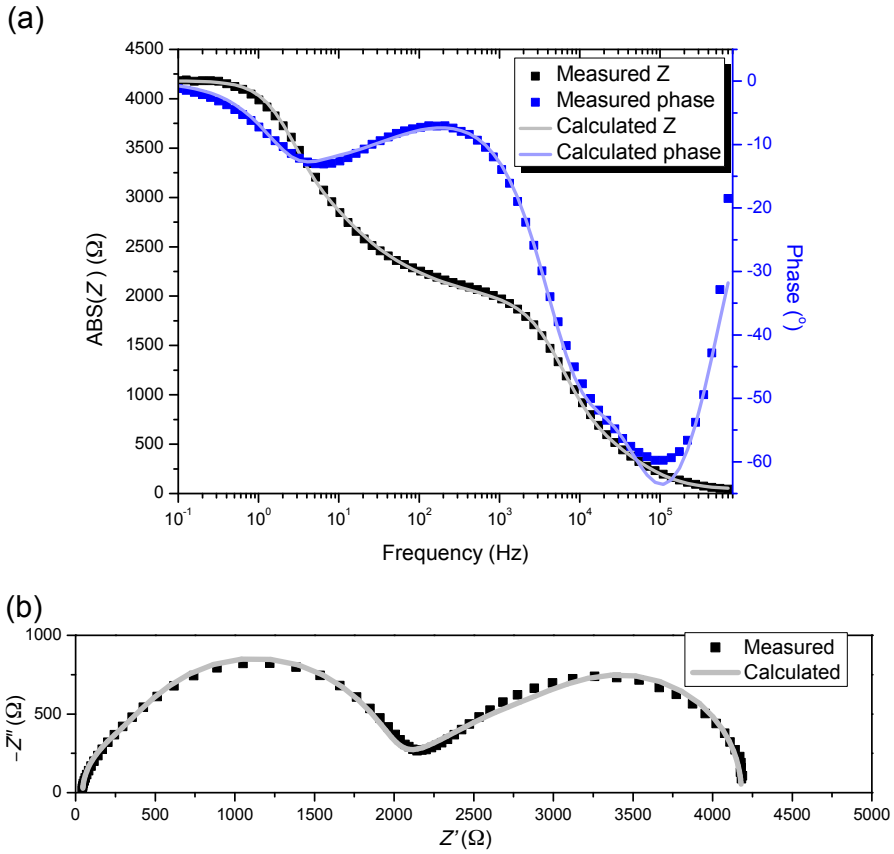

Fig. 4-14 Comparison of measured (dots) and calculated (lines) impedance spectra. (a) Bode presentation (abs(*Z*) and phase versus frequency). (b) Cole–Cole presentation (–*Z*'' versus *Z'*). The fitted parameters are given in Table 4-3.

At 350 K, the ion diffusivity is found to be 1.3×10^{-9} cm^2/s. To obtain the temperature dependence of the diffusivity, the same fitting procedure was applied to the IS data between 300 K and 350 K using a global fitting protocol to ensure the continuity of the parameters. The fitted diffusivity as a function of temperature and its Arrhenius plot are shown in Fig. 4-15. At room temperature, the fitted ion diffusivity is 2×10^{-12} cm^2/s, which is not far from other reports in the literature in terms of orders of magnitude: ref 50 estimated ion diffusivity to be 2.4×10^{-8} cm^2/s for $MAPbI_3$ pellets, ref 47 measured ion mobility and estimated the diffusivity to be 3.9×10^{-11} cm^2/s, and ref 60 estimated ion diffusivity to be $\sim 10^{-12}$ cm^2/s.

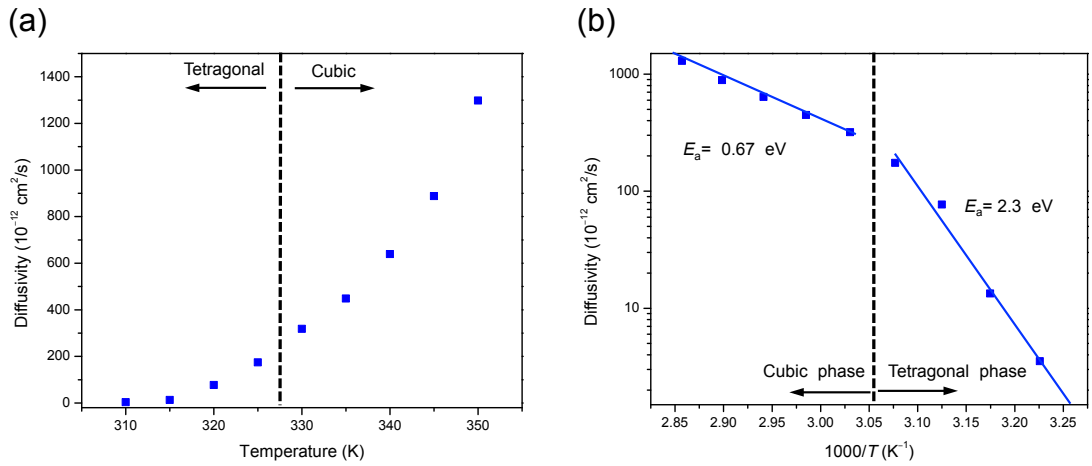

Fig. 4-15 Temperature dependence of ion diffusion constant measured by IS. (a) Fitted diffusivity versus temperature in linear scale. (b) Arrhenius plot and activation energy.

The activation energy of the ion migration is 2.3 eV in the tetragonal phase and 0.67 eV in the cubic phase. A clear difference between the 2 phases was found, which is generally not observed in previous reports.[57, 61 , 62] The reason for this might be because the tetragonal-cubic phase transition in HOIP is classified as second order,[19,63,60] and not abrupt. However, one might expect that the ionic conduction is closely related to the spacing in the crystals and therefore more sensitive to the crystalline phase change than electron or hole conduction.

The cubic phase activation energy is in good agreement with the theoretical prediction of the activation energy of ion migration (0.2 – 0.9 eV).[38,39,40,64] A general survey of the literature shows that of all the possible mobile species, iodide ions have the smallest activation energy and lowest formation energy,[65,66] and therefore usually assumed to be the dominating mobile species. However, the specific activation energy value varies from report to report and it is therefore difficult to identify a single mobile species. Besides, the low formation energy of Schottky defects in HOIP,[67] which create stoichiometric amounts of anion and cation vacancies, suggests that multiple species may be involved simultaneously.

The tetragonal phase activation energy (2.3 eV) is high compared to most simulation results and seems counterintuitive. It is likely that, at the interfaces, the ions falls into traps formed at imperfect crystal planes. At lower temperatures, these ions would be harder to

activate and therefore lead to the high apparent activation energy. The occurrence of interfacial pile-up of ions has also been suggested in other literature reports.[48,59,68,69]

Ample amount of evidence of the structural change of HOIP under illumination has been provided in the literature:[8] Gottesman *et al.*[70] suggested that dipoles reorient during illumination and induce slow lattice distortion. Quilettes *et al*.[45] provided experimental evidence of halide redistribution in HOIP under illumination. Deng *et al.*[71] proposed that the hysteresis of HOIP solar cells may come from light-induced self poling effect. As discussed above, ion migration is closely related to the crystal arrangement and the trap states. Therefore, the above experimental method has the potential gaining more insight into the structural change under illumination in HOIP.

The illumination-dependent dielectric measurement of an ITO/PEDOT:PSS/$MAPbI_3$ (250 nm)/Au sample is shown in Fig. 4-16. The illumination was provided by a fiber illuminator and the power estimated using a radiometer (*IL 1400 BL*).

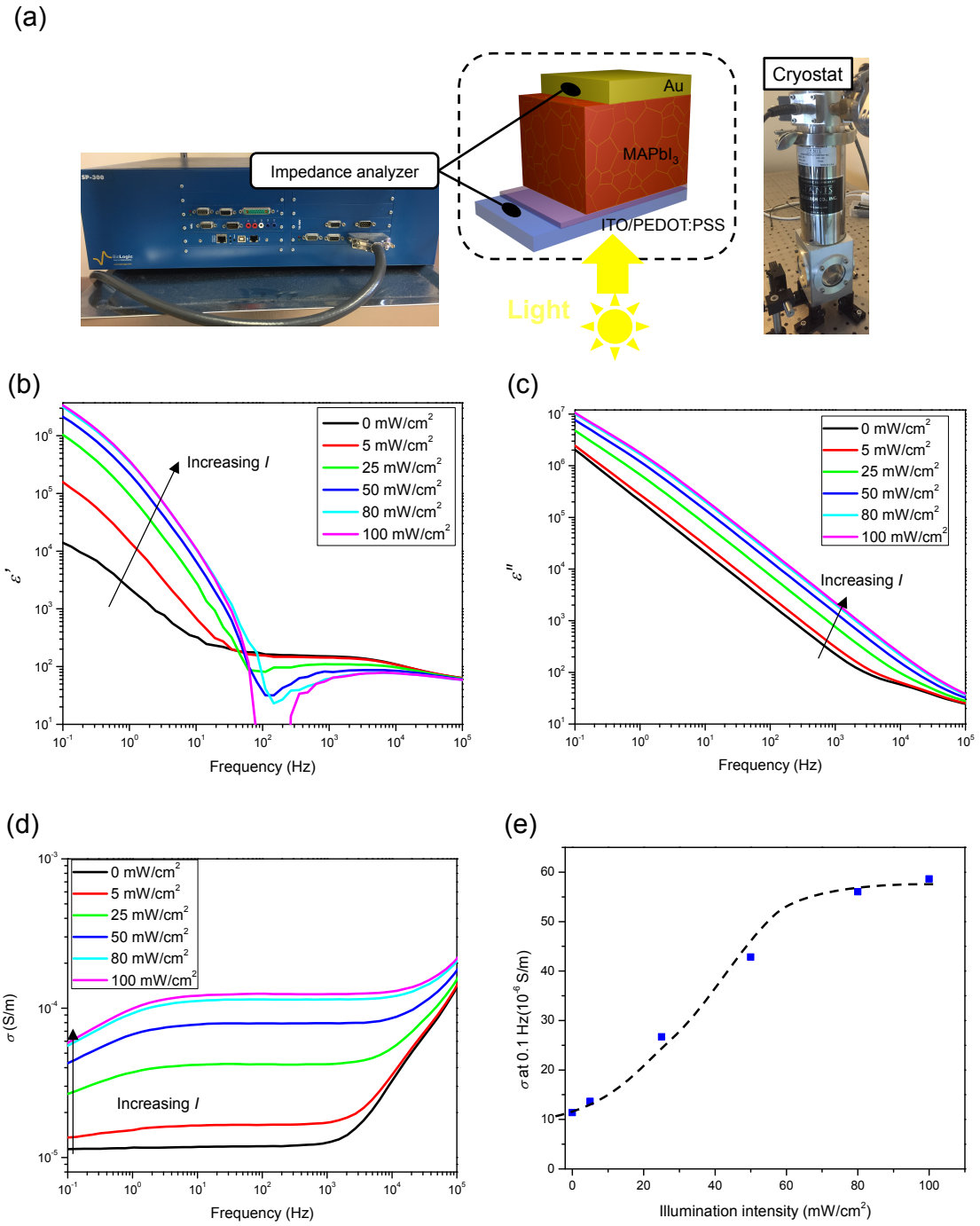

Fig. 4-16 Illumiation dependent dielectric measurement of an ITO/PEDOT:PSS/$MAPbI_3$ (250 nm)/Au sample. (a) Experimental setup. (b) Real part of the permittivity ε'. (c) Imaginary part of the permittivity ε''. (d) Conductivity ($\sigma = \varepsilon''\varepsilon_0\omega$). (e) Conductivity at 0.1 Hz versus illumination intensity. The dashed line is a guide to the eye.

With increasing illumination intensity, the low frequency permittivity increased by up to 2 orders of magnitude at 100 mW/cm^2. The corresponding increase in conductivity is shown in Fig. 4-16 (c), which seems to saturate at high illumination intensity (d). A similar

photoinduced giant dielectric constant effect has been reported in the literature and was attributed to the structural change of $MAPbI_3$,[8] or to charge accumulation at interfaces.[49]

One pronounced feature of the illumination effect is the apparent decrease of ε' over the 100–1000 kHz frequency range (Fig. 4-16 (a)), which is different from the previous results (Fig. 4-11). The effective dielectric constant actually becomes negative at 100 mW/cm^2 (Fig. 4-17 (a) inset). In the Cole–Cole plot, the effect presents itself as an inductive loop at middle frequencies (Fig. 4-17 (b), (c)). The "negative capacitance" or inductive phenomenon indicates a releasing of previously stored energy, and has already been reported in the literature,[72,73] and observed in HOIP interfaces.[74] It is generally associated with charge injection and recombination through interfacial states,[73] or electrochemical reactions.[51] In this case these states seem to be photogenerated. Closer examination is necessary at this point to elucidate this observation of light-induced negative capacitance effect in the HOIP layer.

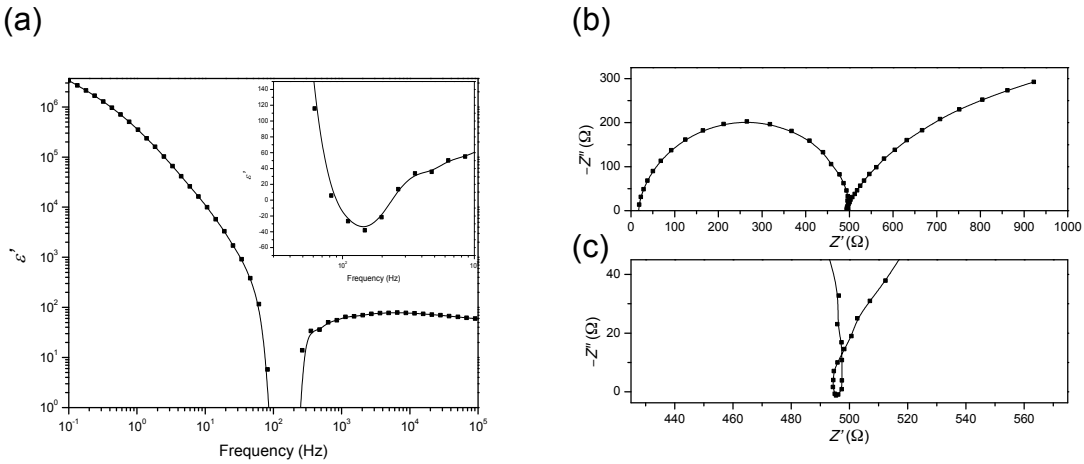

Fig. 4-17 Negative capacitance effect under 100 mW/cm^2 illumination. (a) Real part of the permittivity (inset: zoom in around 100 Hz, showing negative effective dielectric constant). (b) Cole–Cole presentation of the whole frequency range (100 kHz to 0.1 Hz). (c) Zoom in on the Cole–Cole presentation near the intercept. The inductive loop is clearly observed.

The photoinduced change of the HOIP crystals is of special interest in the literature: Several reports suggested that, under illumination, MA^+ ions in HOIPs are more ordered and the lattice less distorted, hence reducing the bonding between MA^+ ions and the inorganic frame.[70,75,76] As a result, the release and diffusion of ionic species are facilitated

under illumination ("softening" of the lattice, Fig. 4-18).[64] This is consistent with another recent report demonstrating that defect density decreases by one order of magnitude under illumination,[45] which demonstrated that illumination has certain effect on the structure of crystals.

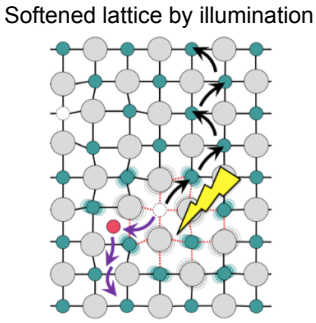

Fig. 4-18 Illustration of HOIP lattice softening under illumination. Adapted with permission from ref 64. Copyright 2016 American Chemical Society.

To evaluate the diffusivity under illumination, the temperature dependent dielectric measurements were conducted under 25 mW/cm^2 illumination on the same sample structure as before. The light intensity was chosen to avoid the inductive effect as discussed above and a green light LED (532 nm) was used as the light source due to its stable output. The dielectric data obtained is shown in Fig. 4-19.

The temperature dependent phenomenon under illumination is quite distinct from the dark condition: it is less thermally activated (Fig. 4-19 (a), (b)), has a larger low frequency dispersion (Fig. 4-19 (c)), and the low frequency conductivity actually decreases with increasing temperature (Fig. 4-19 (d)). All these observations point to an underlying change in the $MAPbI_3$ crystal structure.

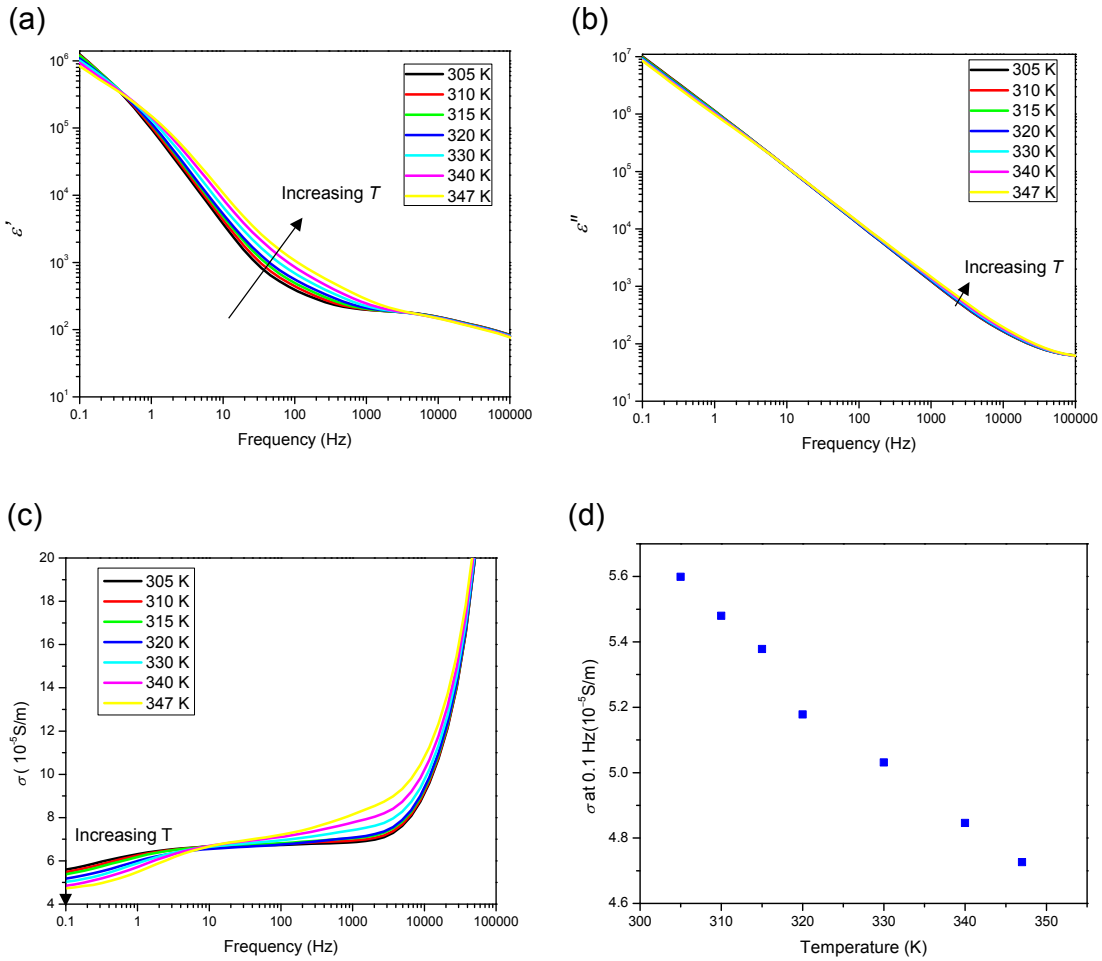

Fig. 4-19 Temperature dependent dielectric measurement of an ITO/PEDOT:PSS /$MAPbI_3$ (250 nm)/Au device under 25 mW/cm^2 illumination. (a) Real part of the permittivity ε'. (b) Imaginary part of the permittivity ε''. (c) Conductivity ($\sigma = \varepsilon'' \varepsilon_0 \omega$). (d) Conductivity at 0.1 Hz versus temperature.

The effect of this change can be quantified by applying the same equivalent circuit analysis in Fig. 4-13 to the variable temperature data under illumination. The fitted diffusivity versus temperature and ensuing Arrhenius plot are shown in Fig. 4-20. Compared to the dark condition in Fig. 4-15, the ion diffusivity is higher and the activation energies in both phases are lower, especially in the tetragonal phase. Both observations are consistent with the photoinduced structural change in HOIP as explained above, *i. e.*, enhancement of ion diffusion. It is noted that at 350K, the diffusivity under illumination and dark condition are comparable.

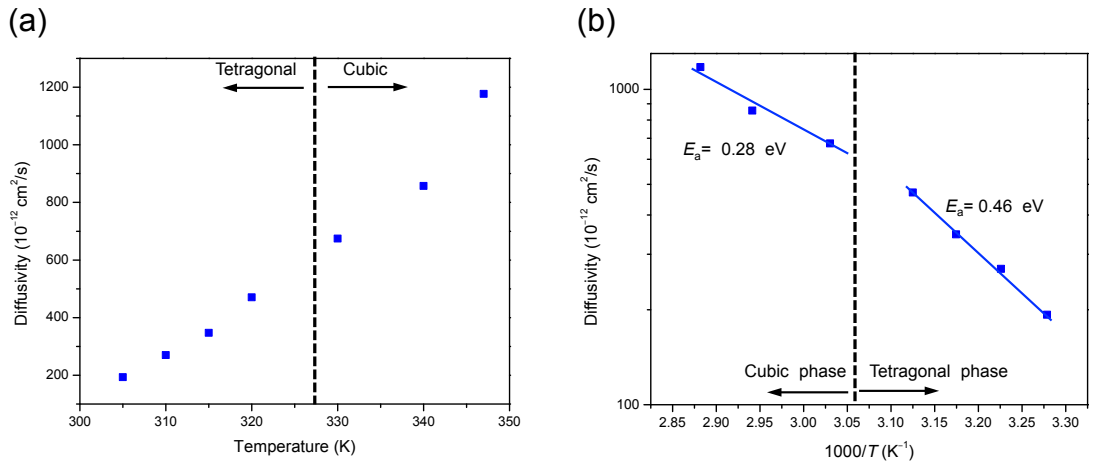

Fig. 4-20 Temperature dependent ion diffusion constant measured by IS under 25 mW/cm^2 illumination (532 nm). (a) Fitted diffusivity versus temperature in linear scale. (b) Arrhenius plot and calculated activation energies.

In summary, this section presented an experimental analysis of ion migration in $MAPbI_3$ perovskites using impedance spectroscopy. It was argued that the low frequency (~< 100 Hz) permittivity is dominated by ion migration, the effect of which is analyzed under various experimental conditions by equivalent circuit fitting. By comparing with available studies in the literature, satisfactory and consistent explanations of the observed effect were presented. Specifically, the hypothesis of photogenerated structural change of $MAPbI_3$ is supported.

4.4 Conclusion

In this chapter, we systematically studied the dielectric response of the HOIP layer in planar devices. The simple layer structure allows more straightforward analysis of the IS data and several insights into the dielectric response were obtained. Specifically, the high frequency permittivity was found to be of dipole origin. Equivalent circuit fitting was successfully applied to the temperature dependent data to obtain the ion diffusivity and activation energy, which were found to be consistent with simulation results in the literature. Possible mechanisms responsible for the illumination-induced effects were discussed.

References

[1] Kremer, F., & Schonhals, A., *Broadband Dielectric Spectroscopy*, Springer, New York, 2003.

[2] Barsoukov, E., & Macdonald, J. R., *Impedance Spectroscopy Theory, Experiment, and Applications*, 2nd edition, John Wiley & Sons, Inc., New Jersey, 2005.

[3] Lin, Q., Armin, A., Nagiri, R. C. R., Burn, P. L. & Meredith, P. Electro-optics of perovskite solar cells. *Nat. Photonics* **9,** 106 (2014). DOI: 10.1038/NPHOTON.2014.284

[4] Neukirch, A. J. *et al.* Polaron stabilization by cooperative lattice and cation rotations in hybrid perovskite materials. *Nano Lett.* **16,** 3809 (2016). DOI: 10.1021/acs.nanolett.6b01218

[5] Zhu, X. Y. & Podzorov, V. Charge carriers in hybrid organic-inorganic lead halide perovskites might be protected as large polarons. *J. Phys. Chem. Lett.* **6,** 4758 (2015). DOI: 10.1021/acs.jpclett.5b02462

[6] Collavini, S., Völker, S. F. & Delgado, J. L. Understanding the outstanding power conversion efficiency of perovskite based solar cells. *Angew. Chemie Int. Ed.* **54,** 9757 (2015). doi:10.1002/anie.201505321 DOI: 10.1002/anie.201505321

[7] Edri, E. *et al.* Elucidating the charge carrier separation and working mechanism of CH3NH3PbI(3-x)Cl(x) perovskite solar cells. *Nat. Commun.* **5,** 3461 (2014). DOI: 10.1038/ncomms4461

[8] Juarez-Perez, E. J. *et al.* Photoinduced giant dielectric constant in lead halide perovskite solar cells *J. Phys. Chem. Lett.* **5,** 2390 (2014). DOI: 10.1021/jz5011169

[9] Almond, D. P. & Bowen, C. R. An explanation of the photoinduced giant dielectric constant of lead halide perovskite solar cells. *J. Phys. Chem. Lett.* **6,** 1736 (2015). DOI: 10.1021/acs.jpclett.5b00620

[10] Young, K. F. & Frederikse, H. P. R. Compilation of the static dielectric constant of inorganic solids. *J. Phys. Chem. Ref. Data* **2,** 313 (1973). DOI: 10.1063/1.3253121

[11] Shen, Y. & Gupta, M. C. Investigation of electrical characteristics of P3HT:PCBM organic solar cells. *2012 38th IEEE Photovolt. Spec. Conf.* 002770 (2012). DOI: 10.1109/PVSC.2012.6318167

[12] Mihailetchi, V. D. *et al.* Electron transport in a methanofullerene. *Adv. Funct. Mater.* **13,** 43 (2003). DOI: 10.1002/adfm.200390004

[13] Onoda-Yamamuro, N., Matsuo, T. & Suga, H. Dielectric study of CH3NH3PbX3 (X = Cl, Br, I). *J. Phys. Chem. Solids* **53,** 935 (1992). DOI: 10.1016/0022-3697(92)90121-S

[14] Hu, M. *et al.* Distinct exciton dissociation behavior of organolead trihalide perovskite and excitonic semiconductors studied in the same system. *Small* **11,** 2164 (2015). DOI: 10.1002/smll.201402905

[15] Maeda, M., Hattori, M., Hotta, A. & Suzuki, I. Dielectric studies on CH3NH3PbX3 (X = Cl and Br) single cystals. *J. Phys. Soc. Japan* **66,** 1508 (1997). DOI: 10.1143/JPSJ.66.1508

[16] Ishai, P. Ben, Talary, M. S., Caduff, A., Levy, E. & Feldman, Y. Electrode polarization in dielectric measurements: a review. *Meas. Sci. Technol.* **24,** 102001 (2013). DOI: 10.1088/0957-0233/24/10/102001

[17] Khamzin, A. A., Popov, I. I. & Nigmatullin, R. R. Correction of the power law of ac conductivity in ion-conducting materials due to the electrode polarization effect. *Phys. Rev.*

E **89,** 032303 (2014). DOI: 10.1103/PhysRevE.89.032303
[18] Onoda-Yamamuro, N., Matsuo, T. & Suga, H. Calorimetric and IR spectroscopic studies of phase transitions in methylammonium trihalogenoplumbates (II). *J. Phys. Chem. Solids* **51,** 1383 (1990). DOI:10.1016/0022-3697(90)90021-7
[19] Weller, M. T., Weber, O. J., Henry, P. F., Di Pumpo, A. M. & Hansen, T. C. Complete structure and cation orientation in the perovskite photovoltaic methylammonium lead iodide between 100 and 352 K. *Chem. Commun.* **51,** 4180 (2015). DOI: 10.1039/c4cc09944c
[20] Wehrenfennig, C., Liu, M., Snaith, H. J., Johnston, M. B. & Herz, L. M. Charge carrier recombination channels in the low-temperature phase of organic-inorganic lead halide perovskite thin films. *APL Mater.* **2,** 081513 (2014). DOI: 10.1063/1.4891595
[21] Labram, J. G. *et al.* Temperature-dependent polarization in field-effect transport and photovoltaic measurements of methylammonium lead iodide. *J. Phys. Chem. Lett.* **6,** 3565 (2015). DOI: 10.1021/acs.jpclett.5b01669
[22] Chen, T. *et al.* Rotational dynamics of organic cations in the CH3NH3PbI3 perovskite. *Phys. Chem. Chem. Phys.* **17,** 31278 (2015). DOI: 10.1039/c5cp05348j
[23] Even, J. Pedestrian guide to symmetry properties of the reference cubic structure of 3D all-inorganic and hybrid perovskites. *J. Phys. Chem. Lett.* **6,** 2238 (2015). DOI: 10.1021/acs.jpclett.5b00905
[24] Onsager, L. Electric moments of molecules in liquids. *J. Am. Chem. Soc.* **58,** 1486 (1936). DOI: 10.1021/ja01299a050
[25] Rupprecht, G. & Bell, R. O. Dielectric constant in paraelectric perovskites. *Phys. Rev.* **135,** A748 (1964). DOI: 10.1103/PhysRev.135.A748
[26] Trainer, M. Ferroelectricity: Measurement of the dielectric susceptibility of strontium titanate at low temperatures. *Am. J. Phys.* **69,** 966 (2001). DOI: 10.1119/1.1374251
[27] Brivio, F., Walker, A. B. & Walsh, A. Structural and electronic properties of hybrid perovskites for high-efficiency thin-film photovoltaics from first-principles. *APL Mater.* **1,** 2011 (2013). DOI: 10.1063/1.4824147
[28] Frost, J. M. et al. Atomistic origins of high-performance in hybrid halide perovskite solar cells. *Nano Lett.* **14**, 2584 (2014). DOI: 10.1021/nl500390f
[29] Zheng, F., Takenaka, H., Wang, F., Koocher, N. Z. & Rappe, A. M. First-principles calculation of the bulk photovoltaic effect in CH3NH3PbI3 and CH3NH3PbI3-xClx. *J. Phys. Chem. Lett.* **6,** 31 (2015). DOI: 10.1021/jz502109e
[30] Pecchia, A., Gentilini, D., Rossi, D., Auf Der Maur, M. & Di Carlo, A. Role of ferroelectric nanodomains in the transport properties of perovskite solar cells. *Nano Lett.* **16,** 988 (2016). DOI: 10.1021/acs.nanolett.5b03957
[31] Stroppa, A., Quarti, C., De Angelis, F. & Picozzi, S. Ferroelectric polarization of CH3NH3PbI3: A detailed study based on density functional theory and symmetry mode analysis. *J. Phys. Chem. Lett.* **6,** 2223 (2015). DOI: 10.1021/acs.jpclett.5b00542
[32] Liu, S. *et al.* Ferroelectric domain wall induced band gap reduction and charge separation in organometal halide perovskites. *J. Phys. Chem. Lett.* **6,** 693 (2015). DOI: 10.1021/jz502666j
[33] Leguy, A. M. A. *et al.* The dynamics of methylammonium ions in hybrid organic-inorganic perovskite solar cells. *Nat. Commun.* **6,** 7124 (2015). DOI:

10.1038/ncomms8124
[34] Quarti, C. *et al.* The Raman spectrum of the CH3NH3PbI3 hybrid perovskite: Interplay of theory and experiment. *J. Phys. Chem. Lett.* **5,** 279 (2014). DOI: 10.1021/jz402589q
[35] Lee, J. H., Lee, J.-H., Kong, E.-H. & Jang, H. M. The nature of hydrogen-bonding interaction in the prototypic hybrid halide perovskite, tetragonal CH3NH3PbI3. *Sci. Rep.* **6,** 21687 (2016). DOI: 10.1038/srep21687
[36] Deretzis, I. *et al.* Spontaneous bidirectional ordering of CH3NH3+ in lead iodide perovskites at room temperature: The origins of the tetragonal phase. *Sci. Rep.* **6,** 24443 (2016). DOI: 10.1038/srep24443
[37] Bakulin, A. A. *et al.* Real-time observation of organic cation reorientation in methylammonium lead iodide perovskites. *J. Phys. Chem. Lett.* **6,** 3663 (2015). DOI: 10.1021/acs.jpclett.5b01555
[38] Azpiroz, J. M., Mosconi, E., Bisquert, J. & De Angelis, F. Defect migration in methylammonium lead iodide and its role in perovskite solar cell operation. *Energy Environ. Sci.* **8,** 2118 (2015). DOI: 10.1039/c5ee01265a
[39] Haruyama, J., Sodeyama, K., Han, L. & Tateyama, Y. First-principles study of ion diffusion in perovskite solar cell sensitizers. *J. Am. Chem. Soc.* **137,** 10048 (2015). DOI: 10.1021/jacs.5b03615
[40] Eames, C. *et al.* Ionic transport in hybrid lead iodide perovskite solar cells. *Nat. Commun.* **6,** 7497 (2015). DOI: 10.1038/ncomms8497
[41] Zhao, Y. *et al.* Anomalously large interface charge in polarity-switchable photovoltaic devices: an indication of mobile ions in organic-inorganic halide perovskites. *Energy Environ. Sci.* **8,** 1256 (2015). DOI: 10.1039/c4ee04064c
[42] Meloni, S. *et al.* Ionic polarization-induced current–voltage hysteresis in CH3NH3PbX3 perovskite solar cells. *Nat. Commun.* **7,** 10334 (2016). DOI: 10.1038/ncomms10334
[43] Chen, B. *et al.* Impact of capacitive effect and ion migration on the hysteretic behavior of perovskite solar cells. *J. Phys. Chem. Lett.* **6,** 4693 (2015). DOI: 10.1021/acs.jpclett.5b02229
[44] De Bastiani, M. *et al.* Ion migration and the role of preconditioning cycles in the stabilization of the J-V characteristics of inverted hybrid perovskite solar cells. *Adv. Energy Mater.* **6,** 1501453 (2016). DOI: 10.1002/aenm.201501453
[45] deQuilettes, D. W. *et al.* Photo-induced halide redistribution in organic-inorganic perovskite films. *Nat Commun* **7,** 11683 (2016). DOI: 10.1038/ncomms11683
[46] Li, C. *et al.* Iodine migration and its effect on hysteresis in perovskite solar cells. *Adv. Mater.* **28,** 2446 (2016). DOI: 10.1002/adma.201503832
[47] Yuan, Y. *et al.* Photovoltaic switching mechanism in lateral structure hybrid perovskite solar cells. *Adv. Energy Mater.* **5,** 1500615 (2015). DOI: 10.1002/aenm.201500615
[48] Almora, O. *et al.* Capacitive dark currents, hysteresis, and electrode polarization in lead halide perovskite solar cells. *J. Phys. Chem. Lett.* **6,** 1645 (2015). DOI: 10.1021/acs.jpclett.5b00480
[49] Zarazua, I., Bisquert, J. & Garcia-Belmonte, G. Light-induced space-charge accumulation zone as photovoltaic mechanism in perovskite solar cells. *J. Phys. Chem. Lett.* **7,** 525 (2016). DOI: 10.1021/acs.jpclett.5b02810
[50] Yang, T. Y., Gregori, G., Pellet, N., Gratzel, M. & Maier, J. The significance of ion

conduction in a hybrid organic-inorganic lead-iodide-based perovskite photosensitizer. *Angew. Chemie - Int. Ed.* **54,** 7905 (2015). DOI: 10.1002/anie.201500014

[51] Zohar, A. *et al.* Impedance Spectroscopic Indication for Solid State Electrochemical Reaction in (CH3NH3)PbI3 Films. *J. Phys. Chem. Lett.* **7,** 191 (2016). DOI: 10.1021/acs.jpclett.5b02618

[52] Ngai, K. L., Jonscher, A. K. & White, C. T. On the origin of the universal dielectric response in condensed matter. *Nature* **277,** 185 (1979). DOI: 10.1038/277185a0

[53] Jonscher, A. K. A new understanding of the dielectric relaxation of solids. *J. Mater. Sci.* **16,** 2037 (1981).

[54] Quarti, C. *et al.* Structural and optical properties of methylammonium lead iodide across the tetragonal to cubic phase transition: implications for perovskite solar cells. *Energy Environ. Sci.* **9,** 155 (2016). DOI: 10.1039/c5ee02925b

[55] Jasinski, P., Petrovsky, V., Suzuki, T. & Anderson, H. U. Impedance studies of diffusion phenomena and ionic and electronic conductivity of cerium oxide. *J. Electrochem. Soc.* **152,** 27 (2005). DOI: 10.1149/1.1861174

[56] Warburg, E. Ueber die Spitzenentladung. *Ann. Phys.* **303,** 69 (1899). DOI: 10.1002/andp.18993030104

[57] Bag, M. *et al.* Kinetics of ion transport in perovskite active layers and its implications for active layer stability. *J. Am. Chem. Soc.* **137,** 13130 (2015). DOI**:** 10.1021/jacs.5b08535

[58] Alexe-Ionescu, A. L., Barbero, G., Lelidis, I. & Scalerandi, M. Relaxation times of an electrolytic cell subject to an external electric field: Role of ambipolar and free diffusion phenomena. *J. Phys. Chem. B* **111,** 13287 (2007). DOI: 10.1021/jp0742160

[59] Almora, O., Guerrero, A. & Garcia-Belmonte, G. Ionic charging by local imbalance at interfaces in hybrid lead halide perovskites. *Appl. Phys. Lett.* **108,** 043903 (2016). DOI: 10.1063/1.4941033

[60] Frost, J. M. & Walsh, A. What is moving in hybrid halide perovskite solar cells? *Acc. Chem. Res.* **49,** 528 (2016). DOI: 10.1021/acs.accounts.5b00431

[61] Milot, R. L., Eperon, G. E., Snaith, H. J., Johnston, M. B. & Herz, L. M. Temperature-dependent charge-carrier dynamics in CH3NH3PbI3 perovskite thin films. *Adv. Funct. Mater.* **25,** 6218 (2015). DOI: 10.1002/adfm.201502340

[62] Wright, A. D. *et al.* Electron–phonon coupling in hybrid lead halide perovskites. *Nat. Commun.* **7,** 11755 (2016). DOI: 10.1038/ncomms11755

[63] Brivio, F. *et al.* Lattice dynamics and vibrational spectra of the orthorhombic, tetragonal, and cubic phases of methylammonium lead iodide. *Phys. Rev. B* **92,** 144308 (2015). DOI:10.1103/PhysRevB.92.144308

[64] Yuan, Y. & Huang, J. Ion migration in organometal trihalide perovskite and its impact on photovoltaic efficiency and stability. *Acc. Chem. Res.* **49,** 286 (2016). DOI: 10.1021/acs.accounts.5b00420

[65] Mosconi, E. & De Angelis, F. Mobile ions in organohalide perovskites: interplay of electronic structure and dynamics. *ACS Energy Lett.* **1,** 182 (2016). DOI: 10.1021/acsenergylett.6b00108

[66] Yang, D., Ming, W., Shi, H., Zhang, L. & Du, M.-H. Fast diffusion of native defects and impurities in perovskite solar cell material CH3NH3PbI3. *Chem. Mater.* **28,** 4349

(2016). DOI: 10.1021/acs.chemmater.6b01348
[67] Walsh, A., Scanlon, D. O., Chen, S., Gong, X. G. & Wei, S.-H. Self-regulation mechanism for charged point defects in hybrid halide perovskites. *Angew. Chemie Int. Ed.* **54,** 1791 (2015). DOI: 10.1002/ange.201409740
[68] Zhang, Y. *et al.* Charge selective contacts, mobile ions and anomalous hysteresis in organic-inorganic perovskite solar cells. *Mater. Horizons* **2,** 315 (2015). DOI: 10.1039/c4mh00238e
[69] Levine, I. *et al.* Interface-dependent ion migration/accumulation controls hysteresis in MAPbI3 solar cells. *J. Phys. Chem. C* **120,** 16399 (2016). DOI: 10.1021/acs.jpcc.6b04233
[70] Gottesman, R. *et al.* Extremely slow photoconductivity response of CH3NH3PbI3 perovskites suggesting structural changes under working conditions. *J. Phys. Chem. Lett.* **5,** 2662 (2014). DOI: 10.1021/jz501373f
[71] Deng, Y., Xiao, Z. & Huang, J. Light-induced self-poling effect on organometal trihalide perovskite solar cells for increased device efficiency and stability. *Adv. Energy Mater.* **5,** 1500721 (2015). DOI: 10.1002/aenm.201500721
[72] Bisquert, J., Garcia-Belmonte, G., Pitarch, Á. & Bolink, H. J. Negative capacitance caused by electron injection through interfacial states in organic light-emitting diodes. *Chem. Phys. Lett.* **422,** 184 (2006). DOI:10.1016/j.cplett.2006.02.060
[73] Mora-Sero, I. *et al.* Implications of the negative capacitance observed at forward bias in nanocomposite and polycrystalline solar cells. *Nano Lett.* **6,** 640 (2006). DOI: 10.1021/nl052295q
[74] Guerrero, A. *et al.* Properties of contact and bulk impedances in hybrid lead halide perovskite solar cells including inductive loop elements. *J. Phys. Chem. C* **120,** 8023 (2016). DOI: 10.1021/acs.jpcc.6b01728
[75] Gottesman, R. *et al.* Photoinduced reversible structural transformations in free-standing CH3NH3PbI3 perovskite films. *J. Phys. Chem. Lett.* **6,** 2332 (2015). DOI: 10.1021/acs.jpclett.5b00994
[76] Liu, S., Zheng, F., Grinberg, I. & Rappe, A. M. Photoferroelectric and photopiezoelectric properties of organometal halide perovskites. *J. Phys. Chem. Lett.* **7,** 1460 (2016). DOI: 10.1021/acs.jpclett.6b00527

Chapter 5

The missing link: Observation and analysis of proton migration in $MAPbI_3$

5.1 "Intermediate relaxation" and its temperature dependence

The dielectric response of sandwiched devices (ITO/PEDOT:PSS/$MAPbI_3$/Au) has been analyzed in the previous chapter. The high (≥ 50 kHz) and low frequency (< 100 Hz) part of the spectra have been attributed to dipole rotation and ion migration, respectively, while the frequency range between (0.1–30 kHz) has not been explored. Zooming in on one typical dielectric spectrum of an ITO/PEDOT:PSS/$MAPbI_3$/Au device in this regime shows one curious feature (Fig. 5-1): Besides the monotonous increase of permittivity with decreasing frequency, an inflection point is observed near 10 kHz. This indicates an additional relaxation process responding in this frequency region.[1] To show this more clearly, the normalized derivative of the real part of permittivity ($-f\,\mathrm{d}\varepsilon'/\mathrm{d}f$) is also plotted. The normalized derivative plot is a common approach to determine the relaxation frequency in the dielectric spectra of high conductivity samples,[2,3] which obscure the peak that should otherwise appear on the ε'' spectra of insulating samples.[1] The relaxation frequency is then determined to be 8 kHz.

The unexplained relaxation process in the ITO/PEDOT:PSS/$MAPbI_3$/Au device will be referred to as the "intermediate relaxation" as its response frequency lies between the 2 mechanisms discussed in the last chapter, *i. e.*, I^- or MA^+ migration and dipole reorientation.

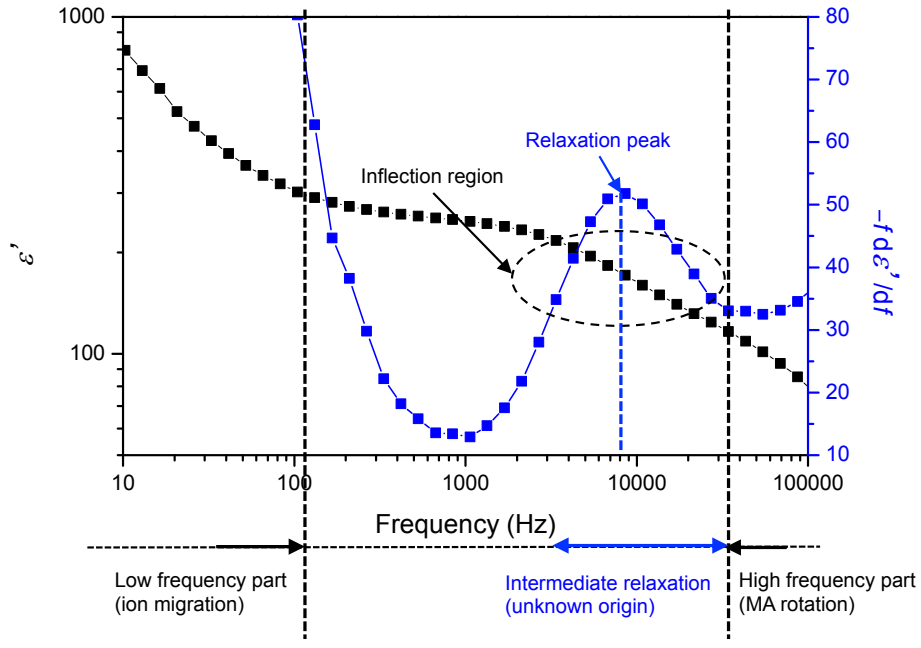

Fig. 5-1 Observation of intermediate relaxation in an ITO/PEDOT:PSS/$MAPbI_3$/Au

device. Data taken from the room temperature curve in Fig. 4-11.

Note that this response is not included in the equivalent circuit simulation presented in section 4.2, designed to focus on the low frequency part. Therefore, the effect of the intermediate relaxation is mixed with the carrier resistance ($R_{carrier}$), bulk capacitance (C_{bulk}), and trace resistance (R_{tr}) (Fig. 4-13). Actually, as the effect is small compared to that of the low frequency ion migration, it is likely to be lost in the fitting process.

As shown in the previous chapter, the temperature dependence of a relaxation process provides important information concerning its nature. The re-plotting of the variable temperature measurement in Fig. 4-11 focusing on the intermediate frequency region is shown in Fig. 5-2. At higher temperatures, the effect of low frequency ion migration moved into this region, causing the relaxation peak to become increasingly difficult to distinguish. However, up to 350 K, reasonable relaxation frequency and peak height can be determined. The relaxation frequency increases with temperature while its peak height decreased. Effects of the tetragonal-to-cubic phase transition can be seen clearly by the different activation energies (115 meV and 58 meV in the cubic phase and tetragonal phase, respectively).

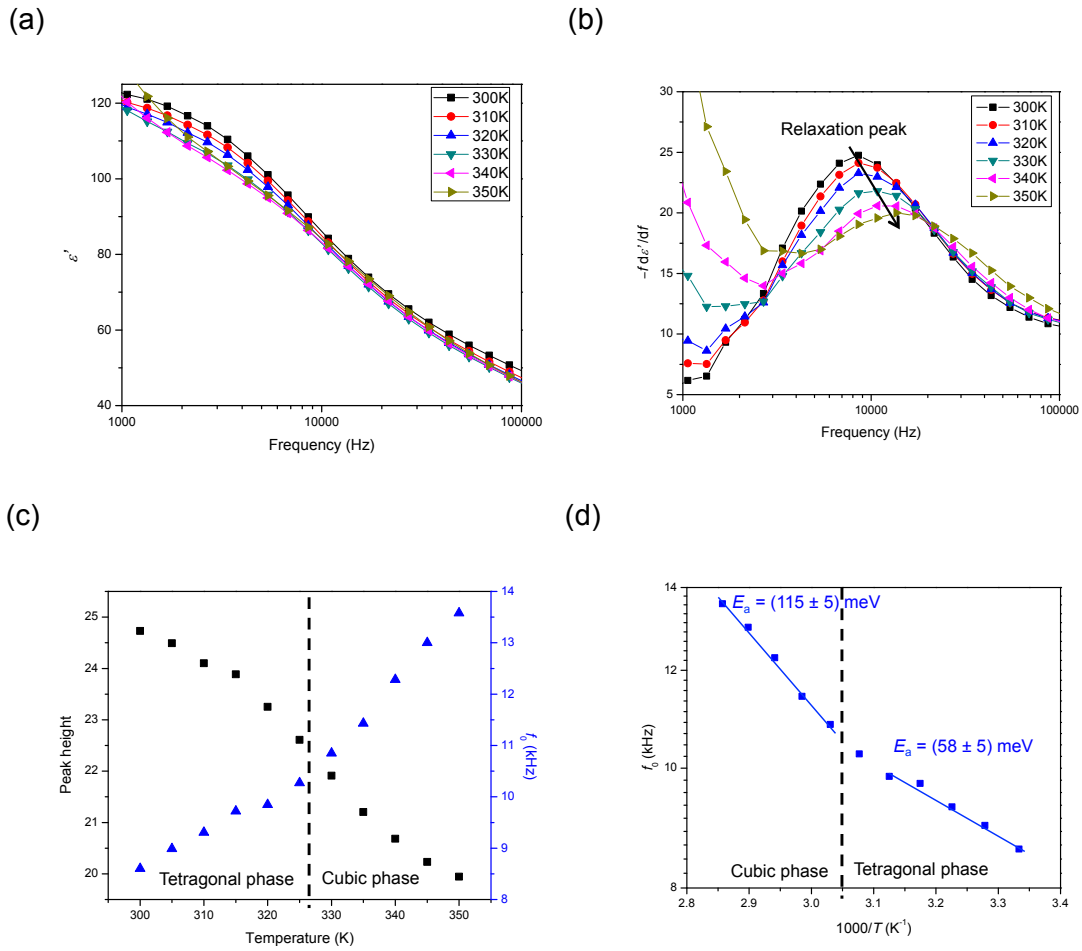

Fig. 5-2 Temperature dependence of the intermediate relaxation from 300 K to 350 K. (a) Real part of permittivity versus frequency (1–100 kHz). (b) Normalized derivative of the permittivity versus frequency to determine the relaxation peak position and height. (c) Peak position and height versus temperature. (d) Arrhenius plot of the relaxation frequency and the fitting of activation energies in the cubic and tetragonal phase.

The temperature range 300–350 K is not enough to clearly analyze the temperature dependence of the relaxation process. For example, the apparent Arrhenius behavior might change when looking at a larger temperature range. As $MAPbI_3$ degrades at temperature as low as 360 K, it is not possible to obtain the data of higher temperatures. Therefore, further study was carried out on sample temperatures lower than room temperature, with the equipment described in section 3.3.

The result of the dielectric measurements from 270 K to 90 K are shown in Fig. 5-3. Over this temperature and frequency region, the interference from the low frequency ion migration is minimal, allowing clear view on the intermediate relaxation. The effect of tetragonal-to-orthorhombic phase transition occurring at 162 K for $MAPbI_3$ can also be

observed: On the ε' graph (Fig. 5-3 (a)), the spectra of temperature higher than 160 K are separated from the ones lower than 160 K. On the *ε"* graph (Fig. 5-3 (b)), the difference between the 2 phases is also observable but less apparent, possibly due to the less impact of the phase transition on electronic conduction.

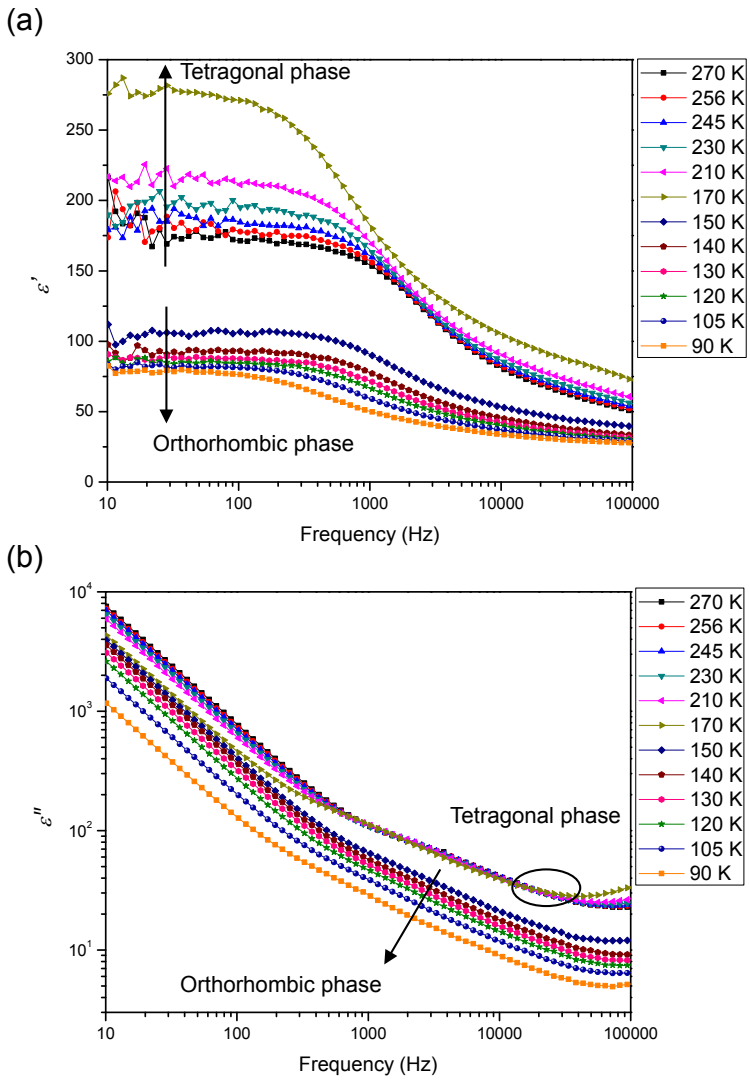

Fig. 5-3 Temperature dependent dielectric measurement of an ITO/PEDOT:PSS/$MAPbI_3$ (200 nm)/Au device from 270 K to 90K. (a) real and (b) imaginary part of the permittivity.

At temperatures below room temperature, the plateau caused by the intermediate relaxation can be observed clearly. Therefore, the relaxation frequency can be determined more reasonably by finding the edge of the plateau using 2 tangential lines, as shown in Fig. 5-4 (a). Mathematically, this point corresponds to the lowest point on the plot of the second derivative of the permittivity (Fig. 5-4 (b)). Same frequency was found by the 2 methods.

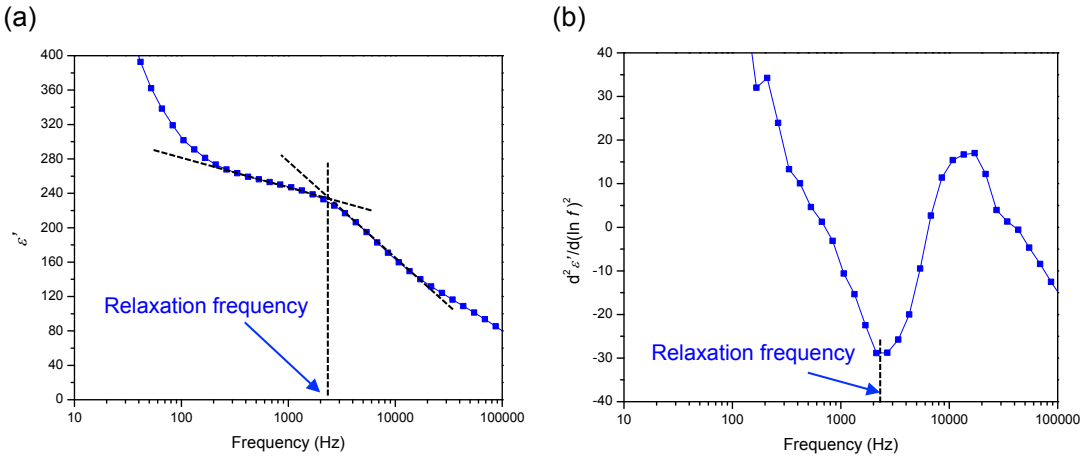

Fig. 5-4 (a) Determination of relaxation frequency by the edge of the relaxation plateau. (b) Second derivative of the permittivity. The relaxation frequency corresponds to the lowest point, as indicated by the blue arrow.

The method employing second derivative suffers from low signal-to-noise ratio at lower frequencies. Therefore, the relaxation frequencies of Fig. 5-3 (a) were determined by the tangential line method, and are represented in Arrhenius form in Fig. 5-5.

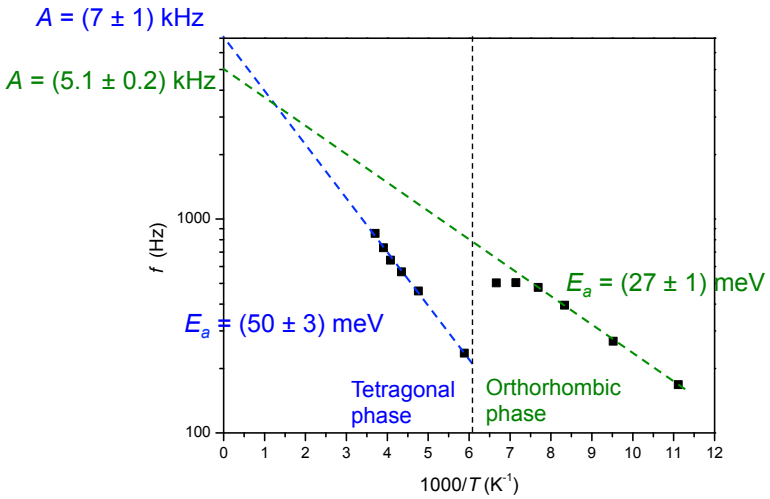

Fig. 5-5 Temperature dependence of the frequency of intermediate relaxation determined by the tangential line method.

In both phases, the relaxation frequency exhibited Arrhenius behavior. The activation energies (E_a) were fitted to be 50 meV and 27 meV in the tetragonal and orthorhombic phases, respectively, while the pre-exponential factors (A) were 7 kHz and 5.1 kHz. These activation energies are low compared to that of ion migration mechanism, which are typically on the order of hundreds of meV.[4,5,6] On the other hand, the activation energies for the rotation of

organic cations in $MAPbI_3$ are similar to these values.[7,8,9] While the exact value varies (from a few meV up to 100 meV), all reports agree that, as the rotation is restricted in the low temperature phase, the activation energy in the orthorhombic phase is smaller than in the tetragonal phase. The same is observed for the intermediate relaxation process.

It is unlikely that the organic cation rotation is the direct cause of the intermediate relaxation as the relaxation time of cation rotation in HOIPs is on the range of ps, *i. e.*, 10^{12} Hz.[8,10] Therefore, the observations above indicate that the intermediate relaxation is strongly affected by the phase transition in a way that is similar to organic cation rotation, but that it is of different origin.

5.2 Origin of the intermediate relaxation

5.2.1 Discussion on the possible origins

To formulate a hypothesis on the origin of the intermediate relaxation process, a general survey of the HOIP literature was carried out, which suggests that three mechanisms are possible: ion migration, dipole domain alignment, or trap state filling (Fig. 5-6, see the references of chapter 4, in particular, a recent review by A. M. Frost & A. Walsh).[11]

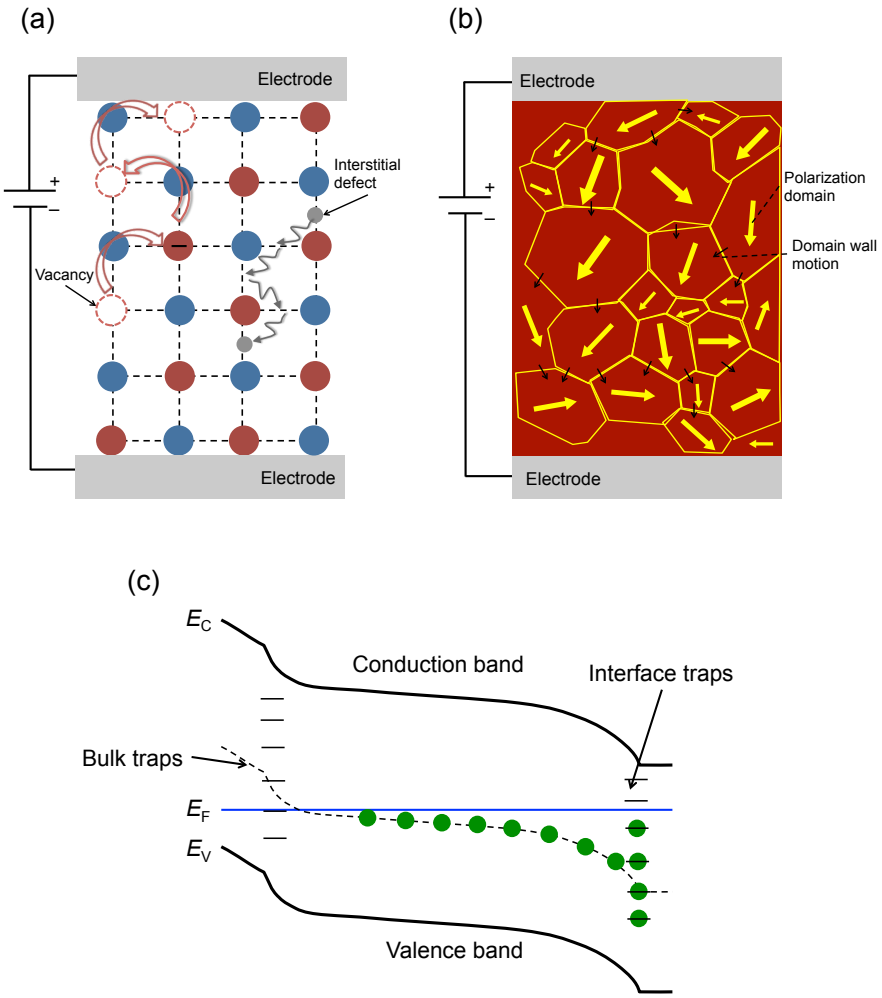

Fig. 5-6 Possible mechanisms responsible for the intermediate relaxation. (a) Ion migration, where vacancies or interstitial defects would facilitate the migration. (b) Dipole domain alignment, where the domains aligns with external electrical field successively (domain wall motion). (c) Trap filling. The traps are considered as electronic in this case. Both interface and bulk traps might present. Figure (c) adapted with permission from ref. 3. Copyright 2014 Royal Society of Chemistry.

From the discussion in section 4.3, the typical time scale of ion migration (attribute to I^- or MA^+) in a 250-nm-thick HOIP film is of the order < 0.1 second at room temperature. Therefore, if ion migration is to account for the intermediate relaxation process, a more mobile species must be involved. The time scale for intermediate relaxation is around 10^{-4} sec, meaning a diffusivity of ~10^{-4} cm^2/s, considerably higher than that of I^-, MA^+, or Pb^{2+}.* The high diffusivity suggests a low energy barrier and a small mass of the moving species.

* This value is estimated from the general relationship between relaxation time and ion diffusion through a 250-nm-thick film, introduced in section 4.3. More discussion on this point is presented in section 5.3.

Considering the composition of $MAPbI_3$, the most likely candidate for this fast ion migration is protons, which might come from the dissociation of the ammonium group of the MA^+ ions ($CH_3NH_3^+ \rightarrow CH_3NH_2 + H^+$) or residual water content from processing.

For the possibility of dipole domain alignment, when no external field is applied, the domains order themselves based on the thermal entropy at the given temperature, and are present in a more or less random state. The applied field deviates the system from thermal equilibrium and aligns the domain in its direction. The dynamics of the domains is determined by the domain wall motion, which, according to the Kolmogorov–Avrami–Ishibashi (KAI) model,[12] has time scales that depend on the applied voltage and film thickness. In ferroelectric perovskite oxides, the relaxation time of the domain switching is typically 10^{-4} seconds (for film thickness ~100 nm and an applied voltage ~1 V).[13,14] In HOIPs, such an relaxation has been proposed to explain the hysteresis effect, and the estimated relaxation time over a 200-nm-thick $MAPbI_3$ film with applied voltage ~1 V is 10^{-4}–10^{-3} seconds,[7] which lies in the same time scale as the intermediate relaxation.

The third and final possibility is the general trap state filling. In this case, the bulk and interface traps near the Fermi level contribute to the dielectric response by the filling of electrons or holes during the application of an AC voltage.[15,16] The trap states can be either on the interfaces, or in the bulk of the material.[17] This model has been used to determine the trap state distribution of $MAPbI_3$.[3†] Note that in this context, the trap states are specifically electronic traps, *i. e.*, from electronic defects.

5.2.2 Identifying the mechanism: kinetic isotope effects

To distinguish between the three possibilities, measurement of isotope effects would be helpful. Kinetic isotope effects (KIEs) measure the change of reaction/transition rate when part of the chemical composition is replaced with its isotope, a technique having long been used in chemistry to identify reaction pathways. When the isotope is directly involved in the

† In this study, Duan *et al.*[3] determined the trap state distribution from a relaxation peak around 10^5 Hz at room temperature and the activation energy of this trap states was found to be around 200 meV. The difference suggests that the phenomenon they observed is different from the intermediate relaxation.

reaction/transition, it is termed a primary isotope effect, while secondary isotope effect designates the case when the isotope exchange affects the process indirectly. Generally speaking, primary isotope effects have a bigger influence on the rate constants than secondary isotope effects.

To understand how isotopes influence reaction rates, the concept of the transition state theory is useful. The principle of KIE according to transition state theory is shown in Fig. 5-7, where the process is pictured as going from an initial state, through a maximum energy saddle point transition state, to a final state. The simplest treatment of KIEs is that the difference in mass between the two isotopes of the same element results in a difference in the zero point energy of the initial state. This then modifies the activation energy, *i. e.*, the energy required for the reaction to occur. Provided that the potential energy well and the saddle point energy are independent of the isotopic composition, the zero point motion of the heavy isotope would be of smaller amplitude, as suggested by a simple harmonic oscillator model. This means that the heavy isotope lies deeper in the initial state, and therefore would have a higher activation energy and lower reaction rate. The tendency of lower rates for the heavy isotope is called the normal isotope effect.

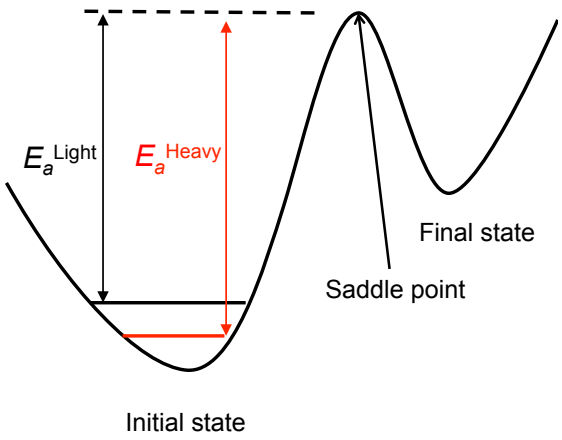

Fig. 5-7 Illustration of normal kinetic isotope effect according to transition state theory

On the other hand, "inverse" isotope effects, where the rates are higher for the heavy isotope, have also been observed. They can be explained by the fact that in these cases the saddle point energy is lower for the heavy isotope, as illustrated in Fig. 5-8 (a). When the curvature in coordinates other than the reaction coordinates dominate the zero point motion, the saddle

point energy would depend on the atomic mass. If the curvature at the saddle point is higher than that of the initial state, the activation energy of the heavy isotope is actually lower compared to the lighter isotope (Fig. 5-8 (b)). This concept has been used to explain the inverse isotope effect observed in the ionic hydrogen bond formed in $H_2O\cdots H^+\cdots OH_2$.[18]

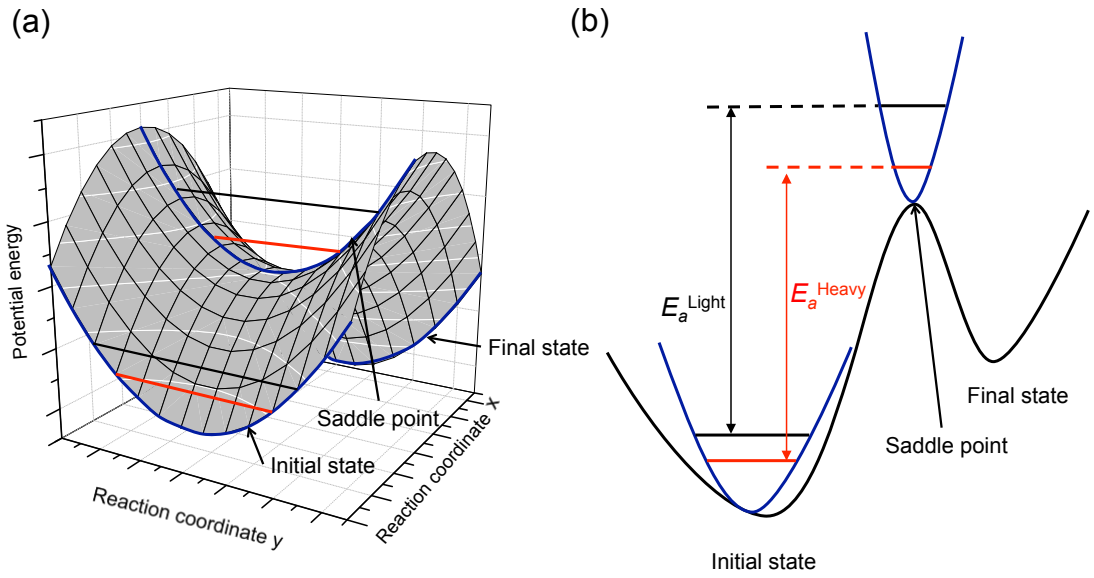

Fig. 5-8 Illustration of inverse isotope effect caused by the curvature at the saddle point. (a) Energy profile including coordinates other than the reaction coordinate. (b) Transition state diagram taking into account the energy profile. The higher curvature at the saddle point compared to the initial state would result in an inverse isotope effect.

For more complex systems, other mechanisms would also set in to affect the outcome of KIE. Some of these mechanisms and their resulting effect on the KIE are listed in Table 5- 1. Therefore, to interpret the outcome of a KIE on a process, some idea of the nature of the process must be known beforehand.

Table 5- 1 Examples of mechanisms contributing to the KIE and their effect on the pre-exponential factors and activation energies. + means tendency for a normal isotope effect, and – indicates an inverse isotope effect. No symbol means that the effect cannot be specified a priori. Table adapted from ref.19.

Mechanisms	A	E_a
Probability of successful jump	–	nil
Zero-point energy polaron effect		–
Tunneling matrix overlap	+	nil

Delocalized excited states	+
Local tunneling states	(reduce isotope dependence)

5.2.3 KIE measurement of the intermediate relaxation process

Based on the above discussion, we can begin to formulate a hypothesis concerning the effect of the KIE on the intermediate relaxation process. As shown in section 5.1, the intermediate relaxation appears to be related to the rotation of organic cations. Though at this point this relation is not clear, it is reasonable to assume that the intermediate relaxation would be affected by the rotor properties of the MA^+ ions, which can be modified by replacing their hydrogen atoms by deuterium. Four possible isotopic MA^+ ions can be obtained by deuterating the hydrogen in the methyl and/or the ammonium group, as listed in Table 5-2. The rotor properties are quantified by their momentum of inertia, which are practically identical for the deuteration of either the methyl or the ammonium group ($CH_3ND_3^+$or $CD_3NH_3^+$). Compared with undeuterated MA^+ ions ($CH_3NH_3^+$), the deuteration of each functional group increases the momentum of inertia by ca. 9%, up to ca.19% when both fragments are fully deuterated ($CD_3ND_3^+$).

Table 5-2 Possible deuteration in MA^+ ions and their moment of inertia. The deuteration of either methyl or ammonium group results in similar moment of inertia (difference ca. 0.03%) while the moment of intetia of fully deuterated MA^+ ions increases ca. 19% versus non-deuterated MA^+. The rotor properties of $CH_3ND_3^+$ and $CD_3NH_3^+$ are therefore expected to be the same.

Formula	Rotor	Moment of inertia (a.m.u. Å^2)
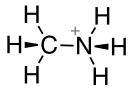	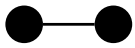	36.3
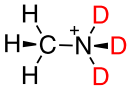	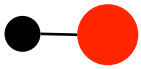	39.1
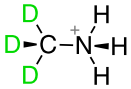	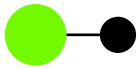	39.7
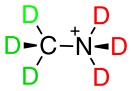	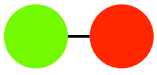	43.2

Observing the effect of these rotors in $MAPbI_3$ can be used to distinguish between the 3 possible mechanisms of the intermediate relaxation: Proton migration, dipole domain alignment, and trap state filling. The key here is that the deuteration of the methyl or the ammonium group are practically the same in terms of rotor properties. Therefore, as the domain wall motion in the second mechanism is directly the result of rotor motion, the same KIE should be present for $CH_3ND_3PbI_3$ and $CD_3NH_3PbI_3$. In the trap filling mechanism, the electronic states of isotopes remain largely the same, and the only way KIE can manifest itself is through changes in the dielectric screening, *i. e.*, polaron effects, which again depend only on the rotor properties.

The case for proton migration is quite different. Protons can be dissociated from the ammonium group but not the methyl group. Therefore, a primary isotope effect would be expected in $CH_3ND_3PbI_3$, whereas a secondary isotope effect is expected in $CD_3NH_3PbI_3$.

To measure the KIE of the intermediate relaxation process, deuterated $MAPbI_3$ was prepared with deuterated methylammonium iodide. Details of the synthesis procedure are shown in Appendix 7.3. It is generally recognized that the film properties strongly depend on the processing condition and precursor composition.[20] Therefore, same preparation procedure was employed for the deuterated $MAPbI_3$ films, and spectroscopic and electronic characterizations on the films were also carried out, showing that the crystallinity and the electronic properties of each isotopic $MAPbI_3$ ($CH_3ND_3PbI_3$, $CH_3NH_3PbI_3$, $CD_3NH_3PbI_3$, and $CD_3ND_3PbI_3$) are indistinguishable from UV–vis absorption, electroluminescence, and X-ray diffraction. Details of the characterization can be found in Appendix 7.3.

The dielectric responses of device structure of ITO/PEDOT:PSS/$CH_3ND_3PbI_3$/Au, ITO/PEDOT:PSS/$CD_3NH_3PbI_3$/Au, and ITO/PEDOT:PSS/$CD_3ND_3PbI_3$/Au were then measured with the same procedure as the experiment in Fig. 5-3 and Fig. 5-5. The results are shown in Fig. 5-9. Similar intermediate relaxation processes were observed in all three deuterated films.

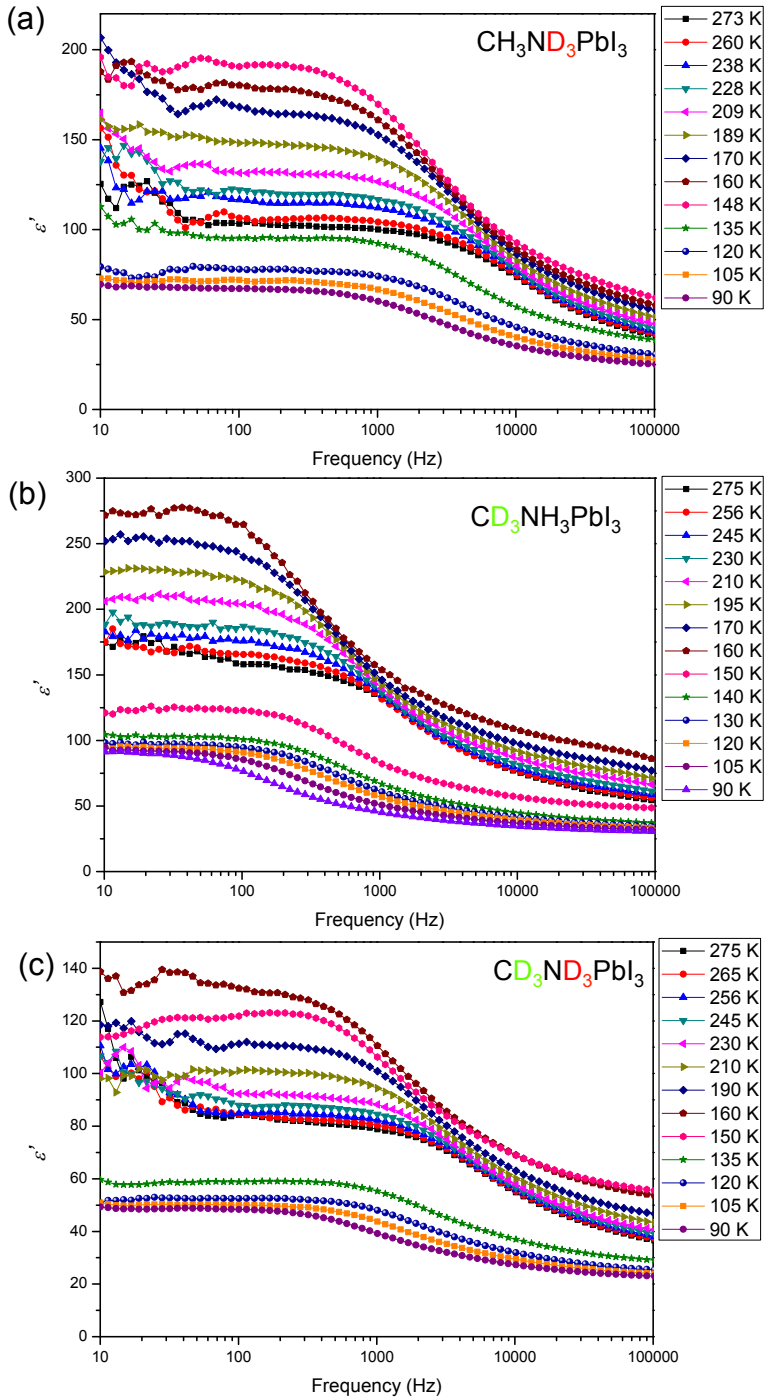

Fig. 5-9 Dielectric measurement of the intermediate relaxation process of deuterated $MAPbI_3$. (a) sample with deuterated ammonium group (ITO/PEDOT:PSS/$CH_3ND_3PbI_3$ (200 nm)/Au). (b) sample with deuterated methyl group (ITO/PEDOT:PSS/$CD_3NH_3PbI_3$ (200 nm)/Au). (c) deuteration of both functional groups (ITO/PEDOT:PSS/$CD_3ND_3PbI_3$ (200 nm)/Au).

The temperature dependence of the characteristic frequencies is shown in Fig. 5-10. In the deuterated films, the characteristic frequencies also follow Arrhenius behavior in both the tetragonal and the orthorhombic phase. The pre-exponential factors and activation energies of

the deuterated/non-deuterated films, fitted from the Arrhenius equation, are summarized in Table 5-3.

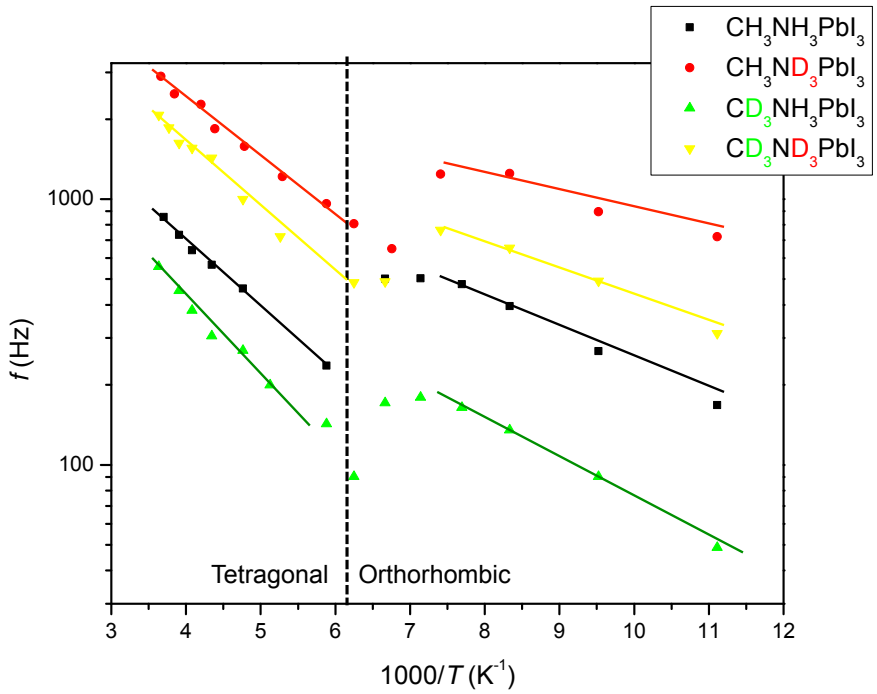

Fig. 5-10 Comparison of the Arrhenius plots of the relaxation frequencies of deuterated/non-deuterated $MAPbI_3$.

Table 5-3 Summary of the pre-exponential factors (A) and activation energies (E_a) of the intermediate relaxation of ITO/PEDOT:PSS/$MAPbI_3$/Au devices with deuterated/non-deuterated $MAPbI_3$. The error bar of the values from the standard deviations of linear fitting is given in parenthesis.

	Tetragonal phase		Orthorhombic phase	
Material	A /kHz	E_a /meV	A /kHz	E_a /meV
$CH_3NH_3PbI_3$	7 (1)	50 (3)	5.1 (0.2)	27 (1)
$CH_3ND_3PbI_3$	17 (2)	43 (2)	4 (1)	14 (3)
$CD_3NH_3PbI_3$	6 (1)	57 (4)	2.1 (0.3)	29 (2)
$CD_3ND_3PbI_3$	20 (3)	54 (3)	4.9 (0.8)	21 (2)

Comparing the relaxation frequencies of $CH_3NH_3PbI_3$ and $CH_3ND_3PbI_3$ shows a strong inverse isotope effect following deuteration of the ammonium group, *i. e.*, a faster transition rate due to the heavy isotope deuterium. On the other hand, the deuteration of methyl group shows a normal isotope effect, where the rate is lower with the heavy isotope.

The two opposing effects are shown clearly in the plot of the activation energies (E_a) (Fig. 5-11). The deuteration of ammonium group (red arrows) decreases E_a (inverse isotope effect), while the deuteration of methyl group (green arrows) increases E_a (normal isotope effect). The same effects were observed in both the tetragonal and the orthorhombic crystalline phases.

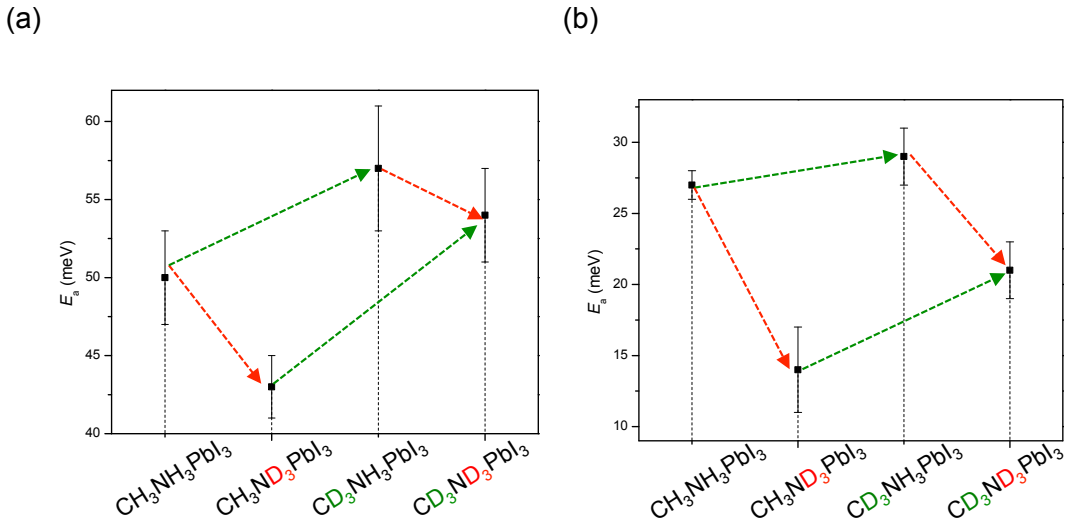

Fig. 5-11 Effect of deuteration on the activation energies. (a) In the tetragonal phase. (b) In the orthorhombic phase. The red arrows indicate the effect of ammonium group deuteration, the green arrows methyl group deuteration.

The difference between the effects of the methyl group and ammonium group deuteration thus rules out the possibility that dipole domain alignment or trap state filling are the underlying mechanisms for the intermediate relaxation process. This leaves us with proton migration, and we observed that the proton migration in $MAPbI_3$ shows an inverse isotope effect.

According to the previous discussion, this would indicate that the proton migration is coupled with the MA^+ ion rotation. One framework describing this coupling is the small polaron theory, which will be discussed in more detail in the next section. Here we note that due to this coupling, the inverse isotope effect of proton migration is actually higher than the values in Fig. 5-11, as the manifested inverse effect has already been slowed down by the slower MA^+ ion rotation.

5.3 Behavior of protons in $MAPbI_3$

The effect of proton migration has been a gap in the study in HOIPs. For inorganic perovskite oxides, the effect of proton migration has been studied since 1981 by placing perovskite oxides in hydrogen-containing,[21,22,23] or a humid atmosphere.[24,25] Supported by simulation results,[26,27] the general agreement of the microscopic mechanism in the literature is that the protons hop between neighboring oxygen atoms while forming transitional hydrogen bonds, a process involving the reorientation of the OH dipoles.[28] In HOIPs, the migration of protons has been considered theoretically by Egger *et al.*[29] using minimum energy path calculation. However, the direct observation of the migration is challenging,[30] possibly due to the instability of HOIPs under water or hydrogen containing atmosphere.

Insight into the proton migration behavior in HOIP can be obtained based the assignment of the intermediate relaxation to proton migration in the last section. With this premise, we attempt to answer some basic questions concerning the protons in $MAPbI_3$, specifically, their conduction properties, source and density, spatial distribution.

5.3.1 Conduction mechanism

The simulation studies by Egger *et al.*[29] suggested that protons might migrate in $MAPbI_3$ by forming transient hydrogen bonds with iodides, with a barrier to be as low as 0.17 eV. The authors also consented that if nuclear quantum effects such as tunneling are taken into consideration, protons may transfer even more quickly. Indeed, the quantum effect on proton conduction is a usual occurrence in the case of perovskite oxides,[31,32] or metals.[19,33] The possibility of Bourgoin–Corbett mechanism has also been conjectured, where the diffusion of protons is enhanced during illumination by capturing photogenerated electrons.

The presence of quantum tunneling effect can be inferred by examining the results of the experiments in section 5.1 and 5.2. In the discussion in section 5.2, we pointed out that the migration of protons is coupled to the MA^+ ion rotation. In the light of ref. 29, it is reasonable to picture this coupling as protons jumping between MA^+ ions and nearest iodides by forming transient hydrogen bonds. This hypothesis is consistent with the observation that the proton transition in the orthorhombic phase is faster than in the tetragonal phase (see Fig. 5-5). As the orientation of MA^+ ions is more or less random in the tetragonal phase (Fig. 5-12 (a)), but points toward the center of the parent cells in the orthorhombic phase (Fig. 5-12 (b)),[34] the

average distance between the ammonium groups and iodide is smaller in the lower temperature phase, causing the observed trend in transition rates.

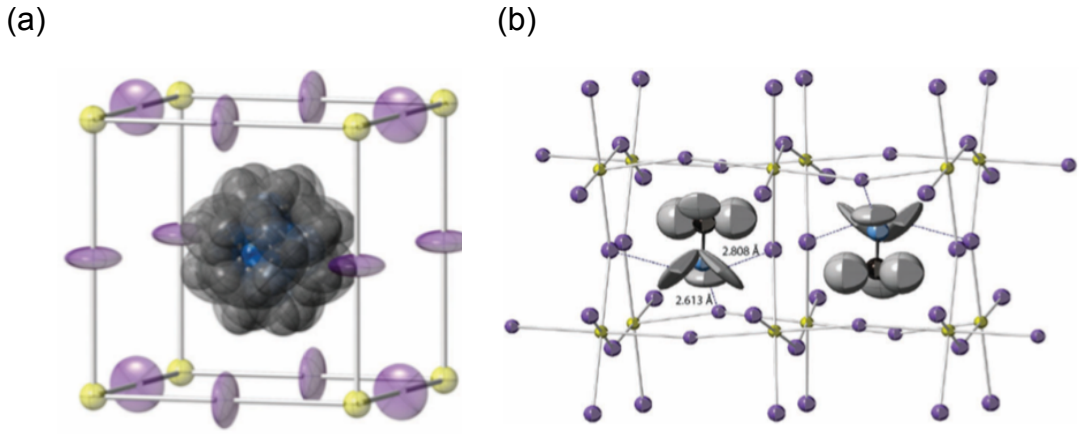

Fig. 5-12 Orientation of MA^+ ions in $MAPbI_3$ crystals. (a) In the tetragonal phase. (b) In the orthorhombic phase. Yellow spheres represent Pb^{2+}, and purple spheres represent I^-. Figures adapted with permission from ref. 34. Copyright 2015 Royal Society of Chemistry.

Proton movement is barely thermally activated, as the activation energies of the proton migration process and MA^+ ion rotation are quite similar (see section 5.1). Thus tunneling is likely to be the mechanism responsible for the H^+ motion. Tunneling is expected to be strongly dependent on distance and orientation and therefore sensitive to the rotation of the MA^+ ions.

The process of tunneling coupled with lattice motion is known as the small polaron theory for diffusion process, which has been developed to explain the diffusion of defects in metals.[‡19,35] According to this theory, the moving species distorts the surrounding lattice, causing its energy to be lower than that of the neighboring states, and the transit happens by tunneling when thermal fluctuation of the lattice makes the energies align. The whole process can be pictured in successive steps (Fig. 5-13): Initially, the migrating species is trapped in a potential well deeper than the neighbor site because it causes the distortion of the lattice (polaron formation, Fig. 5-13 (a)). Then, due to the thermal fluctuation of the lattices, at certain point the energy difference is eliminated (Fig. 5-13 (b)), which allows tunneling

‡ The polarons here are similar to electron/hole polarons discussed in Chapter 4, but different moving species, such as protons or hydrogen atoms, are considered.

between the states (Fig. 5-13 (c), (d)). Finally the lattice relaxes again back into a lower energy state (Fig. 5-13 (e)). In this thermally activated tunneling process, the activation energy is identical to the activation energy of lattice fluctuation. When the lattice fluctuation is coupled with the MA^+ ion rotation, this process fits neatly with the discussion of the proton migration above.

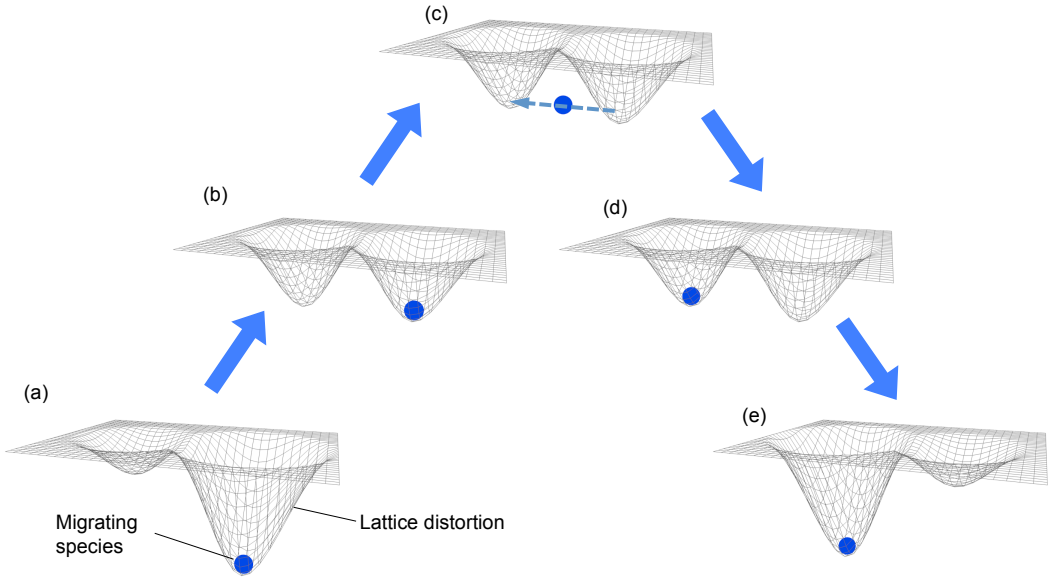

Fig. 5-13 Illustration of the small polaron theory for defect diffusion. (a) Initial state, where the migrating species is trapped in a low potential well due to the distortion of surrounding lattice. (b) Thermal fluctuation of the lattice, bringing the energy levels to align. (c) Tunneling of the moving species through the barrier to the equal energy neighboring state. (d) Potential profile right after tunneling. (e) Relaxation of the lattice into another low potential well. Figure adapted with permission from ref. 35. Copyright 1984 Elsevier.

Another merit of the small polaron theory is that it is consistent with the observed inverse isotope effect. For heavy isotopes, its smaller zero point energy results in smaller zero point motion, which, in the small polaron theory, would reduce the effect of lattice distortion.[36] The less distorted lattice means increased transition rates, hence the inverse isotope effect.

The microscopic jump frequency between neighboring sites is related to the macroscopic diffusivity by the Einstein–Smoluchowski relation:[37]

$$D = \frac{1}{6} L^2 \nu \,, \qquad \text{Eq. 5-1}$$

where D is the diffusivity, L is the distance between neighboring sites, and ν is the jump

frequency.

In the previous chapter, the diffusivity has been derived by equivalent circuit fitting with Warburg elements. For the intermediate relaxation, the fitting procedure is impractical as the peak is embedded in the electronic resistor–capacitor response. In this case, an estimate can still be made by relating relaxation time τ_0 to D according to:[38,39,40]

$$D = \frac{t_D^2}{\tau_0}, \qquad \text{Eq. 5-2}$$

where t_D is the thickness of the diffusion layer.

At room temperature, $\tau_0 = 1/2\pi f_0 \sim 1/2\pi(10^4\ \text{Hz}) = 1.6 \times 10^{-5}$ s. Assuming that the diffusion layer thickness is of the same order of magnitude of the film thickness, it follows that the proton diffusivity is $D \sim 10^{-5}$ cm^2/s. The value is 4–7 orders of magnitude higher than the diffusivity of I^- or MA^+ in $MAPbI_3$,[11,41] but comparable to that of protons of a typical proton conductor.[42,43]

To estimate the jump frequency from the diffusivity and Eq. 5-1, the jumping distance is assigned to be of the order of 10 Å, following the calculation in ref. 29. Therefore, the jump frequency of protons in $MAPbI_3$ between neighboring sites is found to be $\sim 10^{10}$ Hz, comparable to the proton tunneling rate in perovskite oxides.[44]

The fast migration of protons in HOIPs indicates that the protons can easily move to interfaces, where they might interact with the electrodes and/or environmental molecules, causing the degradation of the devices. Water induced deprotonation, as discussed earlier, would also be facilitated by the fast proton migration.[45]

So far, the discussions of proton conduction mechanism are limited to the interaction with the lattice. The possible effect of conduction band electrons is also of interest as they are abundant when HOIPs are under illumination, which is the operating state of solar cells. The effect of illumination on the intermediate relaxation is shown in Fig. 5-14. The relaxation frequency increased with illumination intensity, while the opposite trend was present for the peak height.

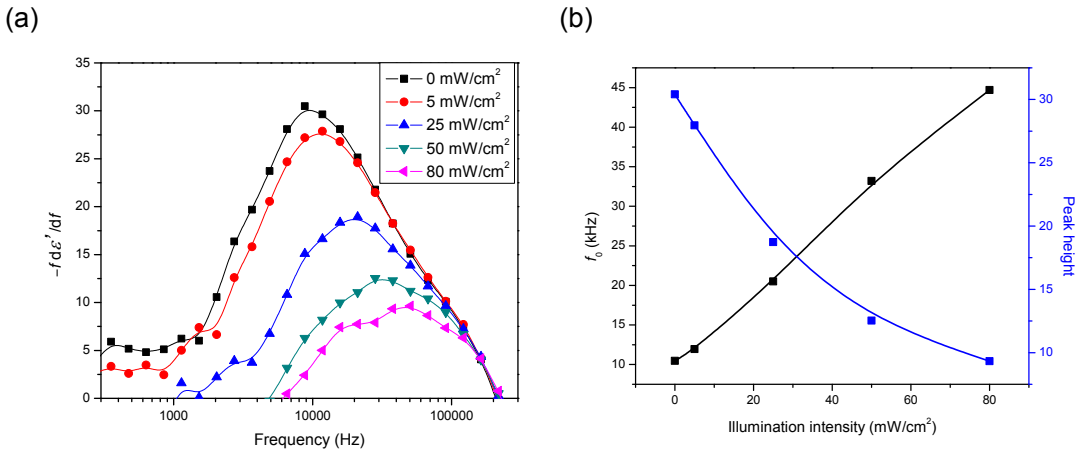

Fig. 5-14 Effect of illumination on the intermediate relaxation. (a) Relaxation peak from dark condition to an 80 mW/cm^2 illumination. (b) Dependence of the peak height and relaxation frequency on illumination intensity. Data from section 4.2 (Fig. 4-16).

The observed effects are consistent with the Bourgoin–Corbett mechanism,[29] according to which protons capture conduction band electrons, turning into hydrogen atoms. Therefore, under illumination, the number of protons is reduced, resulting in the observed smaller peak height. On the other hand, the reaction provides another pathway for proton migration, and according to ref. 29, this pathway has a lower barrier. This implies higher proton diffusivity, and it follows that the relaxation frequency increases with illumination.

The point is further supported by the temperature dependence of the intermediate relaxation under a ca. 25 mW/cm^2 illumination, shown in Fig. 5-15. The relaxation peak remained the same while the low frequency component (slow ion migration) increased significantly. In the Arrhenius plot, the relaxation frequency is shown to be temperature independent. The reduction of activation energy under illumination has been observed for slow moving ions in section 4.3, which is explained by structural change in the lattice. In the case of proton migration, the structural change effect and the Bourgoin–Corbett mechanism might combine together in the case of proton migration, resulting in its virtually zero thermal activation.

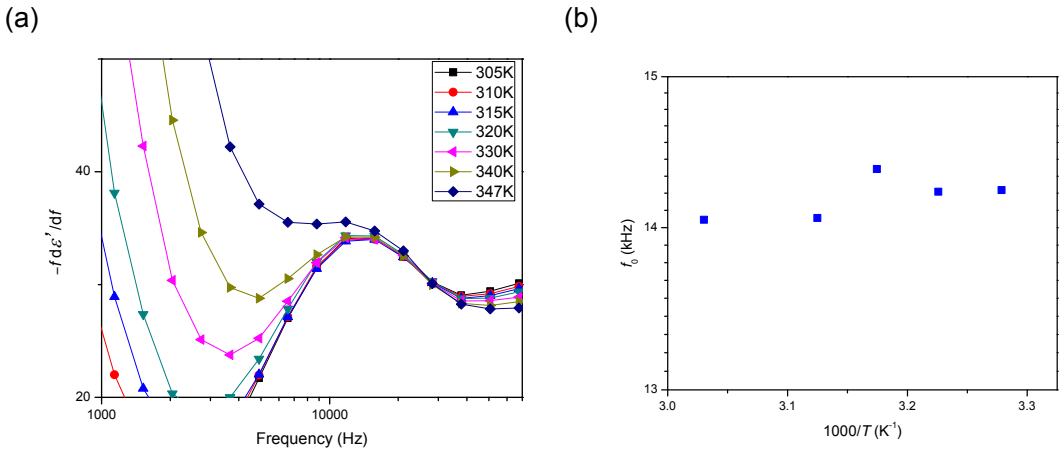

Fig. 5-15. Temperature dependence of the intermediate relaxation under illumination. (a) Relaxation peak from 305 K to 347 K. (b) Arrhenius plot of the relaxation frequency. Data from section 4.2 (Fig. 4-19). The illumination intensity was ca. 25 mW/cm^2.

5.3.2 Sources and location of protons

The proton conduction defects in $MAPbI_3$ might come from intrinsic or extrinsic sources, the former being caused by the dissociation of the ammonium groups in MA^+ ions, and the later from the environment. The observation of KIE indicates that the intrinsic source is more likely. Therefore, from the KIE experiments we can deduce that MA^+ ions dissociate in $MAPbI_3$. On the other hand, the extrinsic proton sources, such water-assisted deprotonation, as proposed by Forst *et al.*,[46] might still have an effect on proton migration. As this might be one of the mechanisms responsible for the degradation HOIP solar cells, further studies are necessary to clarify how the residual water affects the proton migration in HOIPs.

The amount of moving protons can be estimated from the nonlinear capacitance response with increasing bias voltage. For an ideal capacitor, the capacitance is independent of the applied dc voltage or the amplitude of the ac voltage. However, the amount of charges in a given system is limited, and when they are used up under high voltage, the capacitor becomes nonlinear. The number of charges can then be estimated from the decreased capacitance under a DC bias.

The intermediate relaxation peaks under applied bias from 0 V to 0.7 V are shown in Fig. 5-16 (a). The peak height reduced significantly in this voltage region, and the voltage where the peak would disappear completely was estimated to be 0.8 V (Fig. 5-16 (b)). With the

maximum peak height of 1.8 nF/mm^2, the maximum charge responding to the central frequency was found to be 1.4×10^{-9} C/mm^2 with a 200-nm device.

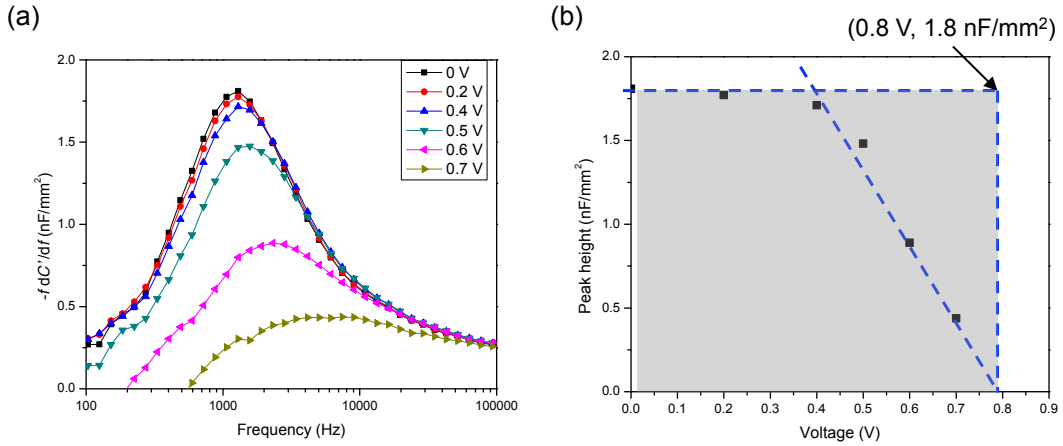

Fig. 5-16 Estimation of proton density from nonlinear capacitor behavior. (a) The intermediate relaxation peak under applied bias from 0 V to 0.7 V. (b) Peak height versus applied voltage. The maximum voltage obtained by linear extrapolating is 0.8 V, with capacitance of 1.8 nF/mm^2.

From the above value, the surface proton density can be estimated to be at the order of 10^{12} cm^{-2}. On the other hand, the surface density of MA^+ ions is at the order of 10^{13} cm^{-2}. Considering the inaccuracy of the proton density estimate, the 2 values are not far from each other. This leads us to suspect that the protons are accumulated near interfaces. Indeed, the general theory of ion/electrode interfaces suggests that ions are likely to accumulated near interfaces,[47] forming Helmholtz double layer and diffusion layer. This formation has been observed for the slow moving ions in $MAPbI_3$/Au interfaces.[48]

To confirm the hypothesis, the intermediate relaxation was measured on samples with different thickness. The dielectric spectra of various $MAPbI_3$ layer thickness are shown in Fig. 5-17 (a) and the normalized derivative of the capacitance in Fig. 5-17 (b). The characteristic frequency and the magnitude of the intermediate relaxation are independent of the film thickness, suggesting the ions accumulated near the interfaces.

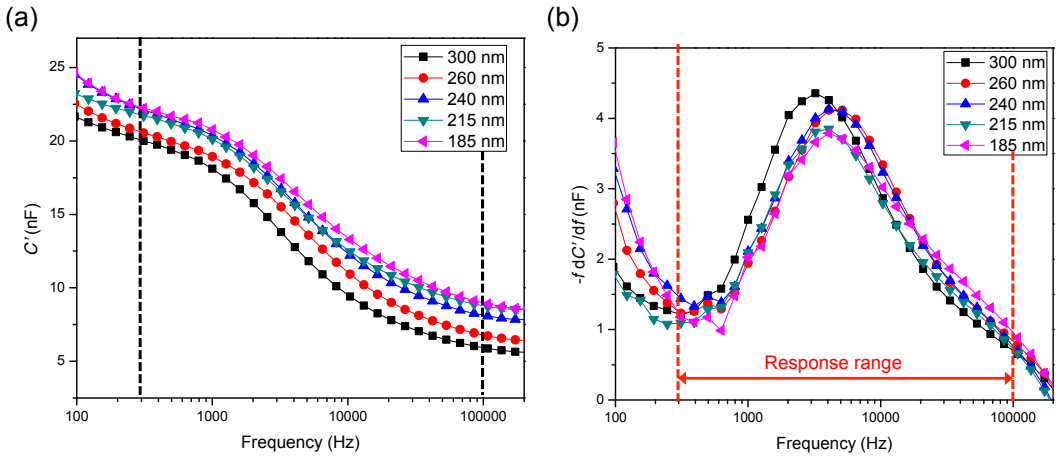

Fig. 5-17 (a) Capacitance spectra and (b) normalized derivative of capacitance of ITO/PEDOT:PSS/$MAPbI_3$/Au with active layer thickness from 300 nm to 185 nm.

The response range of the intermediate relaxation process can be determined from Fig. 5-17 (b) to be 3×10^2–10^5 Hz. On the high frequency end, the capacitance value is the sum of the response of the dielectric processes with high response rates. The capacitance value at the low frequency end is summed with the intermediate relaxation process under study. The plot of the capacitance at 10^5 Hz and the capacitance contributed by the intermediate relaxation, *i. e.*, $\Delta C' = C'(300\ \text{Hz}) - C'(10^5\ \text{Hz})$, are therefore plotted versus the layer thickness in Fig. 5-18 (a) and (b), respectively, to show the two components of the relaxation response.

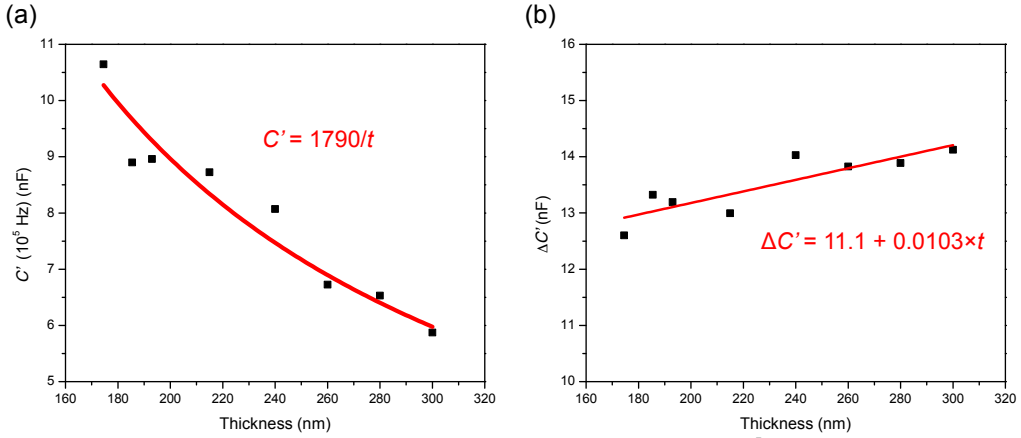

Fig. 5-18 Thickness dependence of the capacitance (a) at 10^5 Hz, and (b) difference between 300 Hz and 10^5 Hz, representing the contribution of the middle-frequency relaxation process.

The thickness dependence of high frequency capacitance fits approximately to a reciprocal function, which is consistent with the bulk related process with constant dielectric constant, *i. e.*,

$$C' = \varepsilon' \varepsilon_0 \frac{A}{t}, \qquad \text{Eq. 5-3}$$

where ε' is the real part of the permittivity, ε_0 is vacuum permittivity, A is the device area, and t is the thickness. With a fitted constant of 1790 nF nm and A = 4 mm^2, the relative permittivity ε' is calculated to be 50.9, in good agreement with the intrinsic permittivity of $MAPbI_3$, measured in section 4.1, and reported in the literature.[49]

The capacitance contribution of the intermediate relaxation (Fig. 5-18 (b)) is almost independent of the thickness, as linear fitting shows a slope of 0.01 nF/nm and an intercept of 11 nF. This supports the idea of interface ion accumulation, whose effect is in parallel to the intrinsic response of the material (Fig. 5-19).

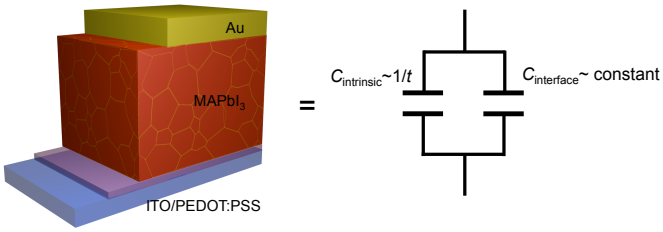

Fig. 5-19 The two components of the ITO/PEDOT:PSS/$MAPbI_3$/Au capacitor

We next attempt to locate which interface is responsible for this relaxation process by changing the sample structure and cross-referencing the interfaces. To do so, an insulating aluminum oxide layer is used to replace the contacts of $MAPbI_3$ layer (Fig. 5-20). In the following experiments, the Al_2O_3 layer was e-beam evaporated under ultra-high vacuum (~ 10^{-7} mbar). With a thickness of 45 nm, the layer showed good coverage of the ITO surface as evidenced by the high resistivity of the covered film.

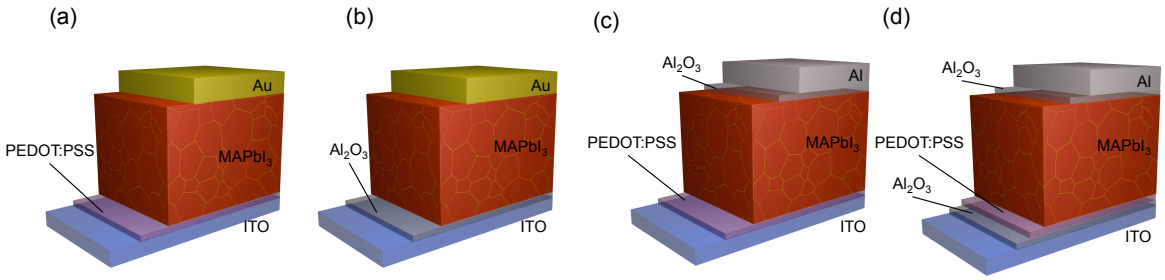

Fig. 5-20 Determining the interface for the mid-frequency relaxation by insulating layer. (a) Original device. (b) Bottom insulation. (c) Top insulation. (d) Insulation on both sides. The replacement of top electrode from gold to aluminum on the top insulation is chosen because aluminum is more strain compatible with the insulation layer aluminum oxide.

The possibility of involvement of ITO/Al_2O_3, Al_2O_3/Al, and $MAPbI_3/Al_2O_3$ interfaces is eliminated by the measurement of $ITO/Al_2O_3/Al$ and $ITO/Al_2O_3/MAPbI_3/Al_2O_3/Al$ devices (Fig. 5-21), which shows no response in this frequency region.

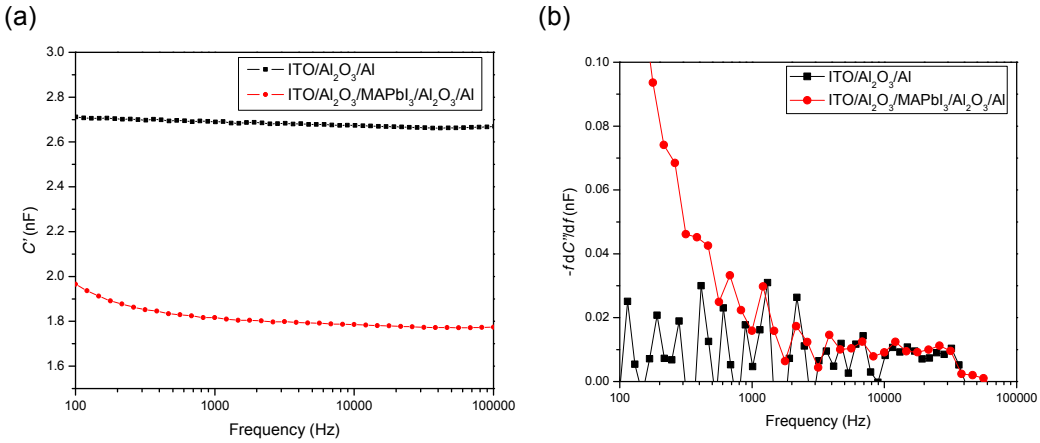

Fig. 5-21 (a) Capacitance spectra and (b) normalized derivative of ITO/Al_2O_3 (90 nm)/Al and ITO/Al_2O_3 (45 nm)/$MAPbI_3$ (280 nm)/Al_2O_3 (45 nm)/Al devices, showing no relaxation response near 10 kHz. The data of the $ITO/Al_2O_3/MAPbI_3/Al_2O_3$/Al device are taken from section 4.1.

The capacitance spectra of $ITO/Al_2O_3/MAPbI_3$/Au, $ITO/PEDOT:PSS/MAPbI_3/Al_2O_3$/Al, and ITO/Al_2O_3/PEDOT:PSS/$MAPbI_3/Al_2O_3$/Al devices were measured and are shown in Fig. 5-22. The relaxation peak is absent in the case of the $ITO/Al_2O_3/MAPbI_3$/Au device but present in the other 2 samples, though reduced in magnitude due to the series capacitor effect. Therefore, we conclude that protons accumulate near the $MAPbI_3$/PEDOT:PSS interface.

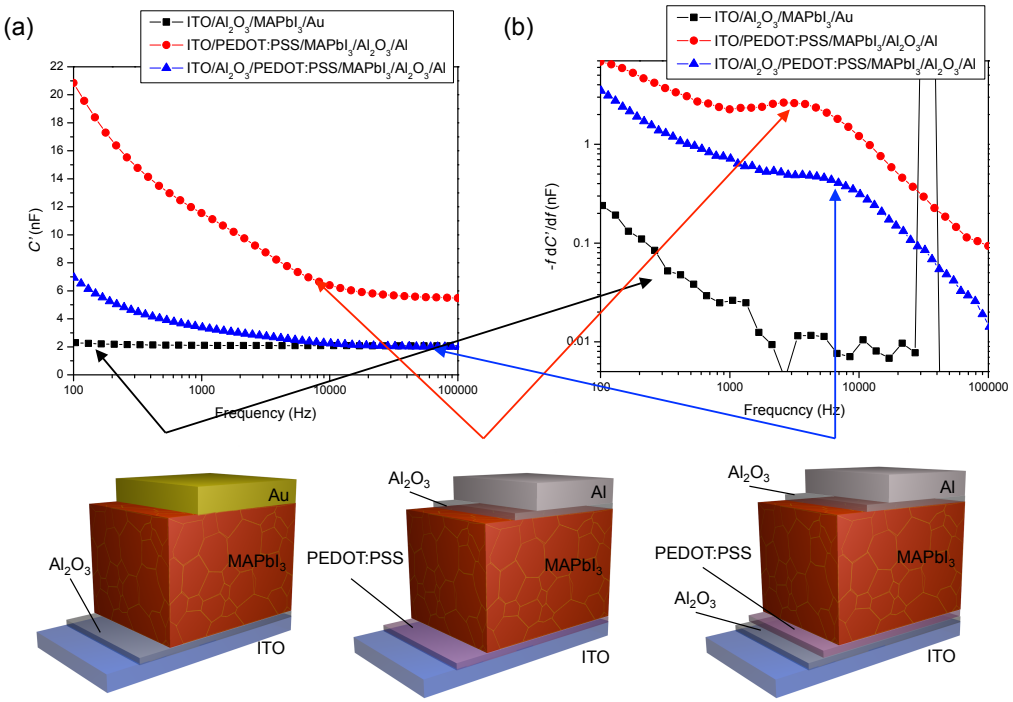

Fig. 5-22 (a) Capacitance spectra and (b) normalized derivative of ITO/Al_2O_3 (45 nm) /$MAPbI_3$ (280 nm)/Au (black) ITO/PEDOT:PSS/$MAPbI_3$ (200 nm)/Al_2O_3 (45 nm)/Al (blue), and ITO/Al_2O_3/PEDOT:PSS/$MAPbI_3$ (200 nm)/Al_2O_3 (45 nm)/Al (red) devices.

It is likely that the accumulated protons in $MAPbI_3$ exchange with the protons of the PEDOT:PSS layer, as PEDOT:PSS has been known to be ion conductor,[50] and the protons from the dissociation of the PSS acid were shown to diffuse into top layers.[51] In our frame work, it is possible to confirm this exchange by observing the intermediate relaxation on the deuterated PEDOT:PSS (PEDOT:dPSS). If the exchange occurs, similar inverse isotope effects should be observed as in the case of the ammonium group deuteration.

The dielectric measurements on deuterated PEDOT:PSS (PEDOT:dPSS) bottom electrode with $CH_3NH_3PbI_3$ and $CH_3ND_3PbI_3$ top layers are shown in Fig. 5-23. PEDOT:dPSS was obtained in similar way of the deuteration of the ammonium group: PEDOT:PSS (*Heraeus*, Clevios-PH) was dissolved in an excessive amount of D_2O and then dried at 60 ^oC (3 times). The resulting PEDOT:dPSS solution was then spin-coated onto ITO substrates for $MAPbI_3$ film preparation at 4000 rpm for 60 seconds.

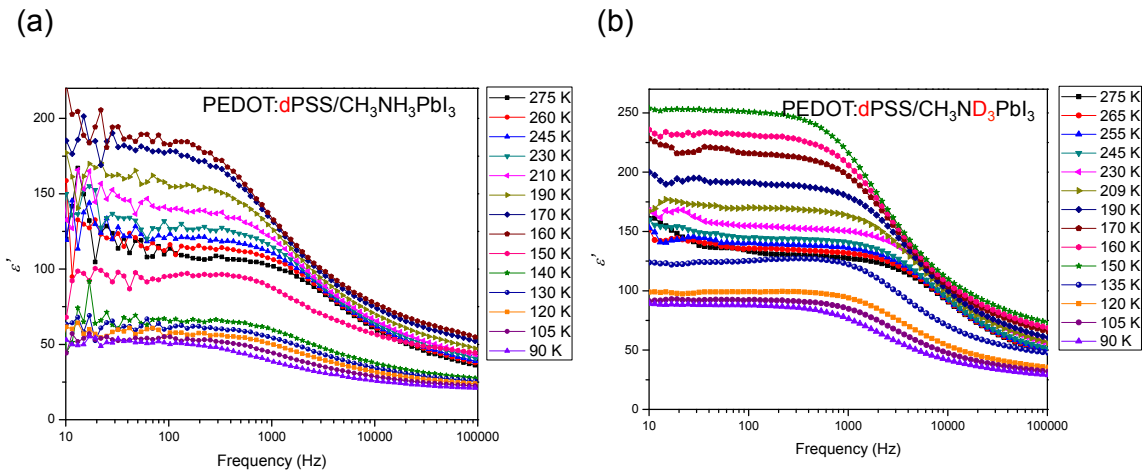

Fig. 5-23 KIE measurement with a deuterated PEDOT:PSS bottom electrode. The sample structures are: (a) ITO/PEDOT:dPSS/$CH_3NH_3PbI_3$ (200 nm)/Au, and (b) ITO/PEDOT:dPSS /$CH_3ND_3PbI_3$ (200 nm)/Au.

The temperature dependent relaxation frequencies of the PEDOT:dPSS experiments are shown in Fig. 5-24. The activation energy of PEDOT:dPSS/$CH_3NH_3PbI_3$ is higher than that of PEDOT:PSS/$CH_3NH_3PbI_3$, possibly due to the change in surface energy from the deuteration process of the PEDOT:PSS solution. However, in terms of the relaxation frequencies, the inverse isotope effect is observed in PEDOT:dPSS/$CH_3NH_3PbI_3$ under most of the temperatures , and the replacement of $CH_3NH_3PbI_3$ with $CH_3ND_3PbI_3$ further increases the effect. This result shows that the exchange of protons between the $MAPbI_3$ and the PEDOT:PSS layer is likely to happen.

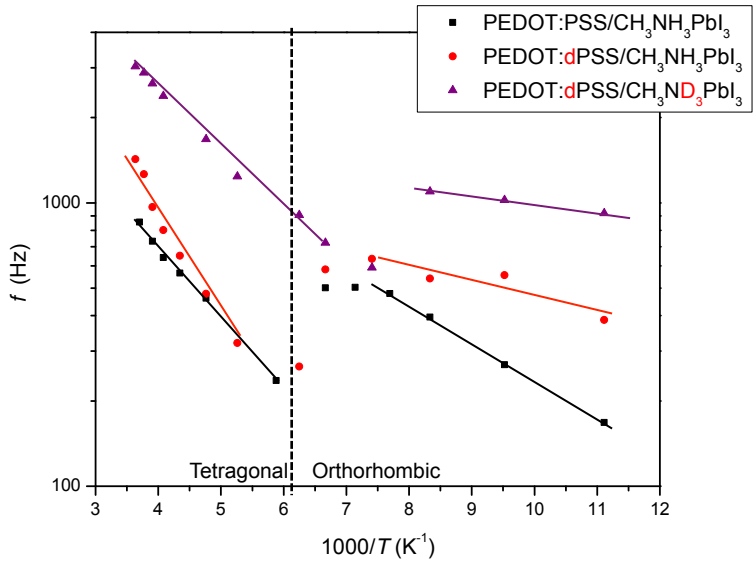

Fig. 5-24 Arrhenius plots of the relaxation frequencies of the $MAPbI_3$ on deuterated PEDOT:PSS. The data of non-deuterated $MAPbI_3$ on non-deuterated PEDOT:PSS from section 5.1 are included for comparison.

5.4 Conclusion

In this chapter, a demonstration and analysis of proton migration in $MAPbI_3$ was made. We argued that proton migration is responsible for the intermediate relaxation process in an ITO/PEDOT:PSS/$MAPbI_3$/Au device in agreement with kinetic isotope effect measurement. Following this assertion, the nature of the protons in $MAPbI_3$ was discussed. Specifically, the conduction mechanism was found to be consistent with the small polaron theory and the Bourgoin–Corbett mechanism. Other general properties of protons in $MAPbI_3$ were also deduced (Fig. 5-25), contributing to the general understanding of the $MAPbI_3$ material. The results should help to mend the gap in the study of the migrating protons in $MAPbI_3$.

The combination of dielectric measurement and an understanding of microscopic mechanisms of HOIP provides a unique opportunity to study a previously non observed effect. This line of investigation has the potential of providing insights into more advanced HOIP device structures and other materials.

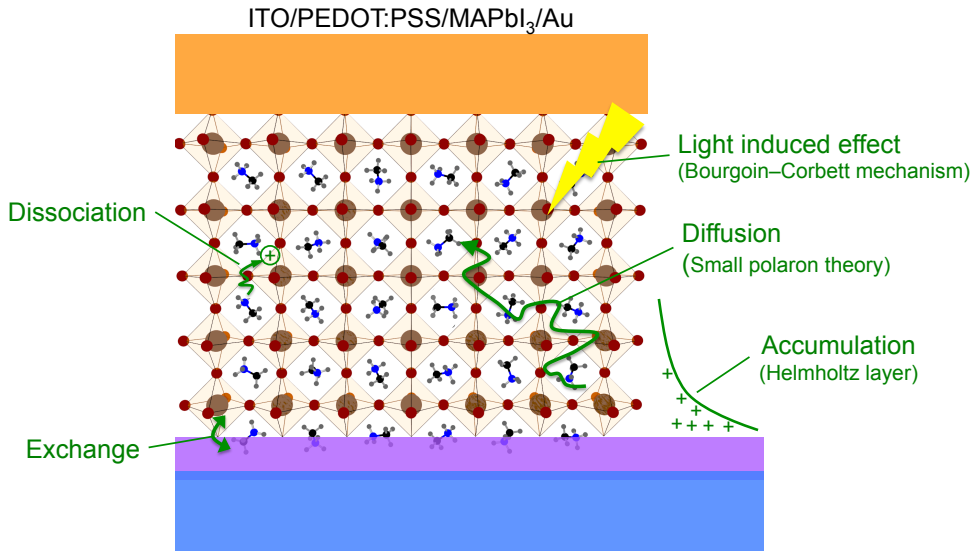

Fig. 5-25 Illustration of the proton-related processes in $MAPbI_3$ discussed in this chapter.

References

[1] Kremer, F., & Schonhals, A., *Broadband Dielectric Spectroscopy*, Springer, New York, 2003.

[2] Carr, J. A., Elshobaki, M. & Chaudhary, S. Deep defects and the attempt to escape frequency in organic photovoltaic materials. *Appl. Phys. Lett.* **107,** 203302 (2015). DOI: 10.1063/1.4936160

[3] Duan, H.-S. *et al.* The identification and characterization of defect states in hybrid organic–inorganic perovskite photovoltaics. *Phys. Chem. Chem. Phys.* **17,** 112 (2014). DOI: 10.1039/c4cp04479g

[4] Azpiroz, J. M., Mosconi, E., Bisquert, J. & De Angelis, F. Defect migration in methylammonium lead iodide and its role in perovskite solar cell operation. *Energy Environ. Sci.* **8,** 2118 (2015). DOI: 10.1039/c5ee01265a

[5] Haruyama, J., Sodeyama, K., Han, L. & Tateyama, Y. First-principles study of ion diffusion in perovskite solar cell sensitizers. *J. Am. Chem. Soc.* **137,** 10048 (2015). DOI: 10.1021/jacs.5b03615

[6] Eames, C. *et al.* Ionic transport in hybrid lead iodide perovskite solar cells. *Nat. Commun.* **6,** 7497 (2015). DOI: 10.1038/ncomms8497

[7] Leguy, A. M. A. *et al.* The dynamics of methylammonium ions in hybrid organic-inorganic perovskite solar cells. *Nat. Commun.* **6,** 7124 (2015). DOI: 10.1038/ncomms8124

[8] Chen, T. *et al.* Rotational dynamics of organic cations in the CH3NH3PbI3 perovskite. *Phys. Chem. Chem. Phys.* **17,** 31278 (2015). DOI: 10.1039/c5cp05348j

[9] Xu, Q. *et al.* Molecular motions and phase transitions in solid CH3NH3PbX3 (X = C1, Br, I) as Studied by NMR and NQR. Zeitschrift für Naturforschung A. **46,** 240 (1991). DOI: 10.1515/zna-1991-0305

[10] Bakulin, A. A. *et al.* Real-time observation of organic cation reorientation in methylammonium lead iodide perovskites. *J. Phys. Chem. Lett.* **6,** 3663 (2015). DOI: 10.1021/acs.jpclett.5b01555

[11] Frost, J. M. & Walsh, A. What is moving in hybrid halide perovskite solar cells? *Acc. Chem. Res.* **49,** 528 (2016). DOI: 10.1021/acs.accounts.5b00431

[12] Avrami, M. Kinetics of phase change. II Transformation-time relations for random distribution of nuclei. *J. Chem. Phys.* **8,** 212 (1940). DOI: 10.1063/1.1750631

[13] Jo, J. Y. *et al.* Domain switching kinetics in disordered ferroelectric thin films. *Phys. Rev. Lett.* **99,** 267602 (2007). DOI: 10.1103/PhysRevLett.99.267602

[14] Tagantsev, A., Stolichnov, I., Setter, N., Cross, J. & Tsukada, M. Non-Kolmogorov-Avrami switching kinetics in ferroelectric thin films. *Phys. Rev. B* **66,** 214109 (2002). DOI: 10.1103/PhysRevB.66.214109

[15] Walter, T., Herberholz, R., Müller, C. & Schock, H. W. Determination of defect distributions from admittance measurements and application to Cu(In,Ga)Se2 based heterojunctions. *J. Appl. Phys.* **80,** 4411 (1996). DOI: 10.1063/1.363401

[16] Burgelman, M. & Nollet, P. Admittance spectroscopy of thin film solar cells. *Solid State Ionics* **176,** 2171 (2005). DOI: 10.1016/j.ssi.2004.08.048

[17] Herberholz, R., Igalson, M. & Schock, H. W. Distinction between bulk and interface states in CuInSe[sub 2]/CdS/ZnO by space charge spectroscopy. *J. Appl. Phys.* **83,** 318 (1998). DOI: 10.1063/1.366686

[18] Scheiner, S. Calculation of isotope effects from first principles. *Biochim. Biophys. Acta - Bioenerg.* **1458,** 28 (2000). DOI: 10.1016/S0005-2728(00)00058-X
[19] Stoneham, A.M. Non-classical diffusion processes. J. Nuclear Mater. **69**, 109 (1978) DOI: 10.1016/0022-3115(78)90239-8
[20] Zhang, W. *et al.* Enhanced optoelectronic quality of perovskite thin films with hypophosphorous acid for planar heterojunction solar cells. *Nat. Commun.* **6,** 10030 (2015). DOI: 10.1038/ncomms10030
[21] Iwahara, H., Esaka, T., Uchida, H. & Maeda, N. Proton conduction in sintered oxides and its application to steam electrolysis for hydrogen production. *Solid State Ionics* **3,** 359 (1981). DOI: 10.1016/0167-2738(81)90113-2
[22] Cordero, F. *et al.* Hydrogen tunneling in the perovskite ionic conductor BaCe1-x Yx O3-δ. *Phys. Rev. B.* **78,** 054108 (2008). DOI: 10.1103/PhysRevB.78.054108
[23] Ishihara, T., *Perovskite Oxide for Solid Oxide Fuel Cells*, Springer, New York, 2009.
[24] Haile, S. M., West, D. L. & Campbell, J. The role of microstructure and processing on the proton conducting properties of gadolinium-doped barium cerate. *J. Mater. Res.* **13,** 1576 (1998). DOI: 10.1557/JMR.1998.0219
[25] Kreuer, K. D. Proton-conducting oxides. *Annu. Rev. Mater. Res.* **33,** 333 (2003). DOI: 10.1146/annurev.matsci.33.022802.091825
[26] Merinov, B. & Goddard, W. Proton diffusion pathways and rates in Y-doped BaZrO3 solid oxide electrolyte from quantum mechanics. *J. Chem. Phys.* **130,** 194707 (2009). DOI: 10.1063/1.3122984
[27] Islam, M. S., Davies, R. A & Gales, J. D. Proton migration and defect interactions in the CaZrO3 orthorhombic perovskite: A quantum mechanical study. *Chem. Mater.* **13,** 2049 (2001). DOI: 10.1021/cm010005a
[28] Yamazaki, Y. *et al.* Proton trapping in yttrium-doped barium zirconate. *Nat. Mater.* **12,** 647 (2013). DOI: 10.1038/NMAT3638
[29] Egger, D. A., Kronik, L. & Rappe, A. M. Theory of Hydrogen Migration in Organic-Inorganic Halide Perovskites. *Angew. Chemie - Int. Ed.* **54,** 12437 (2015). DOI: 10.1002/anie.201502544
[30] Yuan, Y. & Huang, J. Ion migration in organometal trihalide perovskite and its impact on photovoltaic efficiency and stability. *Acc. Chem. Res.* **49,** 286 (2016). DOI: 10.1021/acs.accounts.5b00420
[31] Matsushita, E. Tunneling mechanism on proton conduction in pervoskite oxides. *Solid State Ionics* **145,** 445 (2001). DOI: 10.1016/S0167-2738(01)00942-0
[32] Spahr, E. J. *et al.* Proton tunneling: A decay channel of the O-H stretch mode in KTaO3. *Phys. Rev. Lett.* **102,** 075506 (2009). DOI: 10.1103/PhysRevLett.102.075506
[33] Flynn, A. M. S. and C. P. On the quantum theory of isotope effects in the electromigration and thermomigration of light interstitials. *J. Phys. F Met. Phys.* **3,** 505 (1973).
[34] Weller, M. T., Weber, O. J., Henry, P. F., Di Pumpo, A. M. & Hansen, T. C. Complete structure and cation orientation in the perovskite photovoltaic methylammonium lead iodide between 100 and 352 K. *Chem. Commun.* **51,** 4180 (2015). DOI: 10.1039/c4cc09944c
[35] Hempelmann, R., Diffusion of hydrogen in metals, *J. Less Common Met.* **101**, 69 (1984).
[36] Stoneham, A. M. Theory of the diffusion of hydrogen in metals. *Berichte der Bunsengesellschaft für Phys. Chemie* **76,** 816 (1972). DOI: 10.1002/bbpc.19720760836

[37] Mehrer, H., A., "Random walk theory and atomic jump process." *Diffusion in Solids Fundamentals, Methods, Materials, Diffusion-Controlled Process* ,Springer series in solid stat-sciences, Springer, Verlag Berlin Heidelberg, 2007. 55–66.
[38] Yang, T. Y., Gregori, G., Pellet, N., Gratzel, M. & Maier, J. The significance of ion conduction in a hybrid organic-inorganic lead-iodide-based perovskite photosensitizer. *Angew. Chemie - Int. Ed.* **54,** 7905 (2015). DOI: 10.1002/anie.201500014
[39] Alexe-Ionescu, A. L., Barbero, G., Lelidis, I. & Scalerandi, M. Relaxation times of an electrolytic cell subject to an external electric field: Role of ambipolar and free diffusion phenomena. *J. Phys. Chem. B* **111,** 13287 (2007). DOI: 10.1021/jp0742160
[40] Bazant, M. Z., Thornton, K. & Ajdari, A. Diffuse-charge dynamics in electrochemical systems. *Phys. Rev. E* **70,** 21506 (2004). DOI: 10.1103/PhysRevE.70.021506
[41] Yuan, Y. *et al.* Photovoltaic switching mechanism in lateral structure hybrid perovskite solar cells. *Adv. Energy Mater.* **5,** 1500615 (2015). DOI: 10.1002/aenm.201500615
[42] Braun, A. *et al.* Proton diffusivity in the BaZr0.9Y0.1O3−δ proton conductor. *J. Appl. Electrochem.* **39,** 471 (2008). DOI: 10.1007/s10800-008-9667-3
[43] Chen, Q., Banyte, J., Zhang, X., Embs, J. P. & Braun, A. Proton diffusivity in spark plasma sintered BaCe0.8Y 0.2O3 - δ: In-situ combination of quasi-elastic neutron scattering and impedance spectroscopy. *Solid State Ionics* **252,** 2 (2013). DOI: 10.1016/j.ssi.2013.05.009
[44] Spahr, E. J. *et al.* Proton tunneling: A decay channel of the O-H stretch mode in KTaO3. *Phys. Rev. Lett.* **102,** 075506 (2009). DOI: 10.1103/PhysRevLett.102.075506
[45] Müller, C. *et al.* Water Infiltration in Methylammonium Lead Iodide Perovskite: Fast and Inconspicuous. *Chem. Mater.* **27,** 7835 (2015). DOI: 10.1021/acs.chemmater.5b03883
[46] Frost, J. M. et al. Atomistic origins of high-performance in hybrid halide perovskite solar cells. *Nano Lett.* **14**, 2584 (2014). DOI: 10.1021/nl500390f
[47] Bagotsky, V. S. *Fundamentals of Electrochemistry,* Wiley, Hoboken, 2005.
[48] Almora, O., Guerrero, A. & Garcia-Belmonte, G. Ionic charging by local imbalance at interfaces in hybrid lead halide perovskites. *Appl. Phys. Lett.* **108,** 0–4 (2016). DOI: 10.1063/1.4941033
[49] Onoda-Yamamuro, N., Matsuo, T. & Suga, H. Dielectric study of CH3NH3PbX3 (X = Cl, Br, I). *J. Phys. Chem. Solids* **53,** 935 (1992). DOI: 10.1016/0022-3697(92)90121-S
[50] Rivnay, J. *et al.* Structural control of mixed ionic and electronic transport in conducting polymers. *Nat. Commun.* **7,** 11287 (2016). DOI: 10.1038/ncomms11287
[51] Lee, J.-K. *et al.* Acid-diffusion behaviour in organic thin films and its effect on patterning. *J. Mater. Chem.* **19,** 2986 (2009). DOI: 10.1039/b817286b

Chapter 6

Conclusion and perspectives

6.1 Conclusion

The studies in this thesis began by testing various solution preparation procedures for polycrystalline $MAPbI_3$, the archetypal HOIP material, to identify a procedure that can reproducibly fabricate high quality films. The characterization of the films was then carried out by spectroscopic (UV–vis absorption, XRD, XPS, UPS), electrical (time-of-flight mobility measurement, Kelvin probe), and physical (AFM) techniques. The films were also shown to be useful in solar cell applications. With these films, the processes in the bulk/interface of $MAPbI_3$ perovskites were studied and their properties examined (Fig. 6- 1).

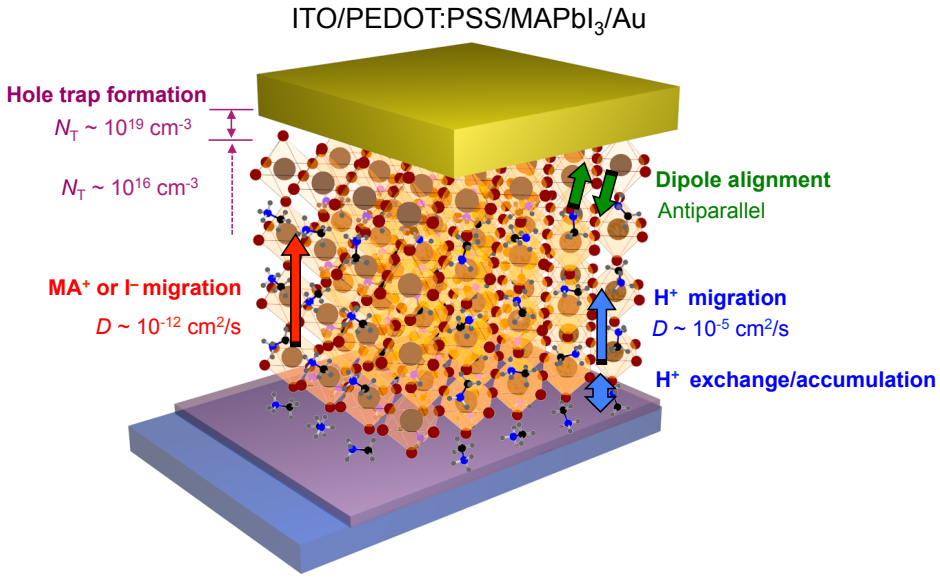

Fig. 6- 1 Summary of the properties of HOIPs studied in this thesis on the device structure of ITO/PEDOT:PSS/MAPbI3/Au, including: Hole trap formation and the bulk and interfaces (section 3.3), dipole alignment (sections 4.2), ion migration (section 4.3), and proton migration and exchange (chapter 5).

The charge transport mechanisms of $MAPbI_3$ were studied by experiment and simulation of the low temperature *J–V–L* characteristics of ITO/PEDOT:PSS/$MAPbI_3$/Au devices. It was found that the experimental data fits well with the model in which a band bending at the $MAPbI_3$/Au interface occurs. The origin of the band bending is argued to be hole traps, whose density and depth profile were calculated from model fitting.

To study the dielectric relaxation mechanisms in $MAPbI_3$, the impedance spectra of various

sample architectures were measured under variable temperature and illumination conditions. By fitting the experimental data to known physical models of relaxation mechanisms, those responsible for the dielectric response of $MAPbI_3$ film emerged, *i. e.*, cation rotation and ion migration. The orientation tendency of cations and the effect of temperature and illumination on ion migration in $MAPbI_3$ were then investigated.

Proton migration in HOIPs, which has been elusive so far, was then examined by impedance spectroscopy and kinetic isotope effect (KIE). By deuterating the methyl groups and/or ammonium groups of the MA^+ ions, KIEs were observed on the intermediate relaxation on the dielectric response of ITO/PEDOT:PSS/$MAPbI_3$/Au devices. After the analysis of the isotope effect on variable temperature experiments, the conclusion was reached that the effect of proton migration in $MAPbI_3$ is responsible for the intermediate relaxation process in ITO/PEDOT:PSS/$MAPbI_3$/Au devices. Further investigations showed that protons exchange between PEDOT:PSS and $MAPbI_3$. Based on the experimental data, characteristics of the migration behavior were deduced.

6.2 Perspectives

Further pursuing of the methods outlined in this thesis should be fruitful in the seemingly inexhaustible research field of hybrid organic-inorganic perovskites. One of the most desirable future directions would be to delve into a functional solar cell device. Specifically, the methods in chapter 3 and 4 provide a starting point for the study of the properties of the HOIP/oxide interface, which has been suggested to be related to the stability of HOIP solar cells.[1] Also, state-of-the-art HOIP solar cells in terms of efficiency are generally made by mixing formamidinium (FA) ions into methylammonium based HOIPs.[2,3] The effect of the mixing ions is likely to be elucidated by the dielectric studies similar to that in chapter 4 and 5, as the MA^+ and FA^+ present significant differences in rotations and proton dissociation.

It might also be interesting to use the characterization methods outlined in chapter 4 to study the effect of processing conditions. For example, the annealing temperature and duration have been shown to affect the grain sizes of $MAPbI_3$ and hence the device performances.[4] It is therefore worthwhile to investigate the origin of this effect with the procedures outlined in this thesis, e. g., how the grain size affects ion migration and dipole orientation. Another

instance would be to apply a magnetic field during the annealing process, which has been shown to affect crystal growth from solutions in other materials.[5,6] If the magnetic field also affects the crystal growth of HOIPs, this provides an opportunity to examine its effect on device performance and various processes. These studies are worthwhile in providing an opportunity to better understand the operation principles of HOIP devices.

References

[1] You, J. *et al.* Improved air stability of perovskite solar cells via solution-processed metal oxide transport layers. *Nat. Nano.* **11,** 75 (2016). DOI: 10.1038/NNANO.2015.230

[2] Yang, W. S. *et al.* High-performance photovoltaic perovskite layers fabricated through intramolecular exchange. *Science* **348,** 1234 (2015). DOI: 10.1126/science.aaa9272

[3] Seo, J., Noh, J. H. & Seok, S. Il. Rational strategies for efficient perovskite solar cells. *Acc. Chem. Res.* **49,** 562 (2016). DOI: 10.1021/acs.accounts.5b00444

[4] Ren, X. *et al.* Modulating crystal grain size and optoelectronic properties of perovskite films for solar cells by reaction temperature. *Nanoscale* **8,** 3816 (2016). DOI: 10.1039/C5NR08935B

[5] Wakayama, N. I. Effects of a Strong Magnetic Field on Protein Crystal Growth. *Cryst. Growth Des.* **3,** 17 (2003). DOI: 10.1021/cg025565g

[6] Higashitani, K., Kage, A., Katamura, S., Imai, K. & Hatade, S. Effects of a Magnetic Field on the Formation of CaCO3 Particles. *J. Colloid Interface Sci.* **156,** 90 (1993). DOI: 10.1006/jcis.1993.1085

Chapter 7

Appendix

7.1 Thin film stacking layer fabrication

7.1.1 Preparation of ITO/PEDOT:PSS bottom electrode

The HOIP films were prepared on PEDOT:PSS covered ITO, prepared according to the following: ITO-covered glasses were purchased from Kintec with 150-nm-thick indium tin oxide and a surface resistance ~15 Ω/sq. Before use, the ITO slides were cleaned with sonication in various solvents (acetone, ethanol alcohol, and isopropyl alcohol in sequence, 15 minutes each) and then underwent UV–ozone treatment for 15 minutes. The poly(3,4-ethylenedioxythiophene) polystyrene sulfonate (PEDOT:PSS, Fig. 7-1) was purchased from Heraeus (Clevios-PH) with conductivity 10–100 S/cm. After filtering thorough a RC 0.45 μm syringe filter, the PEDOT:PSS solution was spin-coated onto the ITO slides at 4000 rpm for 1 minute. The substrates were then put in a vacuum oven and dried at 110 ^{o}C for 1 hour. The resulting PEDOT:PSS film is about 50 nm in thickness. After cooling to room temperature, the substrates were transferred into a nitrogen-filled glove box for use.

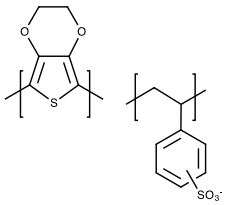

Fig. 7-1 Chemical structure of PEDOT:PSS

7.1.2 One-step method for solution-processed $MAPbI_3$ film preparation

The precursor solution for the HOIP perovskite material was made by mixing solution composed of 0.8 M of lead iodide (PbI_2, Sigma-Aldrich, 99.999%) and 0.8 M of methylammonium iodide (MAI, Sigma-Aldrich, 98%) in dimethylformamide (DMF, Sigma-Aldrich, anhydrous, 99.9%) or γ-butyrolactone (GBL, Sigma-Aldrich, >99.0%) and then stirred at 60 ^{o}C overnight. The solution is then filtered using a PVDF 0.45 syringe filter and spin-coated on ITO/PEDOT:PSS substrates at 6000 rpm for 30 seconds.

The absorption spectrum of the film after annealing at 100 ^{o}C for 15 minutes are shown in Fig. 7-2.

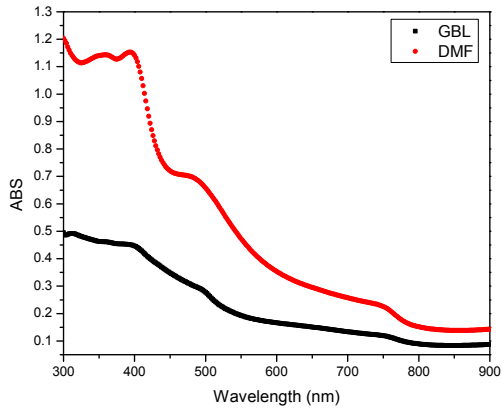

Fig. 7-2 Comparison of absorption spectra of the film prepared by the one-step method from 0.8 M GBL solution (black) and DMF solution (red).

Different spinning speeds were tested. The optical microscopy images and absorption spectra of films prepared using spin-coating speeds of 3000 rpm, 4000 rpm, and 6000 rpm from 0.8 M GBL solution are shown in Fig. 7-3.

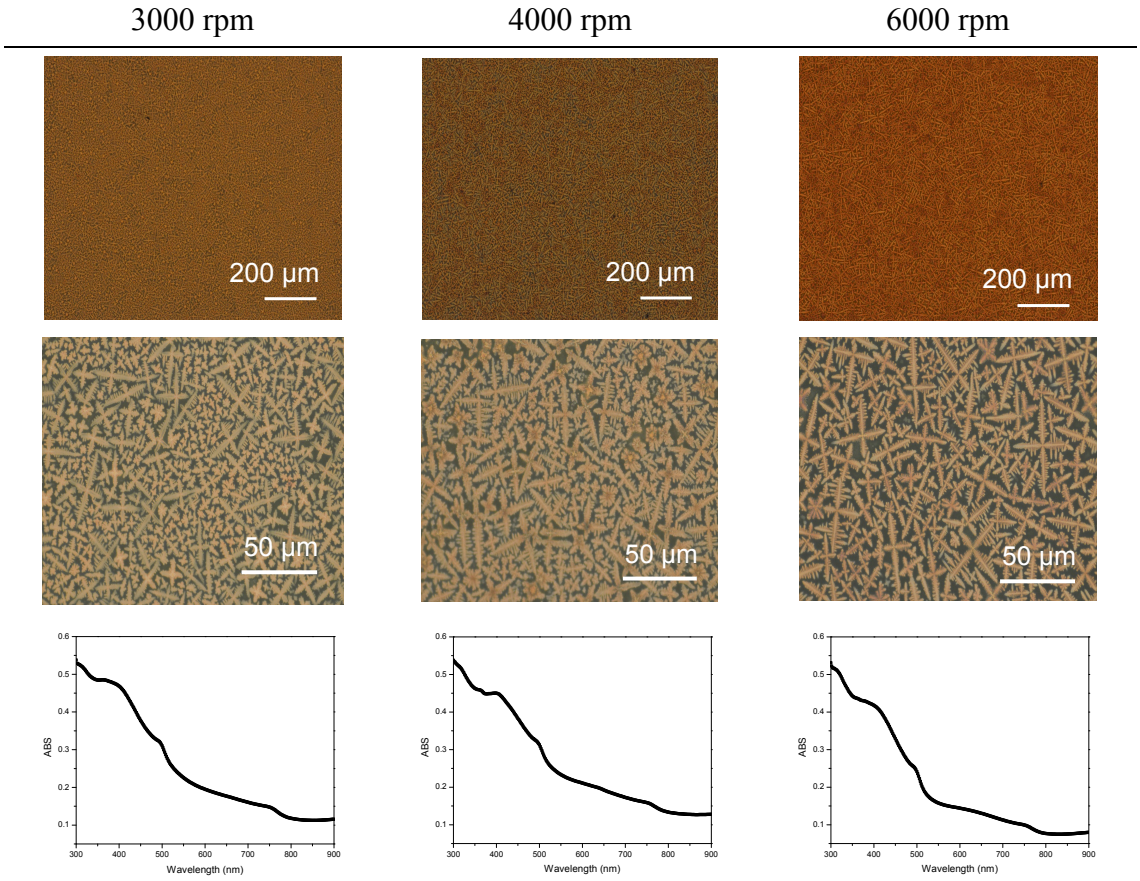

Fig. 7-3 Characterization of $MAPbI_3$ film prepared by mixed solution method. Optical microscopy images (first and second row) and absorption spectra (third row) of films

from 0.8 M GBL solution with different spin-coating speeds (3000 rpm, 4000 rpm, and 6000 rpm).

7.1.3 Dipping method for solution-processed $MAPbI_3$ film preparation

The source of the materials were the same as in 7.1.2. A 0.8 M PbI_2 solution in DMF was stirred overnight at 70 ^oC and then heated to 100 ^oC before use to maximize dissolution. The solution was then cooled down to room temperature and filtered thorough a PVDF 0.45 μm filter. The PbI_2 film was spin-coated at 6000 rpm for 90 seconds. Then, the film was placed on a hot plate at 70 ^oC for 30 minutes to dry. The formation of the HOIP film was achieved by dipping the PbI_2 film into a MAI solution in IPA (10 mg/mL) for 2.5 hours. The dark brown film obtained was rinsed in IPA and then dried at 70 ^oC for 30 minutes. The UV–vis absorption spectrum and the optical microscopy image of the film prepared with this procedure can be found in section 2.1 (Fig. 2-7).

7.1.4 Stacking layer method for solution-processed $MAPbI_3$ film preparation

Materials were from the same source as for the above procedures. A solution of 80 mg/mL PbI_2 in DMF was stirred overnight at 70 ^oC and then heated to 100 ^oC before use. After cooling down to room temperature, the solution was filtered through a PVDF 0.45 μm filter and then spin-coated on ITO/PEDOT:PSS substrates with spinning speed 5000 rpm for 30 seconds. After the film was dried at 100 ^oC for 30 minutes, a second layer was deposited using a 25 mg/mL MAI solution of IPA at 5000 rpm for 30 seconds. The inter-diffusion of the 2 materials was completed by annealing at 100 ^oC for 2 hours. In order to obtain the correct stoichiometry of the final film, different condition of the second layer were also tested (40 mg/ml MAI solution, 5000 rpm for 30 seconds). The optical microscopy images and AFM topographies of the film obtained are shown in Fig. 7-4.

PbI_2 film	MAI 25 mg/mL	MAI 40 mg/mL

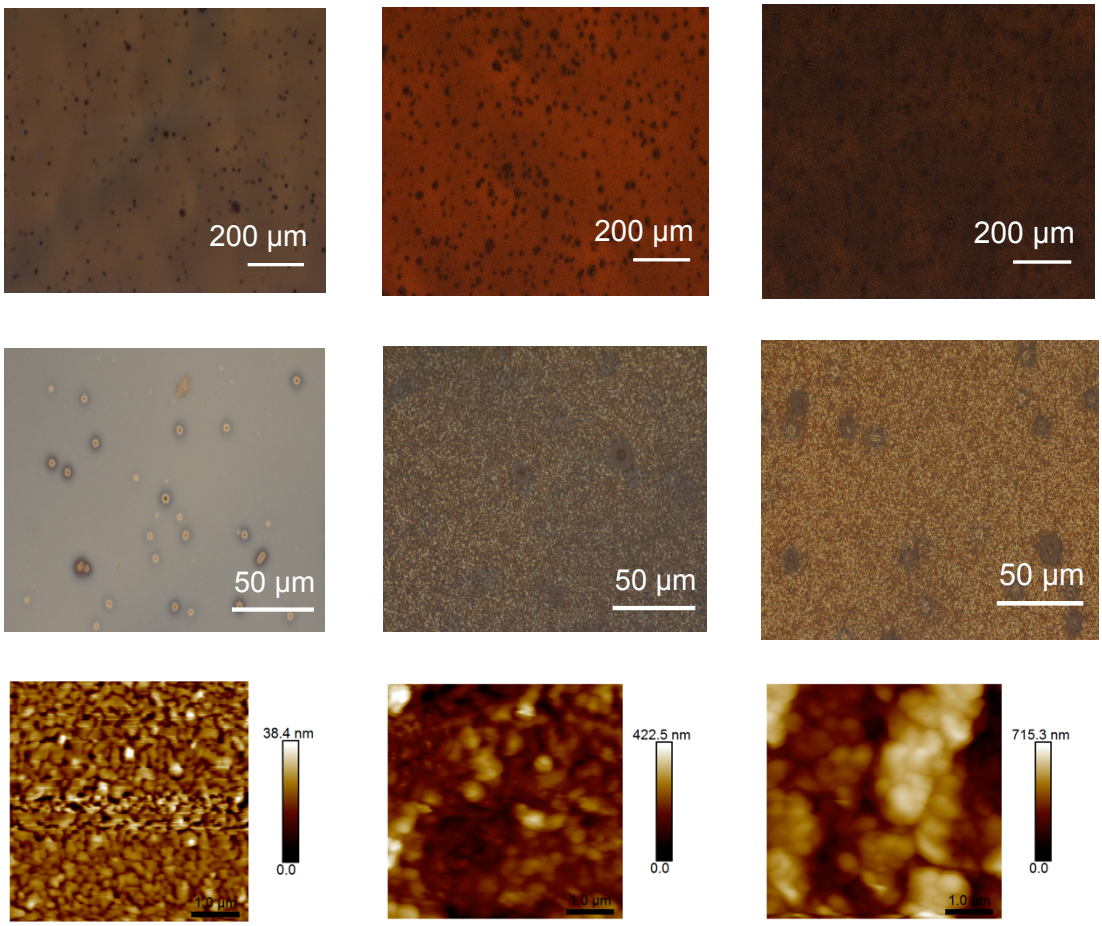

Fig. 7-4 Surface morphology of $MAPbI_3$ film prepared by the stacking layer method compared with spin-coated PbI_2 film. First and second row: optical microscopy images. Third row: AFM topography images.

7.1.5 Solvent engineering with orthogonal solvent washing

The source of PbI_2 , MAI, and GBL are the same as before. Dimethyl sulfoxide (DMSO) was purchased from Sigma-Aldrich (>99.9%). A 0.8 M PbI_2 and an MAI solution were prepared in a 7:3 volume ratio of GBL and DMSO, and stirred overnight at 50 ^{o}C before use. After cooling to room temperature, the solution was filtered through a PVDF 0.45 µm filter and then spin-coated onto ITO/PEDOT:PSS substrates at various speeds for 45 seconds. During the spin-coating, 20 µL of toluene (VWR international, >99.5%) was dropped on the substrate using a mirco pipette. The film was then annealed at 100 ^{o}C for 10 minutes.

Effort was put into optimizing the dropping timing at various spinning speed, as shown in Fig. 7-5.

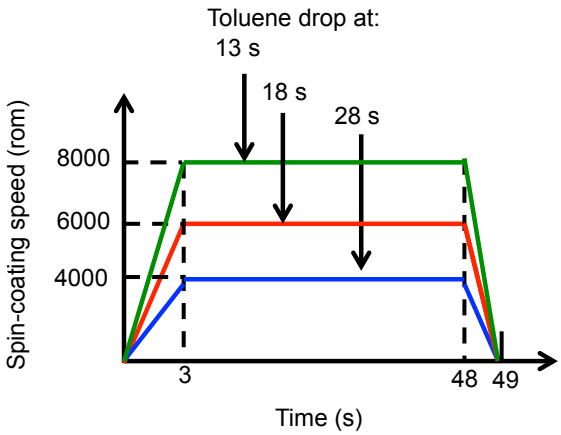

Fig. 7-5 The spin-coating speed profile and the optimal timing of toluene drop

The optimal film morphology is shown in Fig. 7-6 with various spinning speeds, which shows that smooth and compact film of $MAPBI_3$ perovskite is achieved using this method.

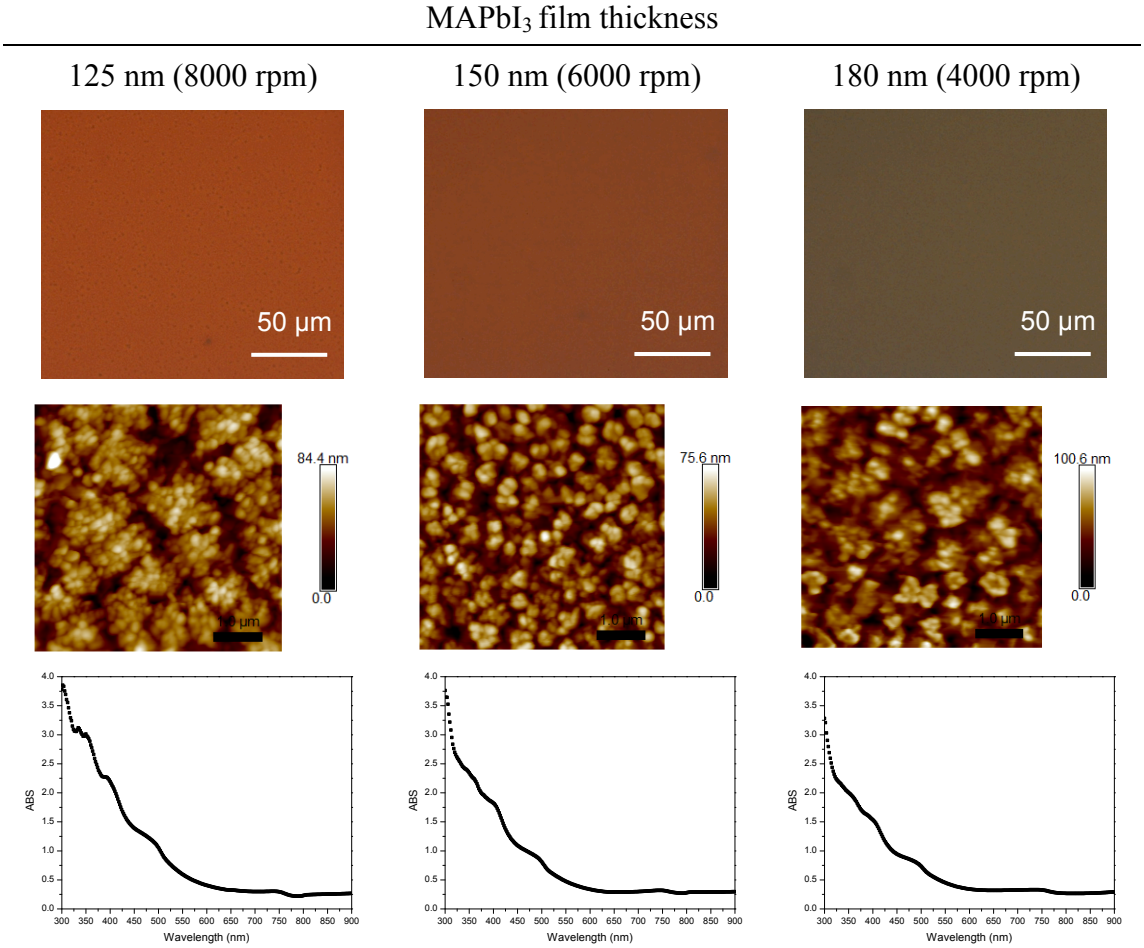

Fig. 7-6 Characterization of $MAPbI_3$ films prepared by the solvent engineering method. Optical microscopy images (first row), AFM topography images (second row) and absorption spectra (third row) of films of spin-coating speed 4000 rpm, 6000 rpm, and 8000 rpm.

To show the applicability of the method on surfaces other than ITO/PEDOT:PSS, we thermally evaporated molybdenum trioxide (MoO_3, 5 nm) and fullerene (C_{60}, 10 nm) under ultra high vacuum (deposition rate 0.5 Å/s and 0.1 Å/s, respectively). Then, the $MAPbI_3$ perovskite is deposited onto the surfaces according to the above procedure. The smoothness of the resulting films (Fig. 7-7) shows that this method can be used on different kinds of surfaces.

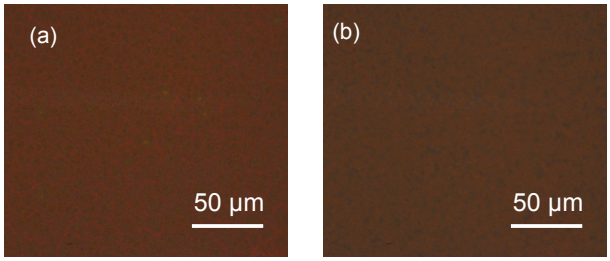

Fig. 7-7 Optical microscopy images of $MAPbI_3$ film on ITO/MoO_3 (a) and ITO/C_{60} (b). Showing the applicability of the solvent-engineering method on surfaces other than ITO/PEDOT:PSS.

7.1.6 Lead acetate as the MAPbI3 perovskite precursor for ultrasmooth film formation

A 40 wt % solution of lead acetate ($PbAc_2$, Sigma-Aldrich, 99.999%) and methylammonium iodide (MAI, Ossila, 98%) (1:3 molar ratio) were prepared in DMF (Sigma-Aldrich, anhydrous, 99.9%) and the solution was spin-coated onto ITO/PEDOT:PSS substrates at 2500 rpm for 120 seconds. The long spinning time ensured a good homogeneity of the film. After spin-coating, the film was transferred onto a 90 ^{o}C hot plate to be annealed for 25 minutes, during which the excess MA^+ and Ac^- ions were removed and the $MAPbI_3$ crystalized, as indicated by the darkening of the film. All procedures were performed in a nitrogen-filled glove box.

7.1.7 Direct solar cell preparation process

To prepare the low work function ITO/TiO_x electrode, a 0.05 M ethanol (99.8%, Sigma-Aldrich) solution of titanium (IV) isopropoxide (TIPT, Sigma-Aldrich, 99.999%) was mixed with 0.1 wt % hydrochloric acid (HCl, Sigma-Aldrich, 37%), while maintaining the

water-to-TIPT molar ratio to be 0.82 and a pH of 1.9.[1] After stirring for 72 hours, the solution was spin-coated onto ITO substrates (cleaned according to previous procedure) at 1000 rpm for 60 seconds in ambient condition. The film was then left in air for 2 hours and then annealed at 150 ^{o}C for 10 minutes in a glove box for the conversion of the precursors to TiO_x. The resulting TiO_x layer is 50 nm in thickness, as measured using a stylus profiler (KLA Tencor).

The ITO/TiO_x film was then treated with titanium tetrachloride ($TiCl_4$, Sigma-Aldrich, 99.9%) by immersing it into a 40 mM aqueous solution of $TiCl_4$ for 30 minutes at 70 ^{o}C. The film was then rinsed with deionized water and dried on a 110 ^{o}C hot plate for 15 minutes. This treatment has been shown to improve the adhesion properties and reduce charge recombination in dye-sensitized solar cells.[2,3] Applied to $MAPbI_3$ film formation, the treatment has a significant effect on the $MAPbI_3$ film morphology, substantially reducing the coarsening of the film (Fig. 7-8).

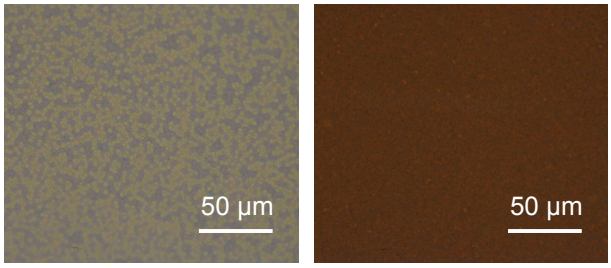

Fig. 7-8 The effect of $TiCl_4$ treatement on the formation of $MAPbI_3$ perovskite thin film on ITO/TiO_x. The optical microscopy image of the film on ITO/TiO_x with (right) and without (left) $TiCl_4$ treatment.

The TiO_x films were then used in a direct structure HOIP solar cell. Generally, the hole transport layer with best performances in this kind of device is 2,2′,7,7′-tetrakis-(N,N-di-p-methoxyphenylamine)9,9′-spirobifluorene (spiro-OMeTAD), whose chemical structure is shown in Fig. 7-9. To prepare the hole transport layer, a solution of 44.2 mg/mL of spiro-OMeTAD (Merck), 1.3% (by volume) 4-tert-butylpyridine (tBP,Sigma-Aldrich, 96%), and 0.6% (by volume) lithium bis(trifluoromethylsulfonyl)imide salt (Li-TSFI, Sigma-Aldrich) in chlorobenzene (Sigma-Aldrich, 99.8%) was stirred overnight before being spin-coated onto the above-mentioned ITO/TiO_x/$MAPbI_3$ layers at 2000 rpm for 45 seconds, resulting in a 30-nm-thick p-doped spiro-OMeTAD layer.[4,5] The device was then completed with thermally deposition of MoO_3 (5 nm) and a silver top electrode (100 nm) with deposition

rates of 0.1 Å/s and 0.5 Å/s, respectively. The active area, as defined by the opening of the metal deposition mask, was 8.6 mm^2.

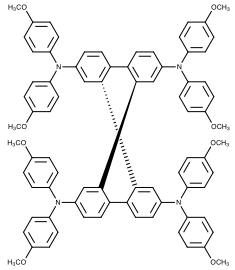

Fig. 7-9 Chemical structure of spiro-OMeTAD

7.1.8 Inverted solar cell preparation process

The ITO/PEDOT:PSS substrates were prepared according to the previously described procedure, after which $MAPbI_3$ perovskite was deposited onto the substrates by the method discussed in section 2.2.2. A 50-nm-thick phenyl-C61-butyric acid methyl ester ($PC_{61}BM$, Solvay) layer was then deposited on the $MAPbI_3$ perovskite layer by spin-coating (2500 rpm, 1 minute) from a 20 mg/ml solution in chlorobenzene (Sigma Aldrich, 99.8%), which had been stirred overnight at 50 ^oC. The device was then completed by thermally evaporating the top electrode (30 nm of calcium / 70 nm of aluminum) under a vacuum of ~10^{-6} mBar. The device area (8.6 mm^2) was defined by the opening of the metal deposition mask.

7.2 Characterization details

7.2.1 Atomic force microscopy

The AFM topography images shown in Chapter 1 were measured with a Veeco diInnova instrument in tapping mode. A heavily doped Si tip with a radius ~20 nm (RTESPA, Bruker, resonance frequency ~300 kHz) was used to probe the surface, and then the data were plotted and analyzed with the NanoScope Analysis software (Bruker). The surface roughness is estimated by the root-mean-square of the surface heights, RMS, according to:

$$\mathrm{RMS} = \sqrt{\frac{1}{N}\sum_{i=1}^{N}(Z_i - \bar{Z})^2}\,, \qquad \bar{Z} = \frac{1}{N}\sum_{i=1}^{N} Z_i\,, \qquad \text{Eq. 7- 1}$$

where N is the total number of points, Z_i is the height at point i.

7.2.2 Solar cell characterization

The light and dark current–voltage characteristics were carried out in a nitrogen-filled glove box using a Keithley 2400 source meter with a scanning rate ~0.2 V/s in both forward and backward direction. The light current was measured under AM 1.5G condition simulated by a HMI lamp, calibrated to 100 mW/cm^2 using a radiometer (IL 1400 BL).

The incident photon-to-current efficiency (IPCE) spectra were measured using a 450 W Xe-lamp as the light source and a monochromator (Triax 180, Horiba Jobin Yvon) to select incident wavelength. After calibrating the light source with a 6-inch integrating sphere (Labsphere) and a silicon photodiode, the current was measured ever 2 nm with an acquisition rate of 0.5 Hz using a Keithley 6487 picoammeter.

7.2.3 X-ray diffraction

The principle of X-ray diffraction is shown in Fig. 7-10. In this configuration, the thin-film sample was mounted at the center stage of a support where the X-ray source and the detector rotate in symmetry (a). During measurement, the source and detector move keeping the same angle on the circumference in order to measure the reflected X-ray. When the incident angle θ satisfies the Bragg condition:

$$2d \sin\theta = n\lambda\,, \qquad \text{Eq. 7- 2}$$

where d is the distance between the crystal planes (Fig. 7-10 (b)), λ is the X-ray wavelength, n is an integer, the constrictive interference between parallel incident beams causes the reflection to spike, as shown in a peak in the detector.

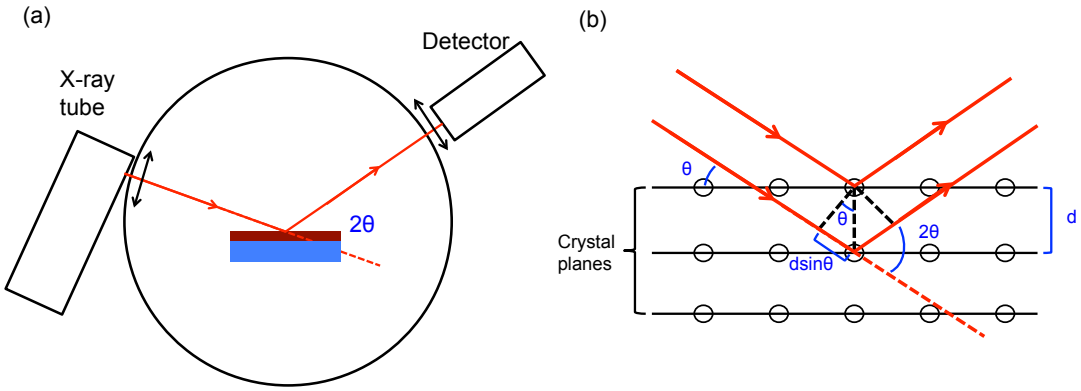

Fig. 7-10 Scheme of the operation principle of X-ray diffraction

At room temperature, $MAPbI_3$ perovskites process a tetragonal lattice structure,[6] whose 3 symmetric axes are orthogonal to each other with one pair of equal lattice constant ($a = b \neq c$). Therefore, the distance d between the lattice planes can be calculated according to:

$$\frac{1}{d^2} = \frac{h^2 + k^2}{a^2} + \frac{l^2}{c^2}, \qquad \text{Eq. 7- 3}$$

where a and c are the lattice constants, and the set of integers (h k l) is the Miller index of the crystal planes.[7]

The XRD patterns shown in section 2.2 were measured with a Philips PW 1730 diffractometer using Cu Kα radiation (wavelength 0.1542 nm).

7.2.4 Photoelectron spectroscopy

The X-ray photoelectron spectroscopy (XPS) and ultra-violet photoelectron spectroscopy (UPS) were performed at the *HEISY-ORG* (Heidelberg integrated system for organic materials) facilities. A monochromatized Al Kα (photon energy = 1486.6 eV) was used as the excitation source in XPS. In UPS, a gas discharge lamp operated with helium to achieve HeI emission (energy 21.22 eV) was the excitation source. A small bias was applied to the sample when recording the secondary electron cutoff. A Phi VersaProbe II spectrometer was used as the photoelectron energy analyzer, with Gaussian broadening of 0.35 eV and 0.13 eV for XPS and UPS, respectively.

7.2.5 Electroluminescence measurement

The current–voltage–luminance characteristics were measured using a Keithley 4200 source meter and the electroluminescence (EL) intensity was monitored using a silicon photodetector (Hamamatsu S2281-01, area 100 mm^2, with a Hamamatsu C9329 preamplifier). For electroluminescence spectra, an optical fiber connected to a spectrometer (Ocean optics HR4000) was posited near the sample surface to record the emitted light during a constant applied bias (typically 1 V) with integration time 60 seconds.

7.2.6 Kelvin probe measurements

The contact potential difference (CPD) was measured using the Kelvin probe technique, where a vibrating gold grid reference electrode (Kelvin probe S, Bescoke Delta Phi, diameter 2.5 mm) is brought close to the grounded sample surface (distance typically < 1 mm). With the difference in work function between the reference electrode and the sample, a capacitive current I is generated according to:

$$I = \frac{\mathrm{d}}{\mathrm{d}t}(CV) = V\frac{\mathrm{d}C}{\mathrm{d}t}, \qquad \text{Eq. 7- 4}$$

where C is the capacitance between the reference electrode and the sample, V is the potential difference. The capacitive current would be canceled when applying a dc bias $V_{dc} = -V_{CPD}$.

The dc bias is controlled using a feedback circuit (Kelvin control S, Bescoke Delta Phi) to minimize capacitive current. Before measurement, calibration is carried out on a freshly peeled highly ordered pyrolytic graphic (HOPG, Veeco, APCS-0200) surface, which has minimum surface contamination and a well-defined work function of 4.6 eV. All measurements were performed under ambient condition.

7.3 Preparation and characterization of deuterated $MAPbI_3$ polycrystalline layers

The deuteration of the ammonium group was carried out by dissolving MAI (Ossila, 99.5%) into deuterium oxide (D_2O, Sigma-Aldrich, 99.9%) with 1:40 molar ratio and then dried at 60 ^oC. The weak acid nature of the ammonium group of $CH_3NH_3^+$ allows the exchange of protons with deuterons from D_2O. The process was then repeated 3 times to ensure complete

substitution of hydrogen into deuterium.

CD_3NH_3I was synthesized by dissolving methyl-d3-amine (CD_3NH_2, Sigma-Aldrich, 99.9%) in a 2 M NaOH (Sigma-Aldrich, >98%)solution to liberate CD_3NH_2 as a gas. The latter was bobbled through a 57 wt % hydriodic acid (Sigma-Aldrich) in a stirred flask immersed in ice bath. After the reaction, the solvent was dried at 60 ^oC and the residuals were recrystallized from ethanol followed by washing with ethyl ether. Part of the material was then subjected to the process of ammonium group deuteration described in the previous paragraph to form CD_3ND_3I. Before use, all materials were put in a 70 ^oC vacuum oven overnight to remove residual water. The chemical formula of the resulting MA^+ ions is shown in Fig. 7-11.

Fig. 7-11 Formula of isotopic MA^+ ions used in this study

To confirm the complete replacement of hydrogen to deuterium, nuclear magnetic resonance (NMR) measurement was carried out on the isotopic methylammonium iodide. The H^1 spectra are shown in Fig. 7-12 (a), where the peaks corresponding to the C-H and N-H bond disappeared with their deuteration. On the other hand, the C–D and N–D signal on the H^2 spectra (Fig. 7-12 (b)) appeared with the corresponding deuteration of functional groups.

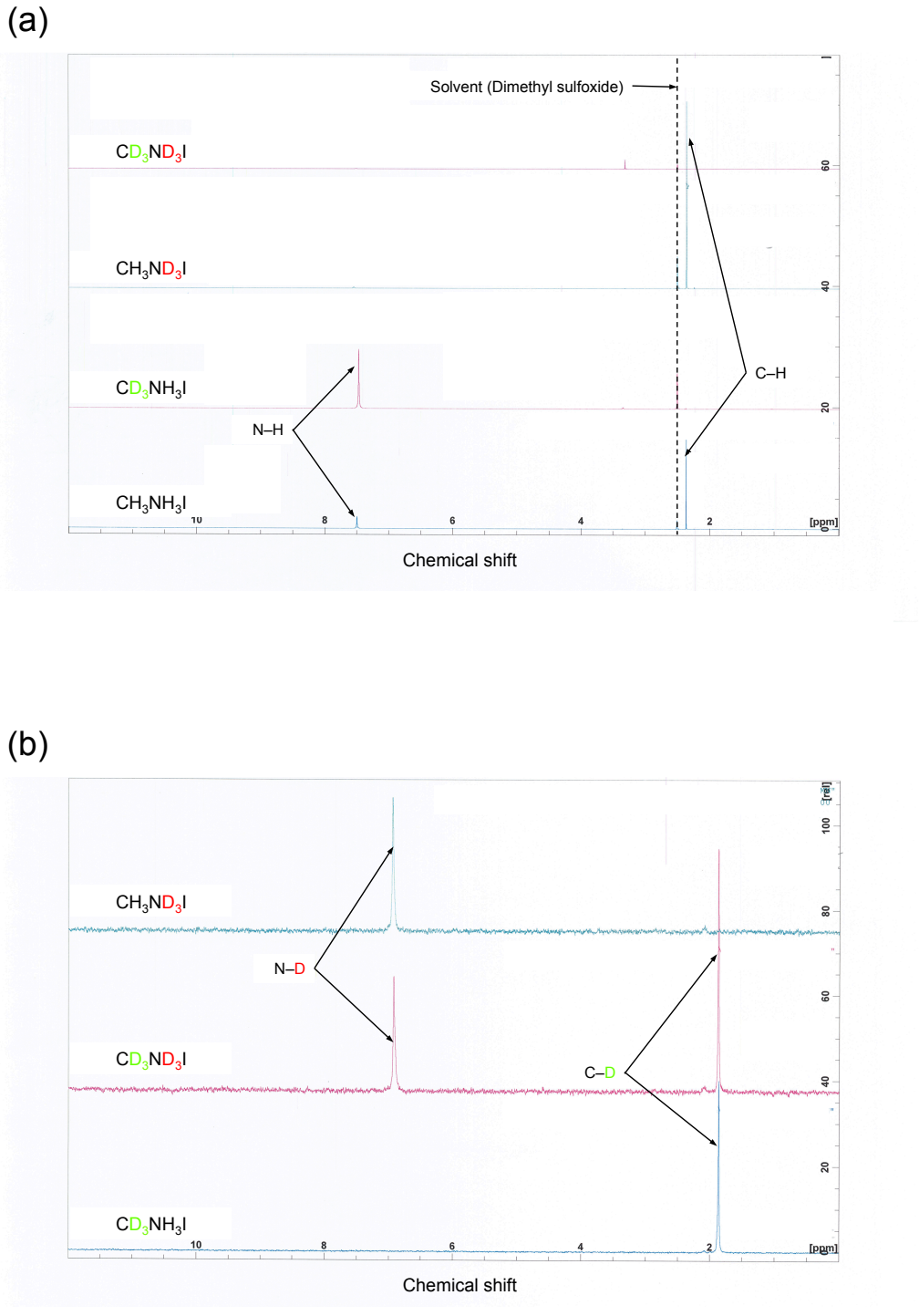

Fig. 7-12 Confirmation of H/D replacement in MAI by NMR measurement. (a) H^1 NMR of CD_3ND_3I, CH_3ND_3I, CD_3NH_3I, and CH_3NH_3I in dimethyl sulfoxide. The peaks corresponding to C–H and N–H have chemical shifts of ~2.4 ppm, and ~7.5 ppm, respectively. (b) H^2 NMR of CH_3ND_3I, CD_3ND_3I, and CD_3NH_3I in dimethyl sulfoxide. The peaks corresponding to C–D and N–D have chemical shifts ~1.8 ppm

and ~7.0 ppm, respectively.

The 3 deuterated MAI (CH_3ND_3I, CD_3NH_3I, and CD_3ND_3I) were then used as the precursor of $MAPbI_3$ polycrystalline film, prepared according to the procedure in 2.2.2. The images of the resulting films are shown in Fig. 7-13. In each case, mirror like surfaces were obtained, indicating the smoothness of the film.

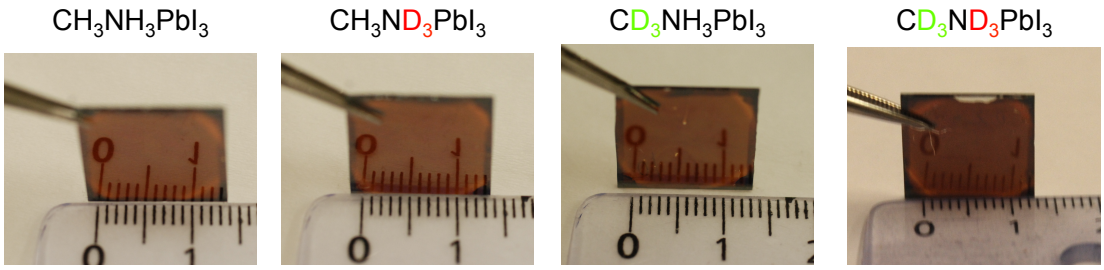

Fig. 7-13 Images of isotopic polycrystalline $MAPbI_3$ film. The mirror-like surfaces demonstrate the smoothness of the films.

To ensure the quality of the film, UV–vis absorption, electroluminescence, and X-ray diffraction spectra were measured (Fig. 7-14) with the reference data from the non-deuterated $MAPbI_3$ film. All the spectra of the deuterated $MAPbI_3$ were consistent with the formation of high quality $MAPbI_3$ films. Besides, no spectral changes were observed, confirming that the structural and electronic properties are not affected by deuteration.

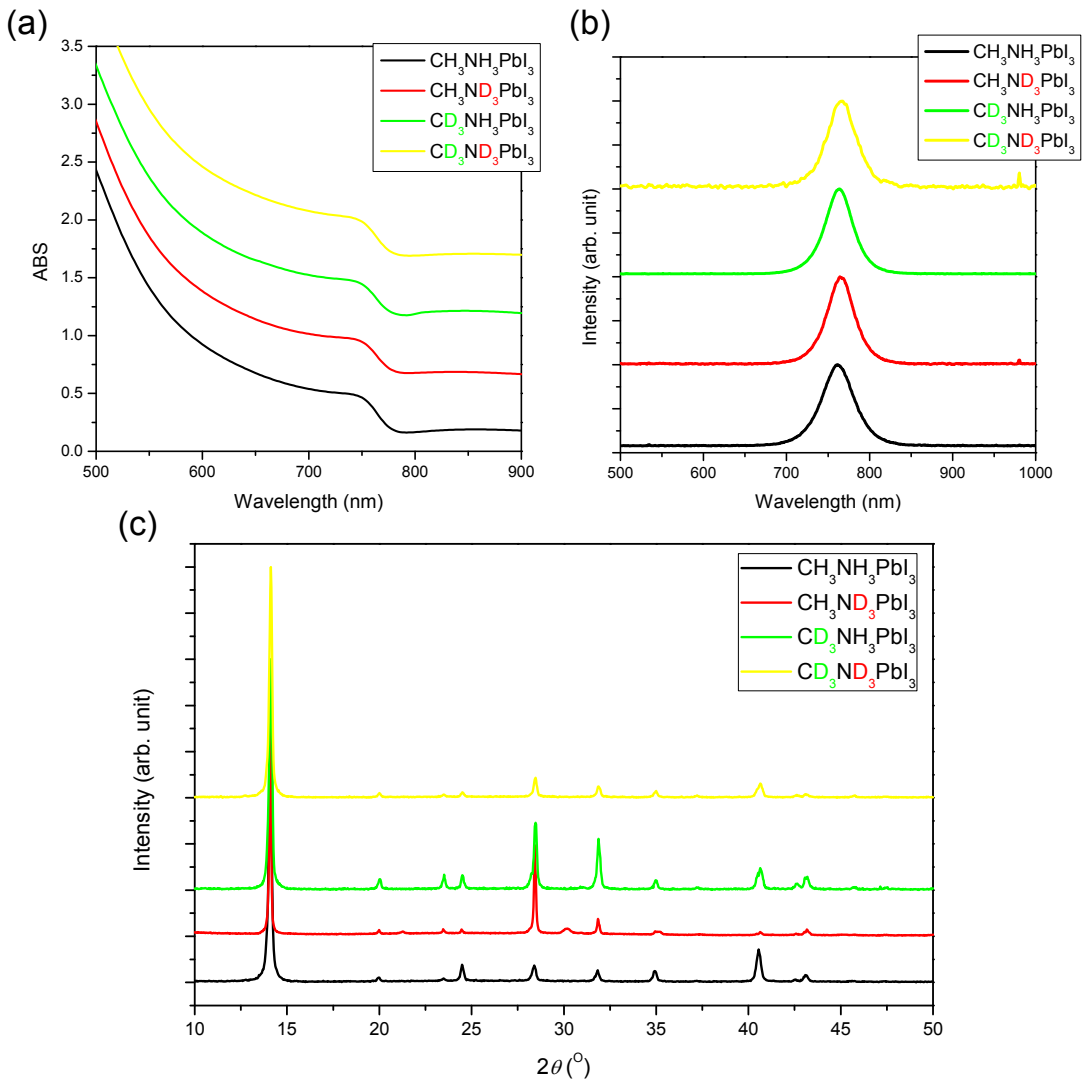

Fig. 7-14 (a) UV–vis absorption, (b) electroluminescence, and (c) X-ray diffraction spectra of deuterated and non-deuterated $MAPbI_3$ films. The data were shifted vertically for easier comparison. The electroluminescence spectra were measured with ITO/PEDOT:PSS/$MAPbI_3$ (200 nm)/$PC_{61}BM$ (50 nm)/Ca/Al devices. The details of electroluminescence and X-ray diffraction measurements can be found in Appendix 7.2.5 and 7.2.3, respectively.

Further confirmation of the quality of the film was carried out by measuring their solar cell characteristics. Inverted solar cells (ITO/PEDOT:PSS/$MAPbI_3$ (200 nm)/$PC_{61}BM$ (50 nm)/Ca/Al) were constructed with the different deuterated $MAPbI_3$ layers, and the current–voltage characteristics under dark and AM 1.5G illumination conditions are shown in Fig. 7-15. In each case, photoconversion efficiency over 12 % was obtained, while some differences with the standard cell were nonetheless present. The point here is that in all deuterated samples, films with high enough quality for acceptable solar cell operation were obtained.

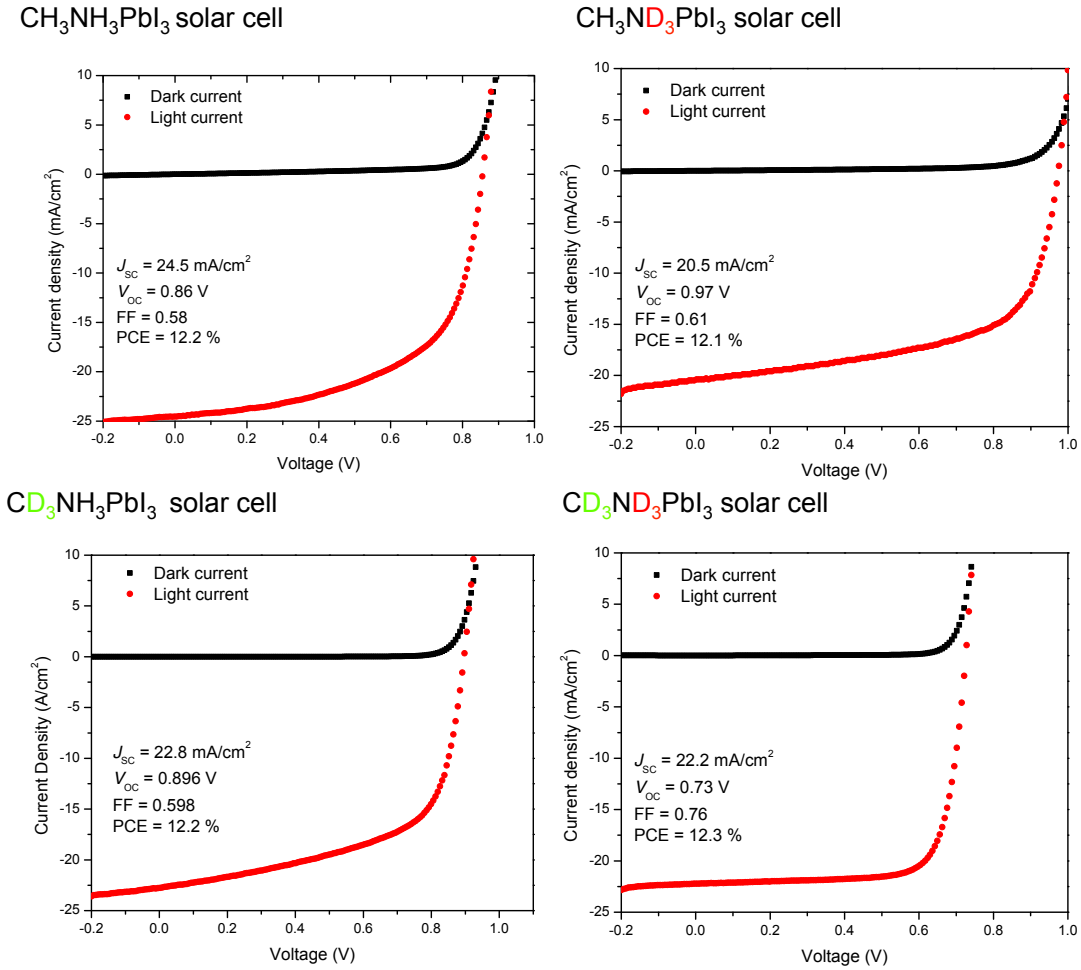

Fig. 7-15 Inverted solar cell characteristics of deuterated/non-deuterated $MAPbI_3$ with sample structure of ITO/PEDOT:PSS/$MAPbI_3$ (200 nm)/$PC_{61}BM$/Ca/Al.

References

[1] Burgos, M. & Langlet, M. Condensation and densification mechanism of sol-gel TiO2 layers at low temperature. *J. Sol-Gel Sci. Technol.* **16,** 267 (1999).
[2] Sommeling, P. M. *et al.* Influence of a TiCl4 post-treatment on nanocrystalline TiO2 films in dye-sensitized solar cells. *J. Phys. Chem. B* **110,** 19191 (2006). DOI: /;.10.1021/jp061346k
[3] Massin, J. *et al.* Molecular engineering of carbazole-fluorene sensitizers for high open-circuit voltage DSSCs: Synthesis and performance comparison with iodine and cobalt electrolytes. *Dye. Pigment.* **118,** 76 (2015). DOI: 10.1016/j.dyepig.2015.02.020
[4] Bui, T.-T. *et al.* Di(p-methoxyphenyl)amine end-capped tri(p-thiophenylphenyl)amine based molecular glasses as hole transporting materials for solid-state dye-sensitized solar cells. *RSC Adv.* **5,** 49590 (2015). DOI: 10.1039/c5ra07226c
[5] Lee, M. M., Teuscher, J., Miyasaka, T., Murakami, T. N. & Snaith, H. J. Efficient hybrid solar cells based on meso-superstructured organometal halide perovskites. *Science* **338,** 643 (2012). DOI:10.1126/science.1228604
[6] Weller, M. T., Weber, O. J., Henry, P. F., Di Pumpo, A. M. & Hansen, T. C. Complete structure and cation orientation in the perovskite photovoltaic methylammonium lead iodide between 100 and 352 K. *Chem. Commun.* **51,** 4180 (2015). DOI: 10.1039/c4cc09944c
[7] Wased, Y., Matsubara, E. & Shinoda, K. "Chpater 4: Diffraction from Polycrystalline Samples and Determination of Crystal Structure." *X-Ray Diffraction Crystallography Introduction, Examples, and Solved Problems*, Springer, 2011, page 107-167.